

**TLS supported volumetric and DFN  
modeling of a fault zone in the Lower  
Buntsandstein, SW Germany**

INAUGURAL – DISSERTATION

Zur Erlangung der Doktorwürde  
der Naturwissenschaftlich-Mathematischen Gesamtfakultät  
der Ruprecht-Karls-Universität  
Heidelberg

vorgelegt von

**Georg Josef Miernik**

Heidelberg, 2020







**TLS supported volumetric and DFN  
modeling of a fault zone in the Lower  
Buntsandstein, SW Germany**

INAUGURAL – DISSERTATION

Zur Erlangung der Doktorwürde  
der Naturwissenschaftlich-Mathematischen Gesamtfakultät  
der Ruprecht-Karls-Universität  
Heidelberg

vorgelegt von

**Dipl.-Geol. Georg Josef Miernik**  
aus Neckargemünd, Deutschland

Heidelberg, 2020

Gutachter:

Prof. Dr. Wolfgang Stinnesbeck  
Prof. Dr. Thilo Bechstädt

Tag der mündlichen Prüfung 21.04.2020



# Table of Contents

<b>Abstract .....</b>	<b>I</b>
<b>Kurzfassung .....</b>	<b>III</b>
<b>List of Symbols and Abbreviations .....</b>	<b>V</b>
<b>1 Introduction.....</b>	<b>1</b>
<b>1.1 Objectives.....</b>	<b>2</b>
<b>1.2 Study Area .....</b>	<b>3</b>
<b>1.3 Geological Setting .....</b>	<b>4</b>
1.3.1 Upper Rhine Graben.....	4
1.3.2 Stratigraphy.....	8
1.3.3 The Studied Outcrop.....	10
<b>2 Methods .....</b>	<b>13</b>
<b>2.1 Fieldwork.....</b>	<b>13</b>
2.1.1 Profile Mapping.....	13
2.1.2 Terrestrial Laser Scanning (TLS).....	13
<b>2.2 Digital Outcrop Model (DOM) .....</b>	<b>15</b>
<b>2.3 Fault Zone Lithology .....</b>	<b>15</b>
<b>2.4 Numerical Modeling .....</b>	<b>16</b>
2.4.1 Fault Zone Modeling.....	16
2.4.2 DFN Modeling.....	17
<b>3 Applied Methodology.....</b>	<b>18</b>
<b>3.1 Fault Zone Lithology and Petrophysics .....</b>	<b>19</b>
3.1.1 Damage Zone .....	19
3.1.1.1 Lithofacies Classification.....	19
3.1.1.2 Porosity and Permeability Determination and Distribution.....	19
3.1.2 Fault Core .....	19
3.1.2.1 Fault Core Facies Classification.....	19
3.1.2.2 Porosity and Permeability Determination and Distribution.....	22
<b>3.2 Digital Outcrop Model (DOM) .....</b>	<b>26</b>
3.2.1 Construction of the DOM.....	26
3.2.2 Data Merging and Digitalization.....	28
<b>3.3 Fault Zone Modeling .....</b>	<b>29</b>
3.3.1 Modeling Framework.....	29
3.3.2 Surface Modeling.....	31
3.3.3 Structural Modeling.....	31
3.3.3.1 Fault Framework.....	32
3.3.3.2 Horizon Modeling.....	32
3.3.3.3 Structural Gridding .....	33
3.3.4 Petrophysical Modeling .....	33
3.3.4.1 Damage Zone .....	33

3.3.4.2	Fault Core.....	33
3.3.5	Facies Modeling.....	35
3.3.5.1	Damage Zone.....	35
3.3.5.2	Fault Core.....	35
<b>3.4</b>	<b>DFN Parametrization .....</b>	<b>36</b>
3.4.1	Fracture Set Subdivision.....	36
3.4.2	Fracture Set Orientation Distribution.....	36
3.4.3	Fracture Shape .....	38
3.4.4	Fracture Set Aperture Distribution.....	38
3.4.5	Fracture Set Length Distribution .....	39
3.4.6	Fracture Set Length Truncation.....	40
3.4.7	Fracture Set Intensity Distribution .....	41
<b>3.5</b>	<b>DFN Modeling.....</b>	<b>42</b>
3.5.1	Fracture Network Calculation .....	43
3.5.2	Fracture Network Property Upscaling.....	45
3.5.2.1	Permeability .....	45
3.5.2.2	Sigma Factor .....	47
<b>4</b>	<b>Results.....</b>	<b>49</b>
<b>4.1</b>	<b>Lithology.....</b>	<b>49</b>
4.1.1	Damage Zone.....	49
4.1.2	Fault Core.....	58
<b>4.2</b>	<b>Petrophysics Determination .....</b>	<b>59</b>
<b>4.3</b>	<b>Digital Outcrop Model .....</b>	<b>60</b>
<b>4.4</b>	<b>Fault Zone Model .....</b>	<b>63</b>
4.4.1	Surface and horizon modeling .....	63
4.4.2	Structural Gridding .....	64
4.4.3	Petrophysics Distribution .....	65
4.4.4	Facies Model.....	65
<b>4.5</b>	<b>DFN Parametrization .....</b>	<b>72</b>
4.5.1	Fracture Set Division and Orientation.....	72
4.5.2	Fracture Set Aperture and Length Distribution.....	73
4.5.3	Damage Zone Fracture Set Length Truncation .....	73
4.5.4	Fracture Set Intensity Distribution .....	76
<b>4.6</b>	<b>DFN Model .....</b>	<b>80</b>
4.6.1	Fracture Networks.....	80
4.6.2	Fracture Network Properties .....	87
<b>5</b>	<b>Discussion .....</b>	<b>95</b>
<b>5.1</b>	<b>Outcrop Lithology and Depositional Environment.....</b>	<b>95</b>
<b>5.2</b>	<b>Fault Zone .....</b>	<b>103</b>
<b>5.3</b>	<b>Volumetric Fault Zone Modeling .....</b>	<b>104</b>
5.3.1	Grid Construction and Resolution.....	104
5.3.2	Fault Facies Model.....	108
5.3.3	Matrix Porosity and Permeability Determination .....	114
<b>5.4</b>	<b>Discrete Fracture Model .....</b>	<b>116</b>



5.4.1	Parametrization.....	116
5.4.2	Fracture Network Properties.....	124
<b>5.5</b>	<b>Implications on Reservoir Quality .....</b>	<b>131</b>
<b>6</b>	<b>Conclusion .....</b>	<b>133</b>
<b>7</b>	<b>References.....</b>	<b>135</b>
Appendix 1	Lithofacies Types after Miall (1977) .....	173
Appendix 2	Fault Core Facies Type Distribution Cases A and C .....	177
Appendix 3	Calculation of Truncation Values.....	181
Appendix 4	Intensity Results of all Geological Units of the DZ.....	185
Appendix 5	Full Aperture and Length Distribution Results.....	191
Appendix 6	Remaining Calculated DFN Results.....	219
Appendix 7	Full List of Fracture Network Property Results.....	229
Appendix 8	All Illustrations of DFN Property Results .....	239
	<b>Danksagung .....</b>	<b>251</b>







## **Abstract**

Fluid flow is governed by primary and secondary porosity of rocks but also by their permeability. Often the values of primary porosities and permeabilities are not sufficient to allow fluids to flow from potential geothermal or hydrocarbon reservoirs. To ensure an efficient productivity, fractured reservoirs come into focus as they might provide an economically viable fluid flow. Subsurface fractured reservoirs are difficult to investigate, outcrop analogues like the one investigated help in a better understanding. The studied outcrop represents a Lower Triassic braided river succession within an arid alluvial plain, affected by the main fault of the western Rhine Graben (southwestern Germany).

The research thesis was carried out with the help of terrestrial laser scanning (TLS) to generate a digital outcrop model (DOM), used to digitize data and serve as basis for the subsequent modeling in two steps. These are (i) the volumetric modeling of the investigated fault zone within the Triassic Lower Buntsandstein, and (ii) subsequent modeling of the discrete fracture network (DFN).

Volumetric modeling comprises three main points: (i) the application of a fault zone facies concept, (ii) stair-stepped fault gridding, and (iii) splitting the fault zone into two geobodies, well established in structural terminology, the damage zone 'DZ' and the fault core 'FC'. For the subsequent DFN calculations a thorough fracture data parametrization was carried out providing six defined fracture sets, the fracture shape, the log-normal aperture distribution, the log-normal length distribution, the  $P_{32}$  intensity, and fracture truncation percentages at bed boundaries (DZ only). DFN upscaling was then conducted with the "Oda" and "Oda Corrected" methods for the fracture permeability calculations.

The resulting volumetric model comprises 13 fault zone facies types. Their distribution within the DZ follows the encountered beds' morphology. Within the FC three facies distribution cases were modeled. Seven different DFN configurations were calculated, consisting of 162 fracture sets in total. Fracture permeability amounts between 190 and 720 D within the DZ and 14,130 to 55,189 D within the FC, while the fracture porosity shows values of about 0.4 % for the DZ and 2.38 % for the FC.

The study shows that volumetric fault zone modeling requires a simultaneous fault facies analysis and grid construction. Because stair-stepped fault grids facilitate a high complexity but lack cell size flexibility, a thoroughly considered choice of the cell size, dependent on the smallest geological objects present, is crucial. Characterization and

processing of fracture aperture constitutes the most important part of the parametrization, as different methods can lead to distinct differences in the modeled final fracture permeabilities, spanning multiple orders of magnitude, even for exactly the same values of mechanical aperture. Inclusion of fracture connectivity lowers the resultant horizontal fracture permeability by 26 to 38 %, while truncation of fractures on bed boundaries can overestimate permeability values. Although the FC shows a significantly higher fracture permeability than the DZ it is affected by extreme fracture permeability cutoffs due to the fault cores' specific architecture, resulting in a conduit-barrier system. Fracture porosities are more insensitive to parameter changes, because of its dependence on the mechanical aperture only.

The presented multi-approach thesis highlights the challenges, limitations, and great possibilities of fault zone models, to help in a better understanding of the impact fault zones might have on geothermal and hydrocarbon reservoirs, and thereby support exploration.

## Kurzfassung

Fließraten im Gestein werden sowohl von der primären und/oder sekundären Porosität, als auch von der Permeabilität bestimmt. Die Werte der primären Porosität und Permeabilität reichen oftmals nicht aus, um die benötigten Fließraten innerhalb eines potenziellen geothermischen Reservoirs oder einer potentiellen Kohlenwasserstofflagerstätte zu liefern. Um eine effiziente Produktivität sicherzustellen, rücken geklüftete Reservoirs in den Fokus, da sie häufig wirtschaftlich verwertbare Fließraten gewährleisten. Da sich jedoch die Verhältnisse im Untergrund schwierig gestalten, können Aufschlussanaloge (wie in dieser Studie) zum besseren Verständnis beitragen. Der untersuchte Aufschluss repräsentiert die untertriassische Abfolge eines verflochtenen Flusses innerhalb einer ariden alluvialen Schwemmebene, welche von der westlichen Haupttrandstörung des Rheingrabens (Südwestdeutschland) geschnitten wird.

Im Rahmen der präsentierten Arbeit wurde terrestrisches Laserscanning (TLS) eingesetzt um ein digitales Aufschlussanalogmodell zu erstellen. Dieses diente zur Digitalisierung der Daten und wurde darüber hinaus als Basis für die nachfolgenden Modellierungsschritte verwendet. Diese beinhalten: (i) die volumetrische Modellierung der untersuchten Störungszone im Unteren Buntsandstein der germanischen Trias und (ii) eine anschließende diskrete Kluftnetzwerkmodellierung.

Die volumetrische Modellierung umfasst drei Hauptpunkte: (i) die Ausarbeitung und Zuordnung einer Störungszonenfazies, (ii) ein „stair-stepped gridding“ der Störungszone, und (iii) die Aufteilung der Störungszone in zwei geologische Körper, welche in der Strukturgeologie als Bruchzone (damage zone, 'DZ') und Störungskern (fault core, 'FC') beschrieben werden. Für die nachfolgenden Berechnungen des Kluftnetzwerks wurde eine umfangreiche Parametrisierung der Kluftdaten durchgeführt. Diese liefert sechs definierte Kluftscharen, die Kluftform, die lognormale Verteilung der Apertur sowie der Kluftlänge, die  $P_{32}$  Intensität, und die prozentualen Anteile der Kluftterminationen an Schichtgrenzen (nur DZ). Um die Kluftpermeabilität zu berechnen, wurde die Hochskalierung der Kluftnetzwerke mit Hilfe der „Oda“ und „Oda Corrected“ Methoden durchgeführt.

Das resultierende volumetrische Störungszonenmodell umfasst 13 Faziestypen innerhalb der Störungszone. Ihre Verteilung innerhalb der DZ folgt der angetroffenen Schichtmorphologie. Im Falle des FC wurden drei verschiedene Fälle der Verteilung der Faziestypen modelliert. Es wurden sieben unterschiedliche Konfigurationen von

Kluftnetzwerken berechnet, welche insgesamt aus 162 Kluftscharen bestehen. Innerhalb der DZ beträgt die Kluftpermeabilität zwischen 190 und 720 D und 14.130 bis 55.189 D im FC. Die Kluftporosität beträgt etwa 0,4 % in der DZ und 2,38 % im FC. Die Arbeit zeigt, dass im Falle einer volumetrischen Modellierung einer Störungszone die Analyse der Störungfazies und die Konstruktion des „grids“ simultan ablaufen müssen. „Stair-stepped grids“ weisen eine hohe Komplexität auf, sind jedoch unflexibel bei der Zellengröße. Deshalb ist vor der Erstellung des „grids“ eine gründliche Überlegung im Hinblick auf die gewählte Zellengröße notwendig. Die Größe hängt vom kleinsten zu modellierenden geologischen Objekt ab.

Die Charakterisierung und Weiterverarbeitung der Apertur stellt den wichtigsten Teil einer Kluftparametrisierung dar. Verschiedene Methoden führen zu großen Unterschieden bei der final modellierten Kluftpermeabilität. Auch wenn exakt gleiche Werte der mechanischen Apertur verwendet wurden, kann die Kluftpermeabilität Unterschiede von mehreren Größenordnungen aufweisen. Berücksichtigt man die Kluftkonnektivität, so verringert sich die horizontale Kluftpermeabilität um 26 bis 38 %, während eine Klufttermination an Schichtgrenzen zu einer Überbewertung der Kluftpermeabilität führen kann. Obwohl der FC, im Vergleich zur DZ, eine signifikant höhere Kluftpermeabilität aufweist, ist er von extremen Schwankungen der Permeabilität betroffen. Diese sind auf die spezifische Architektur des FC zurückzuführen, weshalb dieser Bereich ein kombiniertes System aus Fließwegen, als auch von Barrieren darstellt. Die Kluftporosität ist im Vergleich zur Kluftpermeabilität relativ unempfindlich gegenüber Parameteränderungen, da sie lediglich von der mechanischen Apertur abhängt.

Die präsentierte Arbeit verwendet einen vielschichtigen Ansatz und zeigt die auftretenden Herausforderungen, Grenzen und großen Möglichkeiten der Modellierung von Störungszonen auf. Derartige Modelle tragen dazu bei, den potentiellen Einfluss von Störungszonen auf die geothermische Produktion und Kohlenwasserstofflagerstätten besser abschätzen zu können und damit die Explorationsarbeiten zu unterstützen.



## List of Symbols and Abbreviations

$\alpha$	Angular radius of a confidence cone
$A_k$	Area of fracture $k$
$b$	Distance between two plates / aperture
$\alpha_{95}$	Angular radius of a confidence cone for 95 % confidence
$\delta_{ij}$	Kronecker delta
$e$	Euler number
$F_{ij}$	Fracture tensor
$f_k$	Percolation factor for fracture $k$
$F_{kk}$	Trace of the fracture tensor matrix
$g$	Gravitational acceleration
$\nabla h$	Hydraulic gradient
$H_f$	Fracture height
$\kappa$	Concentration parameter (Fisher distribution)
$\kappa_{\text{INT}}$	Intermediate concentration parameter (Bingham distribution)
$\kappa_{\text{MIN}}$	Minimum concentration parameter (Bingham distribution)
$k$	Fracture
$k_{ij}$	Permeability tensor
$k_m$	Matrix permeability
$k_p$	Fracture permeability
$L$	Length of matrix block
$L_f$	Fracture length
$L_x$	Distance between fractures in x direction
$L_y$	Distance between fractures in y direction
$L_z$	Distance between fractures in z direction
$\mu$	Fluid viscosity
$N$	Total number of fractures in a grid cell
$n$	Number of normal sets
$n_{ik}$	i-component of a unit normal to fracture $k$
$n_{jk}$	j-component of a unit normal to fracture $k$
$n_v$	Number of vectors/orientations
$P_f$	Fracture pressure
$P_m$	Matrix pressure
$\Phi$	Fracture porosity

$Q$	Flow between two plates
$q$	Matrix-fracture flow rate per unit bulk volume
$R$	Length of resultant vector
$\sigma$	Sigma factor
$T_k$	Transmissivity of fracture $k$
$\rho$	Fluid density
$V$	Grid cell volume

AOI	Area of interest
$A_r$	Realized accommodation
B1-4	Minor cycles of the Grés Vosgien Formation
CB	Carbonate breccia
CG	Clay gouge
CI	Connectivity index
DBC	Deformation band cluster
DFN	Discrete fracture network
DOM	Digital Outcrop Model
DZ	Damage zone
eCii	Extended connectivity index along the i axis
eCij	Extended connectivity index along the j axis
eCik	Extended connectivity index along the k axis
EPM	Equivalent porous media
ER	Enhanced range
FC	Fault core
FCFB	Fault core facies body
FCFT	Fault core facies type
FN	Fracture network
G1-2	Genetic unit cycles of the Trifelsschichten
Gc	Gouge, clay unconsolidated
Gs	Gouge, silt unconsolidated
GU	Geological unit
H	Height
HCE	Hydrocarbon exploration
IFN	Implicit fracture network
JRC	Joint roughness coefficient

$k_i$	Fracture permeability in i direction
$k_j$	Fracture permeability in j direction
$k_k$	Fracture permeability in k direction
L	Length
LGR	Local grid refinement
$L_i$	Length ratio of fractures present in a cell projected on the i axis
LiDAR	Light detection and ranging
$L_j$	Length ratio of fractures present in a cell projected on the j axis
$L_k$	Length ratio of fractures present in a cell projected on the k axis
MP	Megapixel
No.	Number
OdaC	Oda corrected
P1	Profile 1
$P_{ij}$	Fracture intensity classification system
$P_{10}$	Number of fractures per unit length
$P_{11}$	Length of fractures per unit length
$P_{20}$	Number of fractures per unit area
$P_{21}$	Length of fractures per unit area
$P_{22}$	Area of fractures per area
$P_{30}$	Number of fractures per unit volume
$P_{32}$	Area of fractures per unit volume
$P_{33}$	Volume of fractures per unit volume
PPMV-pair	Pair of porosity and permeability matrix values
PRF	Pulse repetition frequency
Sc	Sandstone consolidated
SCa	Secondary calcite vein
SCaCB	Cemented breccia
SCB	Shale supported carbonate breccia
Sec	Second
SGS	Sequential Gaussian Simulation
SIS	Sequential Indicator Simulation
Ss	Sandstone spreading
SS	Shale smear
Su	Sandstone unconsolidated
SZ	Slip zone

T1	Trace 1
TGS	Truncated Gaussian Simulation
TLS	Terrestrial laser scanning
URG	Upper Rhine Graben
VBM	Volume Based Modeling
W	Width

## 1 Introduction

The Upper Rhine Graben (URG) has a long exploration history. The oil springs of “Baechel Brunn” were first mentioned in 1498 by the historian Jacob Wimpfeling, making them the first reported oil field in Europe. Originating from the exploitation of these oil seeps near Pechelbronn the hydrocarbon exploration started in 1627 and increased strongly during the 19<sup>th</sup> and 20<sup>th</sup> century with a total of 29 oil and gas fields exploited, and under exploration to this day (Mauthe et al., 1993; Reinhold et al., 2016). In contrast to Paleo- and Neogene successions, the Triassic Buntsandstein did not get much attention as a reservoir rock. However, the price-increase and especially the discovery of oil within the Buntsandstein near Speyer in 2003, during exploration for geothermal waters, moved it into focus.

The deep geothermal energy history within the URG, on the other hand, is much younger with currently (March, 2020) five producing geothermal power plants (two on the French and three on the German side). In Soultz-sous-Forêt (France) the development of deep geothermal energy is driven forward since 1987. Its power plant started production in 2008. In Rittershoffen a second power plant in Alsace produces energy since 2016. On the German side power plants are located in Landau, Bruchsal, and Insheim (start of production in 2007, 2009, and 2012, respectively). Induced seismicity during production in Soultz-sous-Forêt and Landau, and an induced earthquake in 2006 through fracking of a geothermal well in the Basel area lead to increased resistance against such projects and a temporary stop of production in Landau. As a further consequence, also a promising project within the URG in Brühl was stopped due to strong political and public resistance.

Because high production rates are necessary for deep geothermal reservoirs to be profitable, fractured reservoirs are in the main focus of interest. More particularly fault zones bear a high geothermal potential as their damage zone shows an increase in fracture density. The fault core itself, however, can act either as a fluid barrier or a conduit. Caine et al. (1996) describes a fault zone as a lithologically heterogeneous and structurally anisotropic discontinuity in the rock, which points out the complexity as such. To understand geothermal reservoir rocks in the subsurface better, the multidisciplinary research project ‘AuGE’ (Outcrop **A**nalogue **S**tudies in **G**eothermal **E**xploration) was started in 2011. The project was funded by the German Federal Ministry for the Environment, Nature Conservation, Building and Nuclear Safety, and subsequently by the German Federal Ministry for Economic Affairs and Energy

(reference number 0325302D). Main aim of AuGE was the investigation of outcrop analogues of potential reservoirs in the subsurface of the URG, and more specifically the detailed analysis, classification and modeling of fault zones to better understand reservoir relevant processes, and to predict potential issues during geothermal exploration. The research groups involved come from the GeoZentrum Nordbayern, the University of Göttingen, and the Heidelberg University. Two industrial partners, GeoThermal Engineering GmbH, Karlsruhe, and GeoEnergy GmbH, Karlsruhe, provided further support.

### 1.1 Objectives

The primary aim of the part of the project presented here was to investigate the properties of fractured reservoirs in outcrop to assess their geothermal potential within the subsurface of the URG applying a multi-method approach on outcrop analogues.

The thesis deals with the volumetric modeling of a specific outcropping fault zone within the Triassic Lower Buntsandstein. A fault facies concept was applied with subsequent discrete fracture network (DFN) modeling to provide a better understanding of fault zones in general and to present implications on production from potential geothermal and hydrocarbon reservoirs. As the research relied on data and results provided by the project partners, the presented thesis could only be finished with a strong temporal delay.

Its **first** main objective was to construct a digital outcrop model (DOM) to gather, visualize and georeference the data acquired by the project partners and the author. This included terrestrial laser scanning (TLS) and profile mapping synchronized with data by the project partners. The aim of the elaborated DOM was to serve as a basis for the own subsequent volumetric modeling.

The **second** main objective comprises the construction of a volumetric fault zone model with the application of a fault facies concept. Therefore the fault zone was split into two geobodies, well established in structural geology, the damage zone and the fault core, which were treated separately in terms of facies distribution and petrophysical properties. The aim was to: (i) provide a detailed fault zone facies model offering many exciting options for subsequent DFN modeling, (ii) point out the challenges and possibilities of volumetric fault zone modeling, and (iii) evaluate the implication of fault facies on fractured reservoirs with the help of the own facies distribution results.

The **third** main objective was to enhance the volumetric fault zone model with a DFN model, again calculated separately within the two geobodies. For this purpose the

author conducted a thorough fracture data parametrization. The aim of the upscaled DFN model is to: (i) conduct and compare diverse fracture properties, (ii) examine the impact of parametrization and different modeling techniques, and (iii), examine the implication on fractured reservoirs.

## 1.2 Study Area

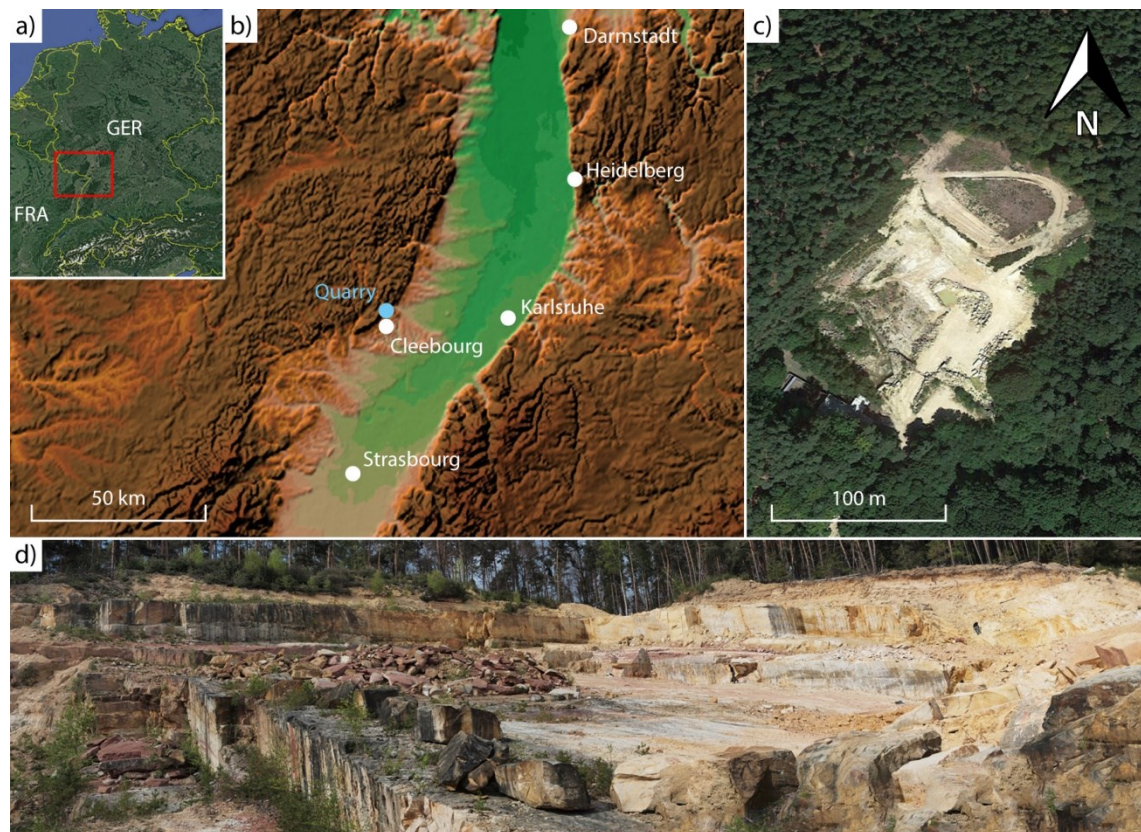


Figure 1: (a) The red rectangle marks the outlines of the study area for project AuGE within Central Europe. (b) Topographic map of the outlined area with the location of the Buntsandstein quarry near Cleebourg at the western graben shoulder of the URG (GTOPO30 elevation data). (c) Aerial view of the Buntsandstein quarry near Cleebourg. (d) Panoramic overview of the quarry facing north (picture by Dominik Soyk). Aerial views a) and c) from Google Earth Pro (Google LLC, 2018).

Project AuGE was focused on the rift basin of the Upper Rhine Graben (URG), which spans parts of Germany, France and Switzerland. With the highest geothermal gradient in Germany of partly over 50 °C/km (Sauer et al., 1982; Prinz and Strauß, 2018) it bears a high potential for geothermal energy production.

Natural outcrops in the URG are often not very good. Artificial outcrops (quarries) were mostly placed in areas distant from fault zones, faults within quarries are quite rare due to economic reasons. This study is focused on a key area, an active quarry at the western graben shoulder of the URG near Cleebourg (Alsace, France). An outcrop of a fault zone

within the quarry Cleebourg was the reason to choose this locality for research. It is located about 3 km south of the French-German border at the coordinates  $49^{\circ}0'48.92''\text{N}$  /  $7^{\circ}53'24.54''\text{E}$  (Figure 1) and has a dimension of about 150 x 200 m.

### 1.3 Geological Setting

#### 1.3.1 Upper Rhine Graben

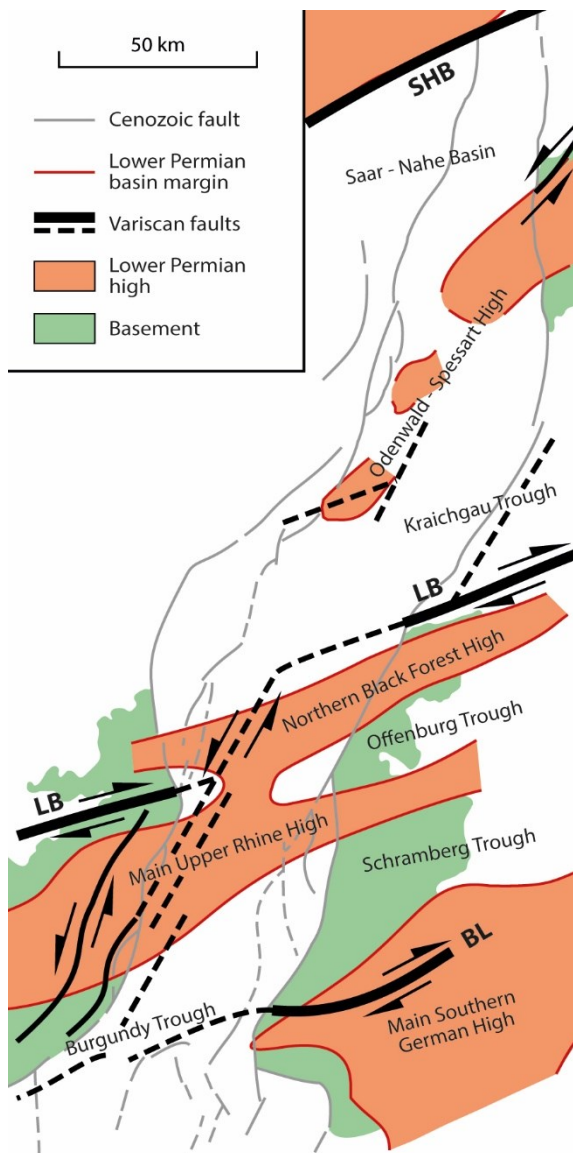


Figure 2: Structural preift setting of the URG area showing the most prominent Variscan faults (SHB: South Hunsrück-Taunus border fault; LB: Lalaye-Lubine-Baden-Baden fault; BL: Badenweiler-Lenzkirch zone), Permo-Carboniferous troughs and highs and superimposed main fault traces of the Cenozoic graben in grey (modified after Schumacher, 2002 and Bauer, 2018).

The main structural trends of the URG area were already established during the Variscan orogeny in Palaeozoic times, in particular during the Permo-Carboniferous phase of wrench tectonics (Ziegler, 1990; Edel and Weber, 1995). Most distinctive is a NE to ENE striking trend with three major dislocation zones (Edel and Fluck, 1989; Schumacher, 2002): (i) the Hunsrück-Taunus border fault (Anderle, 1987), (ii) the Lalaye-Lubine-Baden-Baden fault (Wickert and Eisbacher, 1988), and (iii) the Badenweiler-Lenzkirch (Todtnau fault) zone (Krohe and Eisbacher, 1988) which subdivided the Variscan Internides and led to the formation of Permo-Carboniferous troughs and highs (Figure 2).

Another important Variscan trend is marked by NNE oriented sinistral fault zones that are associated with Lower Carboniferous to Permian intrusive bodies and dyke swarms of the Vosges, Black Forest and Odenwald Mountains. The latter faults are seen as precursors of the Cenozoic URG (Cloos, 1939; Illies, 1962; Schwarz and Henk, 2005; Ziegler



and Dèzes, 2006). After the end of the Variscan Orogeny and at the beginning of the breakup of the Pangean supercontinent the epicontinental Germanic Basin (also called Central European Basin) started to develop and persisted until the Late Jurassic (Ziegler, 1990; Golonka and Ford, 2000; Reinhardt and Ricken, 2000; Scheck-Wenderoth et al., 2008). It extended over 1500 km from the British Isles in the west to Poland in the east and from the North Sea in the north to Switzerland in the south (Ziegler, 1990; Beutler and Szulc, 1999; Feist-Burkhardt et al., 2008). Variscan massifs served as source for clastic sedimentation and the interplay of subsidence, sediment supply, and sea-level fluctuation lead to the formation of different facies types of Triassic to Late Jurassic sediments (Bachmann et al., 1999; Feist-Burkhardt et al., 2008). These Mesozoic successions cover the partly peneplained Variscan basement and rest discordantly on the Permo-Carboniferous series (Schumacher, 2002). Triassic and Jurassic intraplate tectonics hardly had any influence on the prerift structure of the URG, though minor Mesozoic reactivation of late Palaeozoic fault systems is documented (Wetzel and Allia, 2000). Cretaceous sediments do not occur within the URG, because they were either not deposited or subsequently eroded (Ziegler, 1990; Reicherter et al., 2008). Rifting in the South Atlantic and the Pyrenean Orogeny during the Late Cretaceous led to an inversion of the Germanic Basin, which in southern Germany caused the partial erosion of Mesozoic strata (Reicherter et al., 2008).

During the late Eocene the formation of the URG was initiated (Illies, 1965; Illies, 1974; Pflug, 1982; Tobien, 1987; Hüttner, 1991; Ziegler, 1992; Schwarz, 1997; Schumacher, 2002; Dèzes et al., 2004; Schwarz and Henk, 2005; Reicherter et al., 2008). The N-S to NNE-SSW compressional stress field led to the reactivation of Variscan and Permo-Carboniferous ENE-WSW and NNE-SSW oriented dislocation zones in a transtensional strike-slip mode (Figure 3; Berger, 2002) and the individual late Palaeozoic troughs coalesced into the NNE trending graben in the late Priabonian (Schumacher, 2002; Schwarz and Henk, 2005). The following NW-SE to WNW-ESE extension initiated the rifting of the URG (Larroque and Laurent, 1988). Its main phase ended in the early Oligocene, but in the northern parts of the URG lasted until the late Oligocene (Illies and Greiner, 1979; Ziegler, 1992; Ziegler and Dèzes, 2006).

In the early Miocene the stress field of the URG started to rotate from a NW-SE oriented extension to a NE-SW oriented extension (Bergerat, 1985), which led to contraction, local inversion, and sinistral and dextral oblique displacements of the major graben-forming faults (Illies, 1975; Illies and Greiner, 1979; Bauer, 2018). Subsidence and sedimentation took place in the northern part of the URG (Doebel, 1967, 1970). In

contrast, the central and southern segments experienced uplift and partial erosion due to (i) reactivation of the central graben segment around Karlsruhe, and (ii) northern migration of the Alpine forebulge (Illies and Greiner, 1979; Laubscher, 1992; Rotstein et al., 2005; Rotstein and Schaming, 2011).

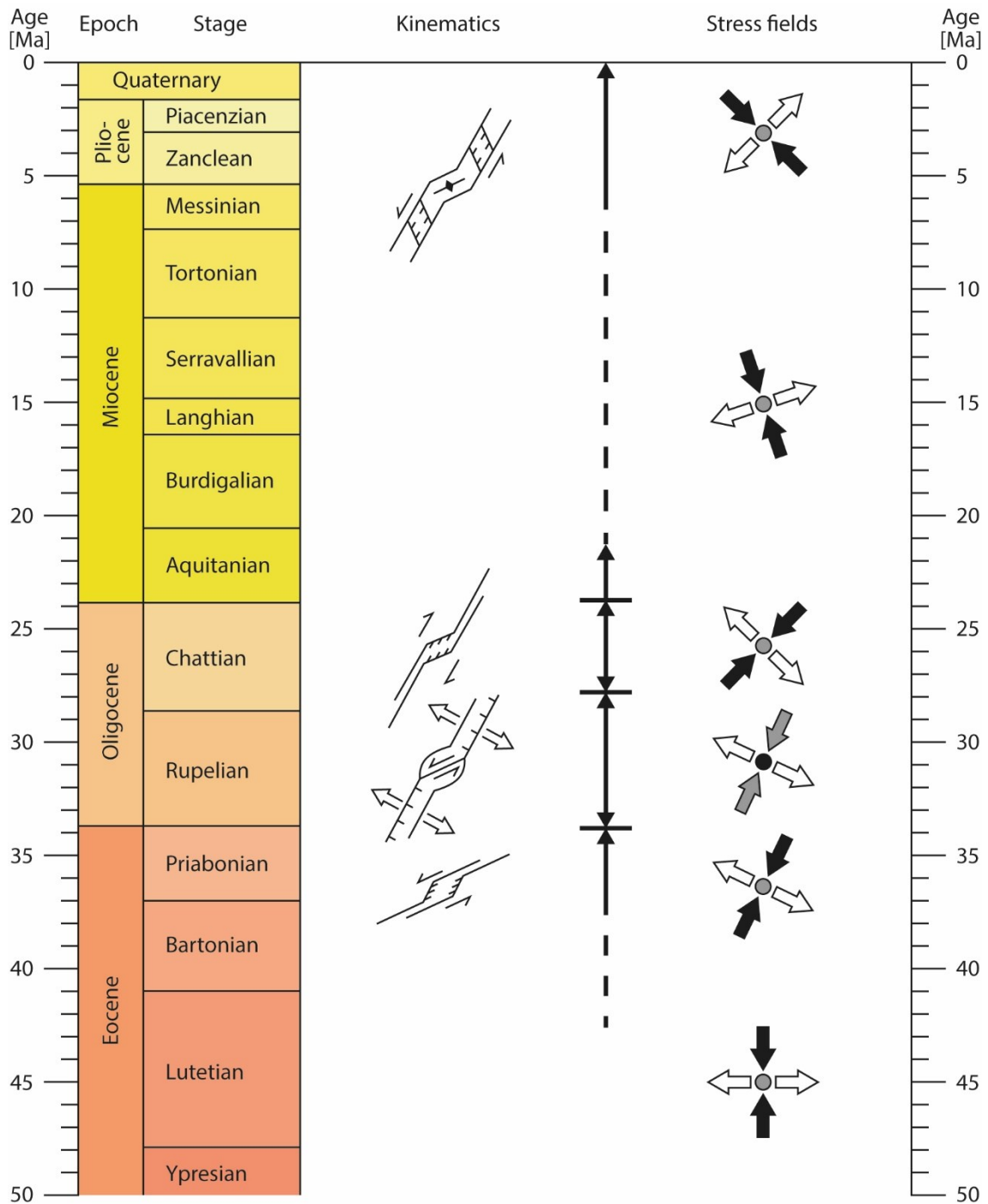


Figure 3: Stratigraphic overview of kinematics and stress field orientations during the URG formation ( $\sigma_1$  black,  $\sigma_2$  shaded,  $\sigma_3$  white; kinematics and stress fields after Schumacher, 2002).

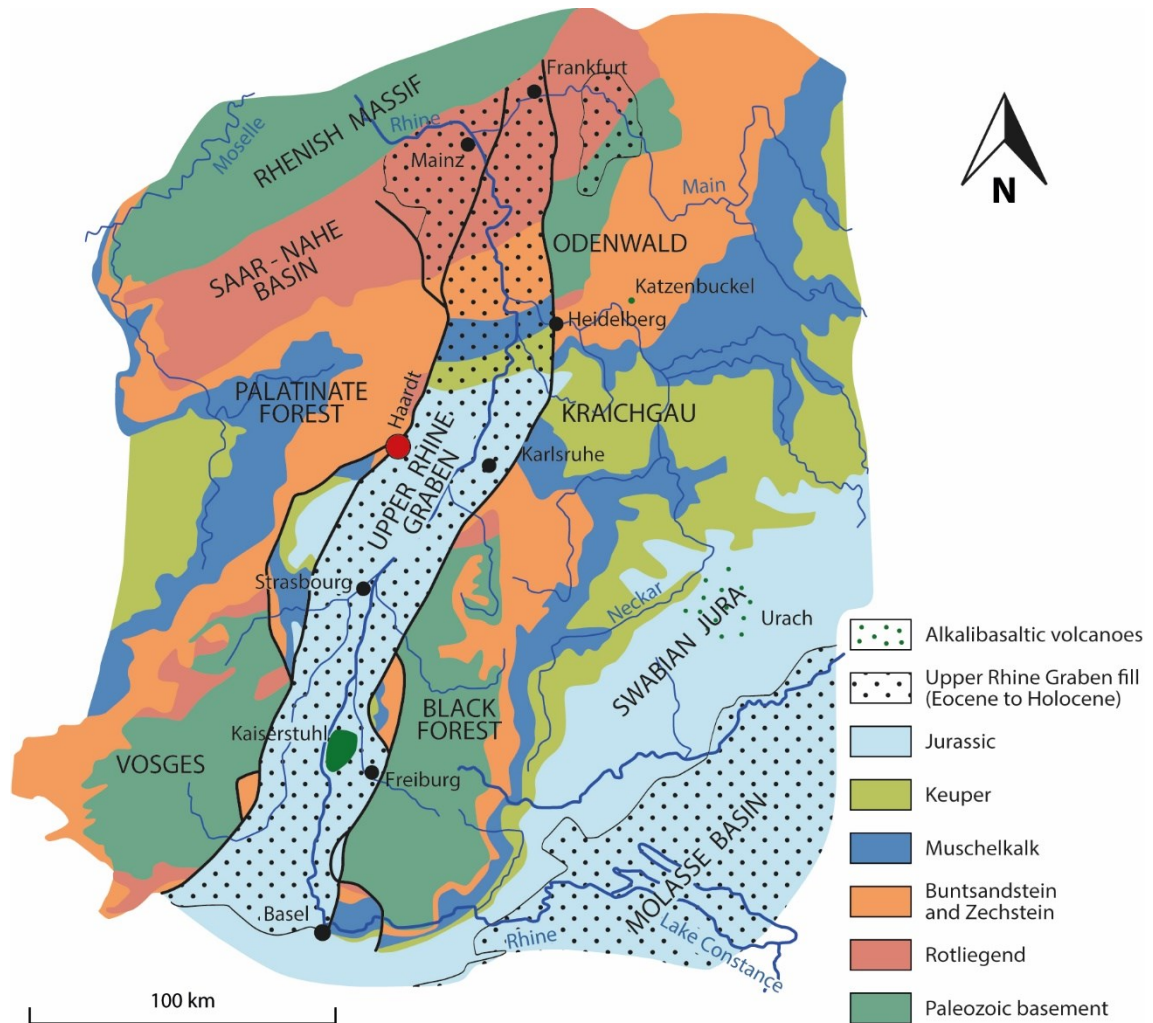


Figure 4: Geological map of the URG area. The stratigraphic succession underneath the Eocene erosional base of the URG and Molasse basin is indicated by the color in addition to the black dotted signature. The large red dot shows the location of the Lower Buntsandstein quarry near Cleebourg. Map modified after Eisbacher and Fielitz (2010).

In Quaternary times subsidence resumed in the southern segments of the URG while the rift shoulders were uplifted (Bartz, 1974; Demoulin et al., 1998). Being still a subject of many studies, the recent tectonic stress field of the URG is characterized by (i) a uniform NW-SE to NNW-SSE oriented maximum horizontal stress with local variations of  $130^{\circ}$  to  $135^{\circ}$  in northern parts, and (ii)  $145^{\circ}$  to  $160^{\circ}$  in southern parts of the URG (Delouis et al., 1993; Plenefisch and Bonjer, 1997; Meixner et al., 2016; Heidbach et al., 2018).

Today the URG forms the central segment of the European Cenozoic rift system (Ziegler, 1994; Prodehl et al., 2006) and extends about 300 km from the Basel area in the south to the Frankfurt area in the north with an average width of 30-40 km (Figure 4). It is characterized by a half-graben structure with variable syn-sedimentary thicknesses. The thickest succession occurs in the northern segment close to the eastern main border

fault near Heidelberg and in the southern segment close to the western main boundary fault (Doebel and Teichmüller, 1979; Wenzel and Brun, 1991; Brun and Gutscher, 1992). In the study area, sediments are up to 3400 m thick close to the eastern margin of the Heidelberg Basin and decrease at the western margin of the URG to about 300 m thickness (Buness et al., 2008).

### 1.3.2 Stratigraphy

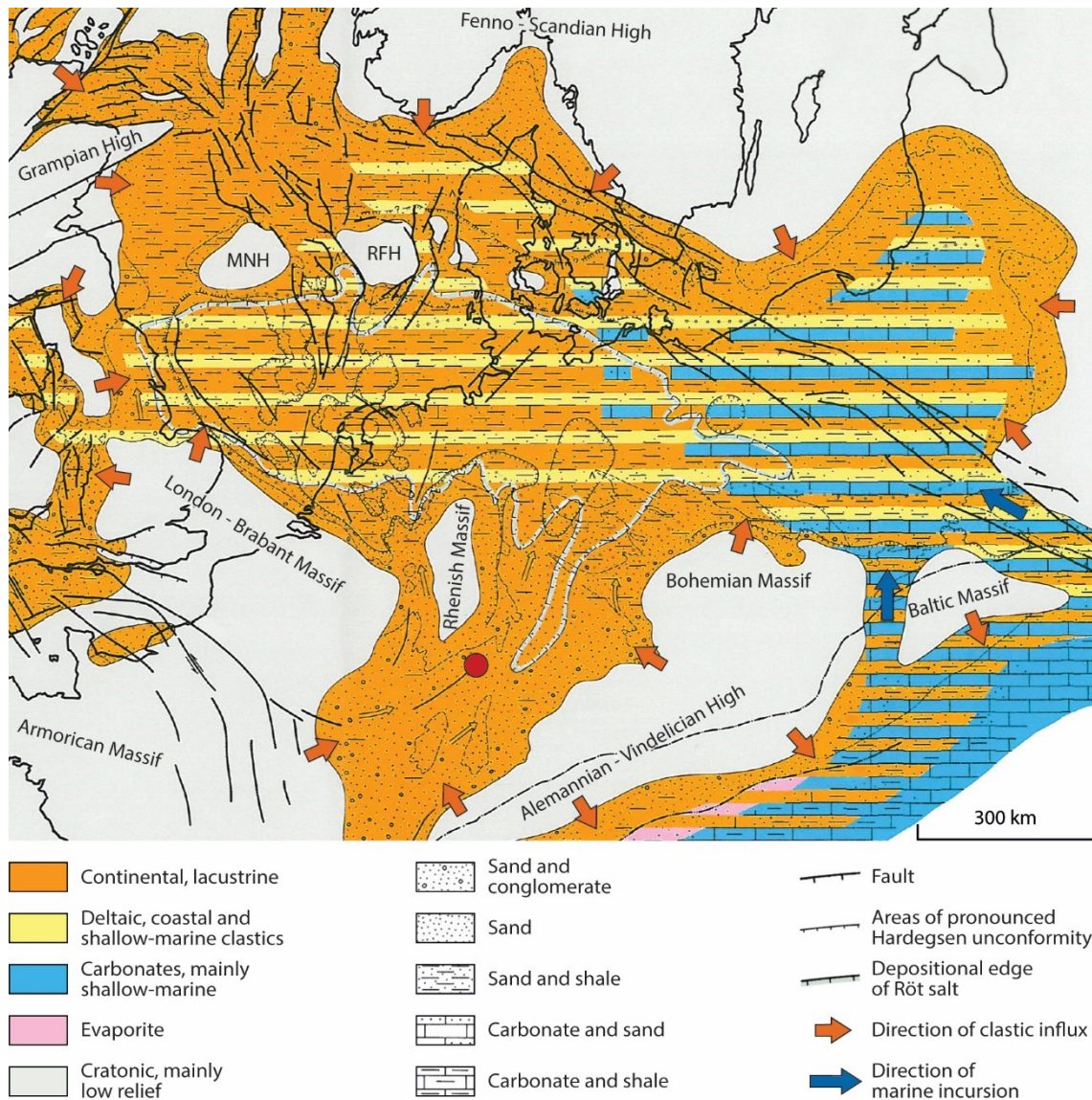


Figure 5: Buntsandstein paleogeography with the location of the studied outcrop (red dot). MNH: Mid North Sea High; RFH: Ringkøbing-Fyn High. Modified after Ziegler (1990).

The Buntsandstein Group of the Germanic Triassic is classified into the Lower, Middle and Upper Buntsandstein, further divided by lithostratigraphic formations, which show distinct lateral variabilities (see Lepper et al., 2006). The stratigraphic subdivision was initially based on solely lithological criteria (von Alberti, 1834), whereas Boigk (1959)

introduced a modern Buntsandstein lithostratigraphy based on geological mapping and wireline logs (Szurlies, 2007). Furthermore the Buntsandstein is characterized by a prominent cyclicity, which is subdivided into 10 to 30 m thick fining upward cycles (Dachroth, 1985; Paul and Klarr, 1988; Geluk and Röhling, 1997; Szurlies, 2001; Roman, 2004). The correlation of this cycles over the Germanic Basin allows for a high-resolution cyclostratigraphic framework, proven by magneto- and biostratigraphic methods, as well as wireline logs (Szurlies et al., 2003; Szurlies and Kozur, 2004; Hagdorn et al., 2009; Soyk, 2015). In addition widely traceable unconformities (Krämer and Kunz, 1969; Ortlam, 1974; Beutler, 1991; Aigner and Bachmann, 1992; Evans et al., 1993; Rettig, 1995; Geluk and Röhling, 1997; Nawrocki, 1997; Radies et al., 2005; Filomena and Stollhofen, 2011) were used to propose a sequence stratigraphic framework (Aigner and Bachmann, 1992; Geluk and Röhling, 1997).

However, in the southern marginal area of the Germanic Basin the above-mentioned cycles cannot be traced and the lithostratigraphic correlation is often uncertain. Reasons are a drastic decrease in sediment thickness, missing or stacked unconformities and an incomplete stratigraphic record. It is therefore very difficult to distinguish the different formations present farther to the north. The differences are due to proximity to the source areas, which caused the eroded material to often bypass the investigated area to basin center in the north, resulting in increased grain sizes and noncontinuous sedimentation in the area of the URG (Figure 5; Backhaus, 1974; Paul, 1982; Dachroth, 1985; Ziegler, 1990; Lepper et al., 2006).

<b>NE-France</b> (Hollinger, 1969, Konrad, 1971; based on Perriaux, 1961)		<b>Palatinate Forest</b> (Backhaus, 1974; Richter-Bernburg, 1974)		<b>Palatinate Forest</b> (German Stratigraphic Commission, 2016)		Sedimentary Cycles
Buntsandstein	Upper	Grès à Voltzia	Voltziensandstein	Upper	Buntsandstein	Röt
		Couches intermédiaires	Zwischenschichten			
	Middle	Zone limite violette	<i>absent in the PF</i>	Middle	Buntsandstein	Hauptkonglomerat
		Conglomérat principal	Hauptkonglomerat			
			Obere Felszone			
		Grès Vosgien	Karlstalschichten			
			Rehbergschichten			
	Trifelsschichten					
	Lower	Couches de Sénonès	Annweiler-Schichten	Lower	Zechstein	Eck

Figure 6: Overview of the lithostratigraphic subdivisions for the Buntsandstein in NE-France (Vosges) and the Palatinate Forest. The studied outcrop is classified as “Grès Vosgien” (Middle Buntsandstein) in France and as “Trifelsschichten” (Lower Buntsandstein) in Germany. Sedimentary cycles after Eisbacher and Fielitz (2010). PF: Palatinate Forest.

This stratigraphic uncertainty led to a controversy about the subdivision of the Buntsandstein strata in especially the western part of the URG, resulting in various classifications for this marginal area and different local names (Andreae et al., 1892; Perriaux, 1961; Hollinger, 1969; Konrad, 1971; Backhaus, 1974; Richter-Bernburg, 1974; M nillet et al., 1989; Bourquin et al., 2006; German Stratigraphic Commission, 2016). Furthermore the location of the studied outcrop close to the German-French border caused geologists to use either the French or the German stratigraphy, which differ. An overview of the most common classifications for the outcrop area is given in Figure 6, while this thesis applies the most recent stratigraphic subdivision after the German Stratigraphic Commission (2016).

### 1.3.3 The Studied Outcrop

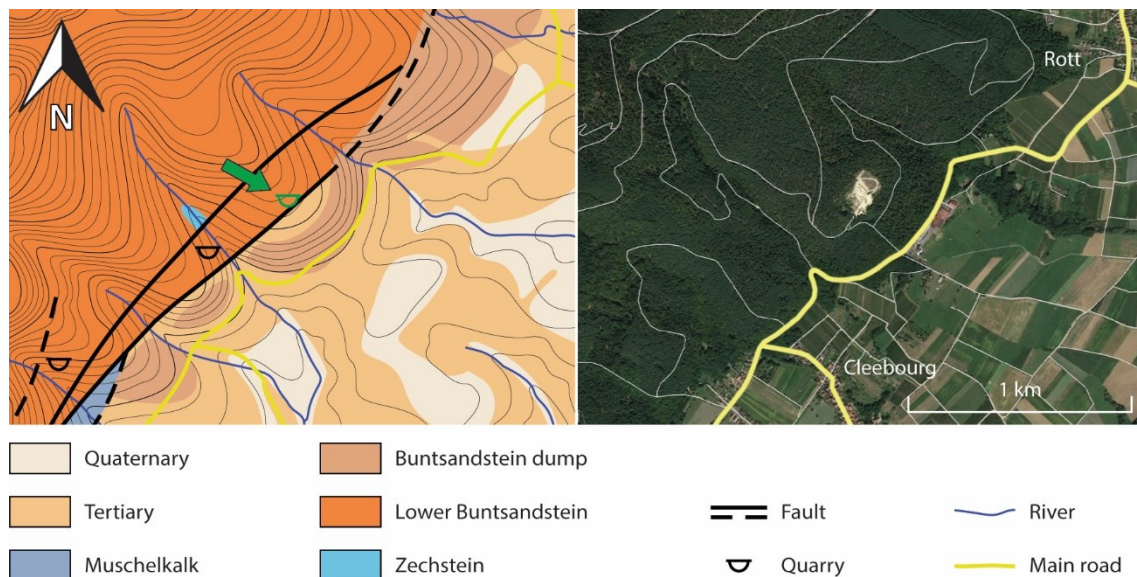


Figure 7: Geological map and (at the same scale) aerial view of the studied outcrop and its environs. The outcrop is marked with a green arrow and signature on the geological map and visible as a bright domain in the forest on the aerial view. The geological map is based on M nillet et al. (1989) with an updated stratigraphy after the German Stratigraphic Commission (2016). Aerial view from Google Earth Pro (Google LLC, 2018).

The southern marginal area of the Germanic Basin comprises three major sedimentary cycles (see Figure 6): Two progradational fluvial cycles (“Eck-Zyklus” and “Hauptkonglomerat-Zyklus”) followed by a third retrogradational fluvial cycle (“R t-Zyklus”; Eisbacher and Fielitz, 2010).

Andreae et al. (1892) classified the studied outcrop as “Lower Gr s Vosgien”, M nillet et al. (1989) as “Gr s Vosgien, undifferentiated” while Eisbacher and Fielitz (2010) allocated the outcrop to the “Trifelsschichten”. Despite these differences in nomenclature all authors refer to the same succession (see Figure 6). By applying the

stratigraphic subdivision of the German Stratigraphic Commission (2016) the studied outcrop will be referred to the “Trifelsschichten” of the Lower Buntsandstein (Figure 7), which is located in the first progradational fluvial cycle called “Eck-Zyklus” by Eisbacher and Fielitz (2010) that started already in the Permian.

During the Early Buntsandstein times the Germanic Basin largely resembled the geometry of the previous Zechstein Basin, but overstepped its former margins. Clastic sediments from the northern and southern basin margins were transported towards the central Germanic Basin, where a playa-lake to shallow marine environment developed (Figure 5; Wolburg, 1961; Trusheim, 1963; Wolburg, 1968; Ziegler, 1990; Feist-Burkhardt et al., 2008; Soyk, 2015). Along the basin margins fluvial, alluvial, lacustrine and minor aeolian sediments were deposited while the transition from predominantly sandy fluvial to mainly shaly playa successions took place just to the north of the Rhenish Massif (Füchtbauer, 1967; Backhaus, 1974; Dachroth, 1985). The thickness of the Lower Buntsandstein reaches 400 to 450 m in the central part of the Germanic basin and 280 to 340 m in the more southward Rhön and Fulda area (Backhaus and Reul, 1971; Ziegler, 1990; Feist-Burkhardt et al., 2008), while for the southern marginal basin area, where the studied outcrop is located, a maximum thickness of 250 m is reported for the Buntsandstein Group (Eisbacher and Fielitz, 2010). This thickness information comprises not only the Lower Buntsandstein, but

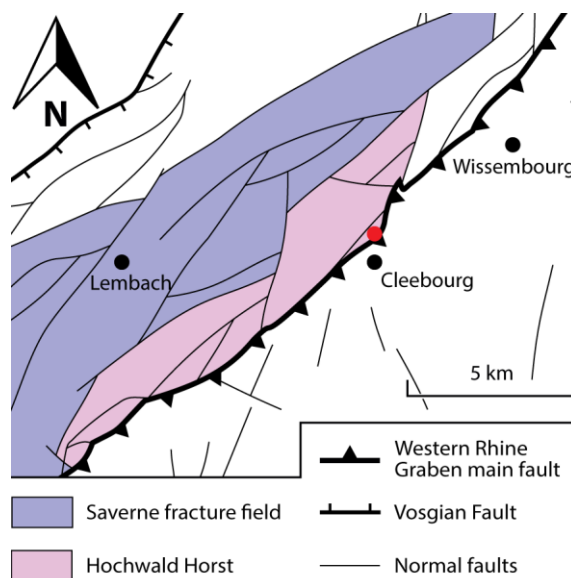


Figure 8: Tectonic setting of the proximate area of the studied outcrop (marked as red dot) showing the north-eastern part of the Saverne fracture field and the Hochwald Horst. Based on maps and data from Stapf (1988); M enillet et al. (1989); and Stapf (1996).

also the “Karlstalschichten” of the Middle Buntsandstein, indicating an even smaller thickness for the Lower Buntsandstein on its own.

In the southwest of Wissembourg (Figure 8) the Germanic Basin is split into several mainly southeastward tilted blocks within the 10 km wide Saverne fracture field, which is confined by the Vosgian Fault in the west and the Rhine Graben main border fault in the east (Eisbacher and Fielitz, 2010). These blocks comprehend normal conjugate to left-lateral shear fault systems, forming small horsts and grabens (Bossennec et al., 2018).

The studied outcrop is located in the northeast of the Saverne fracture field on the edge of the 2 km wide Hochwald Horst (Figure 8), which is part of a flexure zone with layers dipping up to 40° in south-eastern direction (Eisbacher and Fielitz, 2010). A large fault can be observed within the studied outcrop, which is probably the Rhine Graben main fault with a displacement of 900 to 1200 m (Doebel, 1967; Doebel and Olbrecht, 1974; Eisbacher and Fielitz, 2010). This will be discussed in chapter 5.2.

The whole outcrop represents a foot wall (Figure 9). The fault core crops out with a minimum thickness of 14 m (Bauer et al., 2015), and a 50 to 60 m thick damage zone, its external limits not visible. Both parts of the outcrop are clearly differentiated by a slip surface. The fault core is characterized by consolidated to unconsolidated material composed of sand, silt and clay and structural elements of mostly slip surfaces and deformation bands (Bauer et al., 2015). The damage zone shows mainly fine to medium grained sandstones with a relatively good sorting (Bossennec et al., 2018). These sandstones are yellowish-light to brownish bleached and represent the “Haardtrand Fazies”, mixed with bright-white bleached and red sandstones (Soyk, 2015).



Figure 9: View in north-west direction of a part of the studied outcrop representing a fault zone. The damage zone and the fault core are separated by a slip surface marked roughly by a red line. Geologists for scale are marked by a red arrow (picture by Dominik Soyk).



## 2 Methods

The main part of this study regards the numerical modeling of the fault zone. To provide the framework for the modeling classical geological fieldwork, as well as terrestrial laser scanning (TLS) and subsequent development of a digital outcrop model (DOM) was carried out. In addition data provided by project partners were processed and integrated in this thesis.

### 2.1 Fieldwork

#### 2.1.1 Profile Mapping

To cover the whole succession of the Buntsandstein outcrop near Cleebourg four geological profiles were mapped considering lithology, layer thickness, sedimentary structure, sorting, grain-size, and erosion of bases. Geological compass measurements provided information regarding the layer orientation. Through additional layer tracing the lateral thinning or thickening were examined. Based on this information the succession was subdivided into geological units.

#### 2.1.2 Terrestrial Laser Scanning (TLS)

Laser scanning, also known as LiDAR (Light Detection And Ranging), is a technique that came into the focus of surveying around the millennium turn (Kraus and Pfeifer, 1998; Evans et al., 2001; Persson et al., 2002; Reutebuch et al., 2005). TLS, as a more specific section of laser scanning, was applied more widely in the early twenty-first century as the equipment became smaller and more robust. Along with new software being developed, which was able to deal with more complex data, the method obtained practical use for fieldwork in different parts of applied science with a very high potential for geology (Fröhlich and Mettenleiter, 2004; Slob and Hack, 2004; Buckley et al., 2008; Vosselman and Maas, 2010; Schumann et al., 2011). In this study TLS was accomplished with the scanner ILRIS HD-ER from Optech operated by a laptop (Figure 10), employing proprietary software (see chapter 3.2). This system offers a laser pulse repetition rate of 10 kHz at measurement ranges from 3 to 1800 m at 80 % reflectivity within a 40° x 40° field of view (Optech, 2014). The full parameter list is shown in Table 1. For each scan a 3D point cloud with spatial information was generated and a corresponding high-resolution digital image was taken for subsequent photo projection. Additional GPS and compass measurements allowed the determination of the spatial orientation.

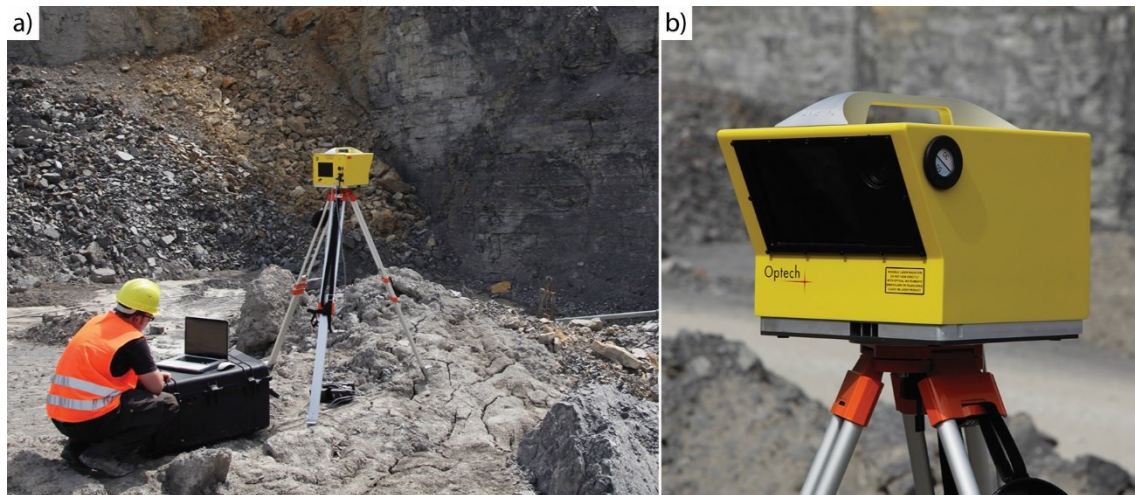


Figure 10: (a) Author operating the setup for terrestrial laser scanning of a Muschelkalk quarry wall. (b) Close-up view of the front side of the TLS unit with a dimension of 32 x 32 x 24 cm.

Table 1: Parameter list for the Optech ILRIS HD-ER terrestrial laser scanner. Laser class in accordance with IEC 60825-1 and US FDA 21 CFR 1040. PRF: Pulse repetition frequency; ER: Enhanced range. After Optech (2014).

Scanner performance	
Range 80 % reflectivity	1800 m
Range 10 % reflectivity	650 m
Minimum range	3 m
Laser repetition rate (peak and effective PRF)	10,000 Hz
Efficiency (effective PRF/peak PRF)	100 %
Raw range accuracy (ER mode enabled)	7 mm @ 100 m
Raw range accuracy (average of 4 shots minimum)	4 mm @ 100 m
Raw angular accuracy	8 mm @ 100 m (80 $\mu$ rad)
Field of view	40° x 40°
Minimum step size	0.001146° (20 $\mu$ rad)
Maximum density (point-to-point spacing)	2 cm @ 1000 m
Rotational speed	0.001 to 20°/sec
Rotational step size (minimum)	0.001146° (20 $\mu$ rad)
Beam diameter (1/e <sup>2</sup> )	19 mm @ 100 m
Beam divergence	0.008594° (150 $\mu$ rad)
Laser wavelength	1535 nm
Laser class	1M
Integrated camera	3.1 MP
Physical and environmental parameters	
Size (L x W x H)	32 x 32 x 24 cm

---

Weight	14 kg
Operating temperature	-20 °C to +40 °C
Storage temperature	-20 °C to +50 °C
Relative humidity	0 – 95 % non-condensing
Power consumption	75 W
Battery operation (standard battery pack)	5 hours operation
Data storage	Removable USB drive

---

## 2.2 Digital Outcrop Model (DOM)

The interest to develop digital techniques for outcrop analysis was driven mostly from the petroleum sector, where quantitative spatial information on geological heterogeneity and elements are necessary to improve the accuracy of numerical geocellular and petrophysical models of subsurface reservoirs (Alexander, 1993; Bryant and Flint, 1993; Tinker, 1996; Bryant et al., 2000; Rarity et al., 2014). With the above mentioned advances in TLS surveying technology during the early twenty-first century it became possible to efficiently collect 3D digital datasets from outcrops allowing reliable measurements and interpretations of geological features combined with its spatial information (Bellian et al., 2005; McCaffrey et al., 2005; Pringle et al., 2006; Thurmond et al., 2007; Verwer et al., 2007; Fabuel-Perez et al., 2009; van Lanen et al., 2009; Fabuel-Perez et al., 2010; Tomás et al., 2010; Benson et al., 2012; Hodgetts, 2013; Rarity et al., 2014). The digital outcrop modeling in this study was conducted with the help of the software Parser (Optech, 2011) and JRC Reconstructor 2 (Gexcel, 2012) and is described in detail in chapter 3.2.1.

## 2.3 Fault Zone Lithology

A fault zone can be described as a zone of focused deformation that can be subdivided into two subdomains, termed “core” and “damage zone”. In the fault core most displacement is accommodated, whereas the latter is mechanically related to the growth of the fault zone (Sibson, 1977; Chester and Logan, 1987; Davison and Wang, 1988; Forster and Evans, 1991; Byerlee, 1993; Scholz and Anders, 1994; Caine et al., 1996; Bastesen and Braathen, 2010; Bense et al., 2013). One of the biggest challenges is to represent and parameterize the complex structure of a fault zone, in particular the fault core, into a geological model (Garven et al., 1999; Lunn et al., 2008; Faulkner et al.,

2010; Bense et al., 2013). For this purpose the lithological properties of both subdomains (damage zone and fault core) are treated separately in this thesis.

The classification of the lithofacies types of the damage zone was carried out after Miall (1977, 1978), whereas in the more complex fault core a “fault core facies model” was established inspired by the “fault facies model” after Fredman et al. (2008), Braathen et al. (2009), Bastesen and Braathen (2010), and Fachri et al. (2011). For a detailed description the reader is referred to chapter 3.1.2.

### **2.4 Numerical Modeling**

The numerical modeling was performed with the reservoir modeling software Petrel version 2016.3 (Schlumberger, 2016), which provides the user with a vast amount of modeling and visualization techniques. This software was used to construct an outcrop analogue reservoir model of a fault zone with a volumetric fault core, which was subsequently enhanced with a discrete fracture network (DFN) model.

#### **2.4.1 Fault Zone Modeling**

Outcrop-analogue based models of geobodies were progressively developed since the 1990s, especially within the hydrocarbon industry. Main motor of this development was the great uncertainty about the values of structural and sedimentological parameters of 2D and 3D seismic data, relevant for the interpretation of reservoirs and other geobodies of interest (Alexander, 1993; Bryant and Flint, 1993; Strobl et al., 1997; Bryant et al., 2000; Vennin et al., 2003; Pringle et al., 2004; Enge et al., 2007). Outcrop analogue reservoir modeling represents the approach of bridging large-scale low density seismic data and small-scale high density well data. For the construction of the fault zone model in this study a series of basic outcrop analogue data was needed, which was georeferenced and provided with the help of the DOM (chapter 0). Further steps comprise the surface modeling, structural modeling, and property modeling. Structural modeling includes the substeps fault framework modeling, horizon modeling, and structural gridding, while the property modeling encompasses the substeps petrophysical and facies modeling. The procedure is described in detail in chapter 3.3.

#### 2.4.2 DFN Modeling

The characterization of fractured rocks may be one of the most challenging problems for geologists. Fracture networks represent the main pathways for fluid flow and transport in low-permeable rocks and are therefore of utmost economic interest for petroleum geology, geothermal exploration, and the generation of ore deposits (Faybishenko et al., 2000; Berkowitz, 2002; Neuman, 2005; Adler et al., 2012; Karra et al., 2018). Hence, multiple modeling approaches have been developed over the past decades to capture the features of fracture networks and allow fairly accurate predictions. The discrete fracture network (DFN) method is one of these approaches. Its strength is the ability to consider the volume, size, and geometric properties like length, orientation, and aperture of fracture networks to characterize the spatial distribution of fractures (Liu et al., 2018). DFN was therefore the modeling approach of choice for many different studies in the last decade (Karimi-Fard et al., 2004; Jambayev, 2007; Li and Lee, 2008; Chesnaux et al., 2009; Wilson et al., 2011; Dreuzy et al., 2012; Hoffman and Narr, 2012; Zeeb, 2013; Bisdorn et al., 2014; Lei et al., 2014; Malinouskaya et al., 2014; Agar and Geiger, 2015; Liu et al., 2016; Karra et al., 2018; Wenli et al., 2019), including this thesis. The conducted DFN parameterization, modeling and subsequent upscaling will be addressed in detail in chapter 3.4 and 3.5.

### 3 Applied Methodology

This chapter describes in detail the methodology to build a volumetric fault zone model subsequently combined with a DFN model. An overview of the steps taken is given in Figure 11. Johanna Bauer, Silke Meier and Sonja Philipp (Department of Structural Geology, University of Göttingen) provided the raw fracture data for the Cleebourg quarry, which were processed and adapted to the needs of the applied methodology. Maria Filomena and Harald Stollhofen (workgroup for petrophysics, GeoZentrum Nordbayern) provided petrophysical data and additional geological profiles for the studied outcrop. Data given by the project partners is only presented in its processed form. For the raw data the reader has to contact the original owner.

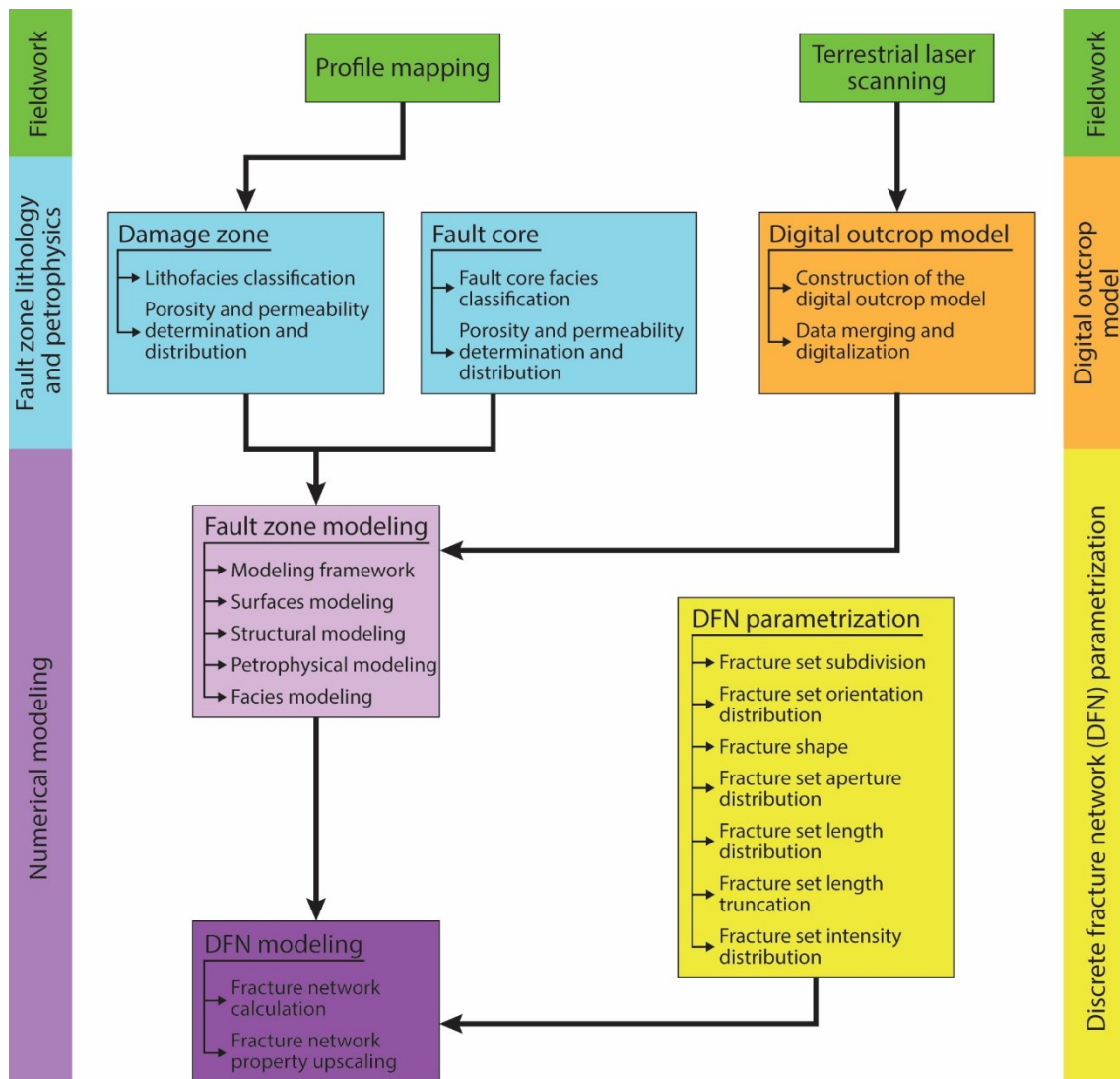


Figure 11: Overview of the workflow within this study. The specified captions (except for the fieldwork) are described in detail in this chapter.

### 3.1 Fault Zone Lithology and Petrophysics

#### 3.1.1 Damage Zone

##### 3.1.1.1 Lithofacies Classification

The classification of the lithofacies types of the damage zone (DZ) applies the terminology of Miall (1977, 1978) with minor modifications, based on data taken during profile mapping. These comprise the lithology, layer thickness, sedimentary structure, grain size, sorting, and the lateral thinning or thickening character of the specific layer. A lithofacies type has been assigned to every geological unit defined.

##### 3.1.1.2 Porosity and Permeability Determination and Distribution

Porosity and permeability values were assigned to the geological units according to the petrophysical data provided by the project partners from the workgroup for petrophysics. In the rare case of absent data for a geological unit the petrophysical values of a comparable unit, belonging to the same lithofacies type, were applied.

#### 3.1.2 Fault Core

##### 3.1.2.1 Fault Core Facies Classification

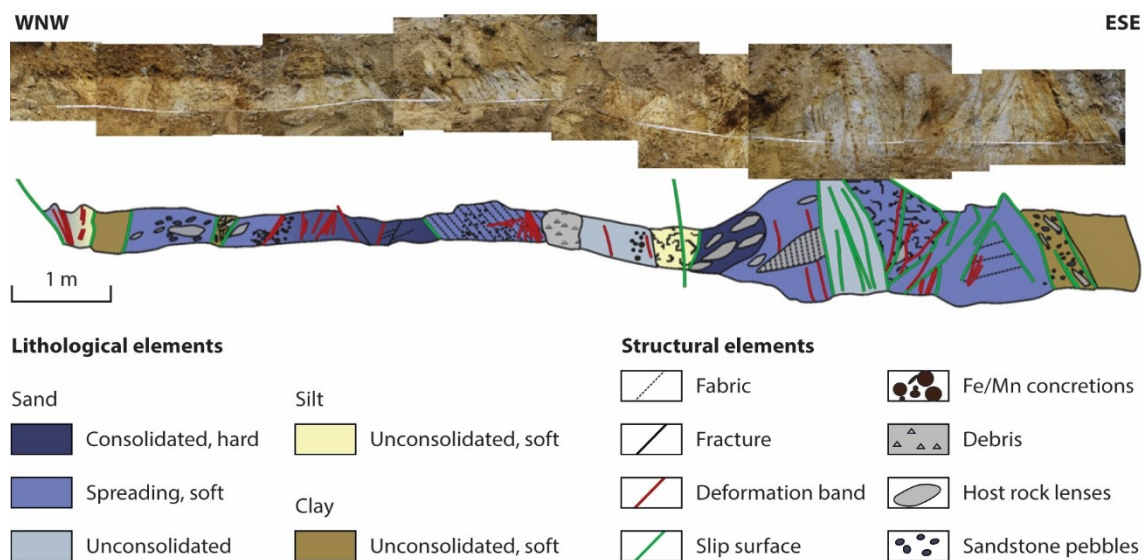


Figure 12: Photograph of the FC and a sketch of its architecture from Bauer et al. (2015) (colors slightly modified for better differentiation) containing structural elements, as well as lithological information along a scanline. FC facies distribution applied in this thesis is based on these results.

To apply a heterogeneous porosity and permeability distribution to the fault core (FC) it was divided into sections of preferably homogeneous properties. For this purpose the author established a “fault core facies model” inspired by the “fault facies model” after

Fredman et al. (2008), Braathen et al. (2009), Bastesen and Braathen (2010), and Fachri et al. (2011). The FC facies model is based on the elaborated FC architecture and lithological description provided by the project partner Johanna Bauer (Bauer et al., 2015, Figure 12). The authors describe different lithological and structural elements. Table 2 provides an overview of the fault core elements incorporated or not in the fault core facies model. Several elements had their terminology modified, or were subdivided for a more detailed handling.

Table 2: Overview of the fault core elements provided by Bauer et al. (2015) and the resulting fault core facies types. Green tick: incorporated element; yellow tick: incorporated element with modified terminology; red cross: not incorporated element; blue arrow: subdivided element based on its aggregation and extension.

Lithological elements (Bauer et al., 2015)		Fault core facies types	
Sand consolidated, hard	✓		Sandstone consolidated
Sand spreading, soft	✓		Sandstone spreading
Sand unconsolidated	✓		Sandstone unconsolidated
Silt unconsolidated, soft	✓		Gouge, silt unconsolidated
Clay unconsolidated, soft	✓		Gouge, clay unconsolidated
Structural elements (Bauer et al., 2015)	Structural sub-elements		
Deformation band	⇒	Single deformation band	✗
Slip surface	⇒	Single slip surface	✗
Fabric	✗	Deformation band cluster	✓
Fracture	✗	Slip zone	✓
Fe/Mn concretions	✗	Deformation band cluster along a slip zone	✓
Debris	✗		
Host rock lenses	✗		
Sandstone pebbles	✗		

It is crucial to comprehend, that the cell size of the Petrel grid is 0.5 x 0.5 x 0.2 m (XYZ, see chapter 3.3.3.3). A fault core facies body needs therefore more than 50 % of these values to be considered as dominant part of a cell. If the values are below, they do not appear. Furthermore a grid cell is limited to one porosity and one permeability matrix value, which had to be considered in the FC division and FC facies type definition. In



contrast to frequent problems in the horizontal dimension, the minimum vertical extent of 0.2 m of a fault core facies body did not imply crucial limitations. For the sake of simplicity the term “pair of porosity and permeability matrix values” will be referred hereinafter to as “PPMV-pair”, the term “fault core facies body” to “FCFB”, and the term “fault core facies type” to “FCFT”.

Prior to the FC division into representable FCFB and the assignment of FCFTs it was inevitable to decide which FC elements could be represented in relation to its description and the technical limitations given and subsequently define them as FCFTs. All five lithological elements were implemented as FCFTs. However, the elements “silt unconsolidated, soft” and “clay unconsolidated, soft” were interpreted as fault gouge and will hereinafter be referred to as “gouge, silt unconsolidated” and “gouge, clay unconsolidated”.

Five structural elements presented by Bauer et al. (2015) were largely descriptive, of unknown importance, or of too low dimension to be incorporated in the model. These are: (i) fabric, (ii) debris, (iii) Fe/Mn concretions, (iv) host rock lenses, and (v) sandstone pebbles. Regarding “fabric” Bauer et al. (2015) gave no further information on petrophysical properties of this structural element. “Debris” is no structural element, it represents dumped earth and rocks covering other elements. “Host rock lenses” were usually too small in their extent to be represented as separate FCFBs. However, an exception for slightly bigger single rock lenses may be possible, which is discussed in chapter 5.3.2. “Fe/Mn concretions” and “sandstone pebbles” were too small in size to be represented as a dominant part of cells. If they should be incorporated, a possible solution is discussed in chapter 5.3.2. The structural element “fracture” represents a special case, as fractures were treated separately in the DFN (see chapter 3.4) and therefore do not belong in the FC facies model.

The remaining two structural elements “deformation band” and “slip surface” are of importance. Five structural sub-elements are defined here depending on their aggregation and extension: (i) single deformation band, (ii) deformation band cluster, (iii) single slip surface, (iv) slip zone, and (v) deformation band cluster along with a slip zone. According to the original description all the deformation bands incorporated in the sub-elements are cataclastic (Aydin, 1978; Aydin and Johnson, 1978; Davis, 1999), although Bauer et al. (2015) did not specifically term the type of the deformation bands found.

Not all structural sub-elements can be represented in the FC facies model regarding the technical limitations of the model. Single deformation bands cannot be incorporated in

the model: they occur less frequently in FCs compared to deformation band clusters and show a width of only 1 cm (rarely 2 cm, Fossen et al., 2007). Also single slip surfaces are too small in their horizontal extent to be included. However, most single slip surfaces confine the lithological elements “gouge, silt unconsolidated” and “gouge, clay unconsolidated” and were therefore treated as a part of these FCFTs.

One broader section of the FC is dominated by structural elements showing a deformation band cluster along with a slip zone (seen in Figure 13 as the right two-thirds of the green SZ). It has a sufficient extent to be treated as a FCFB but bears the complication of two coexisting structural elements. Since this element is dominated by slip surfaces it is treated as a slip zone (Foxford et al., 1996), which also holds a higher sealing capacity compared to deformation bands (Torabi et al., 2013). Hence, two structural elements present were incorporated into the FC facies model as FCFTs, which are “deformation band cluster” and “slip zone”.

With the mentioned limitations seven FCFTs were established, five of lithological and two of structural origin (Figure 13): (i) sandstone consolidated (Sc), (ii) sandstone spreading (Ss), (iii) sandstone unconsolidated (Su), (iv) gouge, silt unconsolidated (Gs), (v) gouge, clay unconsolidated (Gc), (vi) deformation band cluster (DBC), and (vii) slip zone (SZ).

### 3.1.2.2 Porosity and Permeability Determination and Distribution

The FC architecture shows a combination of lithological and structural elements and transitions in between (Figure 12), typical for a FC (Toy et al., 2015; Gabrielsen et al., 2017; Skar et al., 2017). Thus a FCFB commonly does not consist of a single FCFT, may it be of structural or lithological origin. However, considering the technical limitations of the model, a FCFB had to be narrowed down to one PPMV-pair. An additional challenge was, that no petrophysical data were available for the FC from the other working groups. PPMV-pairs for the FCFTs were therefore derived from petrophysical data of the DZ and literature. It soon proved to be problematic to deduce PPMV-pair values for FCFBs, which consist of multiple FCFTs. The FCFBs had therefore to be restricted to one single FCFT based on the extent, frequency of occurrence, and significance of the different FCFTs encountered.

The PPMV-pair information of the FC is imported into Petrel via petrophysical logs of a constructed artificial well based on a scanline traversing the FC (see also chapter 3.3.4.2). For this purpose the author divided the FC into 2D segments of the FCFBs along

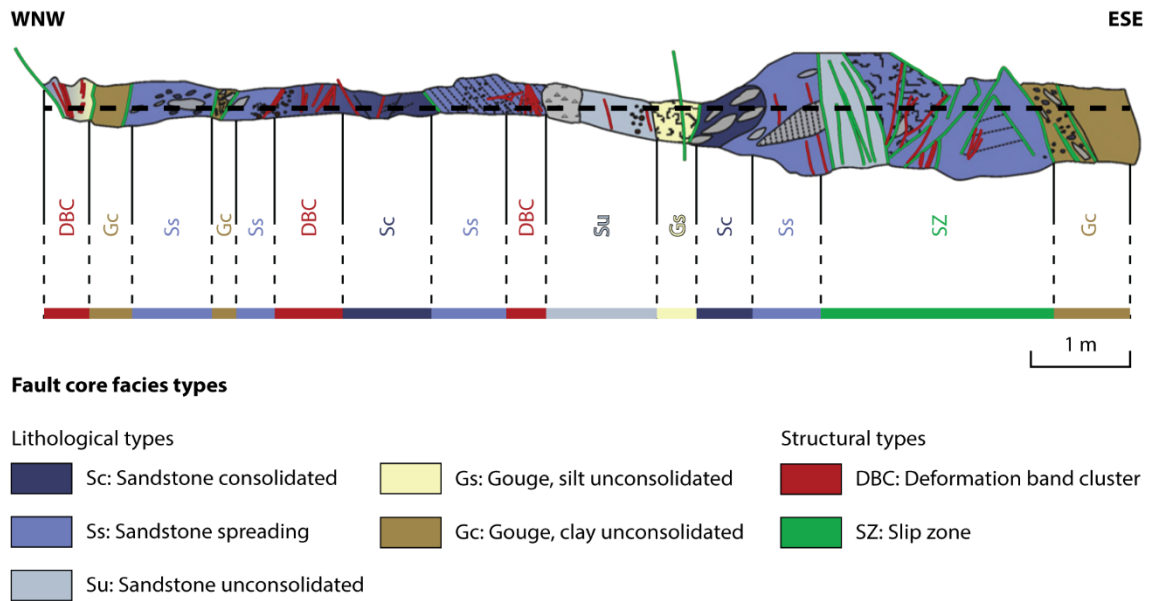


Figure 13: The upper part of the illustrations shows the FC architecture after Bauer et al. (2015) with a black dashed horizontal line representing the scanline traversing the FC. The parts below show the division into 2D sections of the FCFBs with the assignment of the previously established FCFTs. The color code for this FC facies log is derived from Bauer et al., (2015).

the scanline, considering the previously mentioned restrictions. The established FCFTs were subsequently assigned to the FCFBs with the result of a FC facies log (Figure 13). As mentioned above the estimation of the PPMV-pairs of the FCFTs had to be derived from the petrophysical data available and literature. For the lithological FCFT “sandstone consolidated (Sc)” mean values were calculated and used for porosity and permeability based on the unpublished petrophysical data from the project partners available for consolidated sandstone. For the lithological FCFTs “sandstone unconsolidated (Su)”, “gouge, silt unconsolidated (Gs)” and “gouge, clay unconsolidated (Gc)” literature values were used after Manger (1963) for porosity and Bear (1972) for permeability. For the FCFT “sandstone spreading (Ss)” no values could be found in literature, an intermediate value was estimated considering the values used for the FCFTs “Sc” and “Su”.

The PPMV-pairs of the two structural FCFTs “deformation band cluster (DBC)” and “slip zone (SZ)” were estimated according to data from Chilingarian (1964), Fossen et al. (2007), and Torabi et al. (2013). The latter author analyzed the porosity, permeability and capillary pressure of deformed sandstones in FCs (including cataclastic deformation band clusters and FC slip zones) and described the relationship between its porosity and permeability by power-law regressions. Chilingarian (1964) described the relationship between porosity and permeability of sandstones of different grain

sizes while Fossen et al. (2007) gave a review on porosity and permeability values of cataclastic deformation bands with regard to the petrophysical properties of their host rocks. Although deformation bands were examined, these studies did not explicitly distinguish between DZ and FC. It is assumed, however, that the mechanical and petrophysical requirements to form these bands have to be at least similar and are therefore applied to the FC deformation band clusters encountered.

To derive the petrophysical values for deformed rocks in fault zones, the values of undeformed original rocks were needed. Therefore the previously calculated petrophysical matrix values of consolidated sandstone were chosen as the PPMV-pair for the undeformed protolith. Many different studies (Pittman, 1981; Jamison and Stearns, 1982; Harper and Moftah, 1985; Knott, 1993; Antonellini and Aydin, 1994; Gibson, 1994; Knipe et al., 1997; Crawford, 1998; Gibson, 1998; Antonellini et al., 1999; Fisher and Knipe, 2001; Jourde et al., 2002; Shipton et al., 2002; Fossen et al., 2007) show, that the porosity of cataclastic deformation bands is reduced by up to an order of magnitude, compared with the undeformed host rock. Permeability even decreases by two to three (locally as much as six) orders of magnitude. Laboratory measurements conducted by Torabi et al. (2013) show a smaller reduction: porosity values were reduced by half, permeability by one to two orders of magnitude. Based on these information and the PPMV-pair of the host rock a PPMV-pair for single deformation bands was derived. In order to estimate the PPMV-pairs of the two structural FCFTs a figure by Torabi et al. (2013) was used as an visual aid (Figure 14). It summarizes power-law regressions describing the relationship between porosity and permeability and includes results by Chilingarian (1964), which describe the relationship between the porosity and permeability of sandstones of different grain sizes. The here presented data show, that for the same porosity the host rock's permeability (marked as blue star in Figure 14) is a magnitude higher than the permeability of the host rock's power-law regression. Unfortunately the density of the own data is not sufficient to calculate power-law regressions. However, the data by Torabi et al. (2013) show a spread of permeability compared to the same porosity of host rocks by one to two orders of magnitude. In the area of work fine-grained sandstones are present. As also seen in Figure 14, the host rock values of this study match the data for fine-grained sandstone by Chilingarian (1964). Hence, both sources strengthen the chosen host rock's PPMV-pair.

The final estimation of the structural FCFTs DBC (marked as red star in Figure 14) and SZ (marked as green star in Figure 14) was carried out under the consideration of (i)

the specific host rock's PPMV-pair, (ii) the derived PPMV-pair for single deformation bands (marked as yellow star in Figure 14), (iii) the overall trend and relative relation of the power-law regressions, and (ii) two conclusions by Torabi et al. (2013), which state that: (a) for a given porosity, permeability is higher in undeformed host rock samples than in deformed ones and will decrease with the degree of deformation, and (b) the sealing capacity of a FC slip zone is higher than that of single deformation bands and clusters of bands.

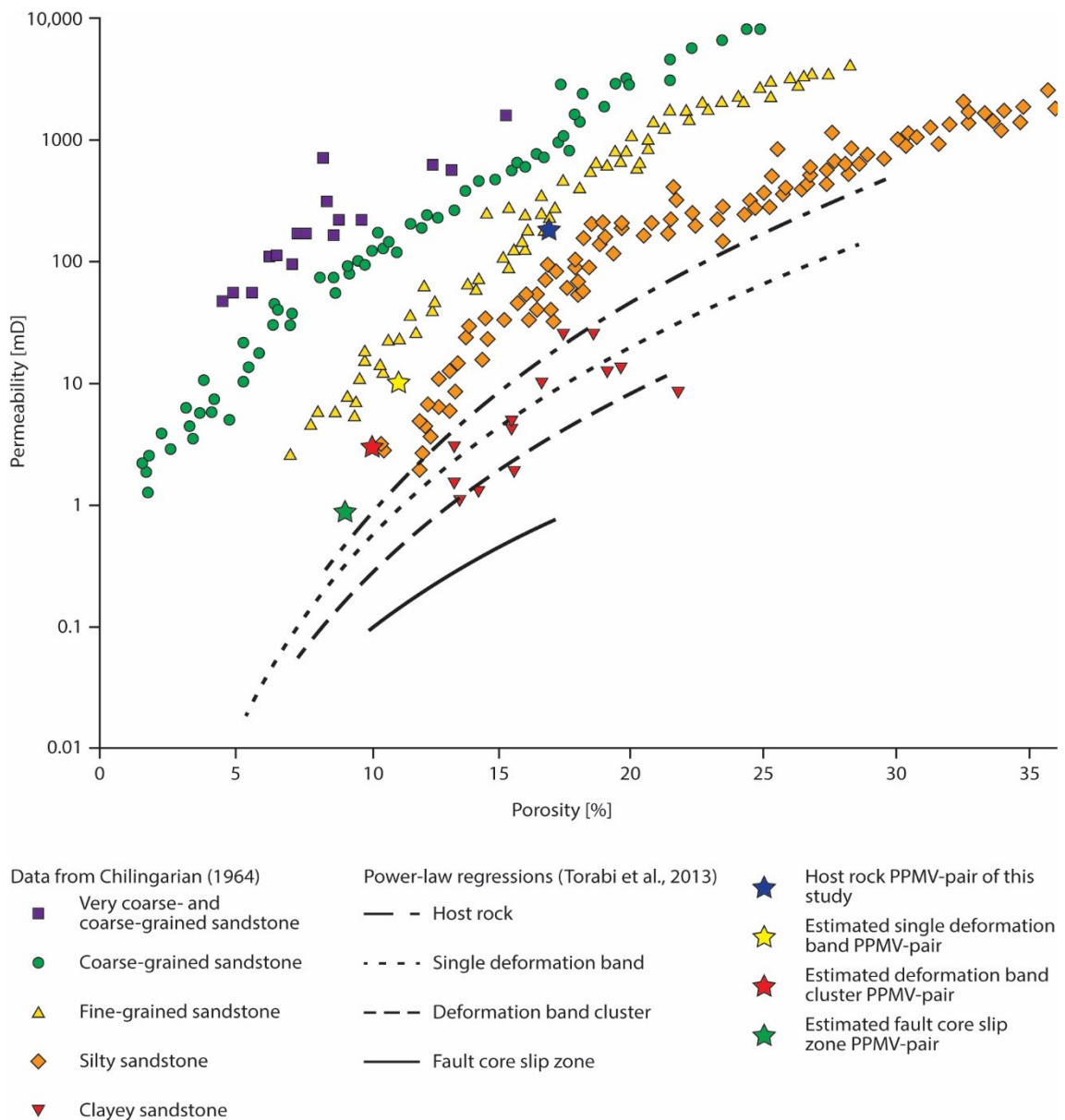


Figure 14: Illustration of the permeability-porosity relationship of sandstones with different grain sizes (Chilingarian, 1964) and of deformed sandstones (Torabi et al., 2013). Porosity and permeability values in fault zones are lower than in undeformed rocks. Stars represent the used host rock data as well as the estimated PPMV-pairs for single deformation bands and the two structural FCFTs. Modified after Torabi et al. (2013).

### 3.2 Digital Outcrop Model (DOM)

#### 3.2.1 Construction of the DOM

In this study the raw ILRIS-HD-ER point cloud data were first preprocessed with the software Parser from Optech (2011), which generates spatially oriented point clouds with an 8-bit reflectance information formatted for export into other programs. All subsequent steps in the digital outcrop modeling process were carried out with the software JRC Reconstructor 2 from Gexcel (2012). After the import of the preprocessed point clouds the following steps were performed (Figure 15):

1. Cutting of the point clouds to remove vegetation for better sight and to crop information from outside the area of interest to reduce data size.
2. Second processing of the point clouds, which comprises three sub-steps:
  - a) Computation of normals: Calculation of a tangent plane for every point considering their 3D neighborhood. Necessary for the “inclination” color mapping of the point clouds in subsequent steps.
  - b) Computation of confidence: A confidence value is calculated for every point representing reliability of the range measurement. Its accuracy depends mainly on the angle between the laser beam and the targets tangent plane, the distance to the target, the material of the object and the intensity of the reflected signal. The confidence value itself is calculated as a weighted sum of the surface normal,

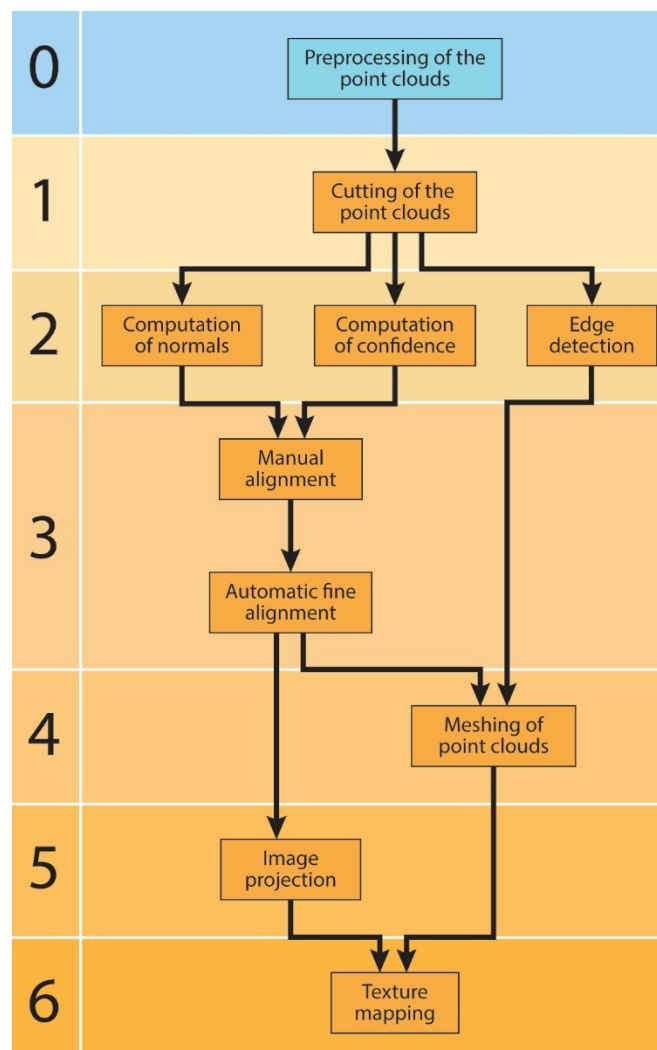


Figure 15: Overview of the steps performed to develop a DOM. Steps performed in the software Parser are marked blue; steps performed in the software JRC Reconstructor 2 are marked orange.

the range value and the reflectance value (Gexcel, 2010a) and is necessary for the “confidence” color mapping of the point clouds in following steps.

- c) Edge detection: Extracts two types of geometrically significant edges from the point cloud. “Jump edges” (or depth discontinuities), which occur when the laser beams passes an edge and hits an object in the background and “crease edges” (or orientation discontinuities), which are characterized by an abrupt change in the surface orientation (Gexcel, 2010a).

These steps derive and add extra information to the point cloud raw grid, which is useful in further processing steps (Gexcel, 2010a).

3. Alignment of the point clouds including two sub-steps:
  - a) Manual alignment (pre-registration) of the point clouds through picking of corresponding points along overlapping parts. This is performed with the help of reflectance, inclination, and confidence color mapping types of the point cloud raw grid (Figure 16). A minimum of three picked point pairs is necessary to align the two point clouds; however, with an increasing amount of point pairs picked the error of the alignment can be significantly further reduced. To guarantee a correct spatial orientation of the final DOM the best-situated point cloud was georeferenced and chosen to serve as basis of alignment.
  - b) Automatic fine alignment (fine registration) based on the previous manual alignment for further reduction of the error (Gexcel, 2010b).
4. Meshing of the point clouds with the implementation of the previously gained edge detection information, which leads to a more complex mesh around edges and thus a higher mesh quality (Gexcel, 2010c). A confidence color mapping was chosen for the generated meshes.
5. For the image projection the high-resolution digital images taken during the fieldwork (TLS phase, chapter 2.1.2) were graphically optimized and subsequently calibrated by manual picking of corresponding points on the image and its matching point cloud (Figure 17). For the calculation of the image projection a minimum of 11 picked pairs of points is necessary, while additional point pairs contribute to a smaller error and thus a more precise projection on its matching point cloud (Gexcel, 2010d).
6. The texture mapping process represents the last step towards a DOM. It utilizes the generated meshes (step 4) and calculated projections (steps 5) and merges both to a texture map, which represents a high-resolution image on a 3D body.

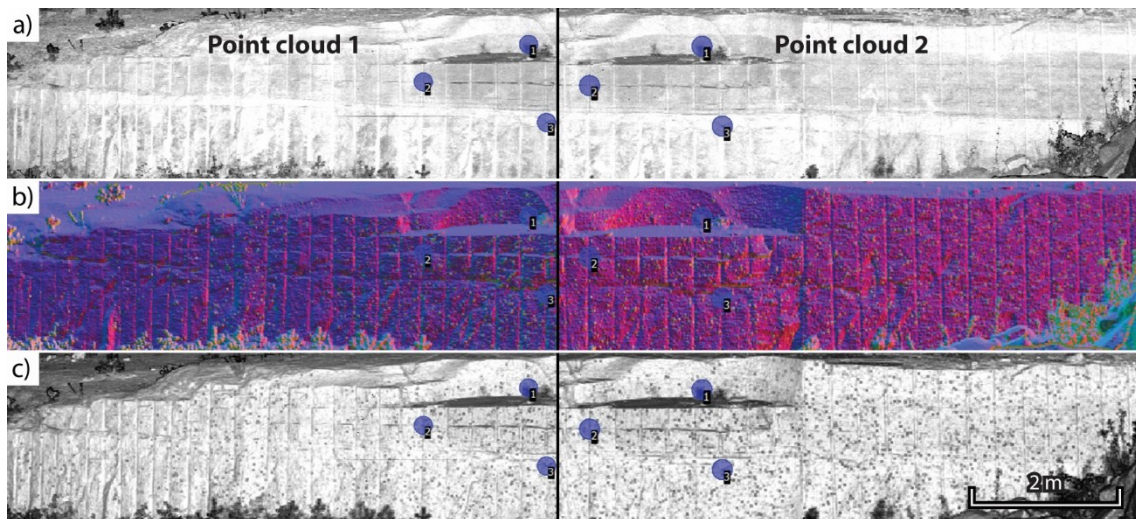


Figure 16: Cutout of the manual alignment process of two point clouds in JRC Reconstructor 2. Corresponding points (blue dots) were picked in the overlapping part of the two point clouds with the help of three color mapping types: (a) reflectance, (b) inclination, and (c) confidence.

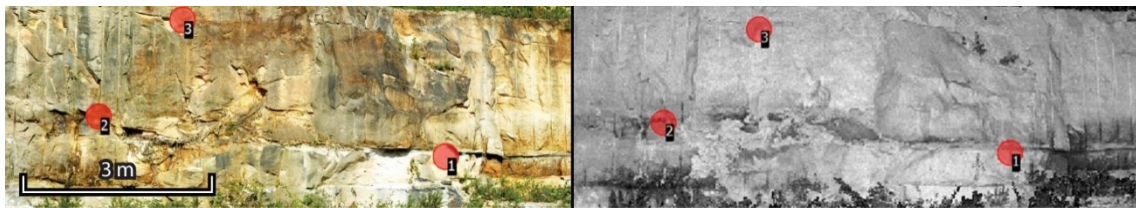


Figure 17: Example of the manual picking of corresponding points (red dots) of a high-resolution digital image (left) and its matching point cloud (right) in JRC Reconstructor 2.

### 3.2.2 Data Merging and Digitalization

The final DOM was used to gather, visualize, and georeference data acquired by project partners and the author, which includes profiles, sampling locations and scanlines. By combining the georeferenced 1D and 2D information and the DOM it was possible to expand and interpret data in 3D. Geological unit boundaries, bed tops, and the FC boundary were picked (Figure 18) and exported including their spatial information for subsequent import into Petrel (Schlumberger, 2016).



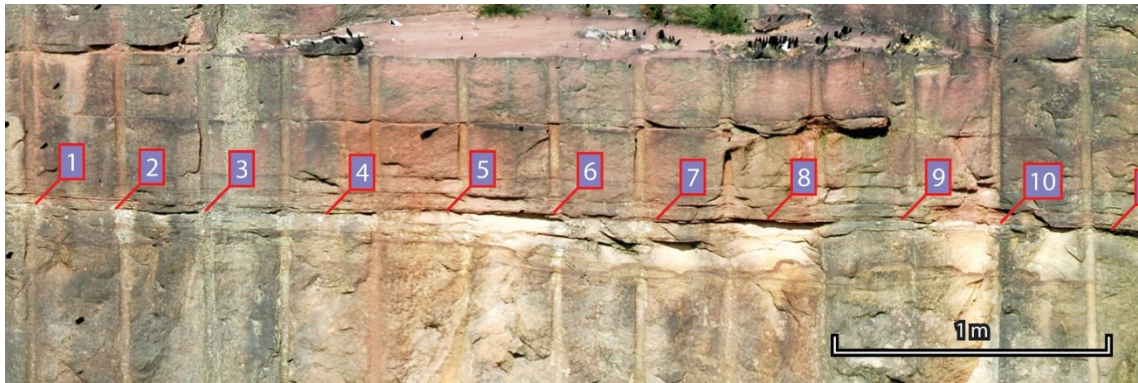


Figure 18: Example of the interpretation and picking of a bedding plane on a 3D texture map of the DOM in JRC Reconstructor 2. Every picked point comprises XYZ coordinate information.

### 3.3 Fault Zone Modeling

#### 3.3.1 Modeling Framework

In order to establish a volumetric fault zone model combined with a DFN model in Petrel (Schlumberger, 2016) a series of basic data was needed, which was georeferenced and provided with the help of the DOM (chapter 3.2.2). This data was imported into Petrel and comprises: (i) a point cloud of the outcrop, (ii) geological profiles, (iii) tops of the geological units, (iv) scanlines, (v) a FC boundary plane, and (vi) FC logs (Figure 19).

(i) The merged point cloud of the outcrop was limited to the area of interest (AOI) and sub-sampled by a factor of 10 to assure a smooth presentability within the modeling software.

(ii) Geological profiles were imported as wells comprising the ones acquired during own fieldwork and additional profiles provided by project partners from the GeoZentrum Nordbayern.

(iii) The tops of the geological units were imported into Petrel as well tops with spatial orientation data (dip angle and azimuth) and points with spatial orientation data. This information was gathered through the interpretation of the available profiles, tracing of unit boundaries, picking of unit boundaries in the DOM, and compass measurements. Furthermore, some horizon tops, which were clearly assignable to tops of geological units but lacked geological compass measurements were cut out of the DOM as small point clouds and imported into Petrel. These small point clouds were then converted into surfaces, which in turn gave the opportunity to compute its mean spatial orientation. Additional points with a spatial orientation could be generated by this method to increase the data density.

(iv) Scanlines provided by project partners from the University of Göttingen were imported as wells containing fracture data.

(v) In order to be able to split the DZ from the FC it was necessary to construct a FC boundary plane: the exposed FC boundary in the DOM was picked and combined with the average spatial orientation of the main fault zone slip surface to position this boundary plane.

(vi) The petrophysical FC logs derived from the FC facies log were imported into Petrel via a constructed well along a scanline traversing the FC. They hold the same position like the FC facies log generated in chapter 3.1.2 (Figure 13).

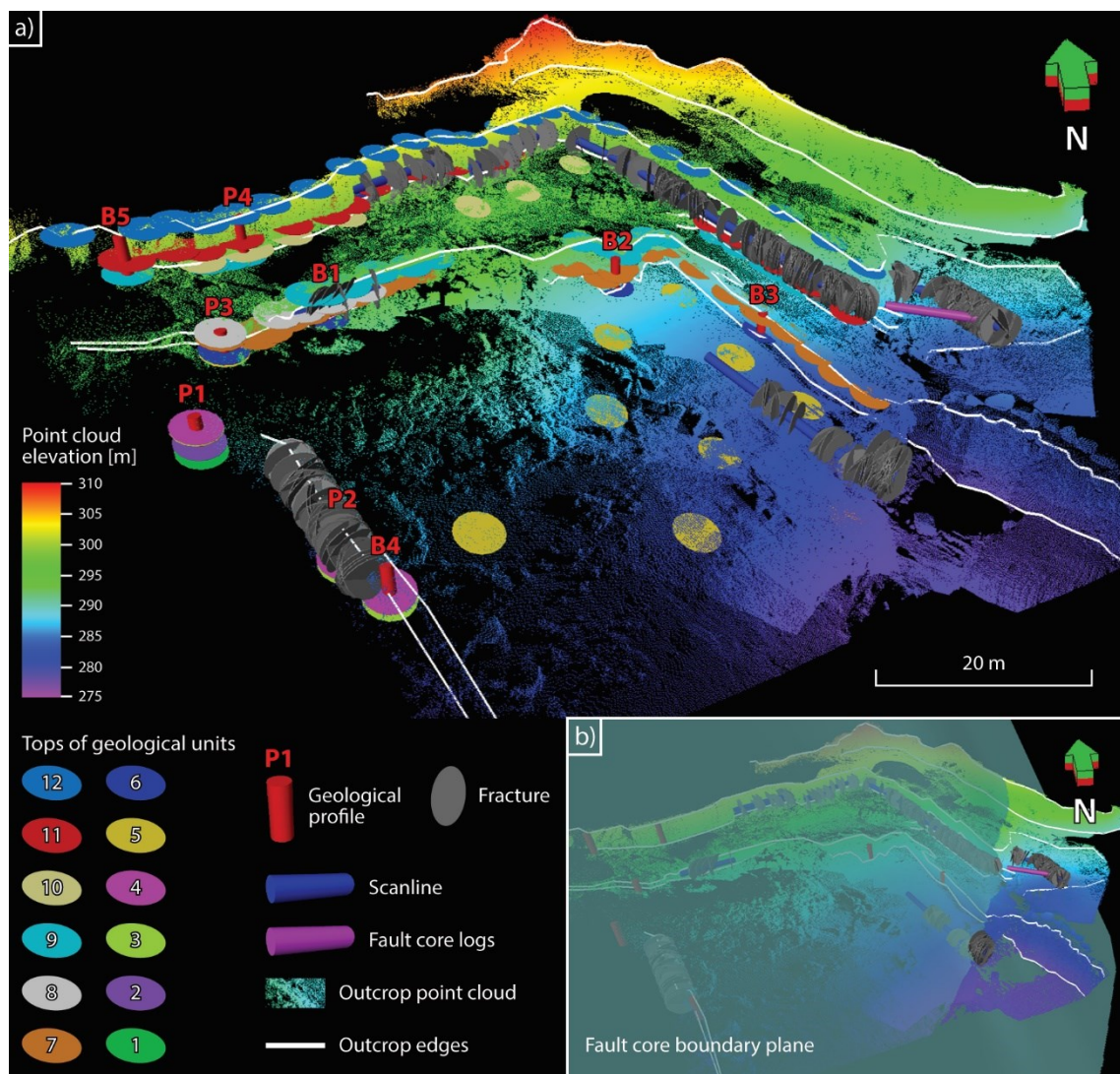


Figure 19: (a) Overview of the data basis used in the fault zone modeling process in Petrel. Profiles A1 – A4 were acquired within this study while B1 – B5 are additional profiles provided by the project partners. Scale represents a mean due to the perspective presentation. The amount of data causes overlapping and partial occlusion. (b) Display of the FC boundary plane (transparent green) splitting the DZ (left part) from the FC (right part).

### 3.3.2 Surface Modeling

Modeling of the top-surfaces of the geological units of the DZ was based on two different data types with a spatial orientation (dip angle and azimuth), well tops and additional points. Multiple algorithms were tested for the surface calculation, two of these proved useful, the “convergent interpolation” and the “conformal gridding” algorithms. In both cases a grid increment of 0.5 m was chosen.

The **convergent interpolation** algorithm is control-point oriented and suited for a wide range of data types and densities. With each iteration the algorithm converges upon the solution (calculated top-surface), adding more resolution, reaching a high performance without data searching or sorting. Each iteration of the convergent interpolation algorithm consists of three sequential steps: (i) refining, increase of the grid resolution, (ii) snapping, re-gridding of the data, and (iii) smoothing, minimizing the grid curvature (Gunnarsson, 2011; Sbrana et al., 2018). This process is data-driven, requires minimal parameter control, and offers a stable extrapolation even at large distances from the data. An advantage is, that this algorithm allows to incorporate the dip angle and azimuth information of the well tops and of additional points to calculate the top-surfaces of geological units. The convergent interpolation algorithm was used in cases of large exposed geological units (no. 7, 9, 10, 11, and 12), which offered a high amount of control-points. The previously conducted FC boundary plane calculation applied also this algorithm with a grid increment of 0.5 m.

The **conformal gridding algorithm** uses the z-values of well tops and additional points and allows to conform the calculated surface to one or two horizons above and/or below that surfaces. This algorithm was used for the top-surface calculation of geological units that had a minor exposure and thus a smaller amount of control points (no. 1, 2, 3, 4, 5, 6, 8, and the base-surface).

In order to make the subsequent horizon modeling process (see chapter 3.3.3.2) less error-prone the calculated surfaces of the DZ were cut close to the FC boundary plane. The surfaces did therefore not extend into the FC. In case of the FC two surfaces were necessary for the subsequent horizon modeling process, a FC top and a FC base surface. In this case the extended part of the surface of unit 12 was used as FC top and the extended part of the base-surface was used as the FC base.

### 3.3.3 Structural Modeling

The structural model was built with the help of the Petrel structural framework, which represents the overall geometry of the model and is the backbone for designing the 3D

grid, which contains the geological and petrophysical information and the subsequently generated reservoir properties (Naji et al., 2010). The three main processes of the structural framework modeling within this study are the fault framework, the horizon modeling, and the structural gridding processes.

#### 3.3.3.1 Fault Framework

The fault framework process was used to separate the DZ from the FC along the FC boundary, which allows to treat both parts independently. For this purpose a fault surface with a grid interval of 5 was generated based on the previously calculated FC boundary plane. This generated fault surface serves solely as a construction aid for the structural framework and has no further geological purpose.

#### 3.3.3.2 Horizon Modeling

The horizon modeling process creates horizons individually by honoring the fault surface and subsequently applying the horizon truncation information. It was performed with the help of the Volume Based Modeling (VBM) technique (Souche et al., 2013), which revolves around the concept of implicit modeling. It relies on the representation of surfaces as iso-values of a volume attribute and is usually referred to as “implicit function”. This function corresponds to the stratigraphic age of the rock units and is embedded and interpolated in an unstructured tetrahedral mesh, normally associated with the construction of multi-z geobody surfaces (Frank et al., 2007; Souche et al., 2013). The VBM technique consists of three main steps: (i) the construction of a tetrahedral mesh for carrying and interpolating the implicit function, (ii) interpolating the values of the implicit function on the nodes of the tetrahedral mesh, and (iii) generating the surfaces representing every implicitly modeled horizon.

The VBM method gives the opportunity to generate a consistent zone model (see chapter 3.3.3.3) with multiple advantages. It is practically insensitive to the complexity of the fault model. Conformable horizons, which belong to the same sequence are modeled simultaneously and cannot cross each other (Lepage and Souche, 2016). Every conformable horizon constrains the geometry of all other conformable horizons of the same sequence and is also constrained by their geometry. This provides the geometry of a horizon and the volume attribute, representing the stratigraphic age of the rock unit. For more detailed information about the VBM technique see Souche et al. (2013) and Lepage and Souche (2016).

In this study “conformable” and “base” horizon types were applied and a “normal” complexity of the model was chosen. The input data comprised the calculated top-surfaces of the geological units and the base-surface of the DZ, the FC top and FC base surfaces (chapter 3.3.2), as well as the fault surface (chapter 3.3.3.1).

### 3.3.3.3 Structural Gridding

With the structural gridding process a fully stair-stepped corner point grid is created in a single process directly from the structural framework. The lateral dimension of the cells was set to 0.5 x 0.5 m (X and Y) with a minimum cell thickness of 0.2 m (Y). The zone layering was set to “follow base” causing the layers to be cut at the top.

### 3.3.4 Petrophysical Modeling

The property modeling process allows to populate the model grid with a multitude of various properties, e.g. porosity and permeability information, distributed either directly in the case of the DZ, or through a stochastic algorithm in the case of the FC. Furthermore the process was used to populate the DZ and FC geobodies with the  $P_{32}$  intensity, which will be addressed in chapter 3.4.7.

#### 3.3.4.1 Damage Zone

The PPMV-pairs of the DZ were assigned directly to the zones created during the structural gridding process in chapter 3.3.3.3. The zones correspond to the geological units, whose PPMV-pairs were previously specified in chapter 3.1.1.2.

#### 3.3.4.2 Fault Core

To populate the FCFBs with the PPMV-pairs of their corresponding FCFTs (chapter 3.1.2.2) an artificial well was constructed based on a scanline traversing the FC (Figure 13). Its exact location was determined and georeferenced within the DOM (chapter 3.2.2), assisted by the project partner Johanna Bauer.

From the constructed FC facies log (chapter 3.1.2.2) a matrix porosity and a matrix permeability log were derived and assigned to the artificial well. To upscale the logs on the grid cells traversed by the artificial well, different averaging methods for the cell values were tested. For this study the “arithmetic” average method was chosen. For the sample selection both logs were treated “as lines” and the “simple” sample selection method was chosen to ensure that every cell along the well trajectory receives a value.

The entire model grid was then populated with porosity and permeability information through the upscaled logs. Multiple algorithms were tested and the Sequential Gaussian Simulation (SGS) algorithm, which is already implemented into Petrel, was chosen as best suited for this process.

The SGS algorithm is a stochastic Geostatistical Software Library (GSLIB) interpolation algorithm. It is based on kriging and is widely used because it works fast and straightforward (Deutsch and Journel, 1998; Delbari et al., 2009). Honoring trends, variograms, input data, and input distributions the algorithm generates local highs and lows between the input data locations. A random seed number supplied by the software or the user initiates the procedure. In the process all grid nodes are visited through a randomly established path. For every grid node the data is kriged to estimate the grid nodes variance. Then a value is chosen from the input distribution to match the variance at the grid node. For the kriging of the subsequently visited cells not only the input data is used but also the values defined just before. This leads to a high constraint of the previously defined cells on the last cells visited, which makes a random order important. For detailed information about the SGS algorithm the reader is referred to Deutsch and Journel (1998), Asghari et al. (2009), Delbari et al. (2009), and Gunnarsson (2011).

Prior to the distribution of the petrophysical properties by applying the SGS algorithm some considerations are required. Since the FCFBs normally do not spread uniformly but rather tend to be elongated parallel to the main slip surface (Caine et al., 1996; Shipton et al., 2005; Færseth, 2006; Manzocchi et al., 2010; Meier et al., 2015; Fachri et al., 2016) an anisotropy factor was introduced to represent this elongation. As no information on the elongation value was available for the investigated case, three cases were tested with different elongation values (A, B and C) for the FCFBs: 10-25 m for case A, 25-50 m for case B, and >50 m for case C.

To receive a more realistic spatial orientation of the elongated FCFBs the spatial orientation of the FC slip surface was also taken into account. For the sake of comprehension it has to be mentioned that a FCFB corresponds to a FCFT (chapter 3.1.2.1) that in turn corresponds to a PPMV-pair, which was derived from the FC facies log (see Figure 13).

In the following the SGS algorithm was first applied to populate the grid with the matrix permeability. It was taken from the matrix permeability log derived from the previously established FC facies log. Subsequently, the matrix porosity was modeled, based on the matrix porosity log and the already distributed matrix permeability. The matrix permeability and matrix porosity are always connected through their common FCFT

(PPMV-pair), the same seed number was therefore used for both distributions. In addition, the calculated porosity was linked to the previously calculated permeability. These provisions guaranteed that a permeability value always suits its correspondent porosity value as defined in the FCFT.

To gain an understanding of the uncertainty of the algorithm it was recommended to perform multiple runs. For each elongation case (A, B, and C, see above) approximately 10 runs of the SGS algorithm with different seed numbers were performed and the geologically most reasonable result was chosen for further modeling steps. This is case B, which seems not only to be best suited but also corresponds to Fachri et al. (2011).

### 3.3.5 Facies Modeling

A facies model was established based on the lithofacies classification of the DZ (chapter 3.1.1.1), the FC facies model (chapter 3.1.2.1), and the resulting petrophysical distribution patterns of the FC (chapter 3.3.4.2).

#### 3.3.5.1 Damage Zone

The lithofacies types of the DZ, which were classified in chapter 3.1.1.1, were assigned directly to the corresponding grid zones, which in turn correspond to the geological units.

#### 3.3.5.2 Fault Core

The FCFTs were assigned directly to the cells holding the corresponding petrophysical properties, which were distributed over the grid model as discussed in chapter 3.3.4.2. For every of the three cases of property distributions (A, B and C) an analogous FCFT distribution was assigned.

### 3.4 DFN Parametrization

Every DFN model is defined by its fracture network characteristics, which makes its parametrization crucial. Since this concerns heterogeneous sub-seismic-scale parameters, outcrop analogues are very important and often used to acquire fracture data (Bonnet et al., 2001; Agosta et al., 2010; Guerriero et al., 2010; Hooker et al., 2013, 2014). For this study the raw fracture data was gathered in the outcrop of Cleebourg by the project partners from the University of Göttingen. This data was processed and reworked accordingly to the needs of this thesis, bringing to issue: (i) the subdivision into fracture sets, (ii) fracture set orientation distribution, (iii) fracture shape, (iv) fracture set aperture distribution, (v) fracture set length distribution, (vi) fracture set length truncation, and (vii) fracture set intensity distribution.

#### 3.4.1 Fracture Set Subdivision

From the raw data a total of 408 fracture measurements were visualized in Stereonet 10 (Allmendinger et al., 2011; Cardozo and Allmendinger, 2013) and subdivided into three fracture sets in the DZ (DZ Set 1, 2, and 3) and three sets in the FC (FC Set 1, 2, and 3).

#### 3.4.2 Fracture Set Orientation Distribution

The orientation and distribution of the previously defined fracture sets was analyzed and described with the help of the distributions described by Fisher et al. (1987) and Bingham (1964, 1974) within the stereographic projection software Stereonet 10 (Allmendinger et al., 2011; Cardozo and Allmendinger, 2013).

The **Fisher distribution** is of rotational symmetry. It is appropriate for cases, where the orientations of the dataset cluster symmetrically about a central axis, showing a circular confidence cone (Figure 20a). It can be seen as the three-dimensional equivalent of a Normal distribution wrapped over the surface of the sphere (Borradaile, 2013). It represents the standard mean vector calculation within Stereonet 10 (Allmendinger, 2018). From the several values reported, the mean orientation (mean dip angle and mean azimuth) as well as the concentration-parameter kappa ( $\kappa$ ) are of importance for this study. Within the Stereonet 10 calculation the direction cosines of all of the individual unit vectors are added up. The reported mean length constitutes the length  $R$  of the resultant vector divided by the number of orientations ( $n_v$ ) summed. The mean dip angle and mean azimuth are derived from the resultant vector normalized to



a unit vector. The concentration-parameter  $\kappa$  is a shape parameter of the Fisher distribution and represents a measure of the degree of preferred orientation within the rotational symmetric population of orientations.  $\kappa=0$  represents a uniform distribution, while  $\kappa$  increases without limits when the clustering of orientations grows. Dependent on the number of orientations two different approximations are used by Stereonet 10, where

$$\kappa = \frac{n_v - 1}{n_v - R} \quad 3.1$$

is used for  $n_v > 16$  (Fisher, 1953; Mardia, 1972), and

$$\kappa = \left( \frac{n_v}{n_v - R} \right) \left( 1 - \left( \frac{1}{n_v} \right) \right)^2 \quad 3.2$$

is used for  $n_v < 16$  (Best and Fisher, 1981; Fisher et al., 1987). In addition to the above cited publications the reader is referred to Priest (1993), Davis (2002), Mardia and Jupp (2009), Borradaile (2013), and Drews et al. (2018) for further information.

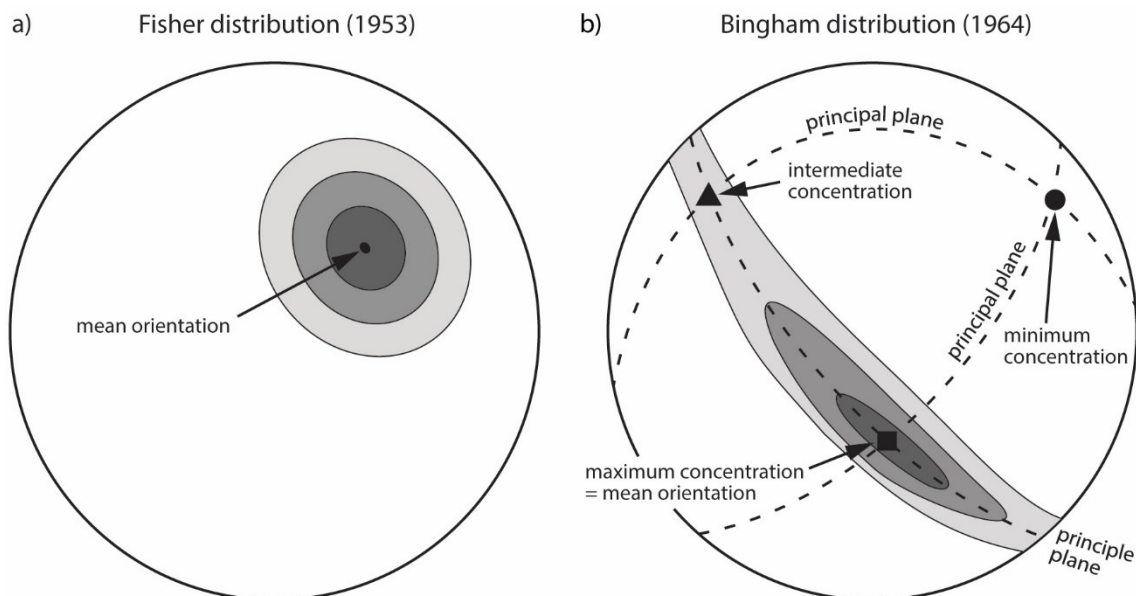


Figure 20: Dataset distributions can be characterized by a mean orientation (as mean dip angle and mean azimuth) and a confidence cone. (a) Fisher distribution of a circular-symmetrical cluster of orientations with density contours represented by cylindrical cones. (b) Bingham distribution of a cluster orientation that possesses a rather orthorhombic symmetry. Its density contours range in shape from ellipses to great circles. After Borradaile (2013).

The **Bingham distribution** (Bingham, 1964, 1974) describes populations of points on a sphere that may range from clusters with circular symmetry, through partial girdles to full girdles with axial symmetry (Borradaile, 2013, Figure 20b). In contrast to a Fisher distribution with a circular confidence cone, the confidence cone of the Bingham distribution will generally show an elliptical form. While a single concentration-parameter ( $\kappa$ ) is sufficient to describe the circular concentration of the Fisher distribution, the Bingham distribution is described by two concentration-parameters ( $\kappa_{\text{INT}}$  and  $\kappa_{\text{MIN}}$ ). These are oriented perpendicular to the peak concentration, where  $\kappa_{\text{INT}}$  represents the concentration of points in the direction of intermediate and  $\kappa_{\text{MIN}}$  in direction of minimum density. The principle directions, as well as the orientation-concentrations are characterized by the use of an orientation-distribution matrix, which was introduced into geology by Scheidegger (1965) and Woodcock (1977). The Bingham calculation within Stereonet 10 can be performed for datasets with more than 25 points and provides the mean dip angle and mean azimuth of the principle direction, as well as the two concentration-parameters  $\kappa_{\text{INT}}$  and  $\kappa_{\text{MIN}}$ . Additional information regarding the Bingham distribution can be found in Bingham (1964, 1974), Onstott (1980), Priest (1993), Mardia and Jupp (2009), and Borradaile (2013).

In the case of a bimodal distribution of a dataset which is obviously following a Fisher distribution, the mean dip angle and mean azimuth were first calculated with the help of the Bingham calculation, because the Fisher calculation could not handle a bimodal distribution. Subsequently the dataset was rotated until it was near-centralized in the stereographic projection to calculate the concentration parameter  $\kappa$  of the Fisher distribution.

### 3.4.3 Fracture Shape

Fractures are seen conceptually as ellipses (Zhang et al., 2002) with an elongation ratio (horizontal length to vertical length)  $> 1$  (Petit et al., 1994). As computing capacity is a greatly limiting factor it is generally necessary to simplify the elliptical form of fractures for DFN modeling. A 16-sided elliptical form with an elongation ratio of 1:2 was chosen.

### 3.4.4 Fracture Set Aperture Distribution

Fracture aperture size is one of the main factors controlling flow in fractures, as it defines the fracture porosity and permeability (National Research Council, 1996; Guerriero et al., 2013; Bisdorf et al., 2016) with a much greater capability of fluid transport than the matrix (Hoffman and Narr, 2012). Its size shows a wide range across

multiple orders of magnitude following a non-linear distribution (Marrett et al., 1999). Many studies show that the aperture distribution can be described by different equation types. Most common are (i) the normal (Hakami, 1995; Hooker et al., 2013), (ii) log-normal (Gale, 1987; Pyrack-Nolte et al., 1987; Johns et al., 1993; Hakami, 1995; Renshaw, 1995; Keller, 1996; Keller et al., 1999; de Dreuzy et al., 2001b; Gillespie et al., 2001; Philipp, 2008; Larsen et al., 2010; Hooker et al., 2012; Hooker et al., 2013), (iii) power-law (Gudmundsson, 1987a; Wong et al., 1989; Marrett and Allmendinger, 1992; Sanderson et al., 1994; Clark et al., 1995; McCaffrey and Johnston, 1996; Marrett, 1997; Bohnenstiehl and Kleinrock, 1999; Marrett et al., 1999; Ortega et al., 2006; Guerriero et al., 2010; Hooker et al., 2011; Le Garzic et al., 2011; Hooker et al., 2012; Hooker et al., 2013, 2014; Bisdom et al., 2016), and (iv) exponential distributions (Nur, 1982; Deschamps et al., 2007).

For every individual fracture set the aperture distribution pattern was examined and a log-normal aperture distribution was chosen as best fitting for this study. Thus for every fracture set an individual mean and standard deviation aperture value was calculated and used as input in Petrel.

#### 3.4.5 Fracture Set Length Distribution

Another crucial parameter for the fracture network characterization is the fracture length, which is one of the main factors controlling the fracture network connectivity. It is also one of the most challenging properties to quantify accurately as it would normally require to completely dismantle the examined rock mass to measure the length (Priest, 1993; Tonon and Chen, 2007; Wenli et al., 2019). The range of the length can vary within a set across several orders of magnitude with a characteristically non-linear distribution with many small and a diminishing number of large fractures (Gillespie et al., 1993; Marrett, 1997; Odling et al., 1999; Gillespie et al., 2001; Hooker et al., 2013). The most common length distributions found in literature are the (i) log-normal (Baecher et al., 1977; Baecher, 1983; Long and Witherspoon, 1985; Rouleau and Gale, 1985; Villaescusa and Brown, 1992; Kulatilake et al., 1993; Aler et al., 1996; Odling, 1997; de Dreuzy et al., 2001a; Leung and Zimmerman, 2012; Liu et al., 2018), (ii) power-law (Segall and Pollard, 1983; Gudmundsson, 1987b; Heffer and Bevan, 1990; Hatton et al., 1994; Belfield and Sovich, 1995; Clark et al., 1995; Marrett, 1997; Odling, 1997; Renshaw, 1999; de Dreuzy et al., 2001a, b; Harris et al., 2003), or (iii) exponential distributions (Call et al., 1976; Cruden, 1977; Priest and Hudson, 1981; Kulatilake et al., 1993; Aler et al., 1996; Olson et al., 2001; Özkaya, 2003).

For this study a log-normal distribution was chosen as it fits the data best. Once again a mean and a standard deviation of the length values was calculated for the fracture sets “DZ Set 1, 2, and 3” and “FC Set 1 and 2” to characterize these in Petrel. For the fracture set “FC Set 3” no length data was available, which posed the challenge of deriving data for its likely distribution from the available information.

Since several studies report a linear relationship between fracture length and aperture (Pollard and Segall, 1987; Vermilye and Scholz, 1995; Özkaya, 2003), the mean length for FC Set 3 was derived from its mean aperture with the help of a length-aperture-factor valid for the FC. This factor was calculated by dividing the mean length by the mean aperture for FC Set 1 and FC Set 2 and subsequently averaging both. The length-aperture-factor was afterwards multiplied with the mean aperture of FC Set 3 resulting in the desired mean length value. To be capable to calculate a log-normal distribution for FC Set 3, an additional standard deviation value was necessary, which was derived with the help of the mean and standard deviation length values from FC Set 1, FC Set 2 and the calculated mean length value of FC Set 3 (see above). To accomplish this a mean-standard deviation-factor was calculated by dividing the mean length value by the standard deviation value for FC Set 1 and FC Set 2 and averaging both. The mean length value of FC Set 3 was subsequently divided by the mean-standard deviation-factor, which gave a standard deviation value for FC Set 3.

#### 3.4.6 Fracture Set Length Truncation

As previously mentioned the fracture length is the most problematic property to measure directly. In addition fractures often terminate on layer boundaries or other fractures, which affects the fracture network connectivity as well. Since the constructed fault zone model was implemented with a division of the DZ into 12 subzones (geological units) the possibility to incorporate a fracture truncation at the top and base of each zone (inherently representing a layer boundary) was given. The modeling software Petrel allows to define a percentage of truncated fractures separately for the top and base of each zone by steps of 10. For each fracture set the amount of truncated fractures at the top and base was calculated considering information about its termination. Since only percentage values in steps of 10 could be prompted the calculated truncation values were rounded.

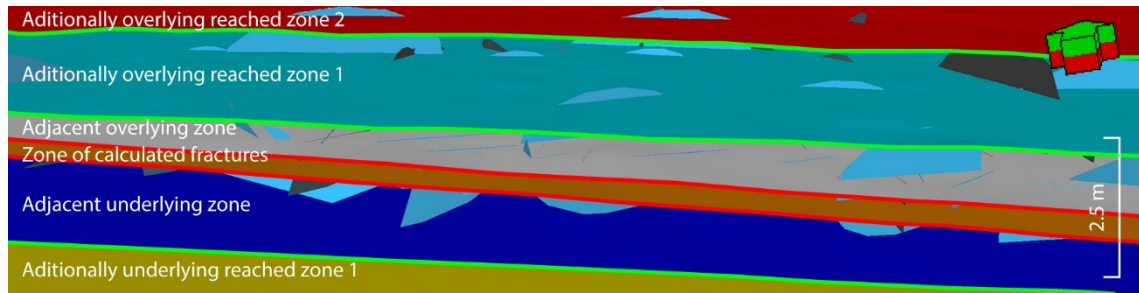


Figure 21: Example of a calculated fracture set for one zone (brown base); lateral inside view in N direction (green-red arrow at the right shows exact spatial orientation). Light blue ellipses represent the extent of fractures. Zone boundaries are illustrated as planes of different colors with their outer borders marked red and green. Red outer borders mark the zone boundaries (grey top and brown base of the zone) used for fracture set calculation and truncation. Green outer borders mark zone boundaries, which were reached by the fractures but could not be integrated in further fracture truncation.

One has to be aware that in the different zones the calculated fractures (chapter 3.5.1) partly also extend into multiple overlying and underlying zones (besides the directly adjacent ones) due to the high vertical model resolution and therefore low thicknesses (Figure 21). It became apparent during modeling that no further truncation was performed at the second over- and underlying tops and bases of the adjacent zones, which seemed highly improbable. For this reason a correction for a geologically more realistic truncation of the fracture sets was added, separately for the top and base, dependent on the number of additional zones reached by the fractures. For every additionally reached zone a truncation percentage of 10 was added to the originally calculated percentage value regarding two framework conditions. First, the top correction of the three uppermost zones (geological units 10, 11, and 12) and the base correction of the three lowest zones (geological units 1, 2, and 3) were performed through a mean correction value as they were too close to the top and base boundaries of the model. The correction value was computed through calculation and subsequent rounding of the mean number of additionally reached zones based on the remaining zones. And secondly the maximum truncation value cannot exceed 90 %. The calculation of the corrected truncation can be found in Appendix 3.

### 3.4.7 Fracture Set Intensity Distribution

To describe the amount of fracturing in a rock mass, several terms are generally used including fracture density, intensity and porosity (Mauldon and Dershowitz, 2000). Older terminology is partly ambiguous. To provide a framework to move between different scales and dimensions a fracture intensity classification scheme, called the  $P_{ij}$  system, has been developed (Dershowitz, 1998; Table 3). The input for fracture

intensity comes typically from boreholes or field measurements in form of linear  $P_{10}$  or areal  $P_{21}$  fracture intensities. However the preferred measure of fracture intensity within DFN modeling is the volumetric  $P_{32}$  intensity, which represents the fracture area per unit volume incorporating a frequency measure and a fracture size component (Dershowitz and Herda, 1992). Unlike the  $P_{10}$  and  $P_{21}$  values it represents a non-directional measure of fracture intensity, which cannot be measured directly, but has to be obtained from  $P_{10}$  or  $P_{21}$  measurements by conversion factors (Esmaili et al., 2015; Rogers et al., 2015).

In this thesis the  $P_{10}$  density was acquired through the scanlines provided by the project partners, which were imported as wells and subsequently converted through an internal Petrel calculation into the desired  $P_{32}$  intensity. For each of the previously defined fracture sets a separate  $P_{32}$  intensity was calculated. Subsequently the calculated  $P_{32}$  values were upscaled onto the corresponding DZ and FC geobodies by applying the previously mentioned SGS algorithm within the property modeling process (see also chapter 3.3.4 and 3.3.4.2).

Table 3:  $P_{ij}$  system used to define fracture intensity in terms of dimension of the sample and dimension of the measure. After Dershowitz (1998) and Rogers et al. (2015).

Dimension of sample	Dimension of measurement			
	0 (Count)	1 (Length)	2 (Area)	3 (Volume)
1D (e.g. borehole, scanline)	$P_{10}$ No. of fractures per unit length	$P_{11}$ Length of fractures per unit length		
2D (e.g. mapping)	$P_{20}$ No. of fractures per unit area	$P_{21}$ Length of fractures per unit area	$P_{22}$ Area of fractures per area	
3D (e.g. geophysical survey)	$P_{30}$ No. of fractures per unit volume		$P_{32}$ Area of fractures per unit volume	$P_{33}$ Volume of fractures per unit volume
Term	Density		Intensity	Porosity

### 3.5 DFN Modeling

By modeling fractures, simulation properties are created, which allow to predict the behavior of reservoirs or geobodies. Most importantly, fracture modeling shows and honors the spatial relationships between the properties of adjacent cells. DFN modeling

is therefore the approach chosen for this study because it bears the ability to incorporate the volume, size, shape, orientation, and aperture of fractures to characterize the fracture networks spatial distribution. As shown in the preceding chapters, many steps are necessary before DFN modeling can be carried out.

### 3.5.1 Fracture Network Calculation

To calculate a fracture network it is necessary to characterize five main properties of the fractures: (i) distribution, (ii) geometry, (iii) orientation, (iv) aperture, and (v) permeability. The structural framework for the calculation is given by the developed fault zone model (chapter 3.3), while the input parameters have been elaborated in chapter 3.4.

The **distribution** defines the intensity, truncation, and physical domain in which the fracture sets are being populated. The calculated  $P_{32}$  intensity was chosen as input. Through splitting of the fault model into the geobodies DZ and FC and the additional subdivision of the DZ into 12 subzones (geological units) various combinations of fracture networks were possible, giving the opportunity to compare their impact on fracture network properties. A total of seven differently distributed fracture networks were calculated.

Through the **geometry** options of Petrel a 16-sided elliptical fracture shape with an elongation ratio of 2 and a log-normal fracture set length distribution was selected. For every discrete fracture a maximum length of 20 m was specified, while a maximum length of 0.2 m was chosen for implicit fractures, also representing the minimum length of the discrete fractures. This means that every fracture below a length of 0.2 m is being modeled implicitly, while all fractures with a length between 0.2 and 20 m are modeled discretely. No smaller maximum length of implicit fractures was chosen due to expected memory problems of the computer. The lower the maximum length of the implicit fractures is, the more probable are computational problems depending on the models scale, resolution, fracture density, and available computing power.

The **orientation** of the fracture sets was defined either by a Fisher distribution or a Bingham distribution with their specific parameters calculated accordingly to chapter 3.4.2.

Within the **aperture** options the log-normal fracture set aperture distribution was supplied and the maximum and minimum fracture aperture was defined. For every fracture set a maximum aperture of 10 mm and a minimum aperture of 0.01 mm was

specified, with an exception for the fracture set of “FC set 1”, where the maximum aperture was set to 20 mm.

The fracture **permeability** is calculated by correlation to the aperture. Fluid flow in fractures is usually modeled with the assumption of laminar flow between parallel plates (Huitt, 1956; Snow, 1965; Klimczak et al., 2010) and the parallel-plate solution for the Navier-Stokes equations (Temam, 2001) leads to the commonly used “cubic law” (Snow, 1965; Witherspoon et al., 1979; Tsang and Witherspoon, 1981; Lee and Farmer, 1993; Oron and Berkowitz, 1998; Wang et al., 2015). It is described by:

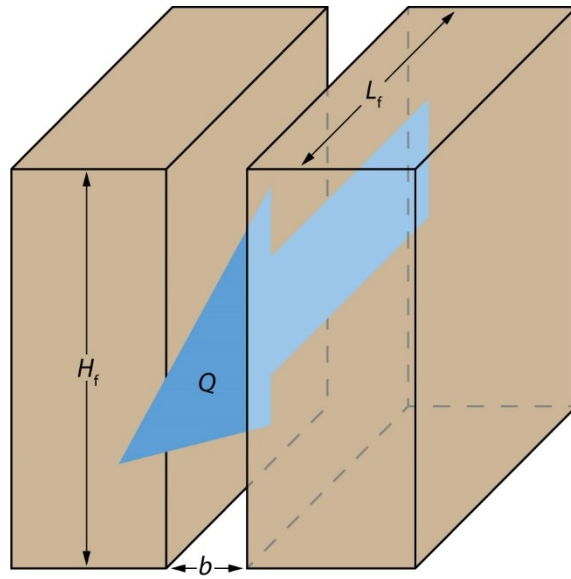


Figure 22: Illustration of the flow  $Q$  between two parallel plates with the aperture  $b$ , the height  $H_f$  and the length  $F_f$ . After Klimczak et al., 2010.

$$Q = \frac{-\rho g b^3 \nabla h}{12\mu} \quad 3.3$$

$Q$  is the flow between the two plates,  $\rho$  the fluid density,  $g$  the gravitational acceleration,  $b$  the distance between the two plates (also referred to as aperture),  $\nabla h$  the hydraulic gradient, and  $\mu$  the fluid viscosity. The total flow between parallel plates of the height  $H_f$  (Figure 22) results from Equation 3.3 and is described by:

$$Q = \frac{-\rho g b^3 \nabla h H_f}{12\mu} \quad 3.4$$

With the simplification of parallel planar plates to represent the fracture surfaces it is shown (Polubarinova-Kochina, 1962; Louis, 1969; Witherspoon et al., 1979; Lee and Farmer, 1993; Sarkar et al., 2004) that through a derivation of Equation 3.3 the hydraulic conductivity  $k_f$  of a fracture is given by:

$$k_f = \frac{(2b)^2 \rho g}{12\mu} \quad 3.5$$



A fractures permeability  $k_p$  can be described after Sarkar et al. (2004) through the combination of Equation 3.5 and Darcy's law by neglecting the fluid properties resulting in:

$$k_p = \frac{b^2}{12} \quad 3.6$$

Equation 3.6 is the one used within the DFN process for the fracture permeability calculation, dependent on the fractures aperture.

### 3.5.2 Fracture Network Property Upscaling

Through the upscaling process the calculated fracture network properties are distributed over the models grid and converted into properties that are essential for dual porosity and dual permeability modeling including the fracture porosity, fracture permeability and the sigma factor. Dual porosity and dual permeability models are characterized through a separate calculation of porosity and permeability for the two domains of the models: the matrix and the fractures. In the following three possibilities of upscaling fracture permeability are described, as well as calculation of the sigma factor. The fracture porosity  $\Phi$  is defined as the percentage share of a grid cell and does not require a detailed depiction.

#### 3.5.2.1 Permeability

To upscale the fracture network permeability the user can choose between the (i) Oda, (ii) Oda corrected, and (iii) flow-based method.

The **Oda** method (Oda, 1985, 1986; Oda et al., 1987) is over 30 years old, has been rederived with variations many times and is used to deduce a permeability tensor in every of the three grid directions. Its advantage is that it can obtain equivalent porous media (EPM) grid cell properties for grid cells based directly on the fracture's geometry within those cells (Dershowitz et al., 2004; Rong et al., 2013; Ghahfarokhi, 2017). The method starts by generating the full 3D DFN. It overlays thereafter an EPM grid on the fractures and subsequently derives the EPM properties for each cell based on the cells DFN. With the information about the fracture areas, and transmissivities, obtained from the DFN, an empirical fracture tensor for a specific grid cell can be calculated by adding individual fractures weighted by their area and transmissivity described by:

$$F_{ij} = \frac{1}{V} \sum_{k=1}^N f_k A_k T_k n_{ik} n_{jk} \quad 3.7$$

$F_{ij}$  is the fracture tensor,  $V$  the grid cell volume,  $N$  the total number of fractures in a grid cell,  $f_k$  the percolation factor for fracture  $k$ ,  $A_k$  the area of fracture  $k$ ,  $T_k$  the transmissivity of fracture  $k$ , and  $n_{ik}$  and  $n_{jk}$  the components of a unit normal to the fracture  $k$ . By the assumption that  $F_{ij}$  expresses the fracture flow as a vector along the fracture's unit, the normal Oda's permeability tensor is derived from  $F_{ij}$ . Assuming that fractures are impermeable in a direction parallel to their unit normal,  $F_{ij}$  must be rotated into the planes of permeability (Dershowitz et al., 2004) by:

$$k_{ij} = \frac{1}{12} (F_{kk} \delta_{ij} - F_{ij}) \quad 3.8$$

In Equation 3.8  $k_{ij}$  is the permeability tensor,  $F_{ij}$  the fracture tensor,  $\delta_{ij}$  the Kroenecker delta, and  $F_{kk}$  the trace of the fracture tensor matrix. In this way the Oda approximation derives an equivalent permeability tensor for every grid cell. While DFN flow-based modeling is limited to about  $10^5$  fractures the Oda method is capable of handling up to  $10^7$  fractures and is the most used and fast algorithm technique in commercial modeling software. However, this advantage is at the expense of the fractures' connectivity as it assumes that all fractures are connected. The Oda method overestimates permeability (Dershowitz et al., 2000; Gupta et al., 2001; Dershowitz et al., 2004; Will et al., 2005; Ghahfarokhi, 2017), therefore the Oda corrected method was introduced.

The **Oda corrected** method is designed to take the connectivity of the fracture network better into account, being as close as possible to the flow based method while still remaining fast in terms of processing time. Therefore an additional connectivity analysis is computed, used for a connectivity correction. While the Oda method computes the fracture permeability in the three grid directions (ki, kj, and kk) the connectivity analysis computes seven additional properties which are: (i) the connectivity index "CI", (ii) the extended connectivity indices "eCii", "eCij", "eCik" along the i, j and k axes, and (iii) the length ratios of fractures present in a cell "Li", "Lj", and "Lk" projected on the i, j, and k axes. In the following the connectivity index CI will be used representative for the fracture connectivity by quantifying the average number of fracture intersections per fracture within a given cell.

The **flow-based** method creates a finite element grid for every grid cell. Subsequently it simulates flow under a pressure gradient to calculate the permeability for every of the three directions (i, j, and k). It is much slower than either of the two Oda methods, but more precise by taking into account the full geometry of the system. The results depend, however, strongly on the defined boundary conditions (Ahmed-Elfeel and Geiger, 2012). The flow-based method was initially applied within this study, however the calculation process was aborted after one week of computational time. After an estimation by Ahmed-Elfeel et al. (2010) and Cottureau et al. (2010) a single flow-based permeability calculation for the number of cells in this study would require about 80 days.

Additionally it should be mentioned that not every permeability upscaling method can handle the IFN (implicit fracture network) part of the whole fracture network. The program developers expanded the Oda method, implemented in Petrel. An additional algorithm was introduced, which allowed upscaling of the whole network (IFN and DFN). In contrast, the Oda corrected and flow-based methods can only be applied to the DFN.

### 3.5.2.2 Sigma Factor

To describe the fluid flow in any model used for simulation of fractured domains the fluid exchange from matrix to fracture is of crucial importance. Its determination is not simple, however, due to the potentially complex interactions between fractures and variously shaped rocks. Barenblatt et al. (1960) originally proposed the concept of dual continuum models, which was chosen up by Warren and Root (1963) who introduced the dual porosity model (Lim and Aziz, 1995; Moinfar, 2013). In both studies the transfer per bulk volume unit between the matrix and the fracture was assumed to take place under pseudo-steady state conditions, which is represented by:

$$q = \frac{\sigma k_m}{\mu} (P_m - P_f) \quad 3.9$$

In this formula,  $q$  denotes the matrix-fracture flow rate per unit bulk volume,  $k_m$  the matrix permeability,  $\mu$  the fluid viscosity,  $P_m$  the matrix pressure, and  $P_f$  the fracture pressure. The characteristics of the fractured rock are represented by the parameter  $\sigma$ , which has the dimension of reciprocal area and is known as “sigma factor” (also referred to as “shape factor”). Warren and Root (1963) then obtained the expression:

$$\sigma = \frac{4n(n+2)}{L^2} \quad 3.10$$

Here  $n$  is the number of normal sets of fractures and  $L$  the characteristic length of the matrix blocks. Kazemi et al. (1976) introduced the application of the sigma factor in numerical simulations. Using a finite-difference formulation for the flow between the matrix and the fracture they showed for a three-dimensional case that:

$$\sigma = 4 \left( \frac{1}{L_x^2} + \frac{1}{L_y^2} + \frac{1}{L_z^2} \right) \quad 3.11$$

$L_x$ ,  $L_y$ , and  $L_z$  represent the distance between fractures in the x, y, and z directions. The sigma factor proposed by Kazemi et al. (1976) is used in various commercially available reservoir simulators (Firoozabadi and Thomas, 1990) including the one used in the presented study. For every version of upscaled fracture networks a sigma factor was calculated.

## 4 Results

### 4.1 Lithology

#### 4.1.1 Damage Zone

The DZ of the Lower Buntsandstein succession was covered by four profiles and five layer traces (Figure 24) and divided into 14 geological units, of which 12 were incorporated in the fault zone model. Unit 2a and 11a were too small in their spatial extent to be captured in the fault zone model. Five lithofacies types after Miall (1978) were recognized within the succession, of which the type “St” was further divided into “St1”, “St2” and “St3” dependent on the geological unit’s grain size, sorting, thickness and trough crossbed size, resulting in a total of seven lithofacies types (Table 4). Each geological unit corresponds to a lithofacies type (Table 5).

Table 4: Lithofacies types used for classification of the geological units identified in this study. Based on Miall (1978) with refinements and additions.








Lithofacies type	Color code	Lithofacies and grain-size	Sedimentary structure	Thickness	Sorting
St1		Sandstone, fine- to coarse-grained, may be pebbly	Small-sized solitary or grouped trough crossbeds	< 40 cm	Well-very well
St2		Sandstone, fine- to very coarse-grained, may be pebbly	Medium-sized solitary or grouped trough crossbeds	40-120 cm	Well
St3		Sandstone, medium- to very coarse-grained, may be pebbly	Large-sized solitary or grouped trough crossbeds	> 120 cm	Poor-well
Sp		Sandstone, fine- to medium-grained	Solitary or grouped planar crossbeds	20-80 cm	Well
Sh		Sandstone, very fine- to medium-grained	Horizontal lamination	< 40 cm	Well-very well
Sl		Sandstone, very fine- to medium-grained	Low-angle crossbeds	80-130 cm	Moderately-well
Fl		Mudstone, siltstone, fine-grained sandstone	Fine lamination	< 25 cm	Well-very well

Table 5: Overview of the geological units and their corresponding lithofacies type.

Geological unit	1	2	2a	3	4	5	6	7	8	9	10	11	11a	12
Lithofacies type	Sp	Sp	Fl	Sl	Sh	St3	Sp	St2	St1	Sl	Sp	St3	Fl	St3



Figure 23: Yellow and white colors caused by bleaching within red sandstones, primarily along bedding planes and around fractures.

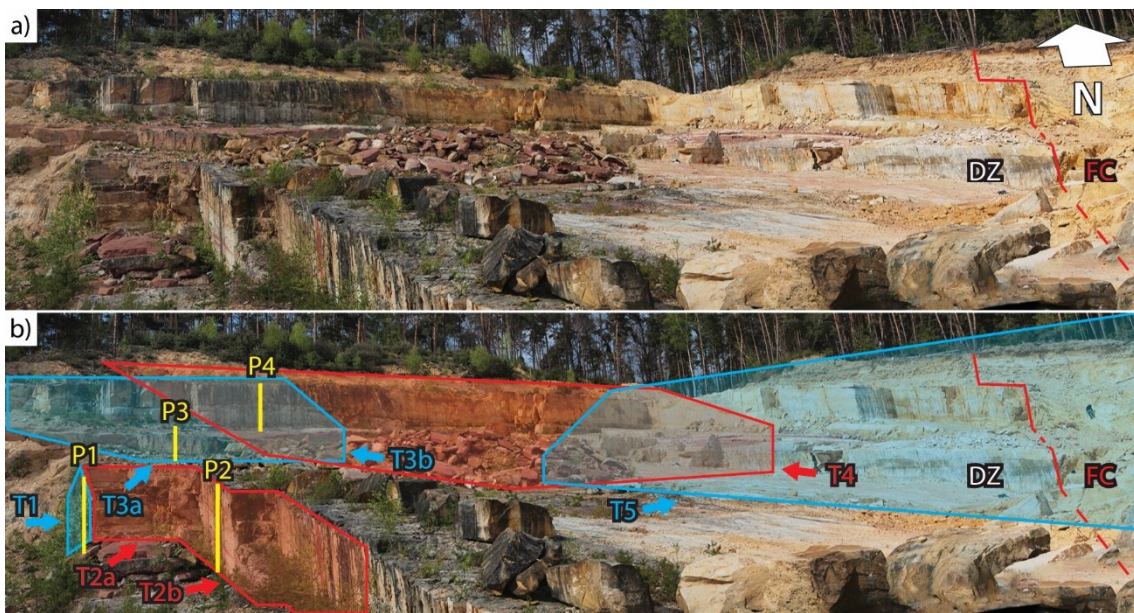


Figure 24: (a) Panoramic overview of the studied outcrop. (b) Same overview with marked locations of profiles (P1-P4) and areas of layer tracing (T1-T5), which are portrayed in detail in the following figures. DZ: damage zone, FC: fault core. Red line on the right marks the border between the DZ and FC.

The succession consists of fine- to medium-grained sandstones with intercalations of mud- to siltstones with a moderate to very well sorting. Sandstone bodies show thicknesses of decimeters to meters and consist primarily of crossbeds with occasionally intercalated sandstone pebbles and mud clasts, mainly found at the base. Thinner successions of up to several decimeters thickness are characterized by lamination. Amalgamation is common within cross-bedded sand bodies. Lateral extent of the beds correlates with its thickness and grain-size. The lateral extents of beds with a thickness of several decimeters to meters cannot be observed because their elongations exceed the outcrop scale. Beds of up to a few decimeters thickness usually thin out after several meters. Thicker beds tend to have larger grain sizes (fine to coarse

sandstone) while thinner beds show small grain-sizes (clay to fine sandstone). Bleaching could be observed in the whole succession, mostly along bedding planes and around fractures, leading to red, yellow and white sandstones (Figure 23). For discussion of the bleaching phenomenon see Soyk (2015).

Specific observations for each geological unit (GU) gathered during profile mapping and layer tracing are described in the following. Figure 24 shows an overview of the locations of profiles P1-P4 and traces T1-T5.

**GU1:** Planar cross-bedded, fine- to medium-grained sandstone of 80 cm thickness with fine white laminar bleaching (mm-cm) along bedding planes. Represents the lowest fully recognizable GU in the outcrop. See P1 (Figure 25) and T1 (Figure 27).

**GU2:** Planar cross-bedded, fine- (to medium)-grained sandstone of 75-80 cm thickness with an erosive basis. Shows white laminar bleaching (mm-cm) along bedding planes and small bleached spots of mainly several mm diameter. See P1 (Figure 25), T1 (Figure 27), and T2 (Figure 28).

**GU2a:** Up to 10 cm thick, fine-laminated, mud- to siltstone showing fining upward. This bed thins out horizontally after several m. It has a too low spatial extent to be incorporated as a GU in the fault zone model. See P1 (Figure 25), T1 (Figure 27), and T2 (Figure 28).

**GU3:** Low angle cross-bedded, (fine to) medium-grained sandstone with a thickness of up to 125 cm. Shows wide areal yellow bleaching (dm-m), as well as white-red banding in multiple places caused by laminar white bleaching (cm). See P1, P2 (Figure 25), T1 (Figure 27), and T2 (Figure 28).

**GU4:** Horizontal laminated, fine- to medium-grained sandstone with a thickness of up to 40 cm, thinning out in northern direction. White-red banding (cm-dm) is common, caused by bleaching along bedding planes. See P1, P2 (Figure 25), T1 (Figure 27), and T2 (Figure 28).

**GU5:** About 2.5 m thick, medium- to coarse-grained sandstone with large-size trough cross-beds. Consists of yellow and white amalgamated sand bodies with poor to moderate sorting at the basal part, elsewhere moderate to well sorting is observed. Mud clasts of several cm length can be found at the erosive base. See P1, P2 (Figure 25), P3 (Figure 26), T1, T2 (Figure 28), T3 (Figure 27), and T4 (Figure 29).

**GU6:** Planar cross-bedded silt- to fine-grained sandstone of up to 20 cm thickness, mostly white bleached. Thins out several meters westward to P3. See P3 (Figure 26), T3 (Figure 27), and T4 (Figure 29).

**U7:** 80-120 cm thick, medium-grained sandstone with medium-size trough cross-beds.

Shows white and yellow bleaching along bedding planes (cm-dm) with isolated pebbles of several cm length. Its thickness decreases westwards of P3. See P3 (Figure 26), T3 (Figure 27), and T4 (Figure 29).

**GU8:** Fine-grained, small-size trough cross-bedded sandstone with a thickness of up to 35 cm and an erosive base. Is completely white bleached and thins out about 15 m eastwards of P3. See P3 (Figure 26), T3 (Figure 27), and T4 (Figure 29).

**GU9:** Low-angle cross-bedded, fine- to medium-grained sandstone of 80 cm thickness with an erosive base. The western extent of the layer is characterized by a distinct red color with places of fine red-white banding (mm-cm) caused by white laminar bleaching. Bleaching intensifies towards the east leading to a thicker cm-dm banding. See P3, P4 (Figure 26), T3 (Figure 27), and T4 (Figure 29).

**GU10:** Up to 40 cm thick, planar cross-bedded, medium-grained. Is completely white bleached and thins out towards the west. See P4 (Figure 26), T3 (Figure 27), and T4 (Figure 29).





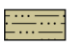

**GU11:** Medium-grained, amalgamated sandstones with a thickness of 135 cm, further characterized by large-scale trough cross-beds. The erosive basal part contains large mud clasts and pebbles (cm-dm) and shows a poor to moderate sorting, which improves to well sorting in the central part of the sand body. Mostly white bleached with rarely yellow spots. See P4 (Figure 26), T3 (Figure 27), and T4 (Figure 29).

**GU11a:** Up to 25 cm thick, laminated siltstone to fine-grained sandstone with a horizontal extent of about 8 m. Mostly red colored with laminar white bleaching in some spots. This GU is too small in its spatial extent to be incorporated in the fault zone model. See P4 (Figure 26), T3 (Figure 27), and T4 (Figure 29).

**GU12:** 3.0-3.5 m thick, amalgamated, medium-grained sandstone with large-size trough cross-beds. The erosive basal part shows large mud clasts and pebbles (cm-dm) with a moderate sorting. The upper part of the sand body is well sorted. See P4 (Figure 26), T3 (Figure 27), and T4 (Figure 29).



**Sedimentary structure and lithology**

-  Trough cross-bedded sandstone
-  Low angle cross-bedded sandstone
-  Planar cross-bedded sandstone
-  Horizontally laminated sandstone
-  Laminated mud- to fine-grained sandstone
-  Mud clast

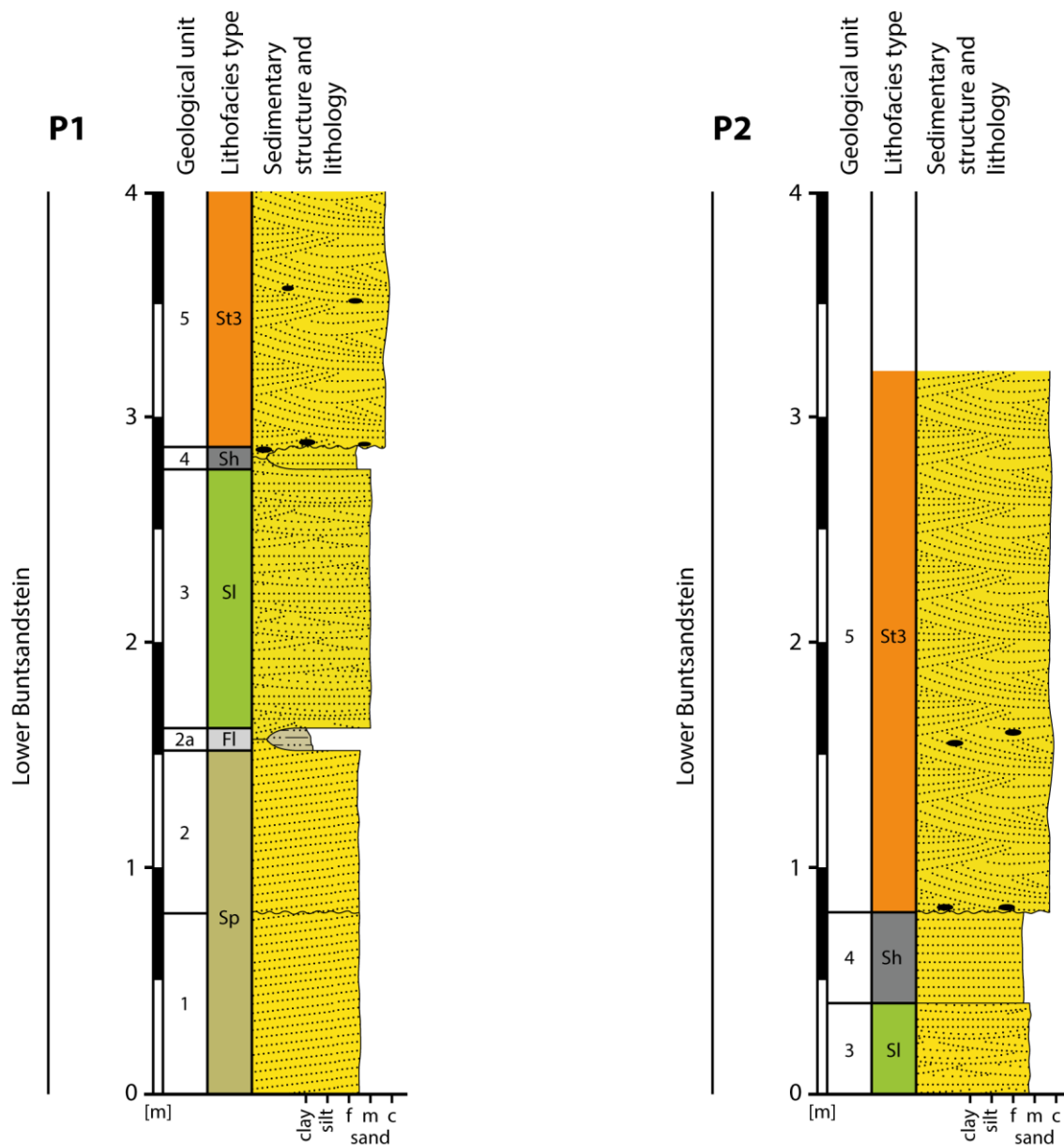

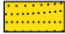







Figure 25: Profiles P1 (4 m) and P2 (3.2 m) covering GU1 to 5 of the lower and middle succession of the outcrop.

**Sedimentary structure and lithology**

-  Trough cross-bedded sandstone
-  Low angle cross-bedded sandstone
-  Planar cross-bedded sandstone
-  Horizontally laminated sandstone
-  Laminated mud- to fine-grained sandstone
-  Mud clast
-  Pebble

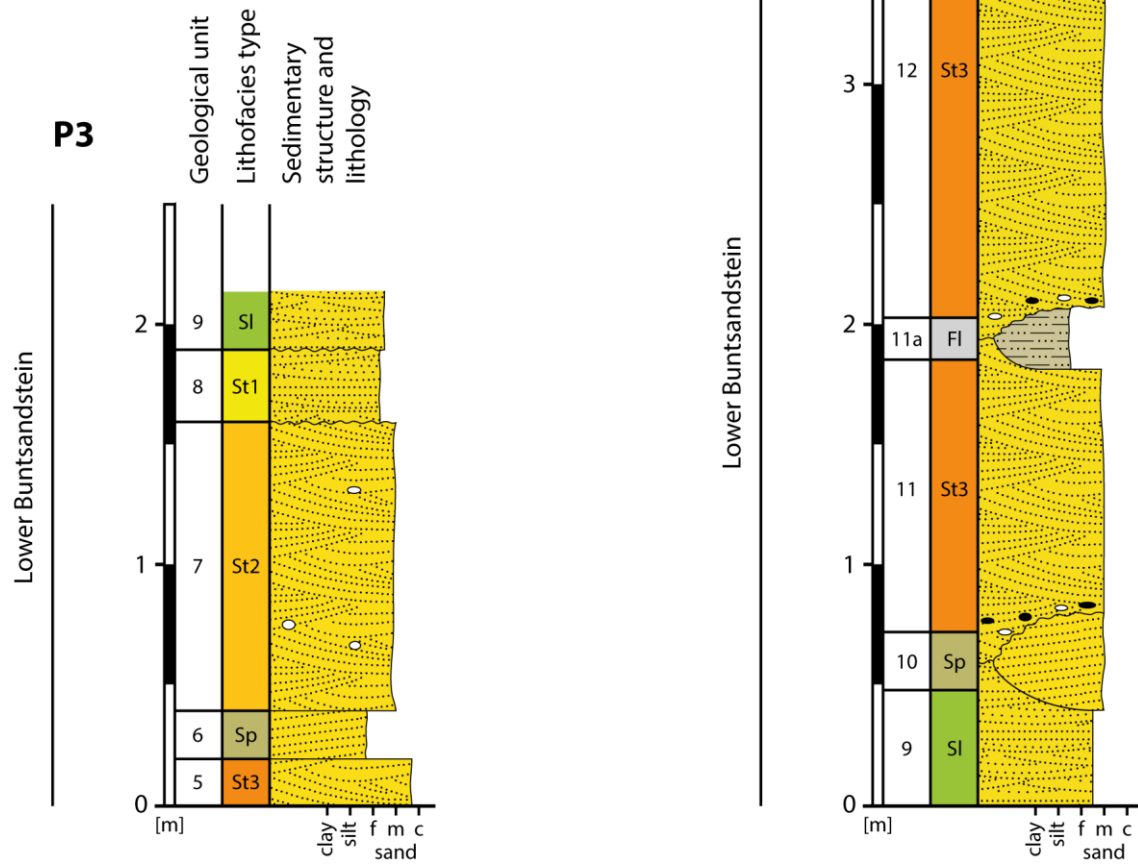


Figure 26: Profiles P3 (2.1 m) and P4 (4.17 m) covering GU5 to 12 of the middle to upper succession of the outcrop.



Figure 27: (a) Trace T1 of the lowermost part of the outcrop showing GU1 to 5 and the position of profile P1 (4m). Images (b) and (c) represent trace T3 from two different angles including GU5 to 12 and profiles P3 (2.1 m) and P4 (4.17 m).



Figure 28: Detailed illustration of trace T2 including GU3, 4 and 5, as well as the position of profile P2 (3.2 m). (a) On the left side the northernmost part of T2 borders directly on T1 around a corner (marked by a red line). (b) Southern part of T2. Blue arrow marks the transition from (a) to (b).



Figure 29: (a) Trace T4 of GU5 to 12 with its left part merging with T3. (b) Trace T5 represents the southern extent of T4 reaching up to the fault core border (red line). The fault core shows a minimum horizontal extent of 14 m (Bauer et al., 2015).

4.1.2 Fault Core

The FC facies model established was inspired by Fredman et al. (2008), Braathen et al. (2009), and Fachri et al. (2011). The model constitutes, together with the FC facies log, the FC lithology results (Figure 30). The determination of the FCFTs is described in detail in chapter 3.1.2.1. It is based on the FC architecture illustration and description of the lithological and structural FC elements by Bauer et al. (2015).

For the FC facies model a total of seven different FCFTs were established, five of lithological and two of structural origin: (i) sandstone consolidated (Sc), (ii) sandstone spreading (Ss), (iii) sandstone unconsolidated (Su), (iv) gouge, silt unconsolidated (Gs), (v) gouge, clay unconsolidated (Gc), (vi) deformation band cluster (DBC), and (vii) slip zone (SZ). The resulting FC facies log has a length of 11 m and comprises 15 sections, each with a horizontal extent of 27-237 cm and a corresponding FCFT.

a) **Fault core facies types**

Lithological types

- Sc: Sandstone consolidated
- Ss: Sandstone spreading
- Su: Sandstone unconsolidated

- Gs: Gouge, silt unconsolidated
- Gc: Gouge, clay unconsolidated

Structural types

- DBC: Deformation band cluster
- SZ: Slip zone

b) **Fault core facies log**

DBC	Gc	Ss	Gc	Ss	DBC	Sc	Ss	DBC	Su	Gs	Sc	Ss	SZ	Gc
46	45	79	27	39	70	90	77	41	113	41	58	69	237	68
Thickness [cm]														






















Figure 30: a) FCFT determined based on results of Bauer et al. (2015). b) FC facies log comprising 15 sections with thicknesses of 27-237 cm. c) Overview of the upper part of the FC (right side) showing the location of the FC facies log (purple line). Position may slightly differ due to temporal differences between acquisition of this specific image and fieldwork conducted by Bauer et al. (2015) within the active quarry.

## 4.2 Petrophysics Determination

For each geological unit of the DZ a PPMV-pair was determined based on the petrophysical data provided by project partners. Within the FC a total of 7 PPMV-pairs were determined, one for every FCFT defined. Table 6 provides an overview of every PPMV-pair used in the subsequent modeling steps. As mentioned earlier, lithofacies type “Fl” is not listed, because the spatial extent of its corresponding geological units (2a and 11a) is too small to be incorporated in the model. For detailed description of the PPMV-pair determination within the FCFTs the reader is referred to chapter 3.1.

Table 6: Overview of the determined porosity and permeability values for the 12 geological units of the DZ and the 7 FC facies types.

Geobody	Geological unit	Facies type	Color code	Porosity [%]	Permeability [mD]
DZ	12	St3		20.75	959.53
	11	St3		18.78	959.53
	10	Sp		10.19	35.87
	9	Sl		16.37	9.62
	8	St1		11.39	9.76
	7	St2		17.82	72.67
	6	Sp		10.19	35.87
	5	St3		17.99	959.53
	4	Sh		12.22	166.195
	3	Sl		18.34	280.62
	2	Sp		10.19	35.87
	1	Sp		10.19	35.87
FC		Sc		16.86	172.05
		Ss		25	400
		Su		40.9	1000
		Gs		55	10
		Gc		49.5	0.01
		DBC		10	3
		SZ		9	0.9

### 4.3 Digital Outcrop Model

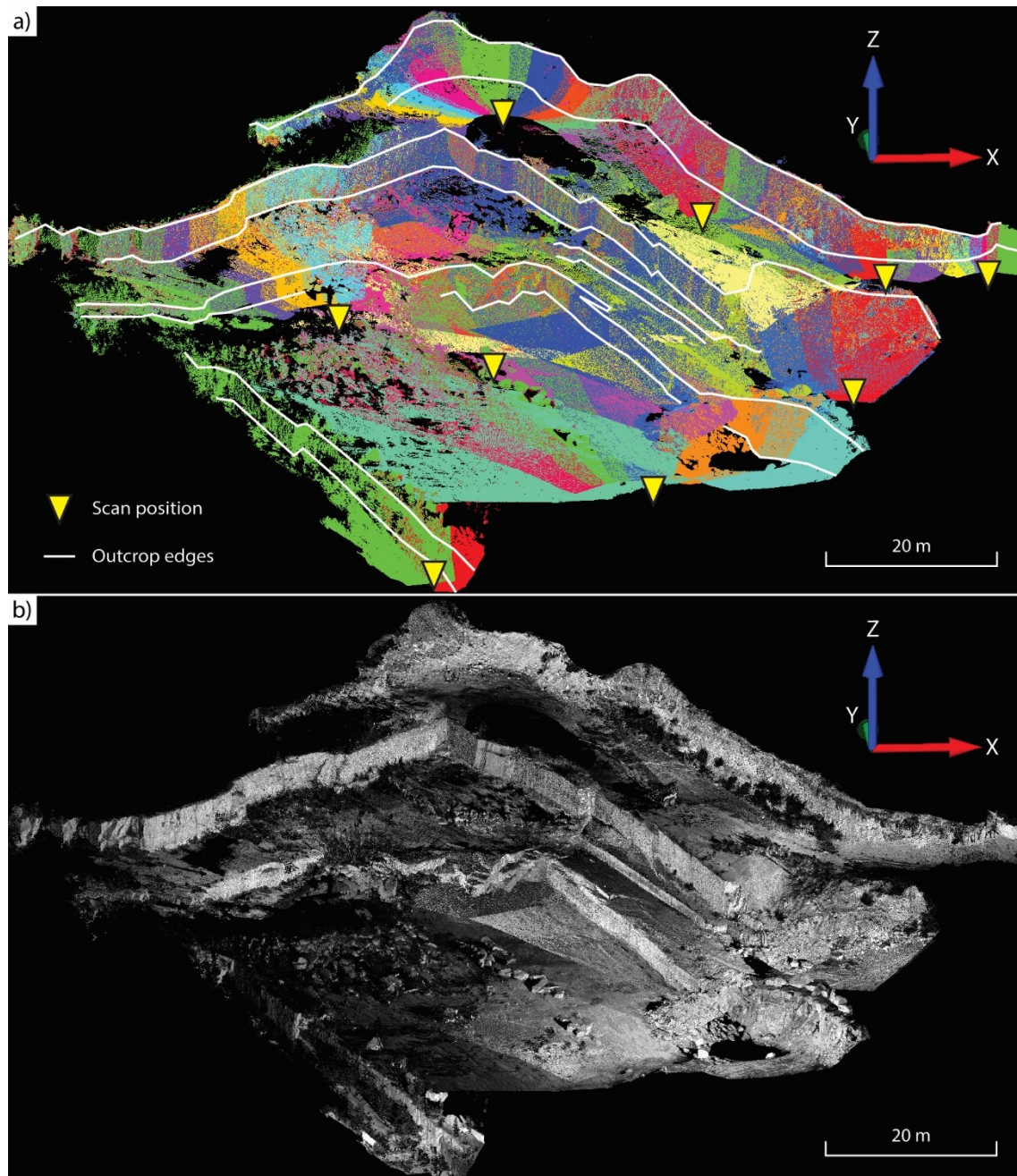


Figure 31: (a) Overview showing the 9 scan positions from which 50 point clouds and 370 photographs were taken. Different colors represent different point clouds overlapping each other. (b) All point clouds merged to a single "master"-point cloud comprising 18.5 million points showing the confidence color mapping. Y= north.

The construction of the DOM was preceded by TLS (see chapter 2.1.2). During the TLS fieldwork phase the outcrop was scanned and photographed from 9 different positions resulting in 50 point clouds (Figure 31) and 370 photographs covering the succession. The point clouds were scanned from ranges between 6 and 74 m with a mean of 25 m.



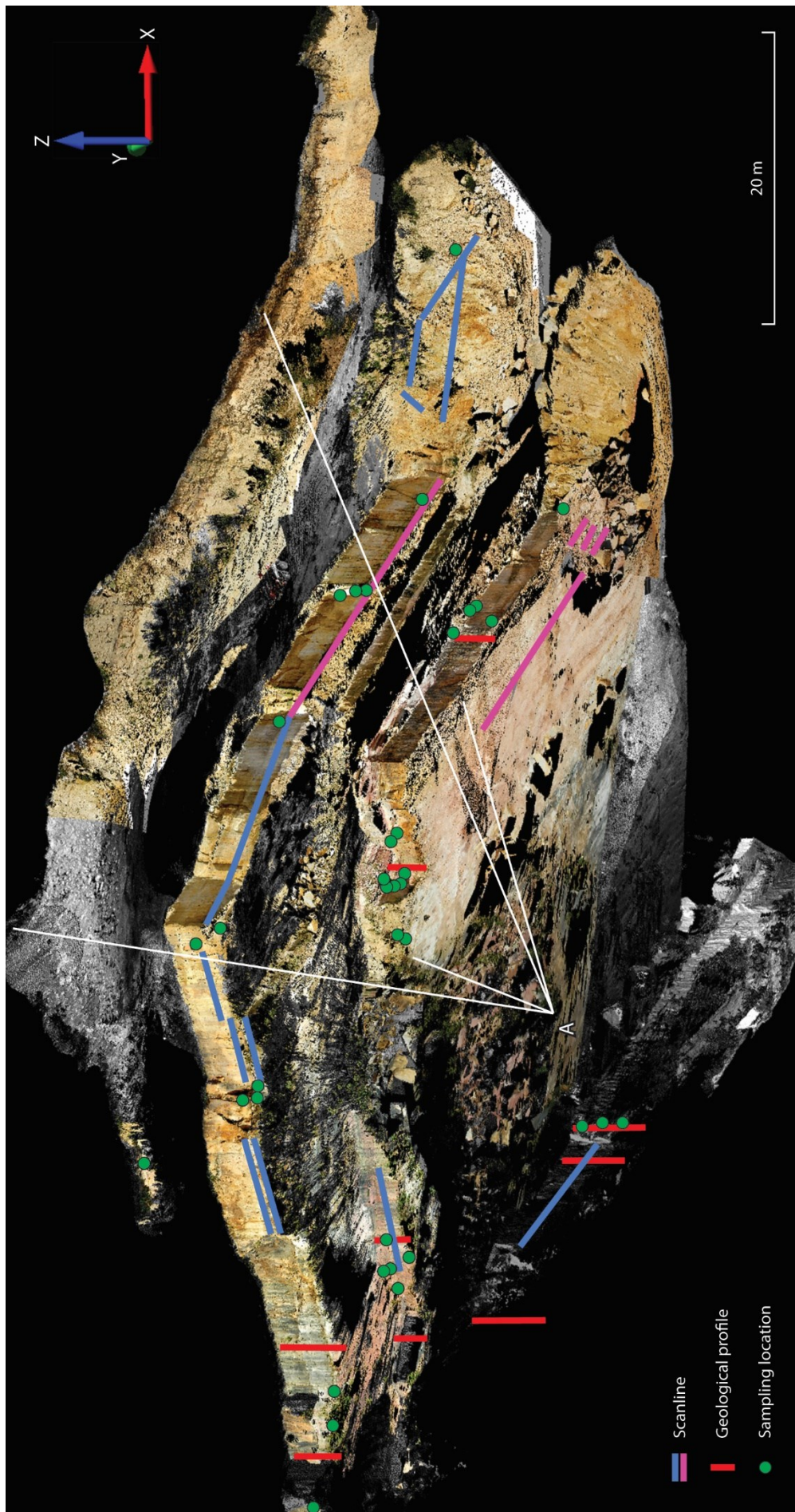


Figure 32: Final DOM with an extent of about 120 x 120 m consisting of 33 colored texture maps and several point cloud filling gaps (grey). Data acquired by the author and project partners was gathered and georeferenced to provide a good overview. Pink scanlines were acquired during earlier stages of excavation than the DOM, and subsequently spatially corrected. Blue scanlines were not affected by the excavation progress. Y = north; A: Angle of view for detailed display in Figure 33.

Their point density amounts to a mean of 22 mm, with a more widely-spaced minimum of 39 and a maximum of 10 mm. The original 22.2 million points were reduced in number by cutting off vegetation and areas of no interest. Thereafter the DOM comprises a total of 18.5 million points, the 50 point clouds consist of 114,460 to 2.4 million points with a mean point count of 444,348.

The final DOM has an extent of about 120 x 120 m and consists of 33 colored texture maps and several point clouds filling in gaps (Figure 32). A detailed view of the central part of the outcrop is shown in Figure 33. In consultation with the project partners 37 sampling locations, 14 scanlines and 9 profiles were brought together and georeferenced in the DOM. Outcrop edges were digitized to enhance the visibility of its structure. Exposed tops of the geological units within the DZ were picked according to the geological profiles and traces, as well as the fault core boundary plane, resulting in hundreds of picked points. These picked points are not explicitly shown, as their amount is too high, but their location corresponds to the traces in chapter 4.1.1.

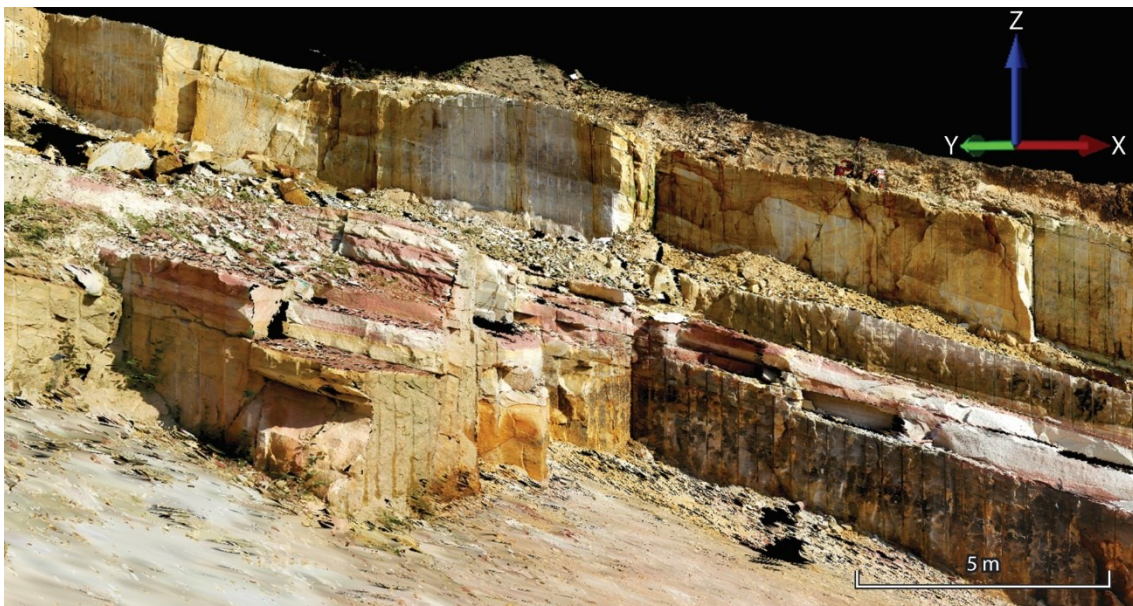


Figure 33: Detailed display of the central part of the final DOM used to gather, visualize and georeference data acquired by the author and project partners. Exact angle of view can be seen in Figure 32. Y = north.

## 4.4 Fault Zone Model

### 4.4.1 Surface and horizon modeling

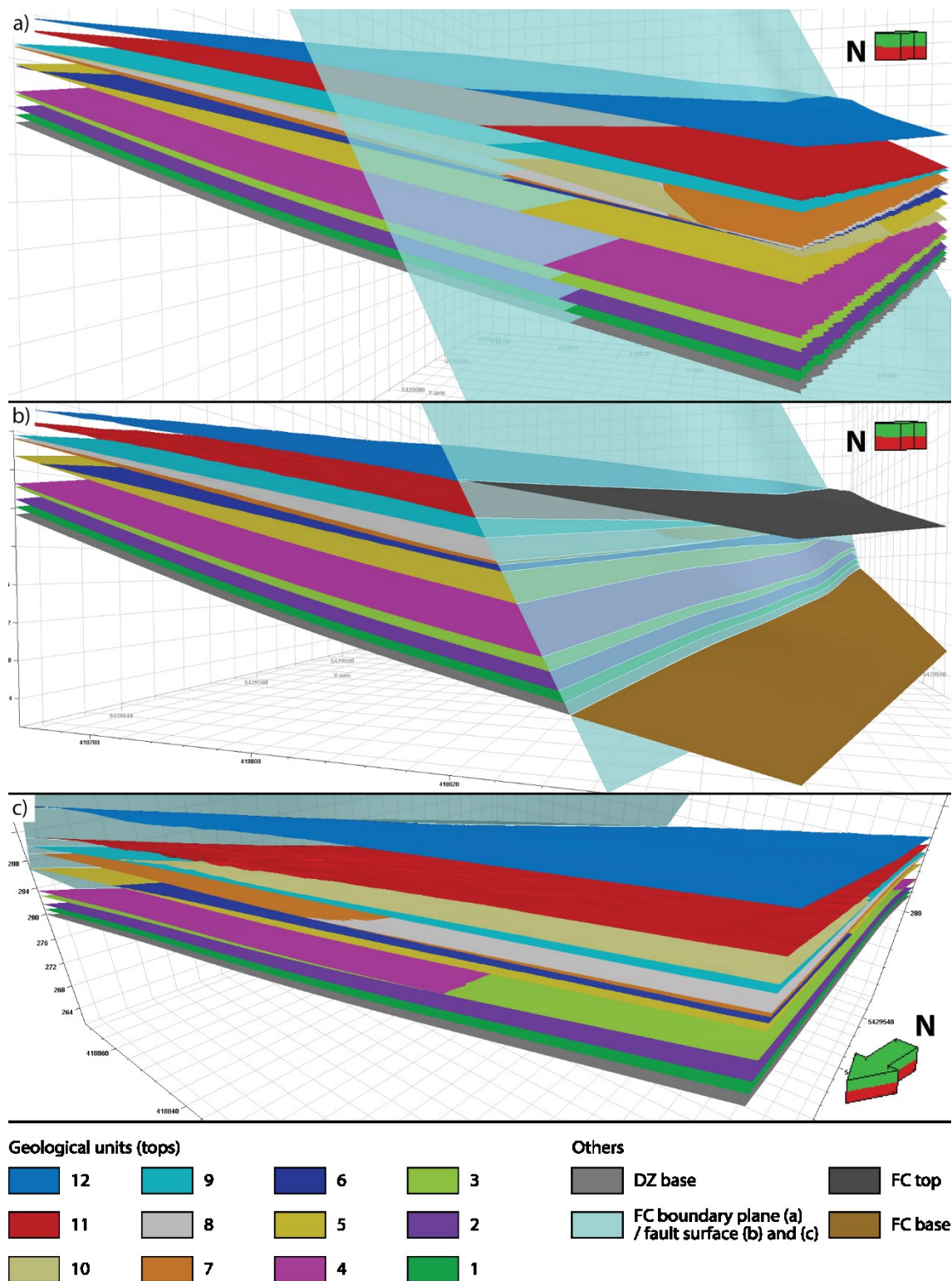


Figure 34: Results of a) the surface calculation confining the 12 tops of the geological units, as well as a base-surface and a FC boundary plane; b) the horizon modeling considering truncation and the geobody separation with the help of the fault surface; c) horizon modeling from a different view direction. View of (a) and (b) in NNW-direction, (c) in SE-direction.

The data gathered and preprocessed during field work and digital outcrop modeling were imported into Petrel and used to calculate 12 surfaces representing the tops of the geological units as well as a base-surface confining the models base and a FC boundary plane (Figure 34a). The FC boundary plane was used within the fault framework process to calculate a fault surface, which in turn was used to separate the DZ from the FC. Figure 34b and c show the result of the subsequent horizon modeling considering truncation information and geobody separation.

#### 4.4.2 Structural Gridding

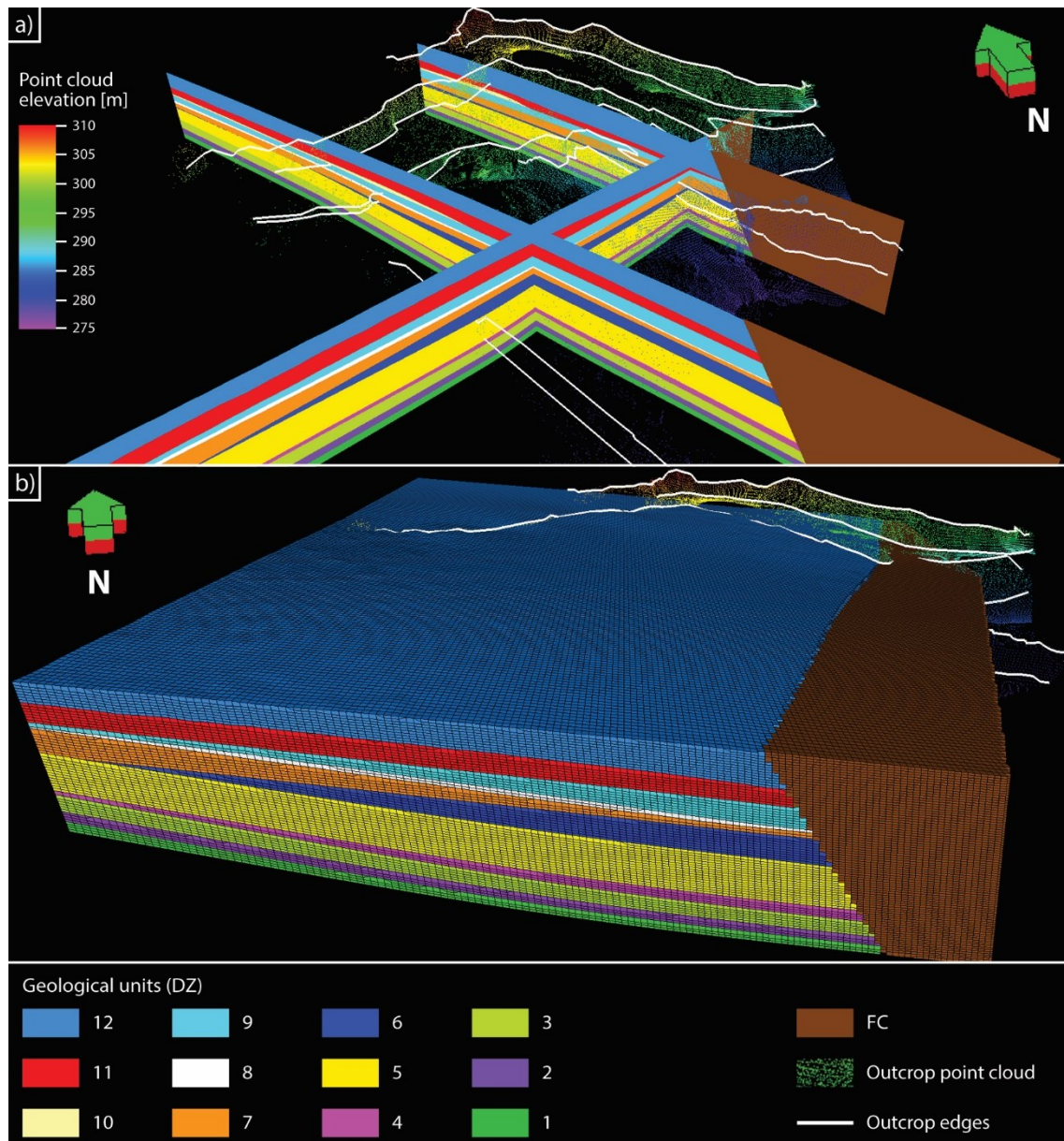


Figure 35: a) Result of the 13 calculated zones; 12 belonging to the DZ (left part) and one to the FC (right part). b) Structural grid with an extent of 100 x 100 x 10-17 m (XYZ) comprising 8.88 million cells. Vertical fluctuation results from thickness variability and truncation of geological units. Outcrop edges and a sub-sampled point cloud by the factor 400 are added to improve the spatial perception.

Based on the results from the precedent chapter a total of 13 zones were calculated comprising 12 geological units in the DZ and one in the FC zone (Figure 35). The created structural grid (Figure 35b) consists of 8.88 million cells (57.2 % DZ and 42.8 % FC) and has an extent of 100 x 100 x 10-17 m (XYZ). Each cell has a dimension of 0.5 x 0.5 x 0.2 m (XYZ).

#### 4.4.3 Petrophysics Distribution

Figure 36 shows the result of the petrophysical property distribution in the DZ. The values were assigned directly to their corresponding geological unit (Figure 36). The results of the porosity and permeability distribution of the FC are shown in Figure 37. Both properties were calculated with the help of the SGS algorithm based on a porosity and permeability log derived from the FC facies log (see chapter 3.1.1.2). Three cases (A, B, and C) of different elongation values for the FCFBs were calculated: 10-25 m for case A, 25-50 m for case B, and >50 m for case C. Case B was chosen for subsequent modeling steps because it represents the geologically most reasonable result and corresponds best to the FCFB elongation results of Fachri et al. (2011). Furthermore, the FCFT percentage fractions of case B are closest to the percentage fractions of the FC facies log, which is shown in chapter 4.4.4. Figure 38 shows the porosity and permeability distribution of the DZ and the FC (case B) combined in one fault zone model.

#### 4.4.4 Facies Model

Lithofacies types of the DZ were assigned directly to the corresponding geological units, while the FCFTs were assigned to the cells holding the corresponding petrophysical properties. Figure 39 shows the final fault zone facies model, which combines the DZ and the FC (case B) and comprises a total of 13 facies types (6 within the DZ and 7 within the FC). Table 7 presents an overview of the percental facies type fractions of the DZ, the FC log, and the three FC distribution cases. Case B is used in subsequent modeling steps because its result corresponds best to the percental facies fractions of the FC facies log, which constitutes the origin for the distribution pattern. A detailed illustration of the distribution pattern of each FCFT for case B is shown in Figure 40. Illustrations of the FCFT distributions for FC case A and C can be found in Appendix 2.

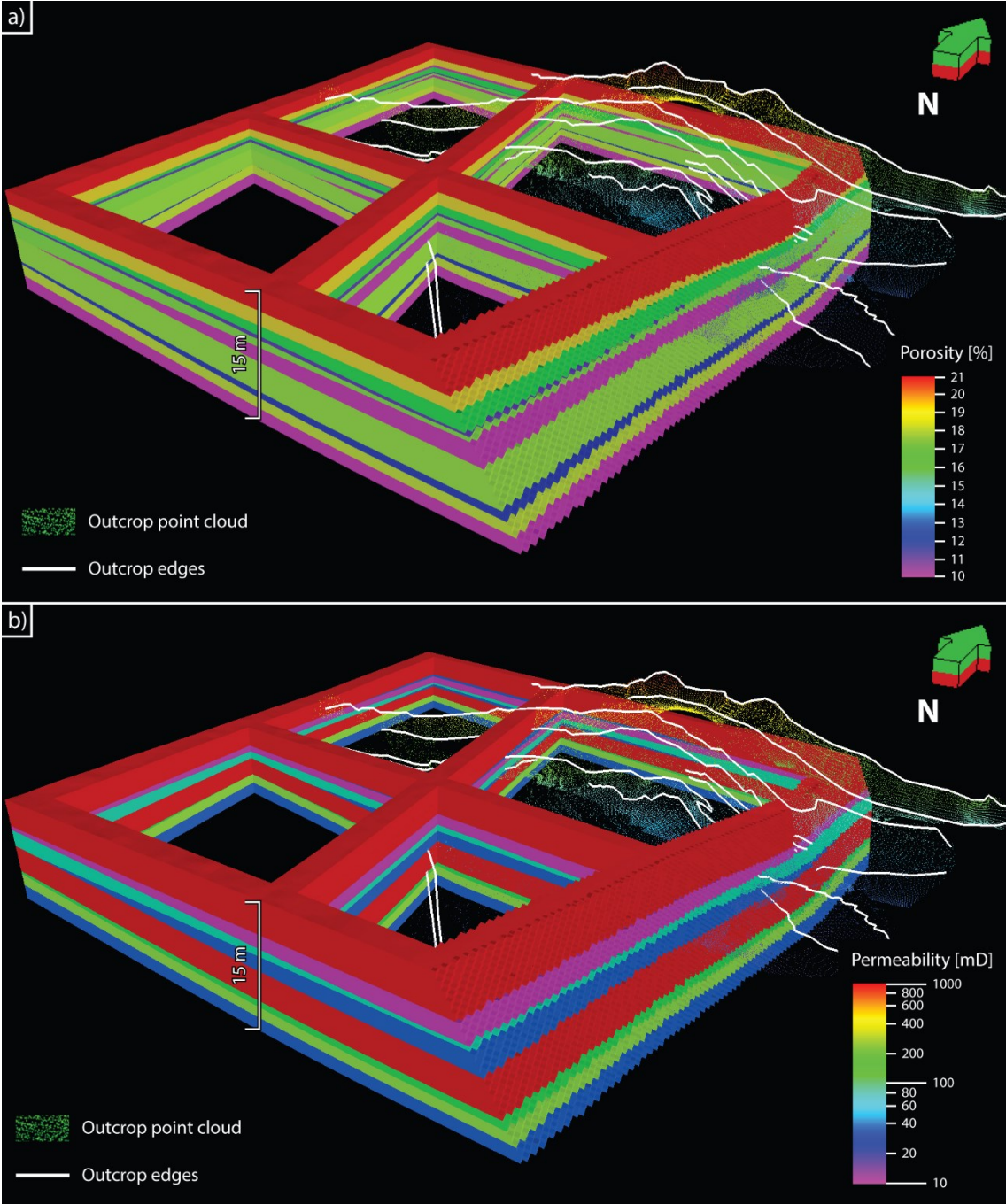


Figure 36: (a) Porosity and (b) permeability distribution of the DZ. Each geological unit received a corresponding PPMV-pair. The illustration shows the structural grid (see Figure 35b) with hidden grid lines to provide a better color display. Inner parts of the DZ are cut out along the i and j axes to allow an internal view.

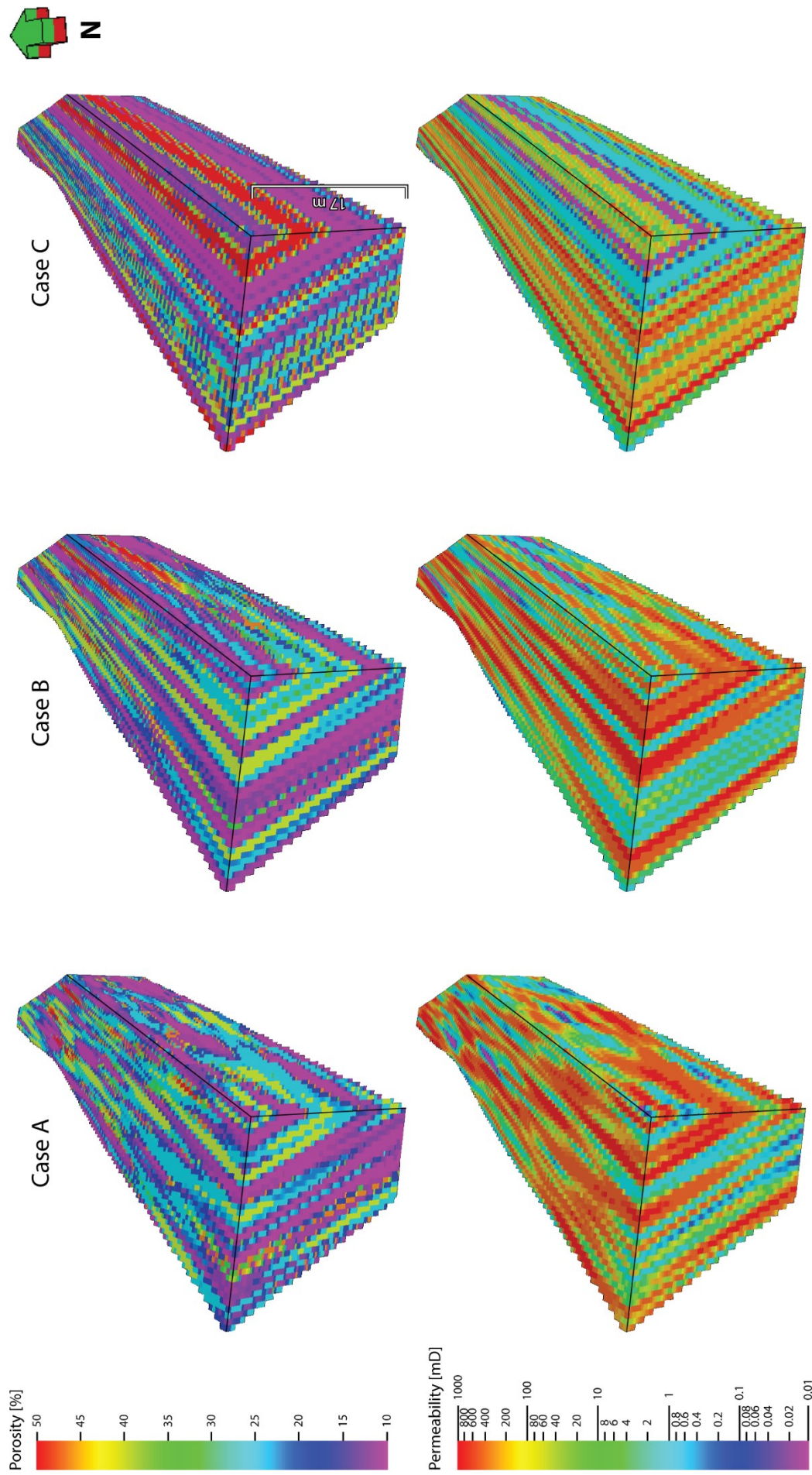


Figure 37: Results of the three porosity (upper part) and permeability (lower part) distributions within the FC. Case A shows a FCFB elongation of 10-25 m, B 25-50 m, and C > 50m.

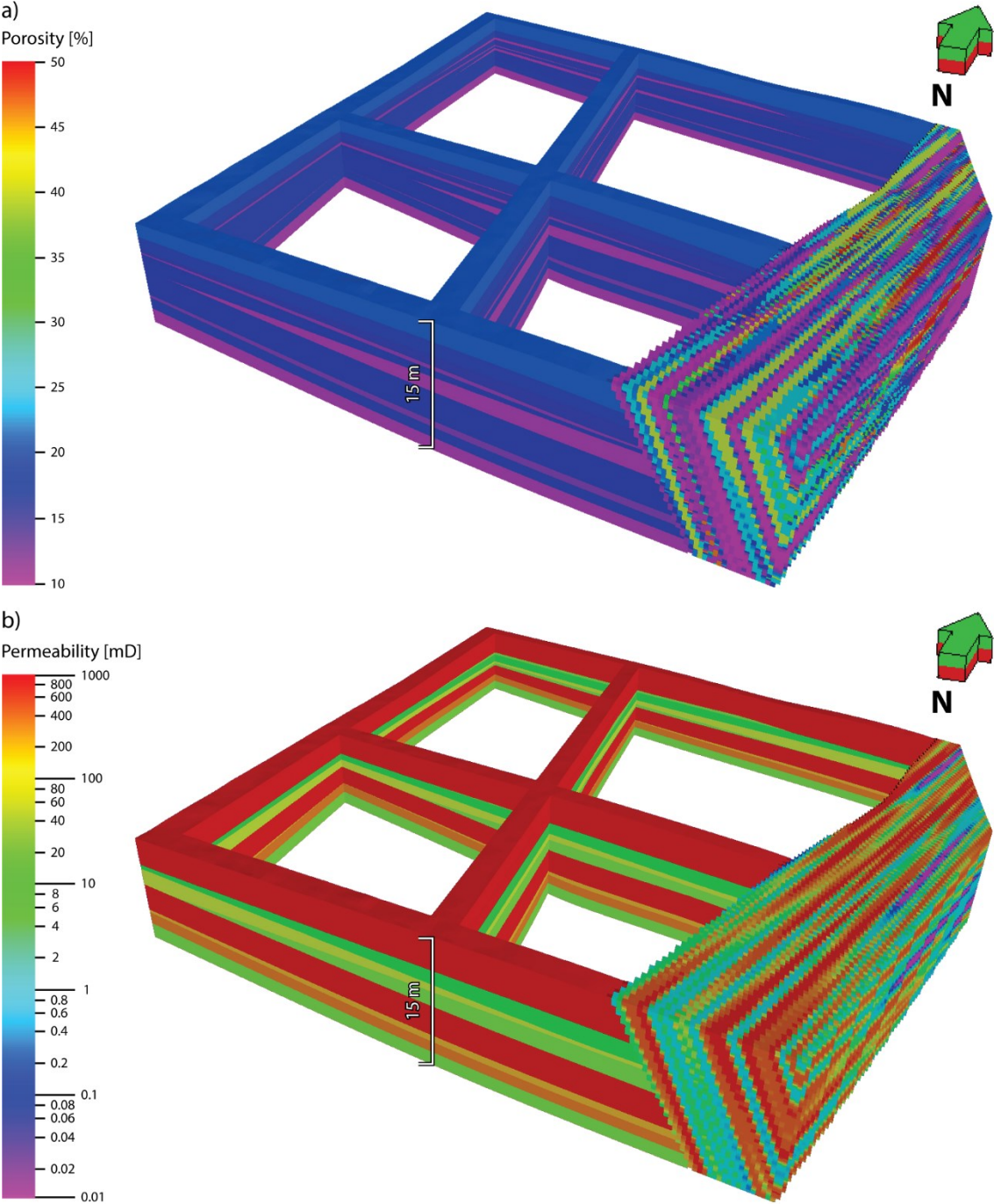
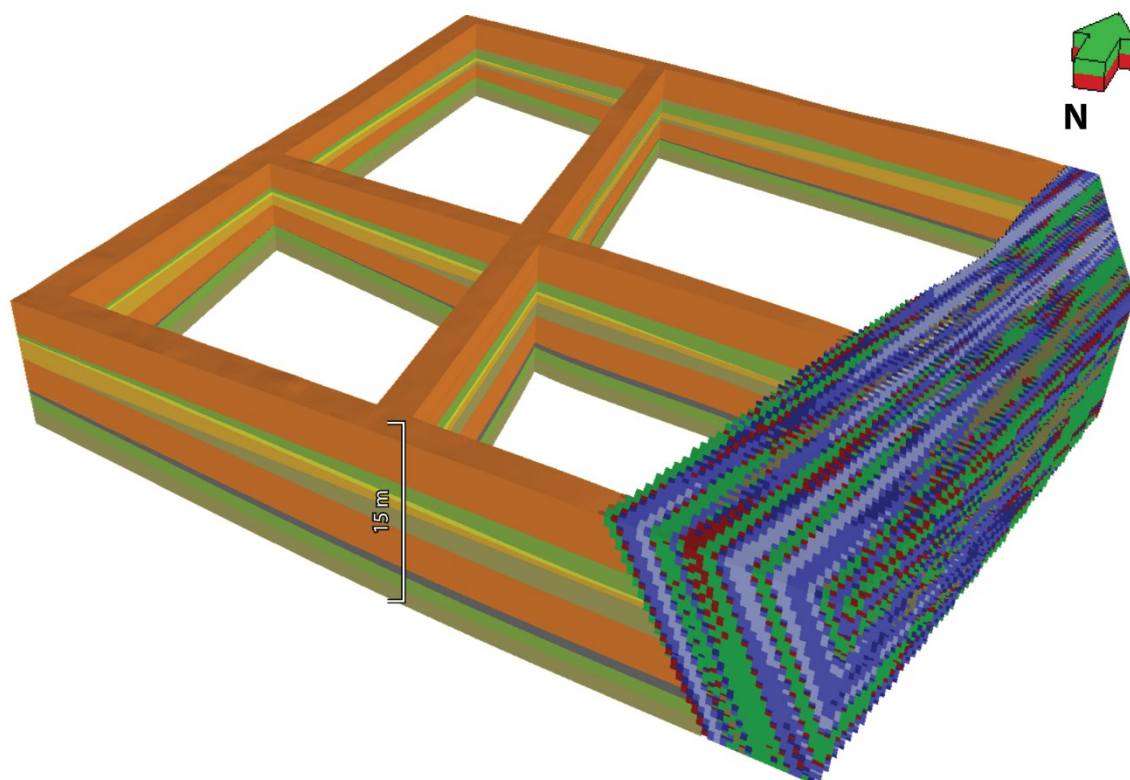


Figure 38: Result of the complete porosity and permeability distribution of the fault zone model combining the DZ and FC (case B) used in subsequent modeling steps. Inner parts of the DZ are cut out to allow an insight.





#### Damage zone facies types

- St1: FSa-CSa, small-sized trough crossbeds
- St2: FSa-CSa, medium-sized trough crossbeds
- St3: MSa-CSa, large-sized trough crossbeds
- Sp: FSa-MSa, planar crossbeds
- Sh: FSa-MSa, horizontal lamination
- Sl: FSa-MSa, low-angle crossbeds

#### Fault core facies types

##### Lithological types

- Sc: Sandstone consolidated
- Ss: Sandstone spreading
- Su: Sandstone unconsolidated
- Gs: Gouge, silt unconsolidated
- Gc: Gouge, clay unconsolidated

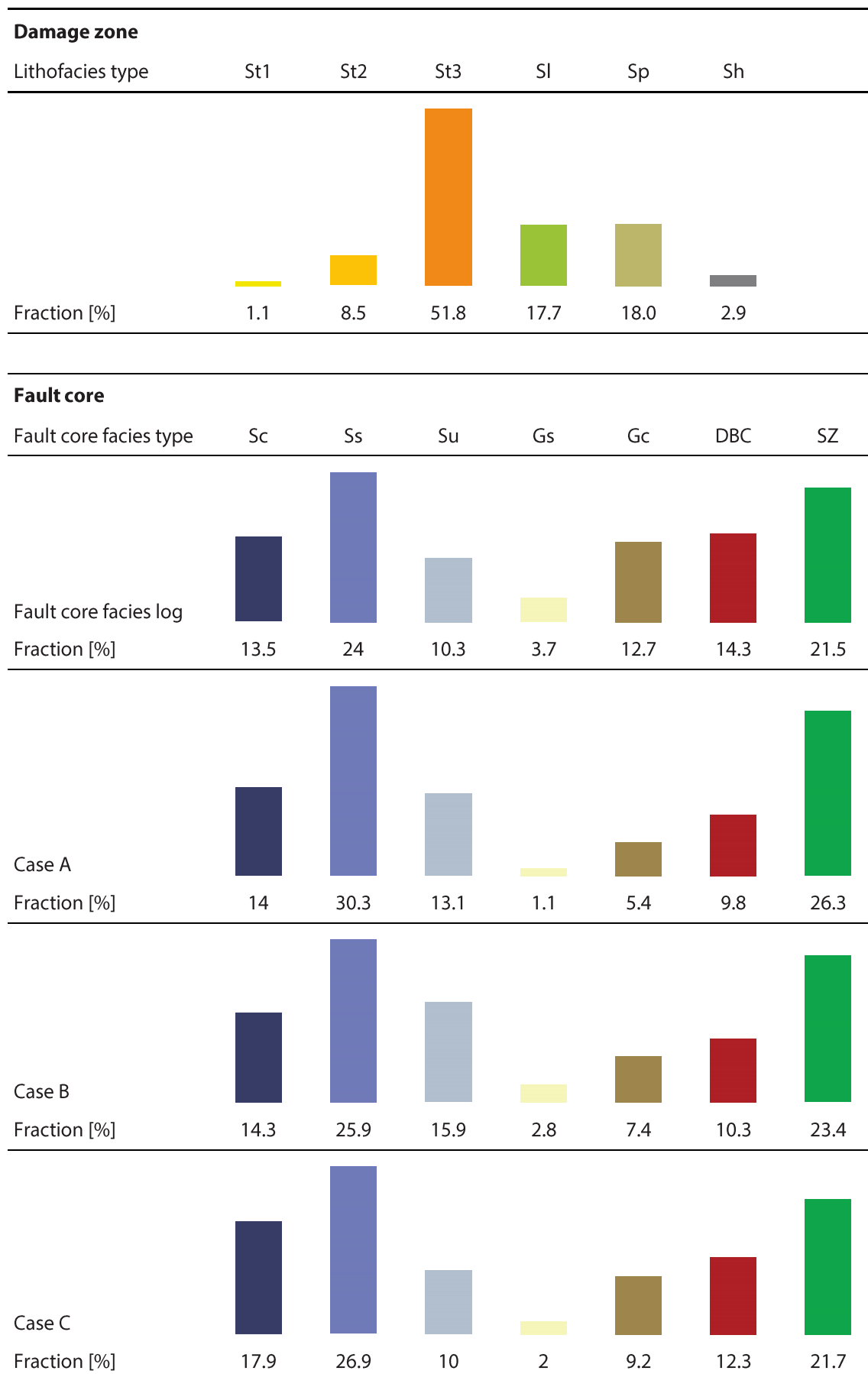
##### Structural types

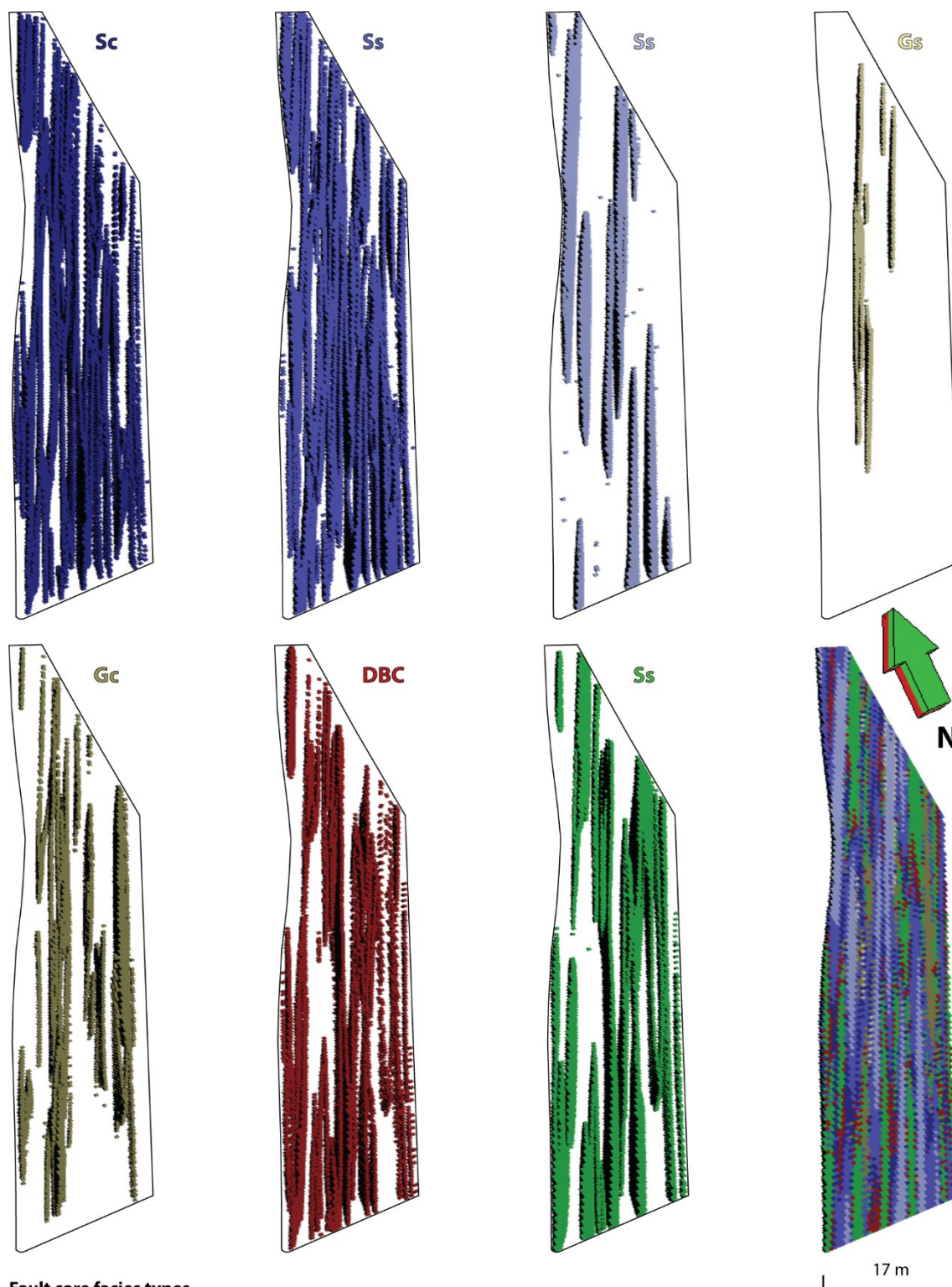
- DBC: Deformation band cluster
- SZ: Slip zone

Figure 39: Final facies model of the fault zone comprising 13 facies types: 6 lithofacies types of the DZ and 7 FC facies types.

## Results

Table 7: Percentual facies fractions for the DZ, FC facies log and FC cases A, B, and C.





**Fault core facies types**

Lithological types

- Sc: Sandstone consolidated
- Ss: Sandstone spreading
- Su: Sandstone unconsolidated
- Gs: Gouge, silt unconsolidated
- Gc: Gouge, clay unconsolidated

Structural types

- DBC: Deformation band cluster
- SZ: Slip zone

Figure 40: Distribution pattern of every single FCFT of distribution case B. A view from above was chosen to provide a display of the individual FC facies bodies within a FCFT. In addition the FC was extended horizontally by a factor of 2 perpendicular to the facies bodies' elongation to gain better visuality.

## 4.5 DFN Parametrization

### 4.5.1 Fracture Set Division and Orientation

A total of 408 fracture measurements were visualized in Stereonet 10, of which 276 are located in the DZ and 132 in the FC. For each of these two geobodies (DZ and FC) the fracture data were divided into three sets (Figure 41) resulting in six fracture sets. Dependent on their distribution pattern a Fisher or Bingham analysis was performed for each of these sets. Fracture set “FC Set 3” had to be analyzed with the  $n_v < 16$  Fisher method (Equation 3.2) because the necessary minimum number of orientations for a Bingham analysis has not been reached, although the observed pattern tends towards a Bingham distribution. Table 8 summarizes the fracture set orientation results.

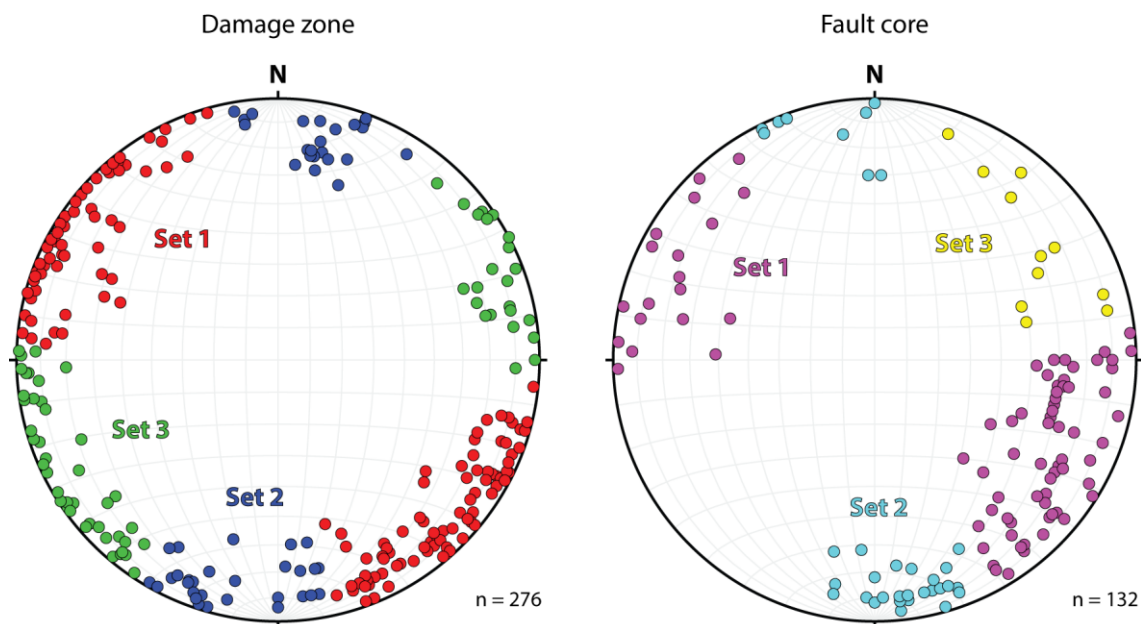


Figure 41: Division result of the raw fracture data into six fracture sets; three within the DZ (left) and three within the FC (right).

Table 8: Result of the Fisher and Bingham distribution analyses for each fracture set previously defined.  $\kappa$  = concentration-parameter of the Fisher distribution;  $\kappa_{INT}$  and  $\kappa_{MIN}$  = concentration-parameters of the Bingham distribution.

Fracture set	Distribution type	Mean dip angle	Mean dip azimuth	$\kappa$	$\kappa_{INT}$	$\kappa_{MIN}$
DZ Set 1	Bingham	87°	128°		4.1	2.2
DZ Set 2	Fisher	89.2°	191°	16		
DZ Set 3	Bingham	88.8°	244.4°		5.5	2.8
FC Set 1	Fisher	75.3°	115.1°	9.8		
FC Set 2	Fisher	82.9°	171.1°	24		
FC Set 3	Fisher	54.1°	67.6°	12.3		

#### 4.5.2 Fracture Set Aperture and Length Distribution

The result of the aperture and length distribution of the defined fracture sets is illustrated in Figure 42 (DZ) and Figure 43 (FC). A log-normal distribution was chosen as best fitting for both data sets. In contrast to Set 1 the FC data shows a lower data scatter for FC Set 2 and 3, which is caused by problems for proper measurements due to the outcrop geometry and spatial extent of the sets. Because no length data was available for the FC Set 3 the values were derived from its aperture data, which is described in detail in chapter 3.4.5. Table 9 shows the results of the calculated mean and standard deviation for each fracture set, as well as the limits used for the aperture and length distribution of the DFN.

Table 9: Calculated aperture and length input parameters of the fracture sets.

Geobody	Set	Aperture [mm]				Length [m]			
		Mean	Std. dev.	Max.	Min.	Mean	Std. dev.	Max.	Min.
DZ	1	0.632	0.556	10	0.01	2.271	2.044	20	0.2
	2	0.661	0.703	10	0.01	2.578	1.937	20	0.2
	3	0.697	0.459	10	0.01	1.421	1.547	20	0.2
FC	1	2.303	3.191	20	0.01	1.506	1.179	10	0.2
	2	2.1	2.054	10	0.01	1.358	1.068	10	0.2
	3	0.775	0.164	10	0.01	0.504	0.455	10	0.2

#### 4.5.3 Damage Zone Fracture Set Length Truncation

For each of the three DZ fracture sets an average fracture length truncation percentage was calculated (Table 10) based on the raw data. Table 11 presents the results of the corrected truncation values of the 12 geological units. A detailed description of the calculation is found in chapter 3.4.6 and Appendix 3.

Table 10: Average truncation values of the three DZ sets.

Fracture set	Truncated at	Average truncation [%]	
		Calculated	Rounded
DZ Set 1	Top	68.39	70
	Base	32.9	30
DZ Set 2	Top	58.5	60
	Base	56.6	60
DZ Set 3	Top	70.59	70
	Base	44.12	40

## Results

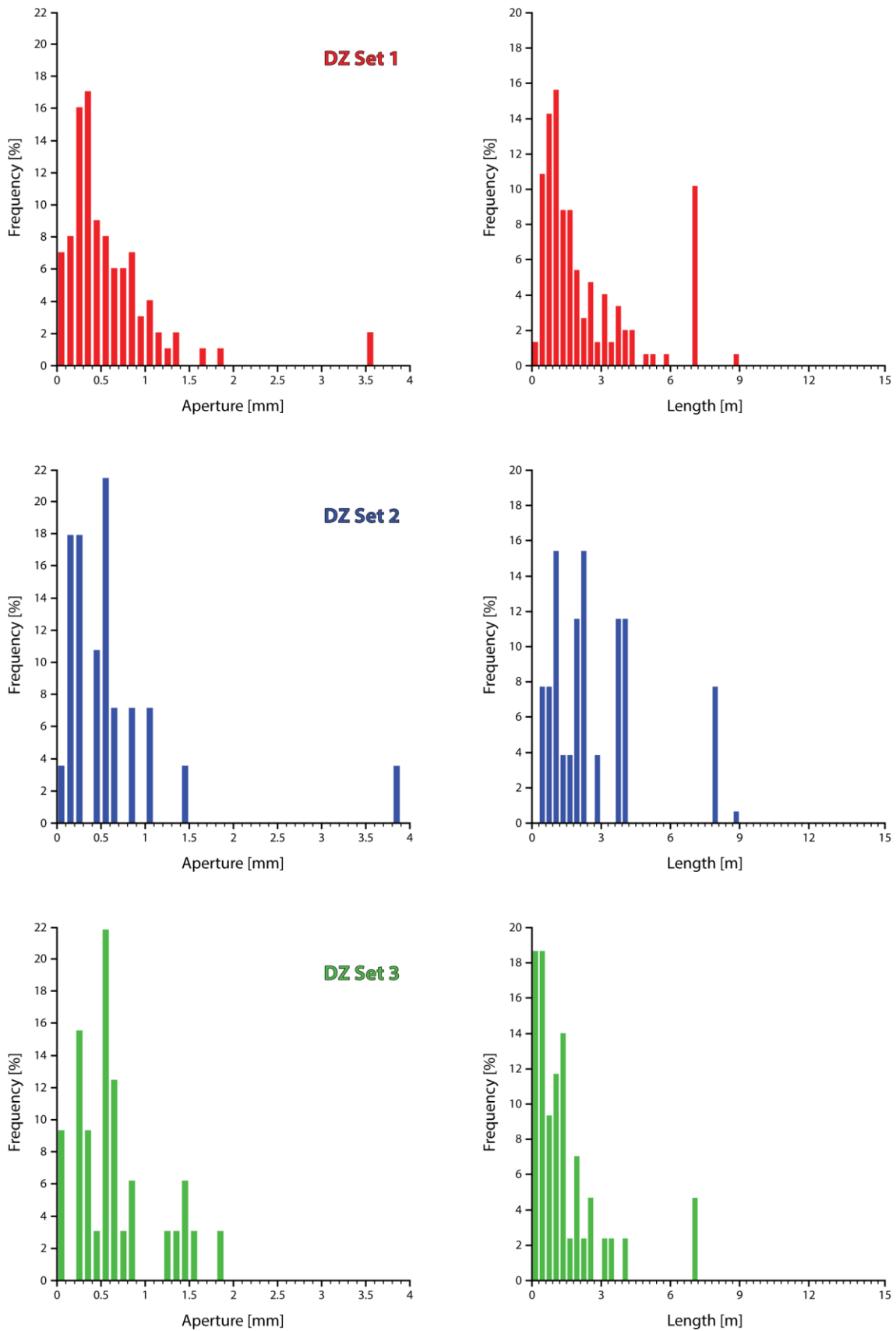


Figure 42: Aperture and length distribution of the defined DZ sets. The aperture axis is divided into 40 steps of 0.1 mm, whereas the length axis is divided into 50 steps of 0.3 m.

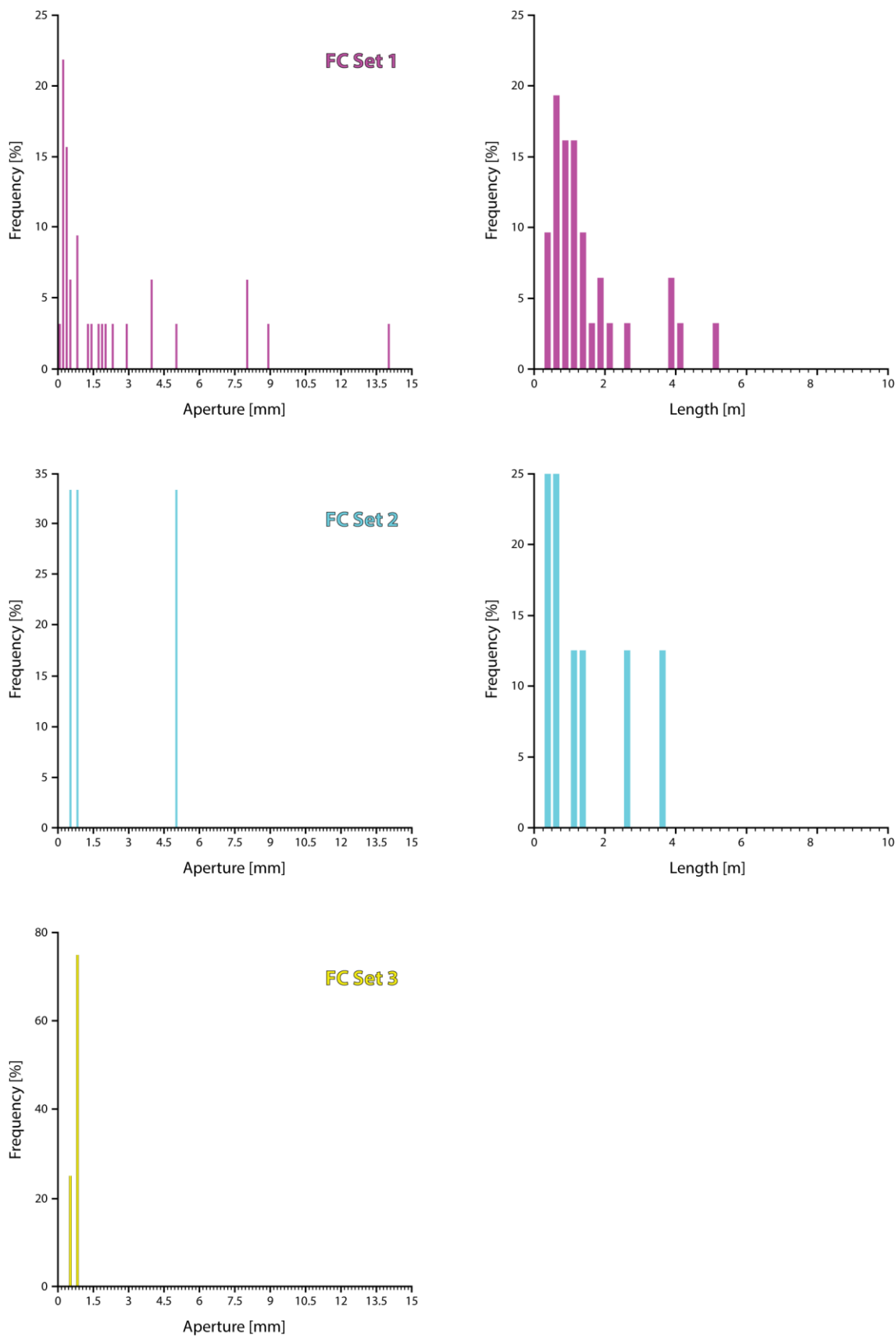


Figure 43: Aperture and length distribution of the defined FC sets. The aperture axis is divided into 100 steps of 0.15 mm, whereas the length axis is divided into 40 steps of 0.25 m.

## Results

Table 11: Result of the corrected fracture length truncation values for each geological unit within the DZ.

Fracture set	Truncated at	Corrected truncation of geological unit [%]											
		1	2	3	4	5	6	7	8	9	10	11	12
DZ Set 1	Top	90	90	90	90	90	90	90	90	90	90	90	90
	Base	60	60	60	60	70	50	60	50	60	70	80	80
DZ Set 2	Top	90	90	90	80	90	90	90	90	90	90	90	90
	Base	90	90	90	90	90	90	90	80	90	90	90	90
DZ Set 3	Top	90	90	90	80	90	90	90	90	90	90	90	90
	Base	80	80	80	70	80	70	70	60	80	80	80	90

### 4.5.4 Fracture Set Intensity Distribution

The preferred measure of fracture intensity within DFN modeling is the volumetric  $P_{32}$  intensity, calculated by the Petrel software. The calculation is based on the  $P_{10}$  density, which in turn was acquired through the scanlines. For each fracture set a corresponding  $P_{32}$  intensity was calculated resulting in a total of six  $P_{32}$  intensities, three for the DZ (Figure 44) and three for the FC (Figure 45). Intensity gaps in the FC geobody arise from the geologically-based decision to not distribute fractures in the DFN modeling process within the FCFTs “Sandstone unconsolidated (Su)”, “Gouge, silt unconsolidated (Gs)”, and “Gouge, clay unconsolidated (Gc)”. Table 12 shows the result of the calculated mean and standard deviation of the  $P_{32}$  intensity for each fracture set, as well as their minimum and maximum values. Figure 46 shows exemplarily the  $P_{32}$  intensities specifically for geological units 2 and 12. For the specific  $P_{32}$  intensities of all geological units of the DZ the reader is referred to Appendix 4.

Table 12: Calculated  $P_{32}$  intensities of the fracture sets.

Geobody	Set	$P_{32}$ intensity [ $m^2/m^3$ ]			
		Mean	Std. dev.	Max.	Min.
DZ	1	2.51	1.52	8.81	0
	2	1.71	1.4	10.58	0
	3	1.72	4.52	34.44	0
FC	1	10.27	4.19	20.96	0
	2	4.39	1.26	8.1	2.72
	3	5.09	2.24	11.28	2.98



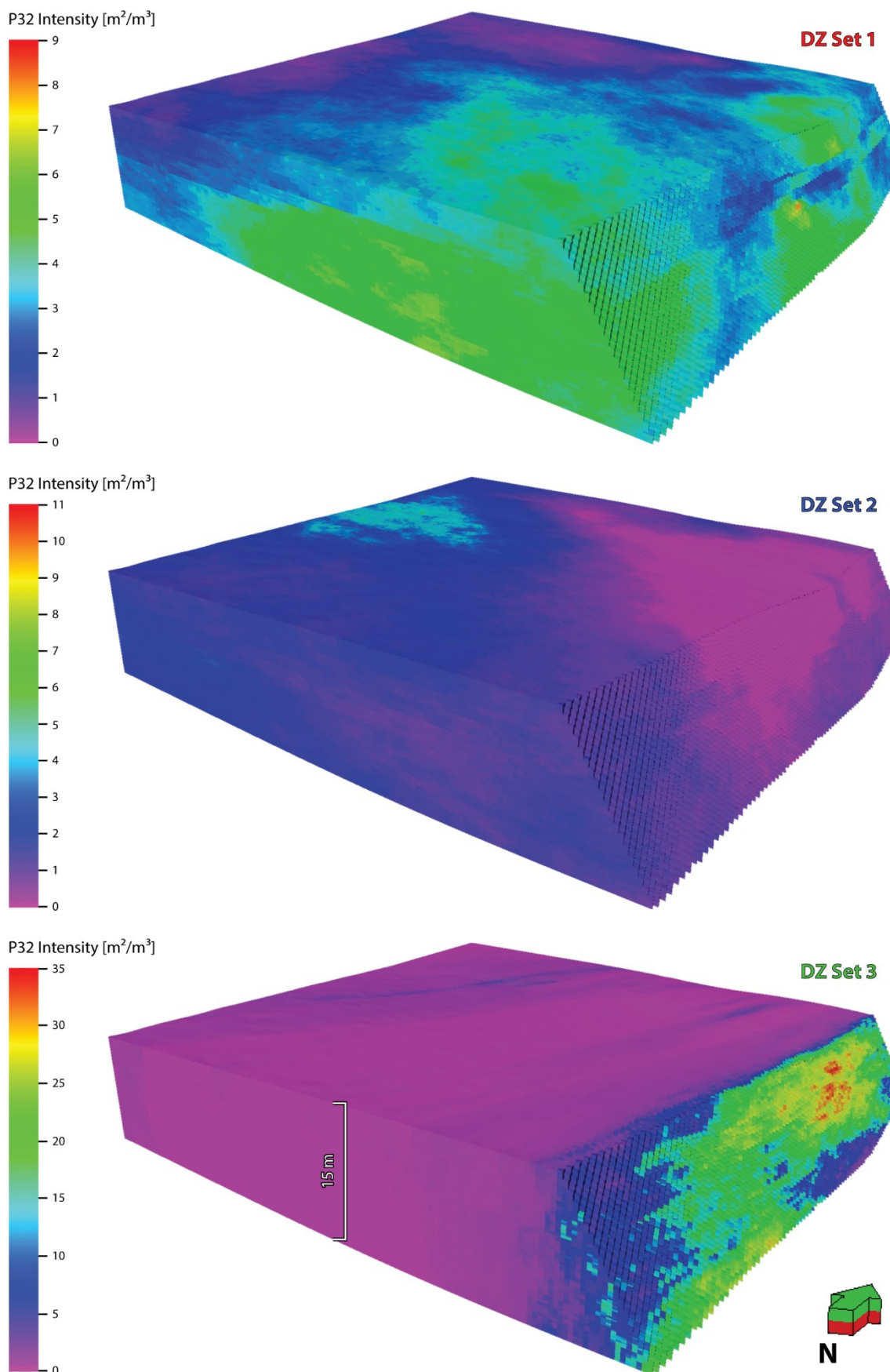


Figure 44: Result of the complete P<sub>32</sub> intensity calculation for Set 1, 2 and 3 of the DZ. For better presentability each fracture set has an adjusted intensity color scale, the sets shown represent dynamic images with variable colors applied in a moving window.

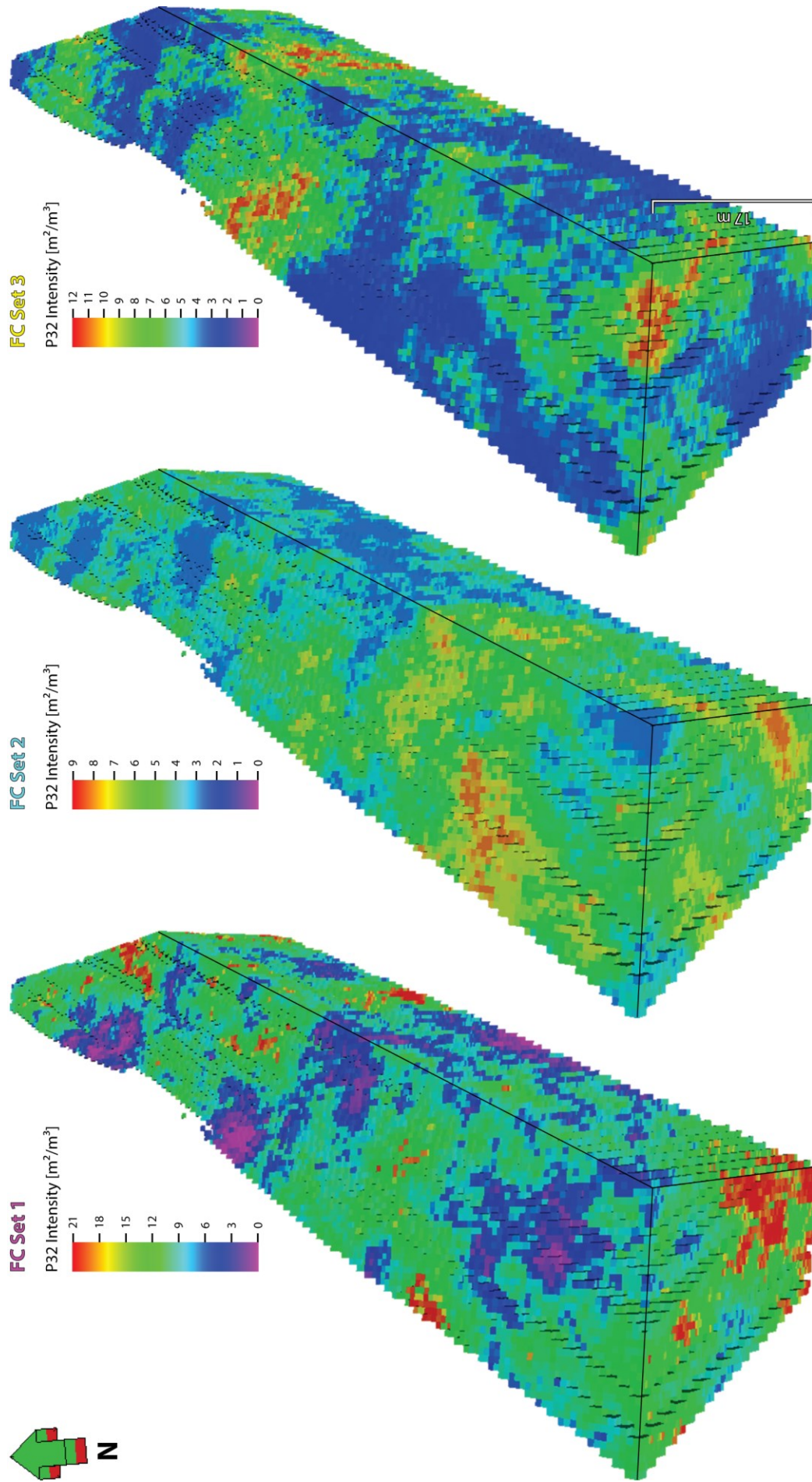


Figure 45: Calculated  $P_{32}$  intensities for FC Set 1, 2 and 3. Gaps of intensity values represent regions covered by the FCFTs "Sandstone unconsolidated (Su)", "Gouge, silt unconsolidated (Gs)", and "Gouge, clay unconsolidated (Gc)", which do not incorporate fractures. Dynamic images had variable contrast applied in a moving window.

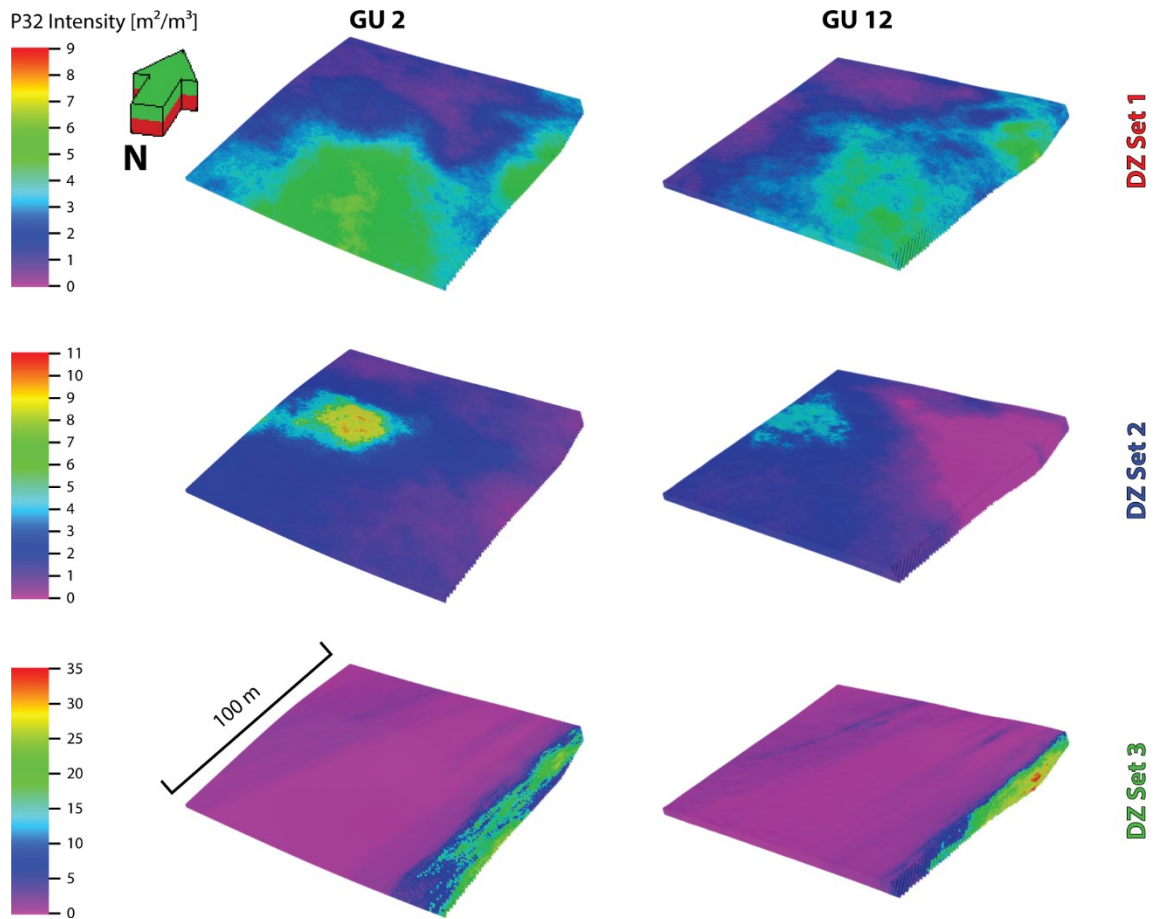


Figure 46: Example of the  $P_{32}$  intensity results specifically for the geological units (GU) 2 and 12 of the DZ. Specific intensity representations for the remaining geological units can be found in the Appendix.

## 4.6 DFN Model

### 4.6.1 Fracture Networks

Seven different fracture networks were generated, which comprise an IFN (implicit fracture network) part and a DFN (discrete fracture network) part, the latter comprises by far the largest share. Each of the calculated fracture networks consists of 3 to 39 separately calculated fracture sets (Table 13) resulting in a total of 162 fracture sets. The fracture networks “G”, “T”, and “Tc” comprise only the DZ geobody. Within the fracture network “G” the fracture sets were populated over the entire grid of the DZ without an additional vertical subdivision. Within the fracture networks “T” and “Tc” each of the 12 geological units was populated separately by the corresponding fracture sets with an additionally performed truncation (T: original truncation values, Tc: corrected truncation values). The fracture network “FC” comprises only the FC geobody, while the fracture networks “G+FC”, “T+FC”, and “Tc+FC” cover both, the DZ and the FC. As a result of the chosen constraints during fracture network calculation (see chapter 3.5.1) our attention is drawn in the following on the DFNs. The IFN part represents in contrast a negligible share of the whole fracture network, which also mirrors its impact on the final fracture network properties (see chapter 4.6.2). It will therefore not be discussed here but in chapter 5.4.2.

Altogether a total of over 2.8 million discrete fracture patches were modeled, divided amongst the seven fracture networks (Table 13 and Figure 47). Results of the fracture aperture and length distribution (based on Table 8) of the DFNs are listed in the Appendix 5. As an example for the DZ the DFN “G” is shown in Figure 48, and for the FC

Table 13: Overview of the generated fracture networks (FN), their physical extent, truncation, and number of calculated discrete fracture patches of the DFN part.

FN	Geobody		DZ variants			No. of fracture sets	No. of discrete fracture patches
	DZ	FC	Subdivision	Truncation	Corrected truncation		
G	✓					3	186,477
T	✓		✓	✓		36	254,087
Tc	✓		✓		✓	36	301,125
FC		✓				3	331,976
G+FC	✓	✓				6	518,453
T+FC	✓	✓	✓	✓		39	586,063
Tc+FC	✓	✓	✓		✓	39	633,101

in Figure 49 (DFN “FC”). To improve the comparability with the aperture and length distributions of the defined fracture sets (chapter 4.5.2) the x-axis of the charts has been limited. Figure 50 illustrates the complete DFNs “G+FC”, “T+FC” (comprising the DZ and FC), and “T” (DZ only), while Figure 51 provides a better presentability of the resulting individual fracture sets for the DFNs “G” and “FC”. Exemplary representatives of individual fracture sets of specific geological units are shown in Figure 52 (geological unit 2 and 7 of fracture network “T”). Results of the complete DFN “Tc+FC”, the remaining individual fracture sets for fracture network “T”, as well the results for fracture network “Tc” can also be found in Appendix 6.

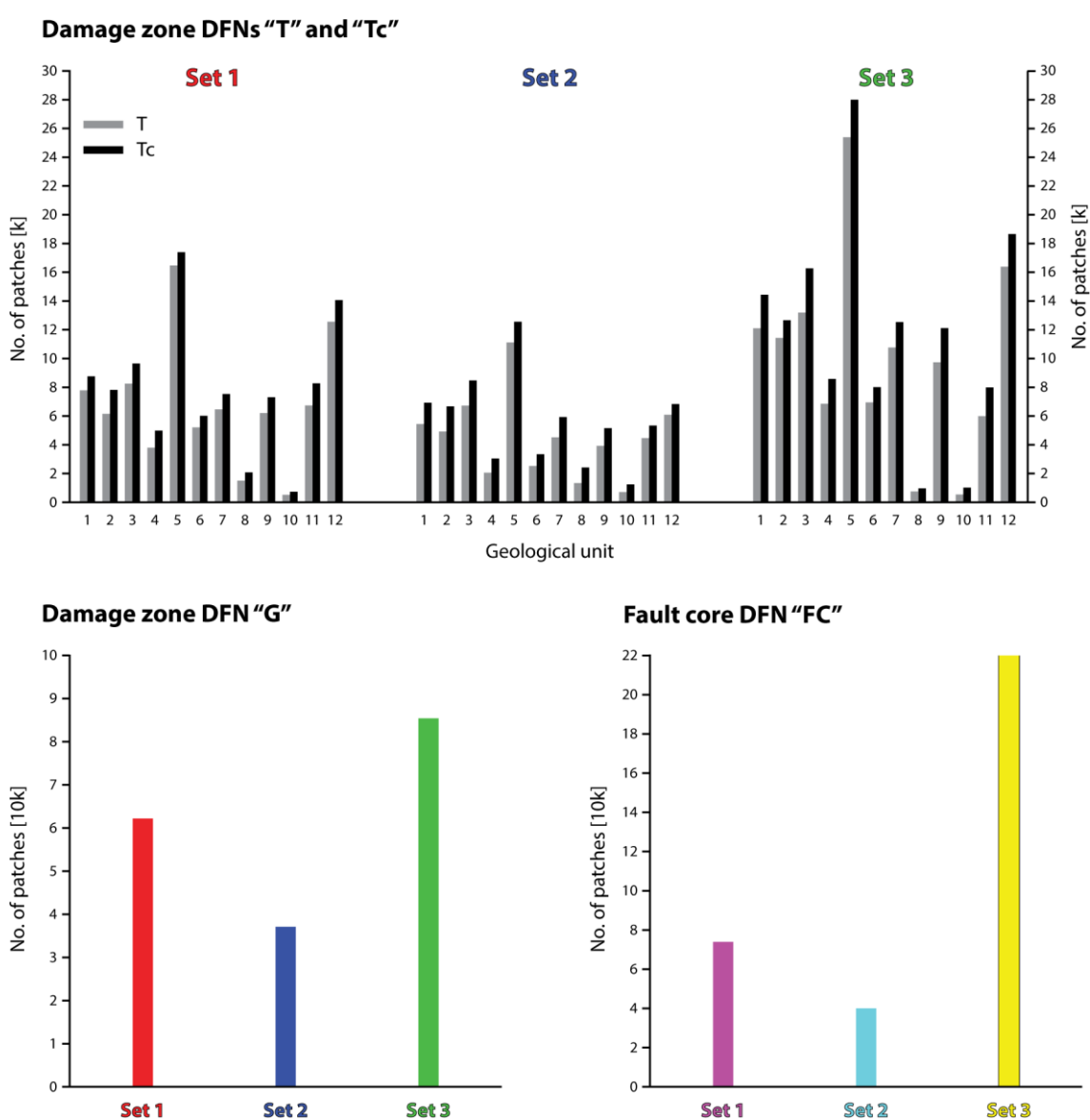


Figure 47: Overview of the amount of calculated discrete fracture patches for the DFNs “G”, “T”, “Tc” and “FC”. The complete DFNs “G+FC”, “T+FC”, and “Tc+FC” constitute a combination of the latter.

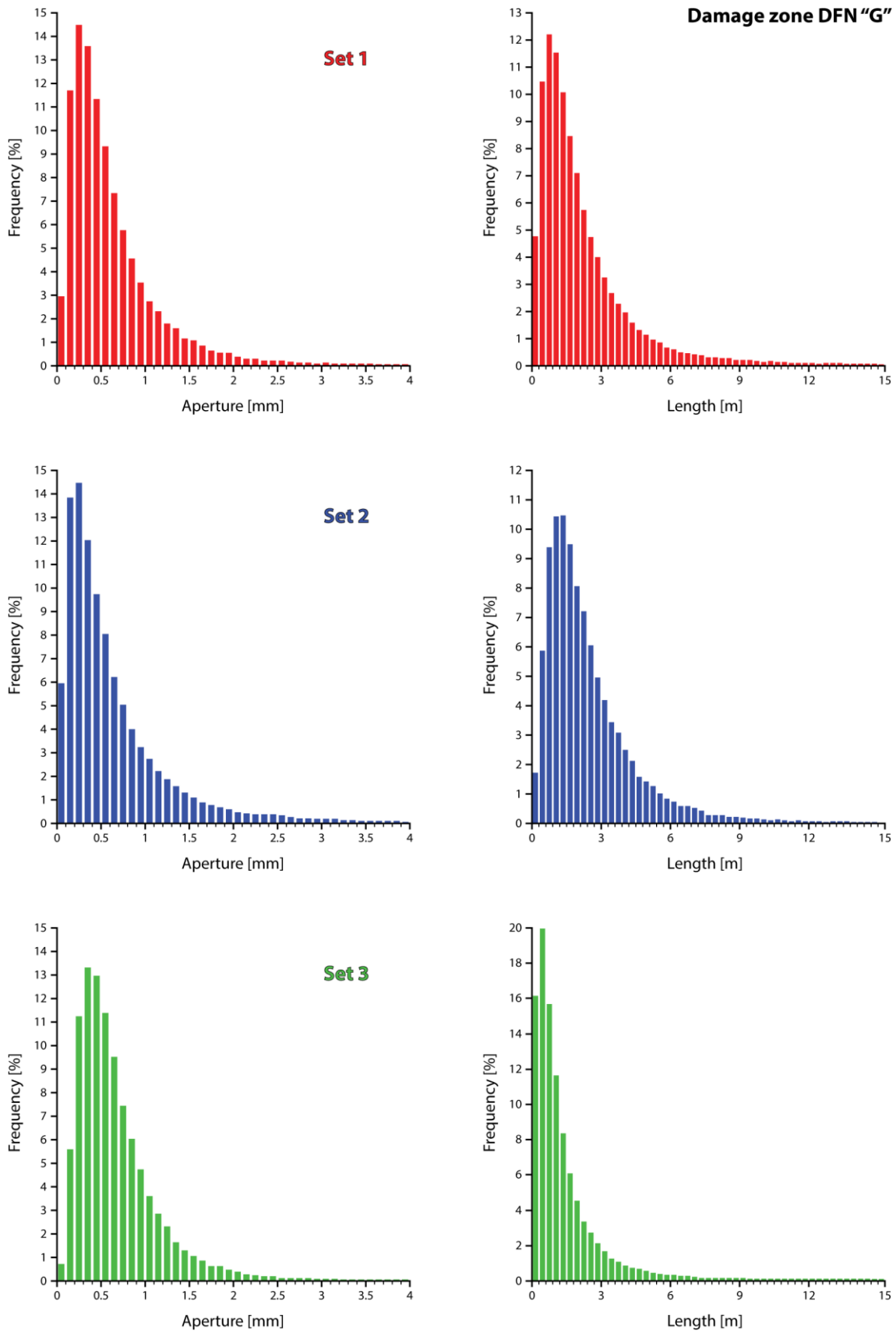


Figure 48: Results for the fracture aperture and length distribution for the DZ Sets 1, 2, and 3 of the DFN "G". For fracture aperture and length results of the DFNs "T" and "Tc" the reader is referred to the Appendix.

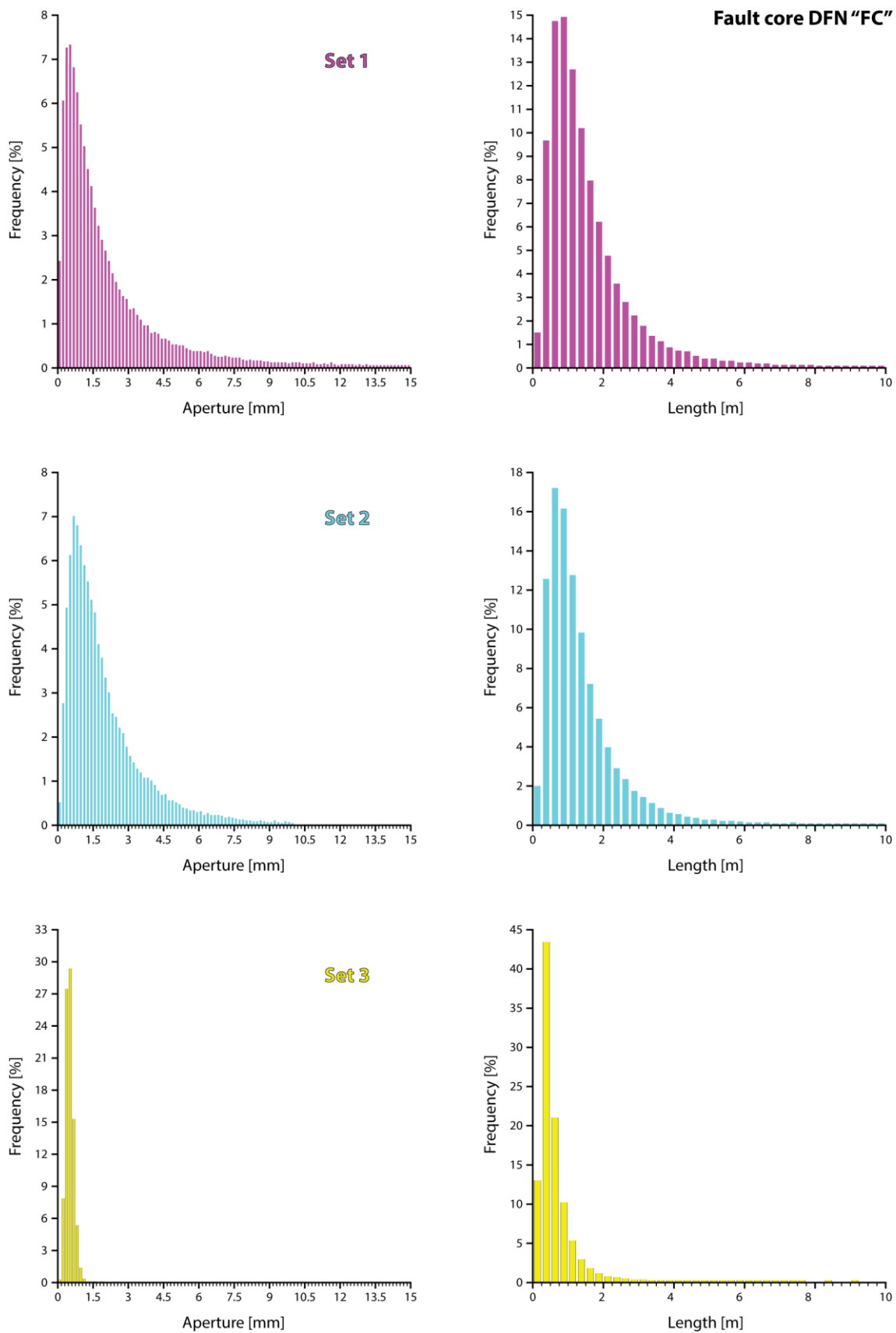
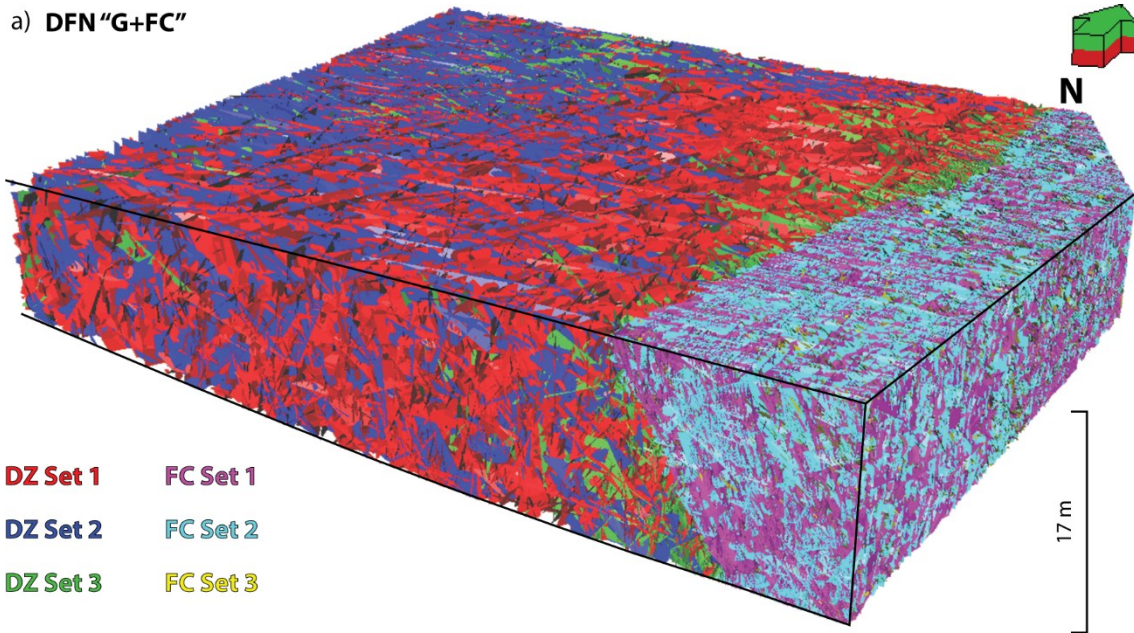
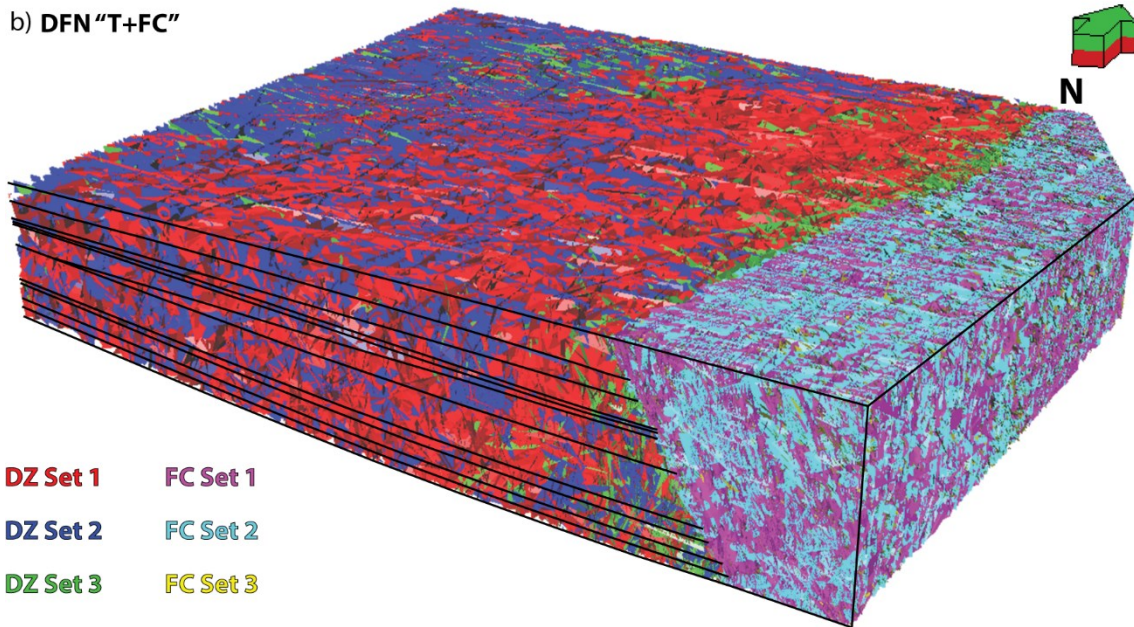


Figure 49: Results for the fracture aperture and length distribution for the FC Sets 1, 2, and 3 of the DFN "FC".

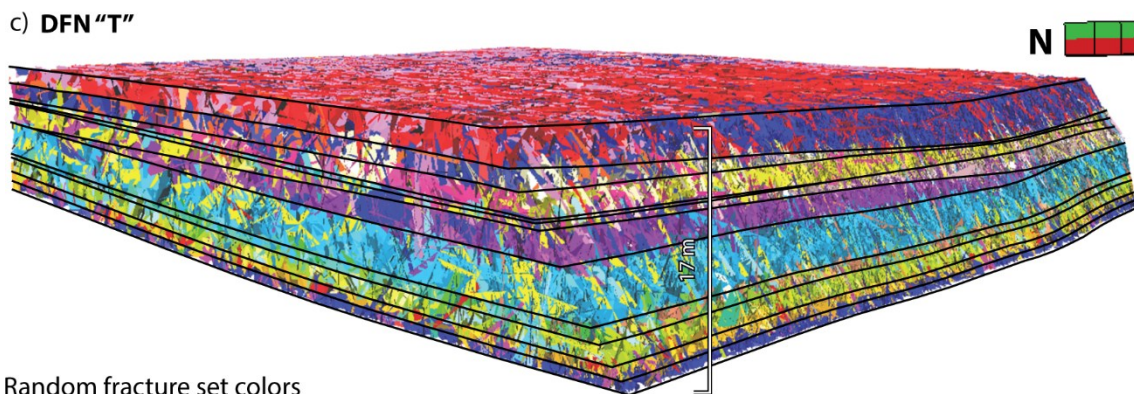
a) DFN "G+FC"



b) DFN "T+FC"



c) DFN "T"



Random fracture set colors

Figure 50: a) Complete DFN "G+FC" comprising the DZ and FC. b) Complete DFN "T+FC" comprising the DZ and FC with an additional division of the DZ in 12 geological units. c) DFN "T" of the DZ with randomly colored fracture sets for better differentiation.



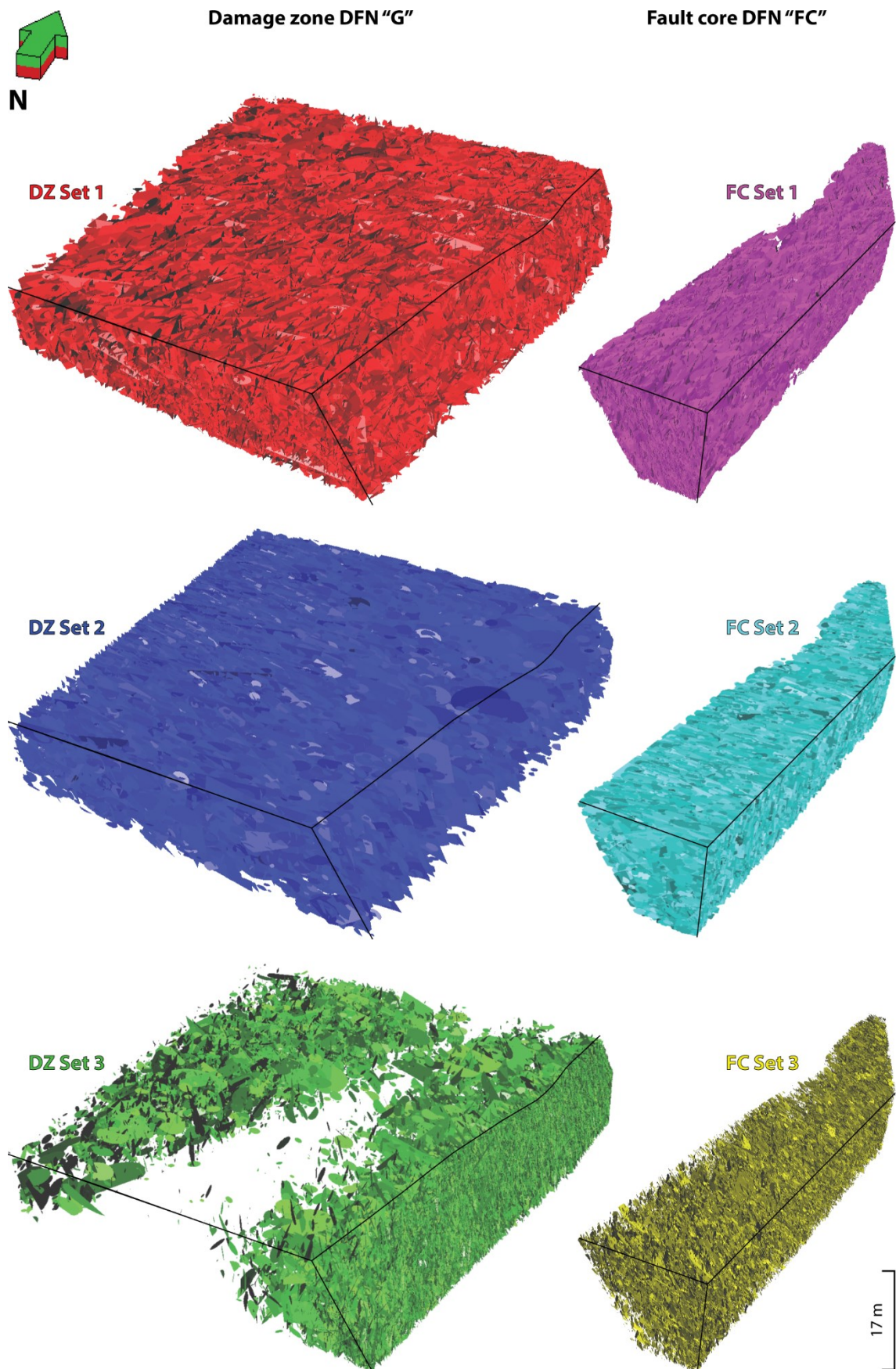


Figure 51: Individual representation of each fracture set of the DFN "G" of the DZ without subdivision and the DFN "FC" of the FC. The combination of both can be seen in Figure 50a.

Damage zone DFN "T"

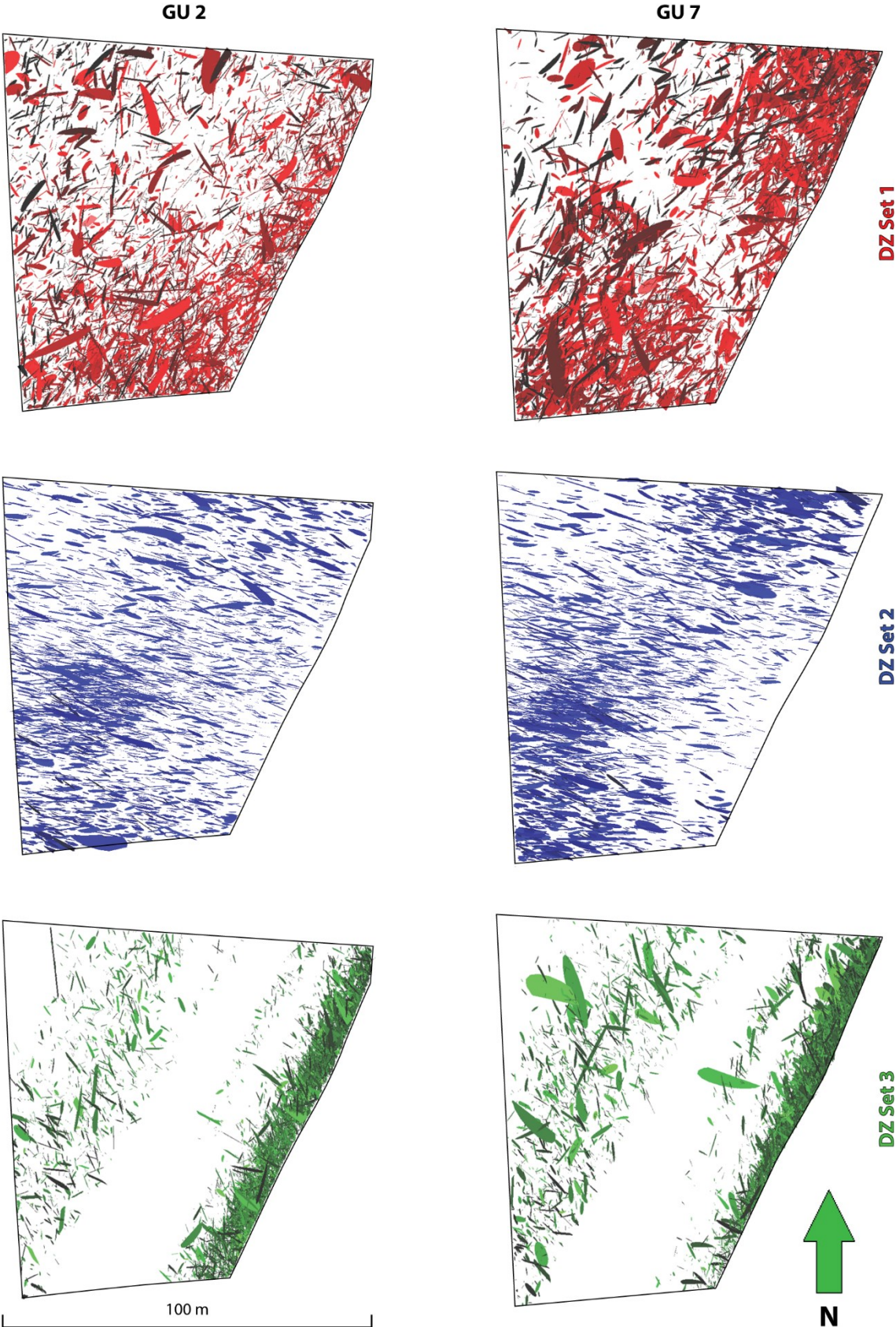


Figure 52: Exemplary illustration of the DZ Sets 1, 2 and 3 for the geological units (GU) 2 and 7 of the DFN "T".

#### 4.6.2 Fracture Network Properties

For each of the seven modeled fracture networks three different variants were chosen to convert the fracture network attributes to properties: (i) Upscaling of the whole fracture network (DFN and IFN) with the Oda method, (ii) DFN upscaling with the Oda method, and (iii) DFN upscaling with the Oda corrected method. Every property calculation variant provides the fracture permeabilities  $k_i$ ,  $k_j$ , and  $k_k$  in the three grid directions, as well as the fracture porosity  $\Phi$ , and the sigma factor  $\sigma$ . For the Oda corrected method the connectivity index CI is additionally calculated and incorporated in the upscaling process of fracture permeability. Table 14 provides an abbreviated list of the results showing the mean values of the calculated fracture network properties. The full list can be seen in Appendix 7.

The **fracture permeability** of the DZ amounts between 0 and 400,000 D. Its mean values are 371 to 533 D for permeability  $k_i$ , 190 to 345 D for  $k_j$ , and 622 to 720 D for  $k_k$ . The FC fracture permeability reaches significantly higher values with a minimum of 0 and a maximum of 2,000,000 D. The mean values of the FC vary between 14,130 to 22,944 D for  $k_i$ , 29,572 to 44,313 D for  $k_j$ , and 51,749 to 55,186 D for  $k_k$ . Within the fracture networks covering both geobodies the mean fracture permeability shows values of 2,515 to 4,000 D for  $k_i$ , 4,733 to 7,147 D for  $k_j$ , and 8,537 to 9,106 D for  $k_k$ . The **fracture porosity** reaches values of  $3.22e-8$  to 5.92 % within the DZ with a mean of 0.38 to 0.41 %. In the FC the fracture porosity has a spread of 0 to 20.46 % with a mean of 2.38 %, while the combined fracture networks show mean values of 0.7 to 0.71 %. The **connectivity index**, being the average number of fracture intersections per fracture in a given cell, amounts in the DZ from 0 to 18.28 with a mean of 1.21 to 1.31. In the FC a minimum of 0 and a maximum of 17.06 is observed, with a mean value of 2.94. The combined fracture networks show a mean CI of 1.51 to 1.56. The results for the **sigma factor** amount values of  $1.2e-11$  to 12,271 per  $m^2$  in the DZ with a mean of 150 to 166 per  $m^2$ . Within the FC the values spread between 0 and 9,255 per  $m^2$  showing a mean of 471 to 527 per  $m^2$ . The mean values of the combined fracture networks range from 207 to 223 per  $m^2$ .

The fracture network property results for the complete DFN "T+FC" upscaled with the Oda corrected method are illustrated in detail. Figure 53 shows the modeling result of the fracture permeability  $k_i$ , Figure 54 of  $k_j$ , and Figure 55 of  $k_k$ . The result of the modeled fracture porosity is illustrated in Figure 56, while the connectivity index CI is displayed in Figure 57, and the sigma factor  $\sigma$  in Figure 58. For the whole fracture network property results the reader is referred to Appendix 8.

## Results

Table 14: Mean values of the fracture network property results comprising the fracture permeability, the fracture porosity, the connectivity index (CI), and the sigma factor. FN: fracture network; PUM: permeability upscaling method; DFN: discrete fracture network; IFN: implicit fracture network.

Geo-body	FN	PUM	Network type		Permeability [D]			Porosity [%]	CI	Sigma [1/m <sup>2</sup> ]
			DFN	IFN	ki	kj	kk			
DZ	G	Oda	✓	✓	497	291	658	0.38		150
		Oda	✓		497	291	659	0.38		150
		OdaC	✓		371	190	622	0.38	1.21	150
	T	Oda	✓	✓	521	332	712	0.4		162
		Oda	✓		522	332	713	0.4		162
		OdaC	✓		381	216	671	0.4	1.29	162
	Tc	Oda	✓	✓	532	345	720	0.41		166
		Oda	✓		533	345	720	0.41		166
		OdaC	✓		386	223	675	0.41	1.31	166
FC	FC	Oda	✓	✓	22,944	44,313	55,186	2.38		471
		Oda	✓		22,942	44,310	55,183	2.38		527
		OdaC	✓		14,130	29,572	51,749	2.38	2.94	527
DZ + FC	G+FC	Oda	✓	✓	4,100	7,147	9,274	0.7		207
		Oda	✓		4,100	7,146	9,273	0.7		217
		OdaC	✓		2,604	4,804	8,712	0.7	1.51	217
	T+FC	Oda	✓	✓	3,992	7,086	9,102	0.71		211
		Oda	✓		3,992	7,086	9,102	0.71		220
		OdaC	✓		2,518	4,739	8,543	0.71	1.55	220
	Tc+FC	Oda	✓	✓	4,000	7,095	9,106	0.71		214
		Oda	✓		4,000	7,094	9,106	0.71		223
		OdaC	✓		2,515	4,733	8,537	0.71	1.56	223

Fracture permeability  $k_i$  of DFN "T+FC" (OdaC)

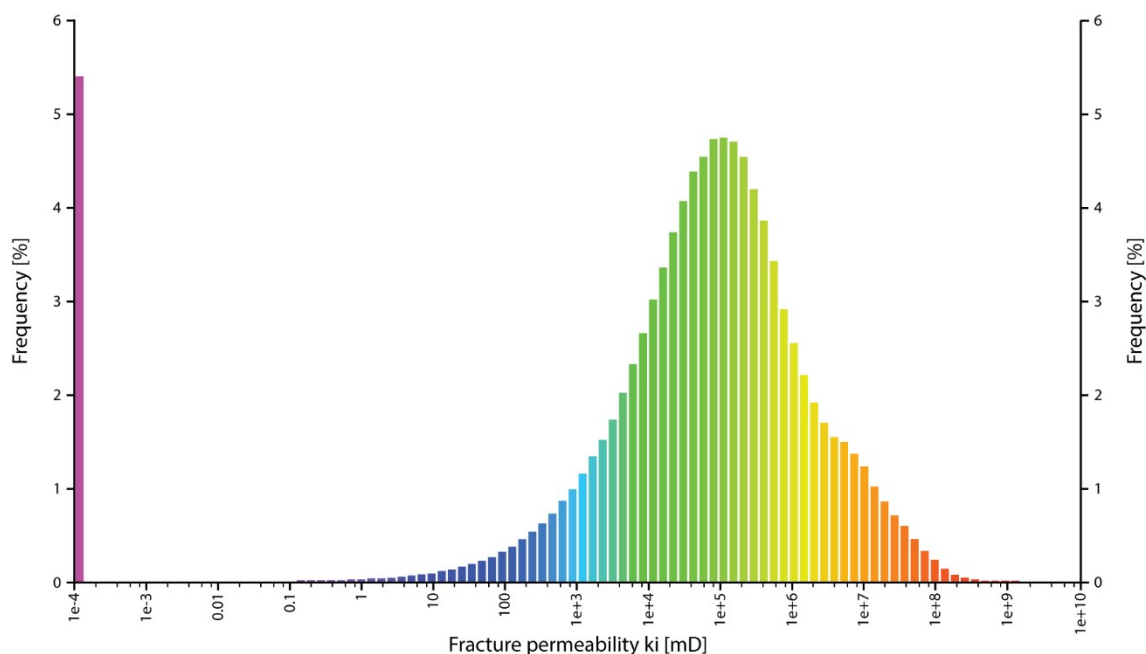
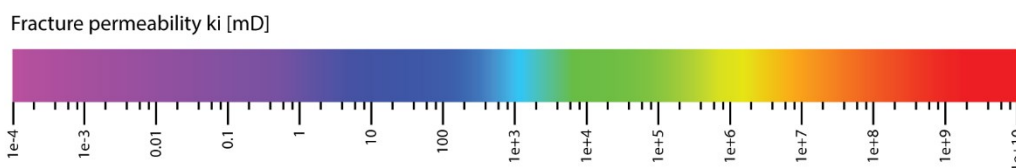
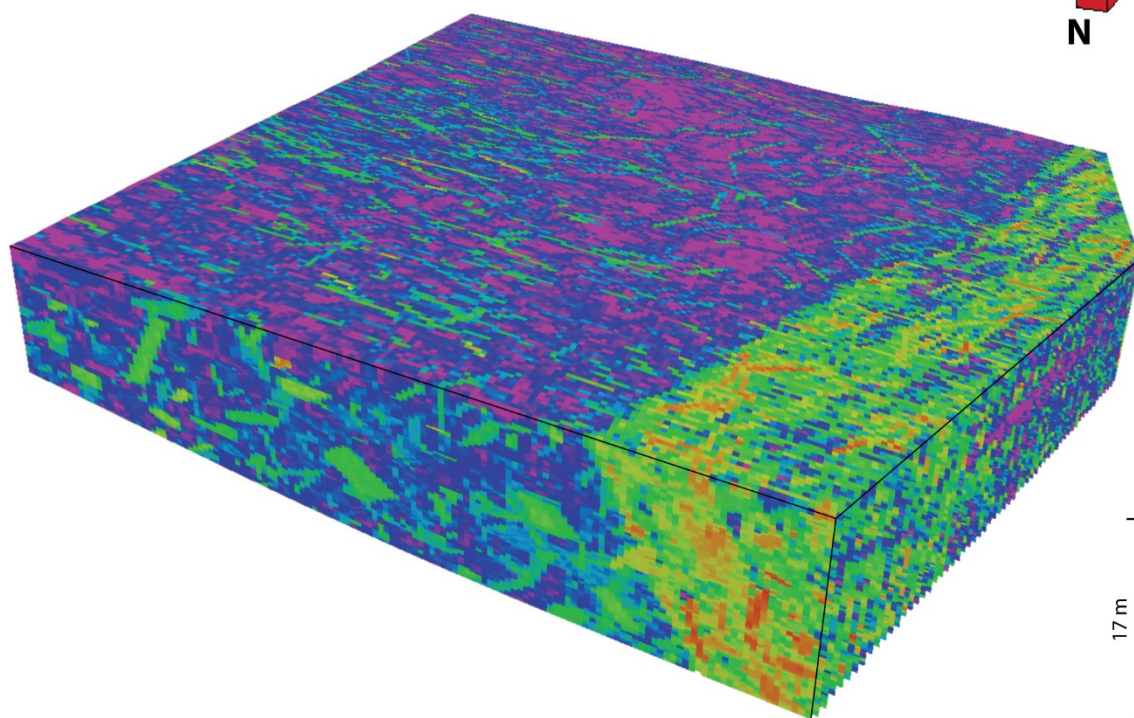
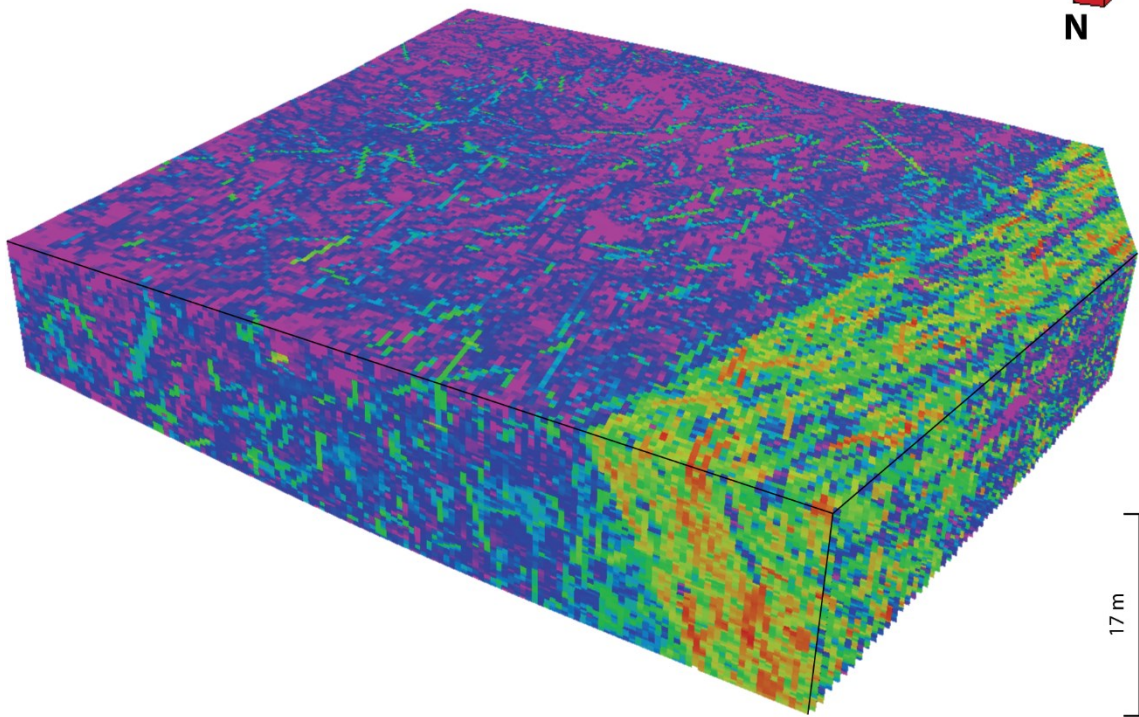


Figure 53: Result of the fracture permeability in i-direction for the DFN "T+FC" upscaled with the Oda corrected method. Values are spread between 0 and 1,115,280,000 mD with a mean of 2,517,822 mD.

Fracture permeability  $k_j$  of DFN "T+FC" (OdaC)



Fracture permeability  $k_j$  [mD]

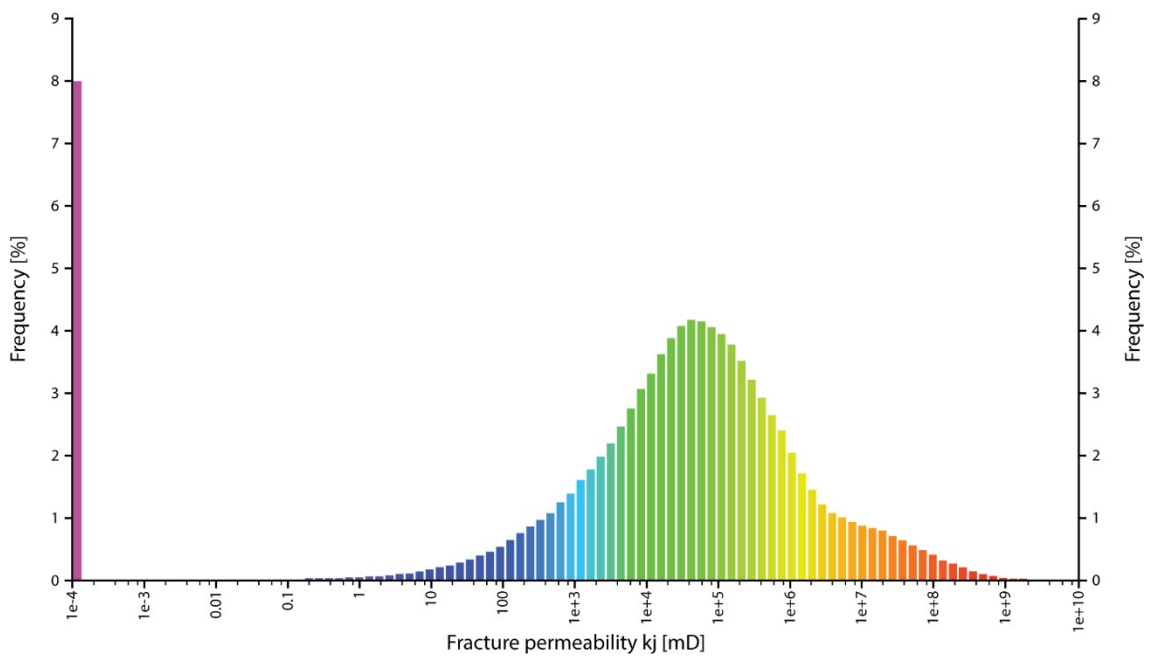
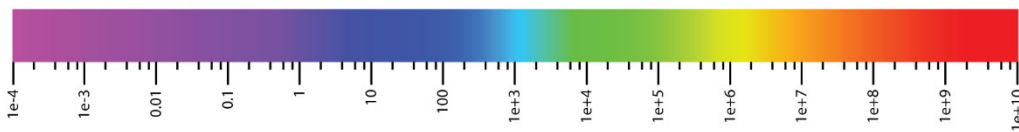


Figure 54: Result of the fracture permeability in  $j$ -direction for the DFN "T+FC" upscaled with the Oda corrected method. Values are spread between 0 and 1,466,669,952 mD with a mean of 4,739,422 mD.

Fracture permeability  $k_k$  of DFN "T+FC" (OdaC)

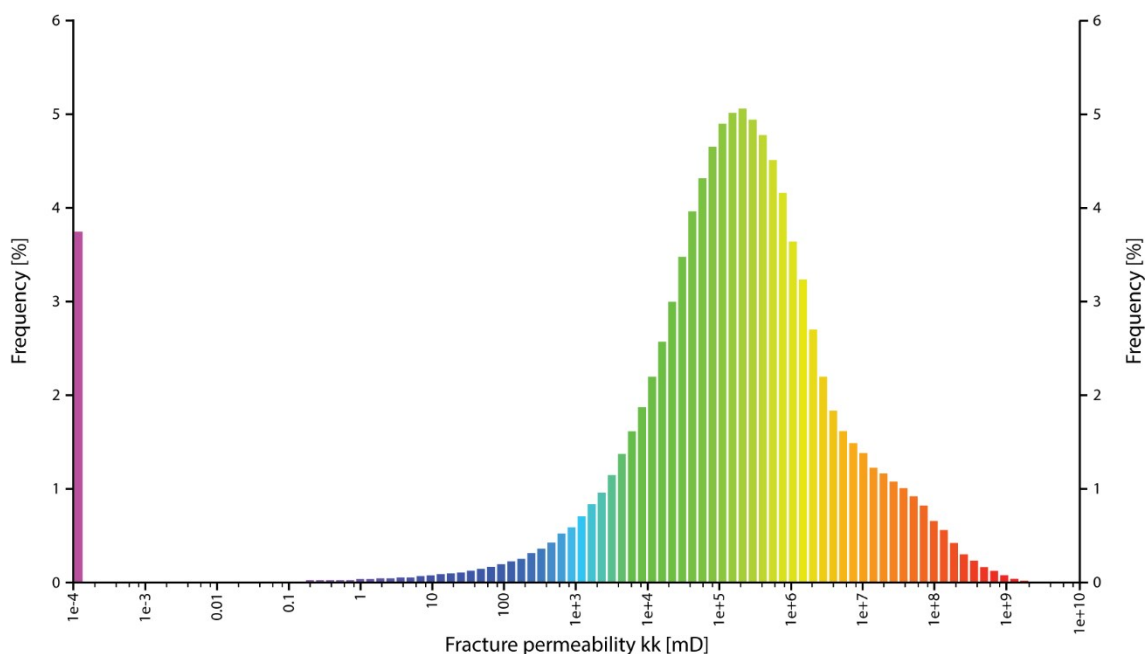
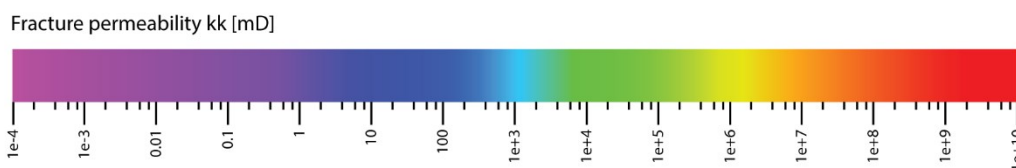
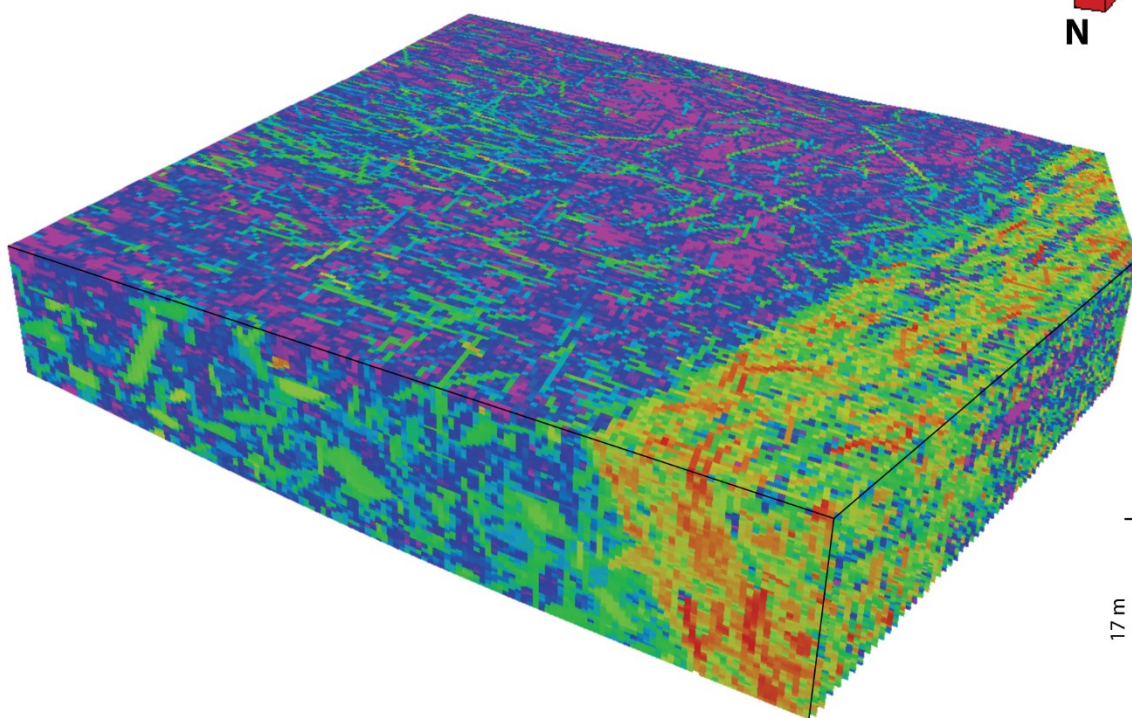


Figure 55: Result of the fracture permeability in k-direction for the DFN "T+FC" upscaled with the Oda corrected method. Values are spread between 0 and 1,852,550,016 mD with a mean of 8,543,210 mD.

Fracture porosity of DFN "T+FC"

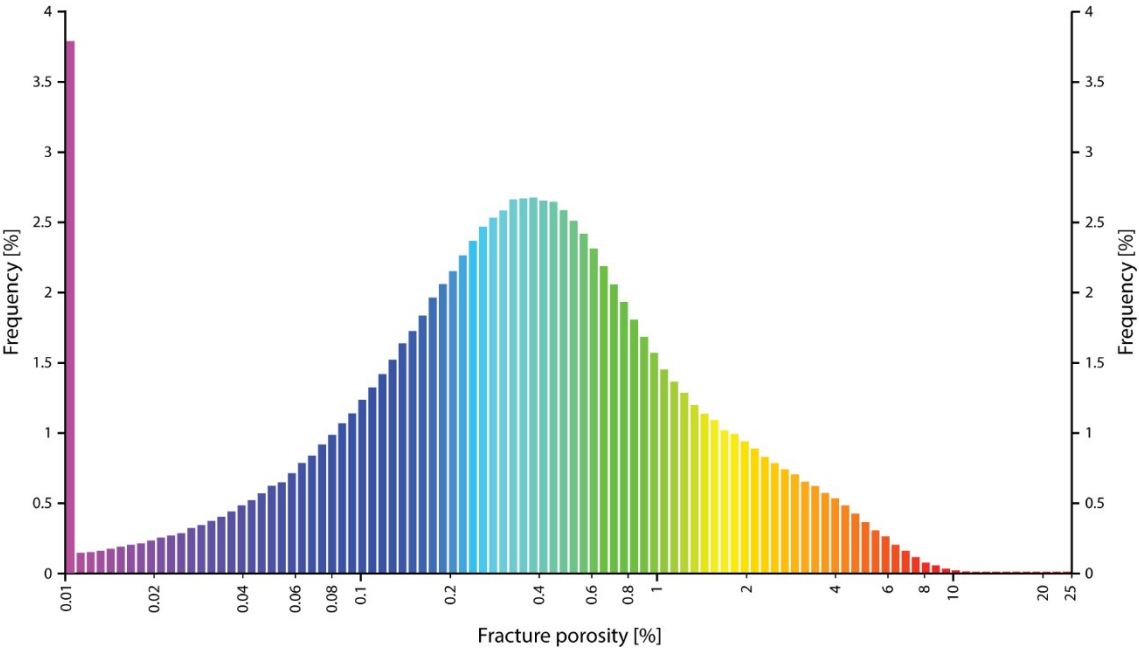
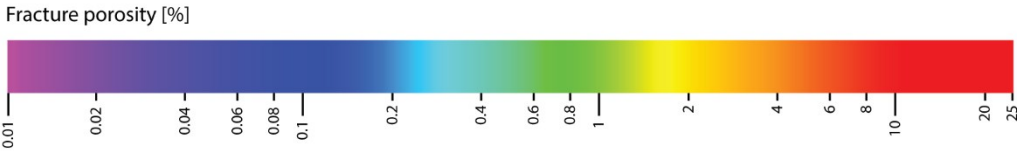
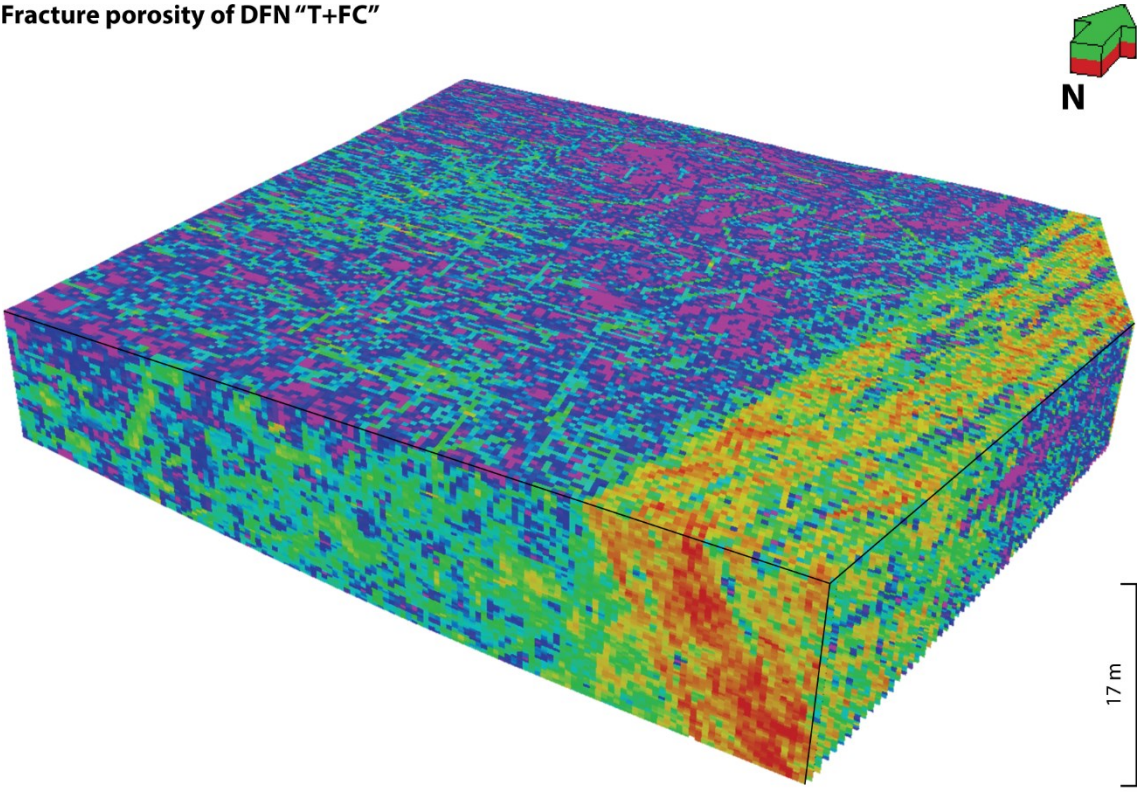


Figure 56: Result of the fracture porosity for the DFN "T+FC". Values are spread between 0 and 20.46 % with a mean of 0.71 %.



Fracture connectivity index of DFN "T+FC"

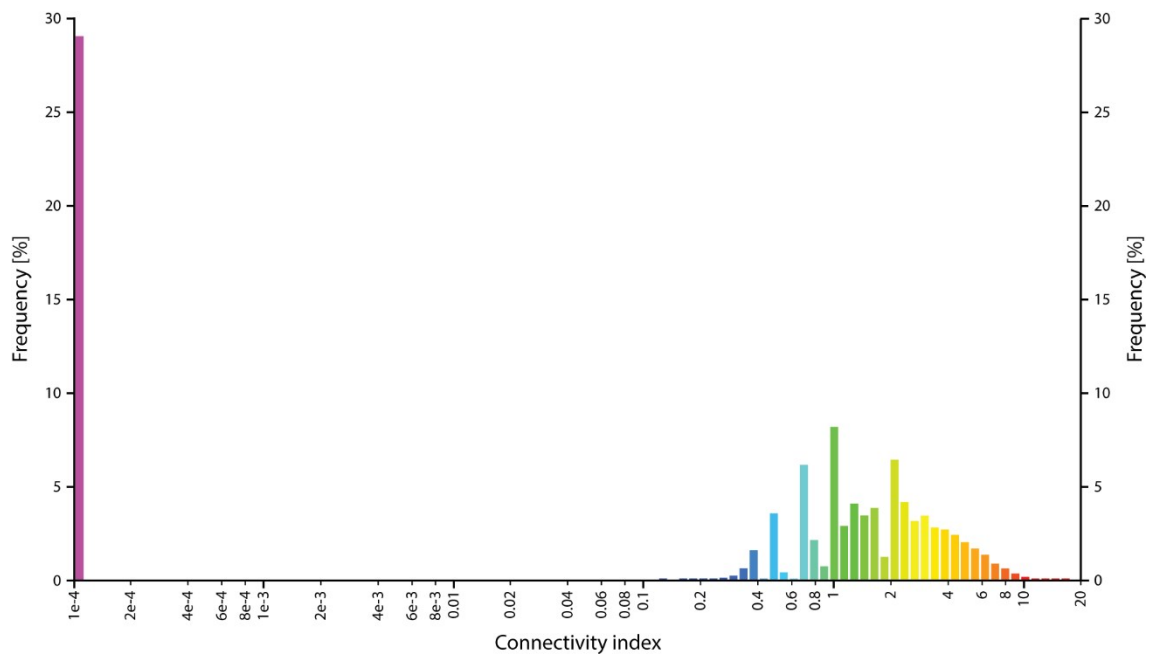
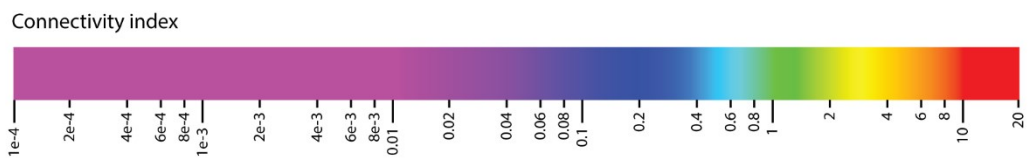
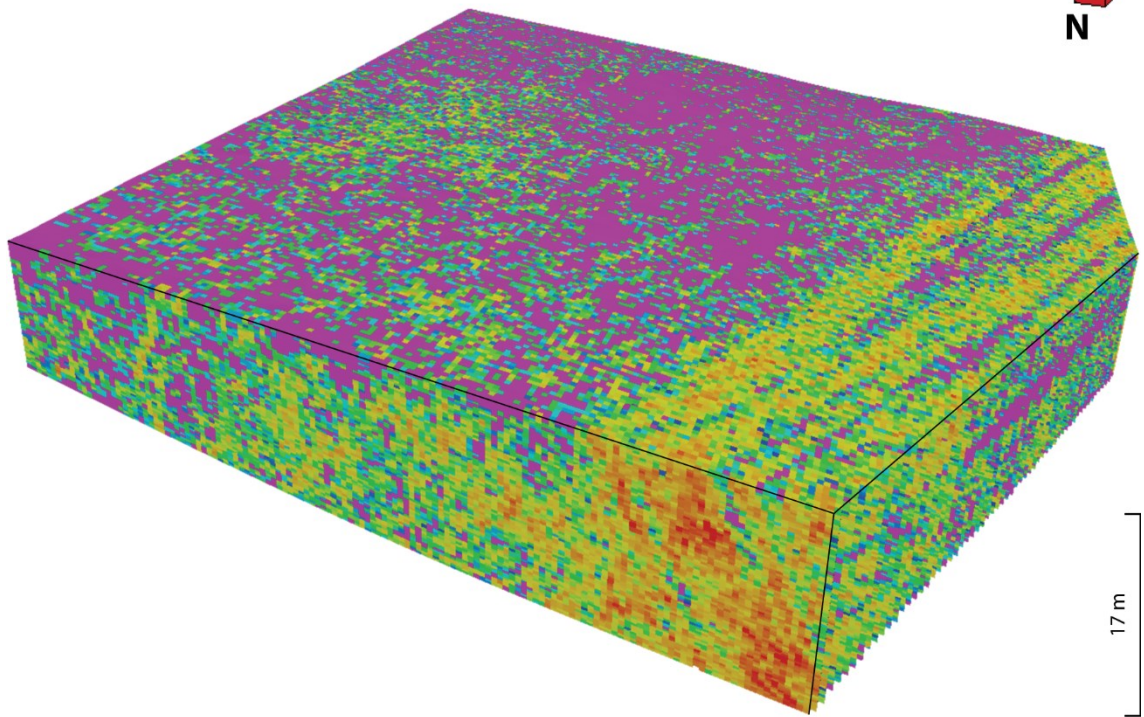


Figure 57: Result of the connectivity index for the DFN "T+FC". Values are spread between 0 and 17.62 with a mean of 1.55.

**Sigma factor of DFN "T+FC"**

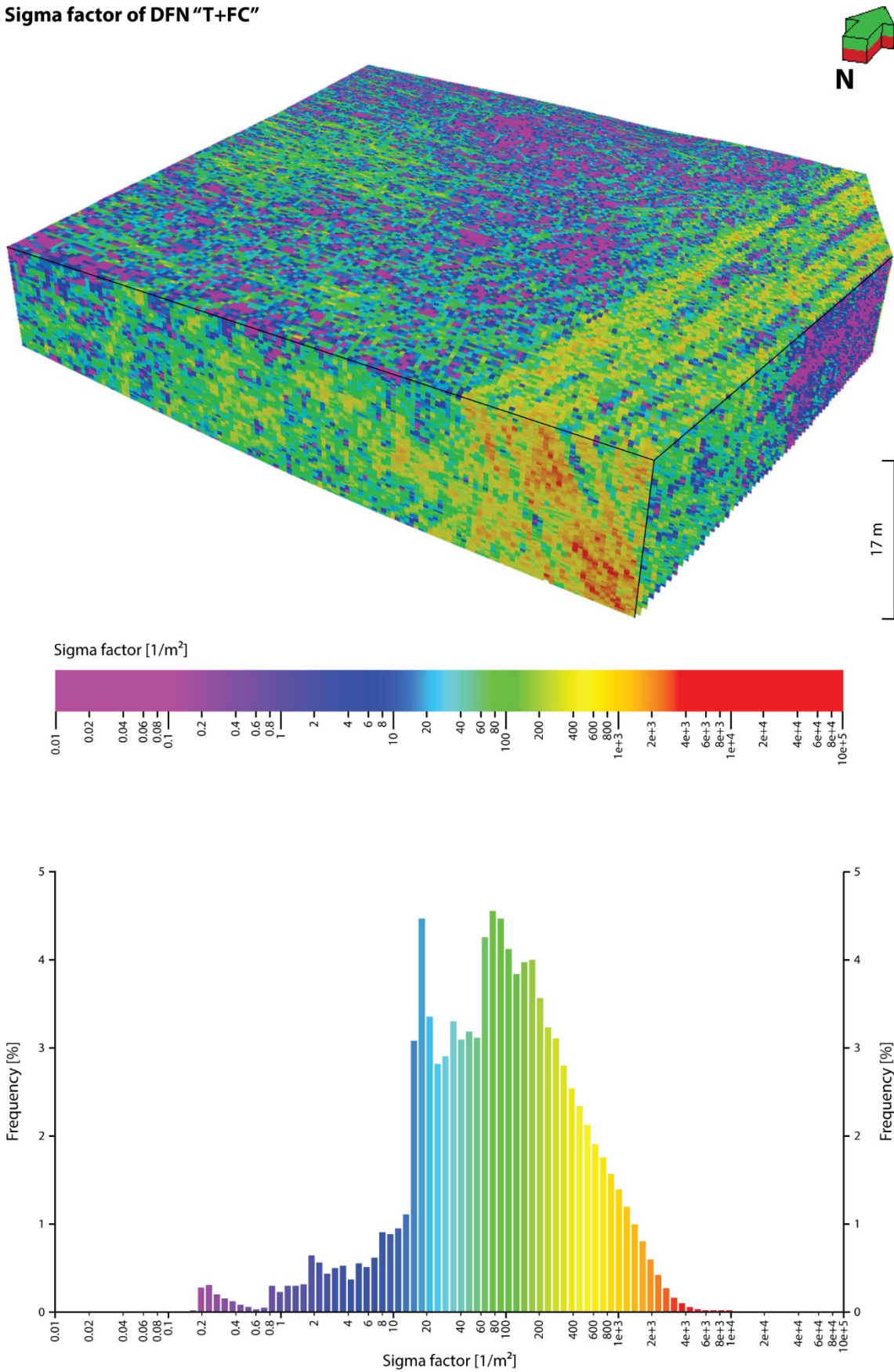


Figure 58: Result of the sigma factor for the DFN "T+FC". Values are spread between 1.2e-11 and 8,978.58 per m<sup>2</sup> with a mean of 220.23 per m<sup>2</sup>.

## 5 Discussion

### 5.1 Outcrop Lithology and Depositional Environment

Seven lithofacies types were recognized based on the lithofacies classification after Miall (1978) with minor refinements and additions: i) Small-size trough cross-bedded fine- to coarse-grained sandstone (St1), (ii) medium-size trough cross-bedded fine- to very coarse-grained sandstone with few pebbles (St2), (iii) large-size trough cross-bedded medium- to very coarse-grained sandstone with few pebbles and mud intraclasts (St3), (iv) planar cross-bedded fine- to medium-grained sandstone (Sp), (v) low-angle cross-bedded very fine- to medium-grained sandstone (Sl), (vi) horizontally laminated very fine- to medium-grained sandstone (Sh), and (vii) fine laminated mud- to fine-grained sandstone (Fl).

The encountered marginal basin facies association of the Trifelsschichten is interpreted as a braided river deposit within an alluvial plain with possible minor intercalations of aeolian deposits. The braided river sediments evolve laterally into ephemeral playa lakes or aeolian deposits towards the basin center. This setting is widely accepted (Backhaus, 1974; Richter-Bernburg, 1974; Clemmensen and Tirsgaard, 1990; Clemmensen, 1991; Röhling, 1991; Aigner and Bachmann, 1992; Van der Zwan and Spaak, 1992; Geluk, 2005; Bourquin et al., 2009; Soyk, 2015). Paleocurrent directions during the Lower Buntsandstein were not investigated in detail. These are assumed to be oriented mainly towards the N or NE with a primary sediment source area located in the Armorican Massif in the WSW, according to Durand (1978), Bourquin et al. (2009), Péron et al. (2005), and Ziegler (1990). The paleogeographic reconstruction by Durand (1978) suggests a distance of about 150 km of the studied outcrop to the sediment source. The recognized facies association and absence of vegetation indicates an arid environment during deposition. Repeated occurrence of aeolian deposits and presence of many pebble- and cobble-sized ventifacts within the European basins during the Olenekian corroborates this assumption (Durand, 2006; Bourquin et al., 2007; Cassinis et al., 2007; Bourquin et al., 2009). Paleoclimate simulations (Péron et al., 2005; Bourquin et al., 2006) even suggest very arid conditions for this period. Figure 59 shows a standardized profile of the studied succession and an interpretation regarding flow velocity, which is discussed in detail below.

**Sedimentary structure and lithology**

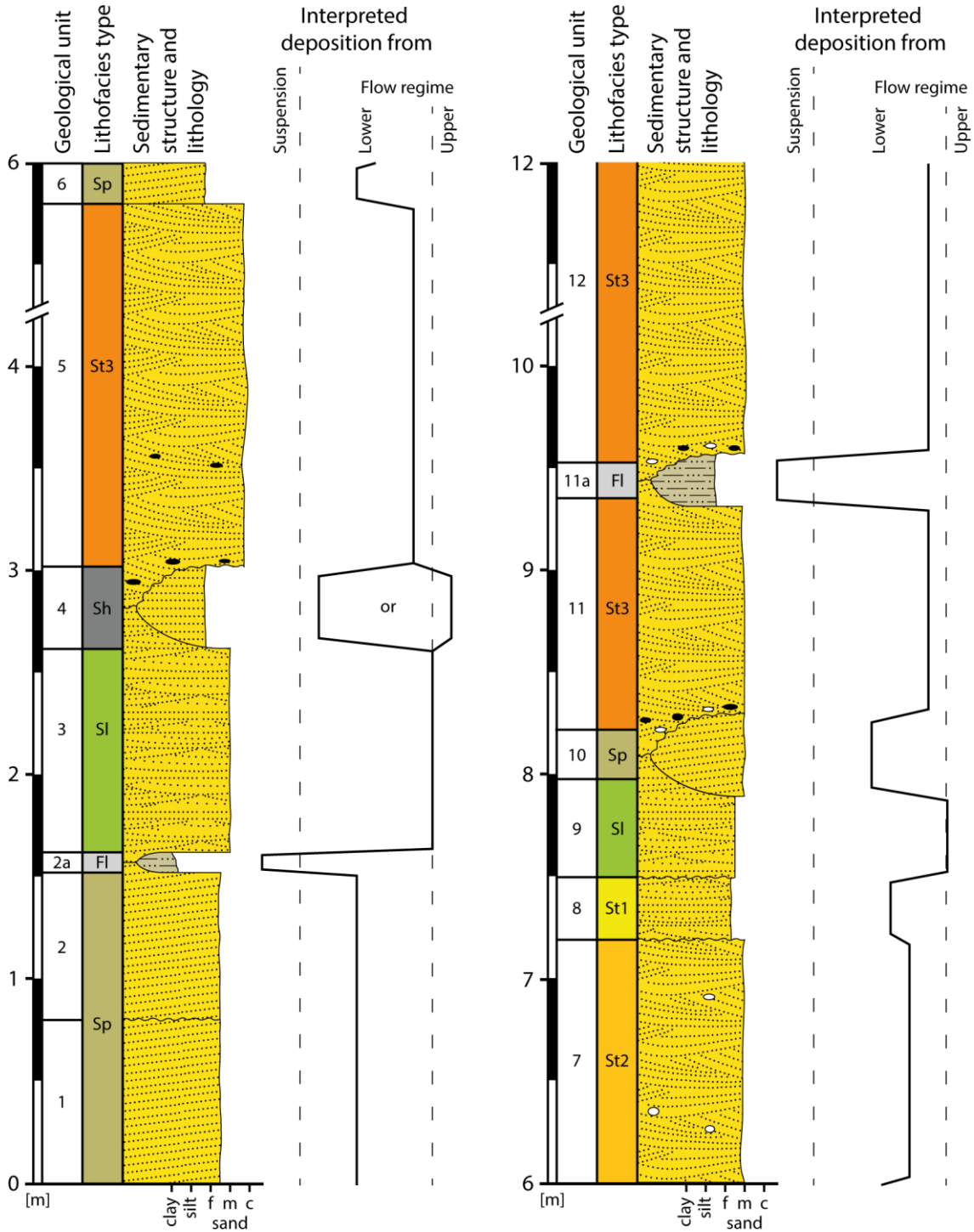
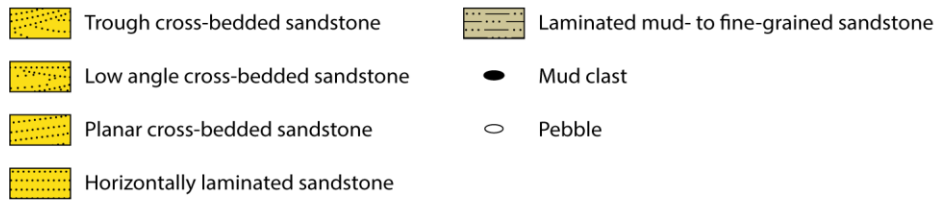


Figure 59: Standardized profile of the studied succession, showing the interpreted flow velocity during deposition of each bed. For graphic reasons, the scale has been shortened for geological units 5 and 12 by 1 m each.

Through cross-bedded fine- to coarse-grained sandstones (St1-St3) are interpreted as subaqueous sinuous-crested to linguoid 3D dunes (Miall, 1977, 1985; Bourquin et al., 2009; Nichols, 2009) representing channel-fill successions. The different vertical thicknesses of the trough cross-bedded dune deposits were caused by varying flow velocities, being relatively low within the “St1” beds, slightly higher in the “St2” beds and even higher in the “St3” beds (Nichols, 2009). Overall these sediments represent the upper part of the lower flow regime (Miall, 1977) with its aforementioned inner differentiation. Although there is a considerable amount of scatter in the data (Nichols, 2009), the height of the dunes can generally be used to estimate water depths during their deposition, which is estimated to amount from several to 10 m (Allen, 1982; Leeder, 1999). The “St1” lithofacies type represents the lowest and the “St3” type the highest water depths. Pebbles and mud intraclasts are typically observed at the erosional base of the “St3” beds. This erosional scours can be interpreted as an additional lithofacies type “Se” (Miall, 1977), which indicates stage fluctuations (Harms and Fahnestock, 1965; McGowen and Garner, 1970; Buck, 1983; Plint, 1983; Tyler and Ethridge, 1983; Miall, 1985). For modeling reasons because of its very low spatial extent this scour lithofacies type was incorporated within the “St” lithofacies type. Mud intraclasts are interpreted as reworked muddy bank material, which was carried by the river flow and typically deposited together with sand in deeper parts of the channels. If preserved, these represent the basal part of the channel-fill successions (Nichols, 2009). This supports the above given interpretation of the “St3” type as being deposited during higher water depths and flow velocities, compared to the “St1” and “St2” beds. This interpretation is corroborated by the only isolated occurrence of pebbles and lacking mud-intraclasts in the “St2” beds, whereas both are absent in the “St1” beds.

Planar cross-bedded fine- to medium-grained sandstone successions (Sp) are interpreted as straight-crested transverse bars dipping downstream and representing the middle part of the lower flow regime, characterizing shallower areas of the channel (Cant and Walker, 1976; Miall, 1977; Levey, 1978; Miall, 1978; Smith, 1978; Blodgett and Stanley, 1980; Church and Jones, 1982; Smith, 1983; Bourquin et al., 2009).

The low-angle cross-bedded, very fine- to medium-grained sandstones (Sl) are difficult to explain. Miall (1978, 1985) interpreted such deposits as scour-fills, antidunes, or crevasse splays. However, the thickness of the “Sl” beds (80-125 cm) is interpreted as too high for a crevasse splay floodplain deposit considering the spatial extent of the remaining beds (in particular the “Fl” lithofacies type). No grading, a lenticular shape, or other characteristics of a crevasse splay (Nichols, 2009) could be observed. Also

crevasse splays are expected to occur less likely within an arid environment braided river deposit but rather in meandering river environments. More probable are scour-fills (associated with an erosive base) or antidunes. The latter are rarely preserved and depend on very high rates of sedimentation (Schmincke et al., 1973; Nichols, 2009). Independent of the type of the “Sl” deposits, this low-angle cross-beds are interpreted as an upper flow regime structure in agreement with Miall (1978), Alexander et al. (2001), Fielding (2006), and Lang et al. (2017). More specifically, Fielding (2006) and Fielding and Webb (1996) describe such sedimentary bedforms as record of a transition from dune to the stability field of upper plane beds. This fits well considering the facies association of the “Sl” beds. These are therefore interpreted as channel-fill successions deposited from the uppermost part of the lower flow regime to the lower part of the upper flow regime.

Only one “Sh” lithofacies type bed was encountered in the studied outcrop, which is characterized by horizontally laminated very fine- to medium-grained sandstone. This sedimentary structure is mainly associated with (i) aeolian sand-sheets, (ii) fluvial plane bed deposits, or (iii) a very sandy floodplain deposit within a channel-fill succession (Hunter, 1977; Miall, 1978; Clemmensen and Abrahamsen, 1983; Bourquin et al., 2009; Nichols, 2009).

(i) An aeolian sand-sheet deposit is feasible, given that aeolian intercalations are known to occur within the studied succession and considering the deposits’ grain-size and well to very well sorting. However, no other aeolian characteristics like adhesion structures (Kocurek and Fielder, 1982; Brookfield, 1992) or wind-ripple laminations at the top of the structure (Hunter, 1977) were observed, but this might be due to erosion of the topmost part.

(ii) Fluvial plane bed deposits occur within lower and upper flow regimes (Boguchwal and Southard, 1990; Nichols, 2009). Fielding (2006) states that most preserved examples of flat and planar bedding in sands and sandstones are thought to reflect the upper plane bed regime. This is particularly the case in very fine to medium-grained sands, which are encountered in the discussed bed.

(iii) A third possibility, according to Bourquin et al. (2009), is the interpretation as thin and very sandy floodplain deposits associated with channel-fill deposits, which would fit within a floodplain facies association as described by Langford and Chan (1989). Considering the over- and underlying beds and their depositional environment, the “Sh” lithofacies type is interpreted either as a fluvial plane bed deposit of the upper flow regime or a very sandy floodplain deposit within a channel-fill succession.

Fine laminated mud- to fine-grained sandstone deposits (Fl) are generally associated with overbank or waning flood deposits of a lower-flow regime or a deposition from suspension (Allen, 1964; Miall, 1977, 1996; Bourquin et al., 2009; Nichols, 2009). Bourquin et al. (2009) also describe such facies types as discontinuous deposits within topographic depressions with thicknesses of up to 15 cm, formed during periods of either low water levels or aridity from suspension. The exceptionally small horizontal extent of the “Fl” beds, their maximum thicknesses of 10 and 25 cm and the generally arid depositional environment contribute strongly to the above given interpretation. Overbank and flood deposits should have a clearly larger lateral extent.

In an early publication, Miall (1978) described six vertical profile types (or models) for braided river depositional environments, of which the “South Saskatchewan type” corresponds best to the studied outcrop regarding its facies assemblage and the dominating “St” facies type. The facies types of the “South Saskatchewan type” are arranged in thinning- and fining-upward cyclic sequences of several to about 7 m thickness (Miall, 1978). However, the lack of paleosols and extensive floodplain deposits, the high degree of erosion and channel amalgamation, as well as the spatial extent of the studied succession make it difficult to define distinct cyclic sequences based on the aforementioned criteria within the studied succession, which was formed in an arid environment. The recent Canadian rivers investigated by Miall (1978) as a template for many braided river successions were formed in a humid and seasonally cold environment. Miall (1985) came therefore to the conclusion that it is no longer useful to talk about facies assemblages or even a “South Saskatchewan type fluvial facies assemblage” because meanwhile a vast amount of case-studies revealed a tremendous variability in fluvial styles. Braided river deposits should therefore be described by eight architectural elements, of which the element “channel” describes the encountered succession best. For more details on the characterization of fluvial deposit the reader is referred to Miall (1985).

More recently, Bourquin et al. (2009) applied the sequence stratigraphic concept of “genetic units”, which constitute the smallest stratigraphic cycles that can be correlated at a regional scale (Mitchum and Van Wagoner, 1991; Homewood et al., 1992; Cross et al., 1993). Sequence stratigraphy of continental settings is based on the interplay of accommodation space and sediment supply resulting in stratigraphic base-level fluctuations (Wheeler, 1964; Galloway and Williams, 1991; Cross et al., 1993; Muto and Steel, 2002). Genetic units based on sedimentological data represent “realized accommodation” ( $A_r$ ) equal to the volume of sediment actually accumulated. They

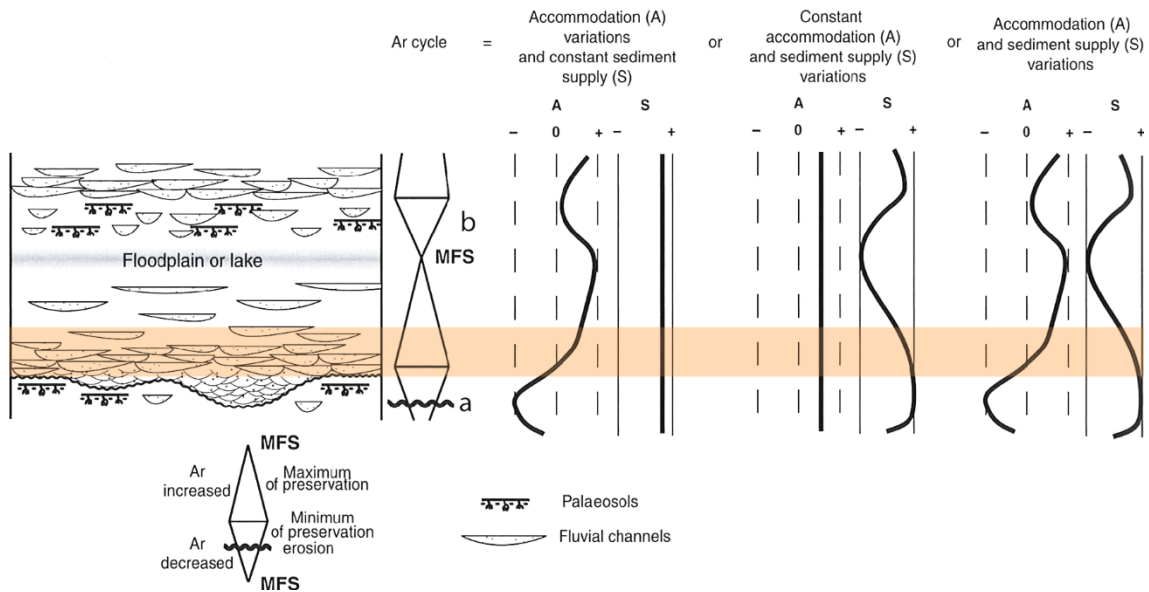


Figure 60: Concept of a genetic unit in fluvial and fluvial-like environments reflecting the realized accommodation ( $A_r$ ) dependent on the interplay of accommodation space (A) and sediment supply (S). MFS: maximum flooding surface. The orange bar constitutes the interpreted depositional period of the studied succession. Illustration after Bourquin et al. (2009).

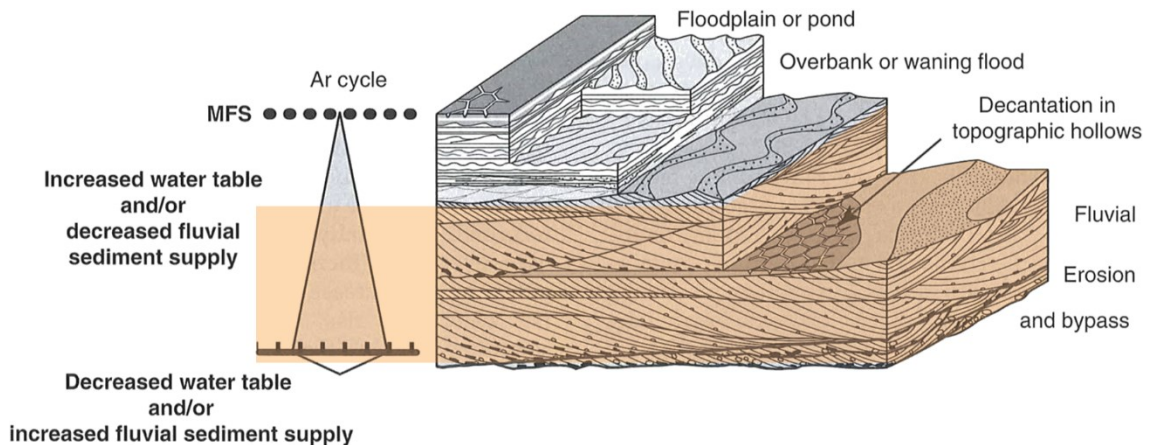


Figure 61: Description of a genetic unit from braided rivers within an arid alluvial plain after Bourquin et al. (2009). The studied succession is interpreted to represent the lower to middle part (marked orange).

reflect varied preservation in fluvial environments (Currie, 1997; Bourquin et al., 1998; Eschard et al., 1998; Muto and Steel, 2000), described either by a period of stratigraphic base-level fall (decrease in  $A_r$ ) or base-level rise (increase in  $A_r$ , Figure 60). Within this system the studied succession is interpreted to be deposited during a period of transition from decreasing to increasing  $A_r$ . This assumption is underpinned by the aforementioned lack of paleosols and extensive floodplain deposits, as well as a high degree of erosion and channel amalgamation, which also reflects the minimum preservation potential represented at this point of transition. More precisely, Bourquin et al. (2009) identified three variations of genetic units within arid continental



environments of the Lower Triassic, of which one is described as “genetic unit from braided rivers within an arid alluvial plain” (Figure 61). This type of genetic unit represents periods of stacking autocyclic sequences of 2 to 5 m thickness, recorded mostly during an increase in  $A_r$ . It is characterized by fluvial sandstones or conglomerates interbedded with clay and siltstone layers, more rarely with aeolian dunes to overbank or waning flood deposits, but also floodplain or pond deposits (Bourquin et al., 2009). Furthermore it differs from the classical fluvial environments (Figure 60) investigated by e.g. Miall (1978) by the aridity of the alluvial plain and lack of paleosols. The investigated succession is interpreted as a fluvial genetic unit with few overbank and floodplain deposits sensu Bourquin et al. (2009). According to these authors the thickness of this type of genetic units within the lower Grés Vosgien Formation amounts to 10 to 25 m. This stratigraphic interval corresponds to the Trifelsschichten (see below and chapter 1.3.2), of which the studied succession holds an average thickness of about 12 to 13 m and consequently constitutes a genetic unit or, more likely, is only part of one or two. The challenge to define a genetic unit within the studied succession lies within the nature of its deposition being characterized by channel amalgamation and a high degree of erosion and reworking, which makes it difficult to clearly identify stratigraphic surfaces (for example a maximum flooding surface). In addition, the outcrop in the investigated quarry is laterally not very extensive, no bounding surface of a genetic unit could be identified. Regarding the lithofacies type assemblage and its thickness, the studied succession it is interpreted to represent the lower to middle part of a genetic unit from a braided river within an arid alluvial plain, as described by Bourquin et al. (2009). It is characterized by a very small period of  $A_r$  decrease merging into a large period of  $A_r$  increase (Figure 61). This interpretation is in good agreement with the previously made assumption of deposition during a period of transition from decreasing to increasing  $A_r$  (Figure 60). The duration of such genetic units is estimated by Bourquin et al. (2009) as tens to hundreds of thousands of years. At such a time scale the deposits are more likely controlled by climatic factors rather than regional tectonics.

Bourquin et al. (2006) investigated the sequence stratigraphic cycles of the Lower Triassic in the Vosges and subdivided the Scythian major cycle covering the Grés Vosgiens Formation into the four minor cycles B1, B2, B3, and B4. Subsequently, Bourquin et al. (2009) subdivided these cycles further into genetic units and recognized two such units in the B1 cycle (Figure 62) within the Soultz-sous-Forêt well, based on sedimentological observations combined with gamma-ray analysis. The B1 cycle within

this well, located 9.4 km south of the studied outcrop, corresponds to the Trifelsschichten in Germany. Within this cycle the studied succession is assumed to be located in the lower to middle part of the second genetic unit. This interpretation is somewhat uncertain, as it lacks gamma-ray data for comparison and is solely based on stratigraphic information, lithofacies assemblage, thickness, and the placement of the lithofacies assemblage and thickness within a genetic unit. In addition the Sultz-sous-Forêt well lies within the Upper Rhine Graben (URG) with the Trifelsschichten analogs located at depths of about 1318 to 1350 m, which underwent stronger compaction than the investigated succession. Nonetheless this own interpretation is supported by the studies of Bourquin et al. (2006) and Bourquin et al. (2009).

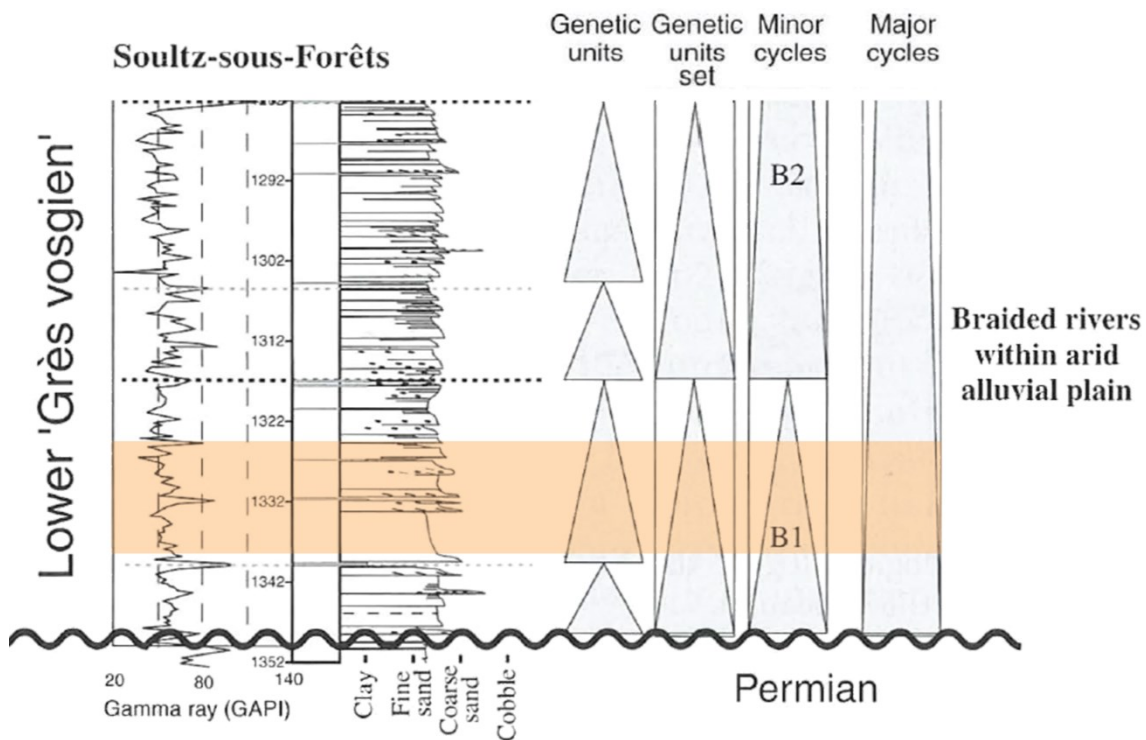


Figure 62: Cutout of an illustration showing cycles and genetic units interpreted by Bourquin et al. (2009) within the Sultz-sous-Forêts well of which the minor cycle B1 corresponds to the Trifelsschichten. The studied succession is interpreted to be located within the orange marked section. After Bourquin et al. (2009), modified.

## 5.2 Fault Zone

By comparing own observations with geological maps and literature (Andreae et al., 1892; Stapf, 1988; M nillet et al., 1989; Stapf, 1996; Eisbacher and Fielitz, 2010) the exhibited fault zone in the studied outcrop is interpreted as the western Rhine Graben main fault within the Hochwald Horst of the Saverne fracture field. In Alsace it is also called “Faille rh nane”, in Germany “Haardtrandst rung” (GeORG-Projektteam, 2013). Based on the existence of fracture fields and small-scale antithetic flexure zones, Meier and Eisbacher (1991) and Wenzel and Brun (1991) assumed the border faults to be planar within the middle and northern part of the URG (Schwarz, 2005). The predominant NW-SE orientation of  $\sigma_1$  since the Miocene (Bergerat, 1985; Heidbach et al., 2010) implies a sinistral transtensive shear for graben parallel NNE-SSW oriented faults (Illies, 1975; Bergerat, 1987; Schumacher, 2002; GeORG-Projektteam, 2013). The encountered fault is interpreted therefore to constitute a planar oblique-slip fault of which only its foot wall and FC can be observed within the studied outcrop. This assumption is corroborated by results of Bauer et al. (2015) who examined fractures and deformation bands within the studied outcrop in terms of fault slip direction.

The displacement of a fault zone can be positively correlated to its trace length, as well as to its DZ and FC thickness (Scholz, 1987; Knott, 1994; Dawers and Anders, 1995; Fossen and Hesthammer, 2000; Shipton and Cowie, 2001; Childs et al., 2009; Faulkner et al., 2011; Bastesen et al., 2013), though a scatter of the relationships over several orders of magnitude is possible (Hull, 1988; Shipton et al., 2006; Childs et al., 2009; Faulkner et al., 2010; Choi et al., 2016). In the studied outcrop, however, the trace length could not be measured, the DZ and FC are not outcropping in its entirety. Despite the known scatter a displacement assumption after Choi et al. (2016) is reasonable by taking a DZ thickness of 50-60 m into account, which results in an assumed displacement of several hundred m. Doebel (1967), Doebel and Olbrecht (1974), and Eisbacher and Fielitz (2010) on the other hand reported a displacement of the Rhine Graben main fault of 900 to 1200 m. Considering that the entire DZ is most likely wider and the DZ width against displacement plots by Choi et al. (2016) show a log-log distribution, it is expected that the true displacement of the encountered fault zone lies within the reported values by Doebel (1967), Doebel and Olbrecht (1974), and Eisbacher and Fielitz (2010). This further supports the previous interpretation, that the encountered fault zone represents the Rhine Graben main fault. This is additionally underpinned by Bauer et al. (2015) who also assume a high displacement fault for a 14 m thick core zone.

### 5.3 Volumetric Fault Zone Modeling

To obtain a profound volumetric model of a fault zone, the fault properties have to be described as volumetric entities composed of distinct elements with distinct physical properties within a defined spatial distribution (Braathen et al., 2009). The concept of facies (Teichert, 1958; Middleton, 1978; Reading, 1986; Tikoff and Fossen, 1999) comprises all the necessities and is therefore applied not only to sedimentary units but also to fault zones (Braathen et al., 2009; Bastesen and Braathen, 2010) to describe their 3D geometry and internal architecture (Medina-Cascales et al., 2019). In addition, the facies concept serves also for the characterization of seismic fault zones (Botter et al., 2017; Cunningham et al., 2019), or, like in the own study, facilitates volumetric fault zone modeling (Flodin et al., 2001; Al-Busafi et al., 2005; Berg and Øian, 2007; Fredman et al., 2008; Fachri et al., 2011; Fachri et al., 2013; Qu et al., 2015; Fachri et al., 2016; Qu et al., 2017).

#### 5.3.1 Grid Construction and Resolution

Prior to modeling facies it was necessary to provide a frame to support all volumetric entities. The morphology of the studied outcrop suggests a subdivision into two geobodies, a DZ and a FC. A balance between the preservation of accurate geometries and an applicable amount of grid cells, which could be handled in a reasonable time by the modeling software, had to be found. This was accomplished with regard to: (i) the amount of geological units in the DZ, (ii) their thickness, (iii) the complexity of the FC architecture, and (iv) the outcrop size. The author decided to choose a minimum global grid cell size of 0.5 x 0.5 x 0.2 m (XYZ), which represents a rather high resolution comprising 8.88 million cells over a 100 x 100 x 10-17 m (XYZ) survey. It should be mentioned, that the “global grid” is defined as the initially created grid, which comprises the whole survey. It stands in contrast to the “local grid”, which is a refined part of the global grid, and usually covers a smaller volume. Similar studies concerning volumetric fault zone models comprise surveys mostly with a dimension of an order of magnitude higher (Table 15, see citations there). However, these studies exported the fault zone part of the grid (called “fault zone grid” or “fault envelope grid”) and subsequently applied a local grid refinement (LGR) and petrophysical modeling to it. The refined fault zone grid was afterwards merged with the coarser global grid for further analysis.

In addition, the mentioned studies used grids with pillar faults, which facilitates the possibility to export, refine, and re-merge the fault zone grid; this does not work with

stair-stepped faults (Qu et al., 2015). Within the own study stair-stepped faults are used to construct and separate the grid into two geobodies (DZ and FC). The model does therefore not have the possibility to export parts of the global grid for separate subsequent LGR and petrophysical modeling. As a result, the presented approach has a disadvantage in cell size flexibility, tending to either possess an unnecessary high cell amount in homogeneous parts of the model leading to higher computational time, or, to a too coarse grid cell size in very heterogeneous parts containing many small geological elements, which will then not be portrayed adequately. On the other side, the great advantage of the used VBM method is, that it is practically insensitive to the complexity of the fault model (Souche et al., 2013); even more sophisticated fault models should be possible with increasing computational power. In case of the own study the mentioned negative aspect of no cell size flexibility within different geobodies is interpreted to not have a strong impact because the area of the chosen survey is relatively small and shows a high heterogeneity in the DZ and the FC. Additional tests with LGR, which are not explicitly presented here, showed that it is possible to apply a LGR to selected parts of the global grid. The resulting refined grids, however, cannot be populated with refined petrophysical properties as stated by Qu et al. (2015), but will keep the coarser resolution of the global grid.

Table 15: Overview of the survey dimension, global and fault zone grid cell size, as well as the fault zone grid width of several studies on volumetric fault zone modeling. Fault zone grid width is perpendicular to the (theoretical) main slip surface. As no LGR was performed within the own study the global grid cell size equals to the fault zone grid cell size, as well as the fault zone grid width equals the width of the survey. Grid and cell sizes are listed in their XYZ extent. \*The study by Fachri et al. (2016) represents a special case with different fault zone grid cell sizes. The listed size is related to the "lens objects" of Fachri et al. (2016).

Study	Survey dimension in XYZ [m]	Global grid cell size in XYZ [m]	Fault zone grid width [m]	Fault zone grid cell size [m]
Fredman et al. (2008)	1000 x 800 x 310	50 x 50 x 5	100	3.33 x 10 x 3.33
Fachri et al. (2011)	1000 x 1000 x 30	25 x 25 x 2	50-100	1 x 8.3 x 2
Qu et al. (2015)	7700 x 7700 x 80	35 x 35 x 5	44-125	3.5 x 7 x 5
Fachri et al. (2016)	6700 x 6700 x 700	261 x 218 x 6	6-10	0.1 x 1 x 1*
Qu et al. (2017)	1000 x 1600 x 200	20 x 20 x 20	80	1 x 4 x 4
The own study	100 x 100 x 10-17	0.5 x 0.5 x 0.2	100	0.5 x 0.5 x 0.2

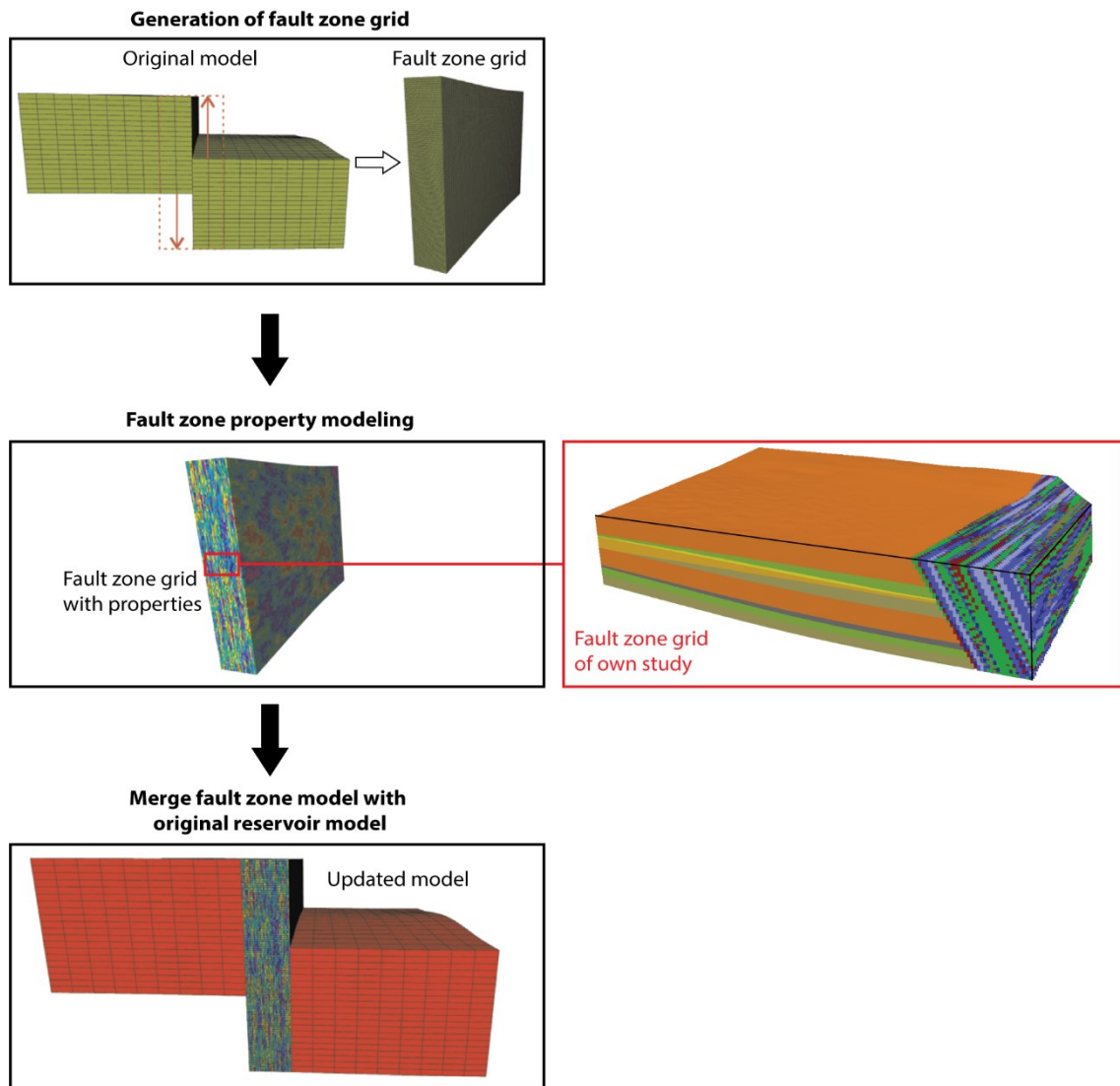


Figure 63: The figure illustrates the difference in dimension and clarifies the scale of comparability of the present study and the studies listed in Table 15. The left side shows a schematic workflow of the fault zone grid export approach (modified after Qu et al., 2015). The right side shows the fault zone grid of the own research study.

Figure 63 (modified after Qu et al., 2015) shows a schematic workflow of the fault zone grid export approach in contrast to the fault zone grid of the own research, depicting the difference in dimension and the scale of comparability (see also Table 8). The dimension and cell size of the refined fault zone grids of the studies listed in Table 8 is comparable to the cell size and survey dimension of the study presented here, although the cell resolution in the own study in remains generally higher. Fachri et al. (2016) present a special case as their method comprises a multilevel LGR with subsequent upscaling from fine to coarse fault zone grids. To the already refined fault zone grid of the “lens object” scale (as listed in Table 15, see also Figure 67c) Fachri et al. (2016) additionally carried out a non-proportional refinement to generate 1 mm thick cells enveloping the “lens object” grid cells. Within Fachri et al. (2016), “lens objects” are

associated to a specific scale of higher grid resolution. For more details see the publication of these authors. It should be mentioned that the proportions of the fault grid cells of the other studies (Table 15) are rather elongated in a vertical direction, while the cells of the here presented study are elongated in horizontal direction. The mentioned studies did not additionally split the fault zone grid in two geobodies but defined it as one LGR geobody, which makes an elongation parallel to the main slip surface preferable regarding the tendency of fault elements to be elongated parallel to it (Caine et al., 1996; Shipton et al., 2005; Færseth, 2006; Manzocchi et al., 2010; Meier et al., 2015). In the case of the own study, however, the fault zone is split into geobodies; the DZ represents the greater share and bears horizontally elongated geological units. In addition, the gridding was carried out with the purpose of the subsequent DFN modeling. A horizontal cell elongation implies a higher vertical grid resolution, which is preferable for the examination of fracture truncation (chapter 5.4), because fracture planes rather show a vertical than a horizontal trend.

In summary, the applied grid resolution and cell elongation constitutes a good balance between a manageable amount of cells and the preservation of geological geometries, also with regard to the subsequent DFN modeling. The combination of the LGR approach of pillar gridded fault models with the complexity of VBM based stair-step fault models would be desirable for future models. An additional LGR in the FC geobody would have provided a further increase of detail by capturing smaller geometries comparable to the exceptionally detailed slip zone modeling of Fachri et al. (2016). The presented fault zone model does not comprise a hanging wall, because the outcrop it is based on does not provide this part. However, with regard to further analysis, it may be beneficial in such cases to enhance the fault zone grid by mirroring the DZ of the foot wall to the hanging wall, constructing a partly synthetic fault zone model with its synthetic part based directly on the prevalent geological conditions (Figure 64).

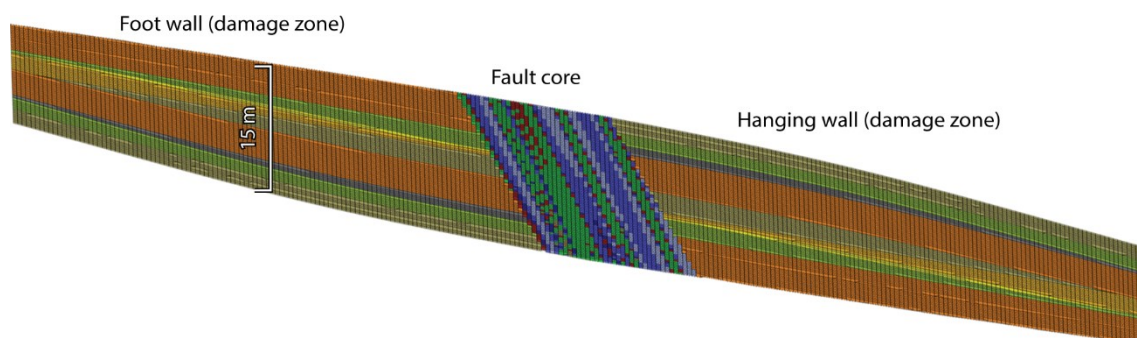


Figure 64: Graphically created example of mirroring the exposed foot wall part of the outcrop to a synthetic hanging wall part. Orthogonal view in north-direction.

### 5.3.2 Fault Facies Model

The two geobodies (DZ and FC) were treated separately for fault facies determination and distribution. The exposed DZ of the fault zone could be treated in a classical way of bed and lithofacies analysis leading to a straightforward determination and distribution of lithofacies types according to the corresponding beds' spatial extent. Only the lithofacies type "F1" could not be incorporated because its maximum vertical extent narrowly exceeded the minimum vertical cell size at only one location of the outcrop. In addition, the "F1" type is encountered only rarely in the outcrop with a low horizontal extent of a maximum of up to 8 m. Furthermore, its petrophysical values are within the range of other fine-grained lithofacies types of the outcrop. The non-incorporation of the "F1" type has therefore no substantial impact on the behavior of the facies model.

In the case of the FC the author established a FC facies model based on the FC architecture and lithological description provided by Bauer et al. (2015) under consideration of the volumetric restrictions (see previous chapter). Seven FCFTs were established, five of lithological and two of structural origin (Figure 66). Braathen et al. (2009) and Bastesen and Braathen (2010) characterized FC elements and applied the facies concept to faults in order to make them applicable for volumetric modeling to forecast structural reservoir heterogeneities. Both studies analyzed faults to recognize comprehensive FC elements in carbonate (Bastesen and Braathen, 2010) and clastic rocks (Braathen et al., 2009). As the focus of their studies was set on fault facies analysis no subsequent volumetric fault zone modeling was performed. Bastesen and Braathen (2010) analyzed 103 faults and recognized six "FC lithologies" (equivalent to the FCFTs of the own study) applicable to all faults: (i) carbonate breccia (CB), (ii) shale supported carbonate breccia (SCB), (iii) cemented breccia (SCaCB), (iv) shale smear (SS), (v) clay gouge (CG), and (vi) secondary calcite vein (SCa). Even though these FC lithologies are revealed from a different lithological host rock and are not elaborated in the respect of volumetric restrictions, many similarities to the FCFTs of the own research study exist. As the dimension of investigation is comparable, Bastesen and Braathen (2010) recognized a similar amount of different FC lithologies (six) as in the study presented here (seven). The breccia type FC lithologies "CB", "SCB", and "SCaCB" are interpreted as the carbonate equivalent of the sandstone FCFTs "Sc", "Ss", and "Su" described here, as they are assumed to make up the major share in FCs with high displacements. Gouges are also incorporated as a FC element in both studies ("CG" in Bastesen and Braathen, 2010, and "Gs" and "Gc" in the own research). Figure 65 shows an overview of different FC compositions of all faults and faults with a high displacement according to Bastesen



and Braathen (2010). As the FC of the study presented here comprises seven different FCFTs, it represents a “composite fault core”. Unfortunately, no further information is given on the percentage of the FC lithology of the composite FCs for a detailed comparison.

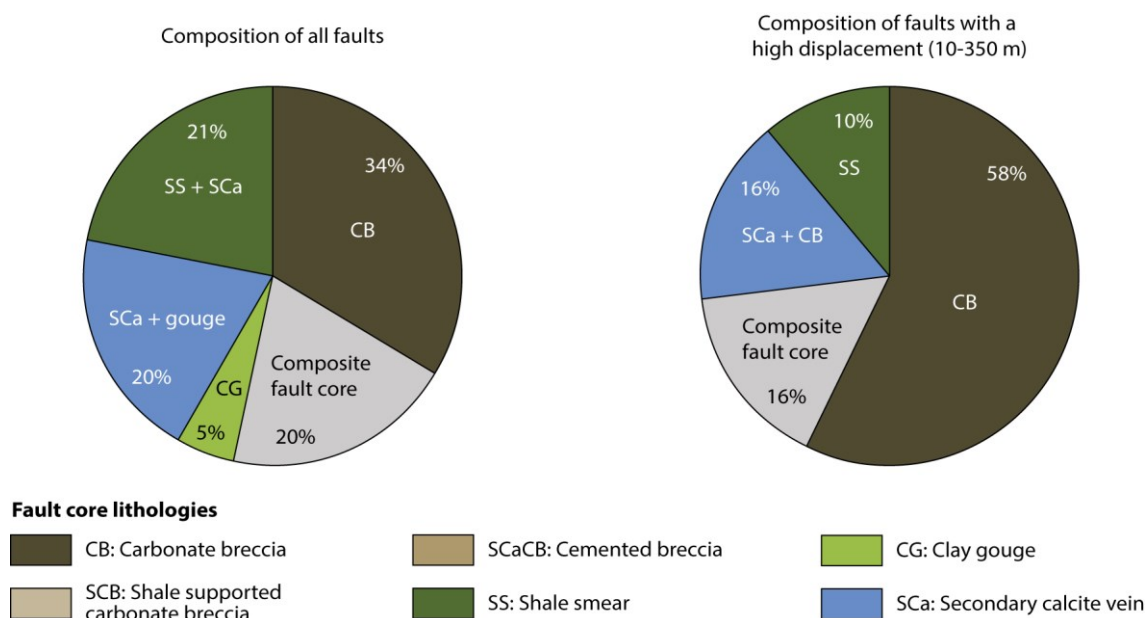


Figure 65: Overview of the elaborated FC lithologies in carbonate rocks by Bastesen and Braathen (2010). Left side shows the FC composition of all studied faults. Right side illustrates the FC composition of faults with a high displacement (after Bastesen and Braathen, 2010). The FC of the own research would be classified as a composite FC.

Braathen et al. (2009) on the other hand analyzed 26 faults in porous sandstone and divided the data sets into three main element categories (Table 16): (i) discrete structures, (ii) membranes, and (iii) lenses. They further analyzed the different elements of each category in detail leading to a fine subdivision, which results in 50 different fault facies types and additional 34 facies shape types. This kind of extraordinary detailed subdivision is not applicable in the own research study by reason of volumetric restrictions and given detail on FC information. However, by contemplating the basic elements of the three main categories presented by Braathen et al. (2009) without the fine subdivision given by these authors, the main categories become comparable to the FCFTs elaborated within the study presented here. “Discrete structures” described by Braathen et al. (2009) comprise the elements “slip surfaces”, “deformation bands” and “fractures” in various forms. The facies types “DBC” (deformation band cluster) and “SZ” (slip zone), classified as structural FCFTs in the own research, would be classified after Braathen et al. (2009) as discrete structures and

Table 16: Comparison of the FCFT categories of this study with the three main FC element categories after Braathen et al. (2009). Fractures (yellow tick) are treated separately through a DFN and are not implemented as a FCFT. The category “lenses” (red tick) are listed for reasons of completeness and are not incorporated in the FC facies model of the own study. DBC: deformation band cluster; SZ: slip zone; Sc: sandstone consolidated; Ss: sandstone spreading; Su: sandstone unconsolidated; Gs: gouge, silt unconsolidated; Gc: gouge, clay unconsolidated.

FCFT	FCFT categories in the own study			Main FC element categories after Braathen et al. (2009)		
	Structural types	Lithological types	Lenses	Discrete structures	Membranes	Lenses
DBC	✓			✓		
SZ	✓			✓		
Sc		✓			✓	
Ss		✓			✓	
Su		✓			✓	
Gs		✓			✓	
Gc		✓			✓	
Other						
Fractures	✓			✓		
Lenses			✓			✓

therefore also as individual fault facies types, likewise fractures. Fractures, however, are treated separately through a DFN in the own study (see chapter 5.4) and are not incorporated as a FCFT. The category “membranes” described by Braathen et al. (2009) constitutes the elements “cataclasites”, “breccias”, “gouge”, and “smears” and are said to often occur along slip surfaces. The FCFTs “gouge, silt unconsolidated (Gs)” and “gouge, clay unconsolidated (Gc)” listed in the own study are mostly confined by slip surfaces (see chapter 3.1.2.1) and are plain descriptions of membranes after Braathen et al. (2009). The sandstone FCFTs “sandstone consolidated (Sc)”, “sandstone spreading (Ss)”, and “sandstone unconsolidated (Su)” also fit best within the membrane category, of which the latter is similar in its occurrence to the two gouge types with only a different grain-size. “Lenses” described by Braathen et al. (2009) are bound on all sides by slip surfaces or membranes, while the lenses in the FC of the outcrop described here are enclosed by the sandstone FCFTs. This further corroborates the interpretation of the sandstone FCFTs as membranes. The above mentioned lenses within the FC correspond to the third main category “lenses” after Braathen et al. (2009), but they are not incorporated in the FCFTs (see discussion in the next section). Under these

considerations, the “lithological types” and “structural types” of the own research study (Figure 66) correspond to the main element categories “membranes” and “discrete structures” described by Braathen et al. (2009), which corroborates the comparability and the validity of the performed subdivision (Table 16).

Unfortunately, not every initial FC element of the studied outcrop could be incorporated in the FC facies model. The spatial extent of “host rock lenses” is too small, with the exception for one single lens, which would provide the necessary minimum extent to fit a grid cell.

The reason of the non-incorporation lies within the method of using a single FC facies log intersecting the FC, which only marginally cuts the big lens at its upper section. To use a stacked set of FC facies logs would give a denser sampling rate and cover a larger area of the FC architecture (Figure 66) but would be too time consuming compared to the benefits, because it is assumed that the overall impact on the FC facies model of the own research study would be small. In case of “Fe/Mn concretions” and “sandstone pebbles” it should be possible to examine their eventual influence on the petrophysical values of the FCFT they are imbedded into. If this influence would be substantial, the addition of these types would either define separate FCFTs, or their influence could be scaled up. However, in case of the own study, their influence on the facies model is assumed to be most likely negligible.

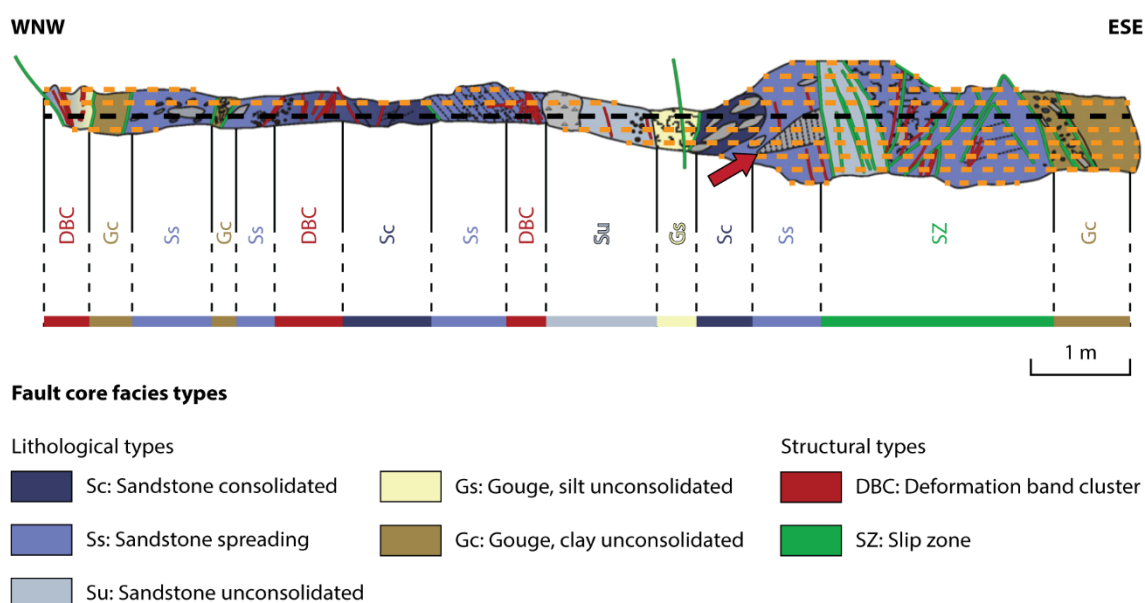


Figure 66: Upper part shows the FC architecture after Bauer et al. (2015). The black dashed horizontal line represents the original FC facies log. The orange dashed horizontal lines represent possible additional FC facies logs, which would enhance the sampling rate, capture the big lens (marked by red arrow), and contribute to a refined percental distribution of the FCFTs, closer to their representation in the outcrop.

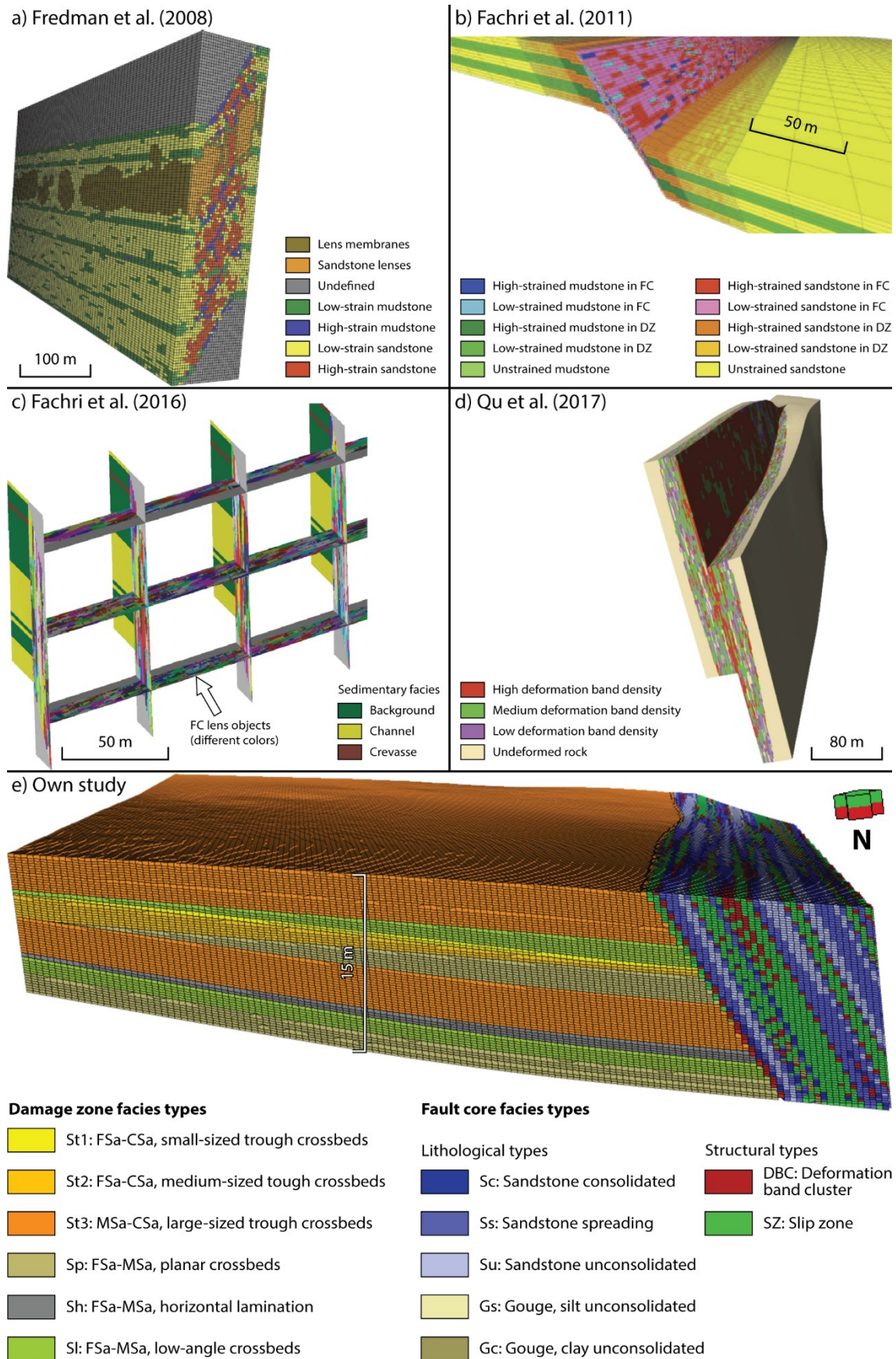


Figure 67: Comparison of the fault facies classification and distribution between (a) Fredman et al. (2008), (b) Fachri et al. (2011), (c) Fachri et al. (2016), (d) Qu et al. (2017), and (e) the own study.

Fredman et al. (2008), Fachri et al. (2011), Fachri et al. (2016), and Qu et al. (2017) presented volumetric fault zone models in combination with the above mentioned fault facies concept (Figure 67). However, these studies used synthetic models (Fredman et al., 2008; Fachri et al., 2011; Qu et al., 2017) or synthetic fault envelopes within a case study (Fachri et al., 2016), while in the own research study a fault zone grid was constructed after a real outcrop. The fault facies distribution described here is related to a natural bed distribution in the case of the DZ. Regarding FC, a FC facies log (Figure 66) derived from a natural FC architectural sketch was upscaled and subsequently distributed with the help of the Sequential Gaussian Simulation (SGS) algorithm. The previously mentioned studies distribute their fault facies through the application of a Truncated Gaussian Simulation (TGS) method (Qu et al., 2017), a displacement function (Fachri et al., 2011; Fachri et al., 2016), or a product distribution factor (Fredman et al., 2008) conditioning the fault envelope, with subsequent application of the Sequential Indicator Simulation (SIS) technique (Fredman et al., 2008; Fachri et al., 2011) and object-based modeling (Fredman et al., 2008; Fachri et al., 2016). The synthetic approaches therefore define their fault facies types somewhat different to the classification given in Braathen et al. (2009) and Bastesen and Braathen (2010) by putting more emphasis on strain and intensity related differentiation. Fredman et al. (2008) included nine facies types in their model (Figure 67a): one undefined, two for the host rock, and six for the fault zone, which was not separated into DZ and FC. The fault facies types include: (i) high-strained sandstone, (ii) low-strained sandstone, (iii) high-strained mudstone, (iv) low-strained mudstone, (v) sandstone lenses, and (vi) lens membranes. Fachri et al. (2011), on the other hand, divided the fault zone into a DZ and a FC defining four fault facies types in the FC and six in the DZ (Figure 67b). The FC facies types are: (i) low-strained sandstone lenses, (ii) low-strained mudstone lenses, (iii) high-strained sandstone lenses, and (iv) high-strained mudstone lenses. The DZ facies types were subdivided based on deformation-band frequency and constitute: (i) unstrained sandstone, (ii) unstrained mudstone, (iii) low-strained sandstone, (iv) low-strained mudstone, (v) high-strained sandstone, and (vi) high-strained mudstone. Fachri et al. (2016) again did not distinguish between DZ and FC, but defined the fault envelope as a FC, which is imbedded in a channelized reservoir environment characterized by sedimentary crevasse, channel and background facies (Figure 67c). Only two FC facies types were defined: (i) lenses, and (ii) slip zones. However, in this case, the same facies types do not necessarily bear the same petrophysical properties. This facilitates a fault facies heterogeneity comparable to the other studies. Qu et al.

(2017) also did not distinguish between DZ and FC and defined the fault envelope as a DZ with four fault facies types (Figure 67d). These are based on deformation band networks and are categorized by their deformation band density: (i) high deformation band density, (ii) medium deformation band density, (iii) low deformation band density, and (iv) undeformed rock. Furthermore, the TSG method used by Qu et al. (2017) to populate the fault facies within the fault zone grid is closest to the SGS algorithm used for FCFT distribution in the own study. In addition Qu et al. (2017) generated five different fault facies elongation scenarios similar to the three FC elongation cases of the own research (A, B and C, see chapter 4.4.4) to investigate the sensitivity of the reservoir to the different settings, which is further discussed in chapter 5.5. Qu et al. (2017) faced the same struggle as during the own work of obtaining good field-data, especially in fault-parallel direction, to quantify the elongation ranges of the fault facies types. Thus, this issue should be targeted for upcoming studies to enhance the realism of volumetric fault zone models.

In comparison to the mentioned volumetric fault zone modeling studies applying fault zone facies, the own research stands out because of the uniquely detailed fault facies classification of a non-synthetic, specific fault zone comprising 13 fault facies types, split into two geobodies (DZ and FC). The restriction by a minimum cell size and the simultaneous preservation of as much detail as possible resting on the fault facies classification schemes after Braathen et al. (2009) and Bastesen and Braathen (2010) constituted a particular challenge. The accomplished detail is possible because the own study concentrates on a much smaller survey volume compared to the models of Fredman et al. (2008), Fachri et al. (2011), Fachri et al. (2016), and Qu et al. (2017). To further enhance the detail of the FC facies model a higher FC grid resolution would be necessary, as discussed in the previous chapter.

### 5.3.3 Matrix Porosity and Permeability Determination

Matrix PPMV-pairs are distributed according to their corresponding facies type, which is discussed in the previous chapter. In case of the lithofacies types of the DZ the determination of the PPMV-pairs is based directly on petrophysical data provided by project partners. The PPMV-pair determination of the FCFTs, on the other hand, presented a challenge as the author intended to present the most probable petrophysical values, even when no data was available for the FC. The detailed PPMV-pair determination can be seen in chapter 3.1.2.2. The PPMV-pair of the lithological FCFT "Sc" was directly derived from petrophysical data of the DZ. Values for the FCFTs

“Su”, “Gs”, and “Gc” could be found in literature (Manger, 1963; Bear, 1972). Although no direct outcrop values could be applied for the “Su”, “Gs”, and “Gc” FCFTs, the derived values are interpreted to be highly reasonable as extensive work was performed on these lithologies by Manger (1963) and Bear (1972). Only for the lithological FCFT “Ss” an assumption had to be made as no values in literature were available, which makes the petrophysical values used for this FCFT more prone to error. However, due to its origin the most probable values could be narrowed down based on the PPMV-pair values of the “Sc” and “Su” FCFTs. The PPMV-pair determination of the two structural FCFTs “DBC” and “SZ” constituted a greater challenge. To establish a connection with the available petrophysical outcrop data of the DZ the author defined the values of the consolidated sandstone “Sc” as host rock values. This, in combination with some previously made assumptions, and applying results by Chilingarian (1964), Fossen et al. (2007), and Torabi et al. (2013), allowed to derive PPMV-pairs for the structural FCFTs “DBC” and “SZ”. Multiple other studies had to be considered as well (Pittman, 1981; Jamison and Stearns, 1982; Harper and Moftah, 1985; Knott, 1993; Antonellini and Aydin, 1994; Gibson, 1994; Knipe et al., 1997; Crawford, 1998; Gibson, 1998; Antonellini et al., 1999; Fisher and Knipe, 2001; Jourde et al., 2002; Shipton et al., 2002). Although not fully satisfying, this method still constitutes the best option available to derive the PPMV-pairs of the two FCFTs from the outcrop data.

To improve the reliability of petrophysical values of distributed FCFTs within volumetric fault zone models based on real outcrops, two additional steps should be undertaken: (i) a fault zone facies study, preferably applying the fault facies classifications schemes after Braathen et al. (2009) for clastic and Bastesen and Braathen (2010) for carbonate rocks, and (ii) a petrophysical analysis of the encountered elements, because FC materials show a range of variation of approximately 10 orders of magnitude (Caine et al., 1996). Although this would be very time consuming, it is inevitable to elaborate a model as close to nature as possible. Furthermore, it would ensure the comparability of the elaborated models, and might lead to a common data base for fault zone models.

## 5.4 Discrete Fracture Model

DFN models are widely applied as they bring along the advantage, in contrast to continuum models, to not underestimate the tendency for flow channeling and provide the opportunity to analyze precisely the effect of different fracture patterns (Li et al., 2016; Bauer et al., 2017). More specific, 3D DFN models (e.g. Chesnaux et al., 2009; Agada et al., 2014; Bisdorn et al., 2014; Bisdorn et al., 2016; Laux, 2017; Panza et al., 2018; Giuffrida et al., 2019) provide better results than 2D DFN models in terms of fracture permeability estimation (Lang et al., 2014; Huang et al., 2016; Liu et al., 2018), but are restricted to 10s to few 100s of meters (Bense et al., 2013) if an outcrop scale detail is targeted. As a DFN model requires a detailed understanding of fracture network characteristics (Bisdorn et al., 2014) a thorough parametrization was conducted (chapter 5.4.1). In the following the results of the presented thesis are compared with studies of similar DFN dimensions, though DFN studies within sandstones are rather an exception and the vast majority was conducted within carbonate rocks. This is attributable to the fact that carbonates constitute lower values of median and maximum porosity for a given burial depth in comparison to sandstones (Ehrenberg and Nadeau, 2005). The relative lack of fractured low-porosity siliciclastic reservoirs compared to carbonates reflects the more common development of fractures in the latter. Fractures are therefore more relevant for economic flow rates within carbonate reservoirs (Ehrenberg and Nadeau, 2005), and more DFN models deal with carbonate rocks therefore. However, in terms of sheer DFN modeling, this has no significance as matrix PPMV-pairs do not have an impact on the elaborated DFN properties (chapter 5.4.2). Only the applied fracture parameters are decisive, which makes DFN models of carbonate and siliciclastic rocks comparable.

### 5.4.1 Parametrization

A detailed parametrization of fracture sets is the backbone to reflect an as close to nature as possible DFN model. Studies in the past mostly used at least one constant parameter (usually aperture, length, or intensity) for the DFN modeling process (e.g. Chesnaux et al., 2009; Wilson et al., 2011; Agada et al., 2014; Laux, 2017; Liu et al., 2018). Often more parameters were chosen as constant, reasoned in the lack of field data, growing computational time, or simply not having a focus on the DFN. More recent studies revealed the importance of a detailed parametrization of the fracture network



characteristics (e.g. Panza et al., 2018; Giuffrida et al., 2019; Parrino et al., 2019; Volatili et al., 2019), including the own study.

**Fracture set division and orientation calculation** was performed separately for the DZ and FC, resulting in three fracture sets each. Although, no distinct sets could be identified due to the wide azimuthal scatter of the data, this does not represent a real problem. Calculating the orientation with the Fisher and Bingham analysis (Bingham, 1964, 1974; Fisher et al., 1987) bears the possibility to reflect datasets of both, circular- and orthorhombic-symmetrical clusters (see chapter 3.4.2), as well as their concentration. Therefore the datasets had to be divided accordingly by the user, as is the case within the presented study: the resulting DFN fracture orientation distribution reflects the original outcrop data.

As **fracture shape** the author chose a 16-sided elliptical form with an elongation ratio of 1:2. Although some studies used elongation ratios of 1:1 (Chesnaux et al., 2009; Boro et al., 2014) it became more common to apply fracture elongation ratios  $> 1$ . Agada et al. (2014) and Bisdom et al. (2014) used relatively wide ratios of 1:5 and 1:8, respectively. More recent studies decided to either combine two elongation ratios of 1:4 and 1:2 (Panza et al., 2018; Giuffrida et al., 2019), or used a 1:2 ratio only (Volatili et al., 2019). The choice of a 16-sided elliptical form for the computed DFNs as in the presented study is rather uncommon, because it has a negative effect on computational time. Rounded fracture patches were observed in Bisdom et al. (2014), however a 4-sided shape remains the standard choice for DFN models (e.g. Chesnaux et al., 2009; Laux, 2017; Panza et al., 2018; Giuffrida et al., 2019; Volatili et al., 2019). Therefore, the 1:2 aspect ratio is considered as an adequate choice, while the 16-sided elliptical shape is a special feature, which might provide a more realistic DFN model. The effect of the chosen shapes on DFN properties was not further investigated within this thesis and might be tested in the future.

Bisdom et al. (2016) and Kluge et al. (2017) state that most fracture models consider a constant **fracture aperture**. As it is one of the main controlling factors in flow defining the fracture porosity and permeability (National Research Council, 1996; Guerriero et al., 2013) it is desirable to characterize the aperture as accurately as possible by defining it through an equation instead of a constant value. For this reason the author plotted the fracture aperture against the frequency for each fracture set. A log-normal distribution was chosen, which, along with the power-law distribution, is one of the most used equation types for fracture aperture definition (see chapter 3.4.4).

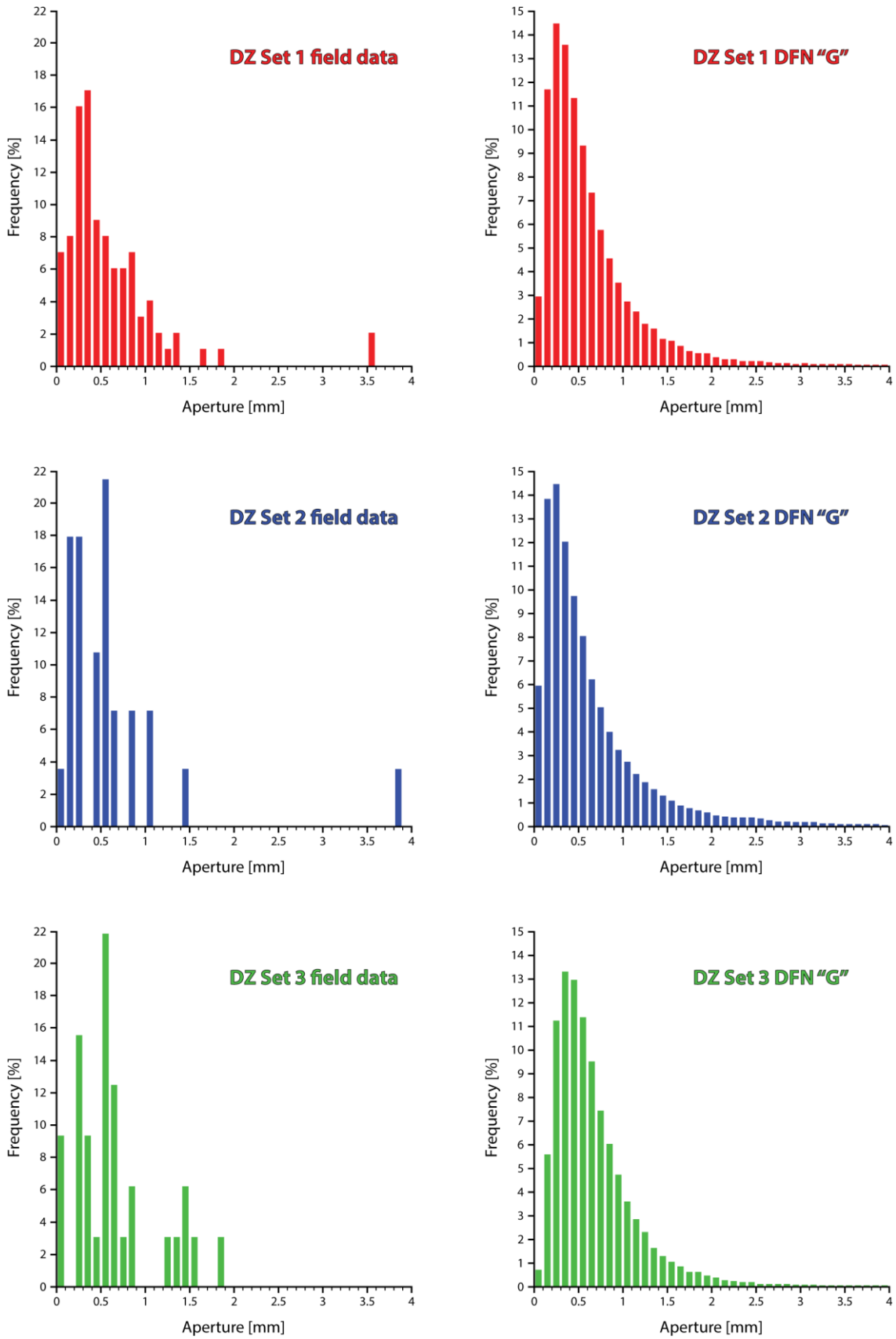


Figure 68: Comparison of the aperture distribution of the field data and its corresponding calculated aperture distribution of the DFN "G" for the DZ Sets 1, 2 and 3.

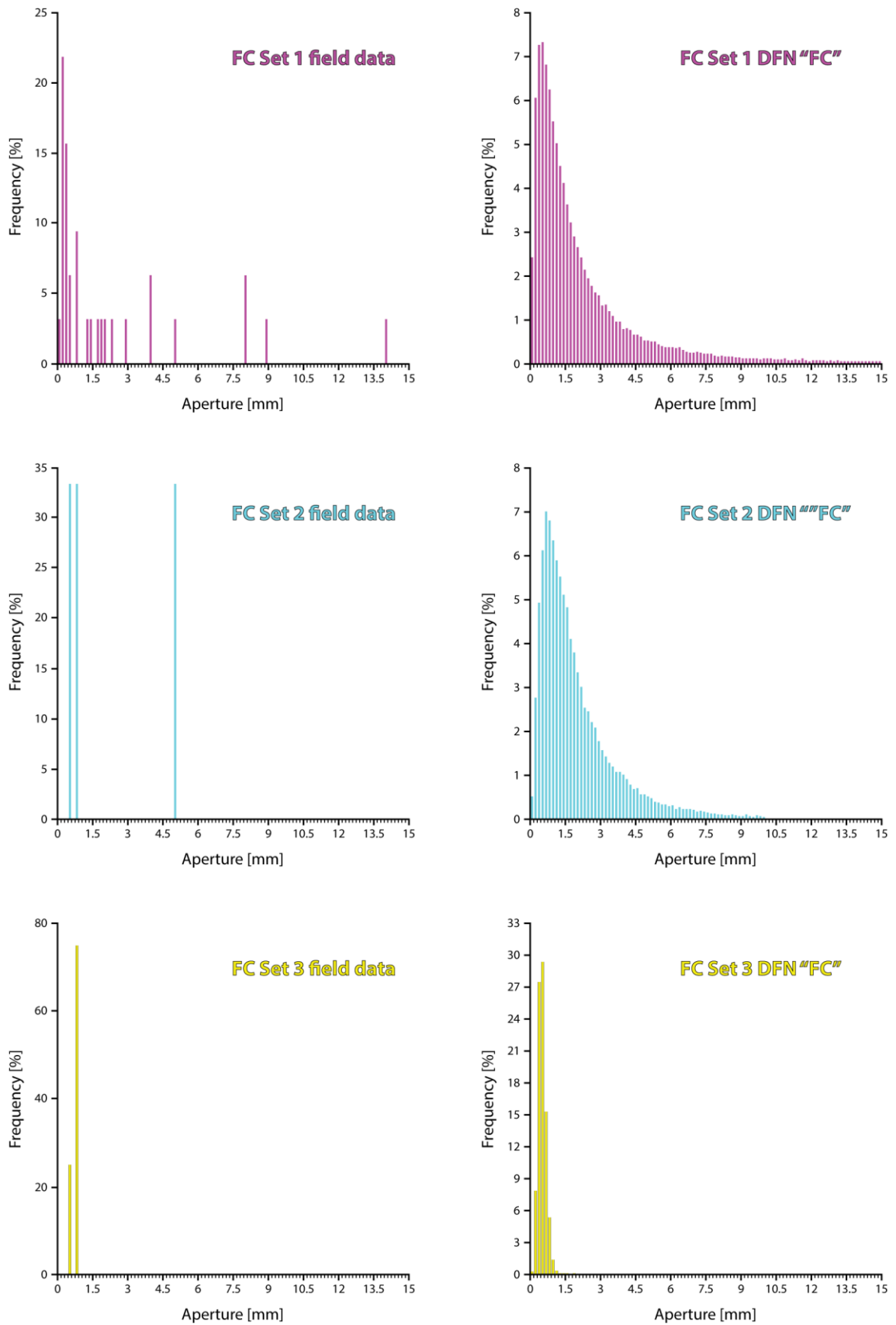


Figure 69: Comparison of the aperture distribution of the field data and its corresponding calculated aperture distribution of the DFN "FC" for the FC Sets 1, 2 and 3.

As an example, Figure 68 shows for the DZ a comparison of the aperture distribution of the field data with the corresponding calculated aperture distribution of the DFN “G”. For the FC a comparison is shown in Figure 69. In both figures the plotted frequency of the field data and DFN differs. This can easily be explained by the fact that not all aperture size classes were measured during field work, while all classes are served in the calculated DFN. The important aspect is the comparable aperture class size, which is 0.1 mm in the DZ (Figure 68) and 0.15 mm in the FC (Figure 69). In consideration of the revealing trend of the field data a log-normal distribution was considered as appropriate. While the aperture distribution of all three DZ sets and FC Set 1 seem to constitute a good fit, FC Sets 2 and 3 obviously suffer from shortage of FC aperture measurements. This is due to: (i) the relatively small exposed part of the FC compared to the DZ and the therefore decreased possibilities of measurement, and (ii) the orientation of FC Sets 2 and 3 showing a more perpendicular orientation to the main slip surface, which further decreases the opportunity of measurement with regard to the already small exposed FC area. To gather a satisfying amount of fracture data in a FC is therefore strongly dependent on the orientation and area of exposure. Alternatively, the user could divide the initial FC fracture data in fewer sets, which would enhance the database for each set. However, this would also increase the inaccuracy of the fracture set orientation analysis. Hence, the author decided to divide the FC into three sets and apply a log-normal distribution based on the available data. Proceeding this way a more realistic model could be expected in contrast to the usage of a uniform aperture. This procedure is strengthened by results of Lei et al. (2014) who compared the influence of uniform, log-normal and power-law distributions of apertures on fracture permeability. Result was a permeability difference by a factor of 2 to 2.5 between a uniform distribution and the distributions by equations.

It is important to note that different types of fracture apertures are distinguished for subsequent fracture porosity and permeability calculation. The mechanical aperture, as used in the presented study, constitutes the physically measured aperture and is the one used for the fracture porosity calculation (Lyons et al., 2016). As fractures are usually rough-walled, which is expected to have an impact on fluid flow (Ran et al., 2014), many studies (e.g. Panza et al., 2018; Giuffrida et al., 2019; Parrino et al., 2019; Volatili et al., 2019) use the hydraulic aperture for the fracture permeability calculation. It is attained by applying a Joint Roughness Coefficient (JRC) to the mechanical aperture, for which a variety of correlations exist. For more information about the JRC the reader is referred to Olsson and Barton (2001), Ran et al. (2014), and Lyons et al. (2016). This

leads to a usually larger mechanical than hydraulic aperture. However, the effects of the reduced hydraulic apertures in complex fracture systems are still subject of investigations (Zhao, 2017); for reasons of simplicity some studies assume therefore still an identical hydraulic and mechanical aperture in DFN models (Zhao, 2017). As no information of fracture wall roughness exist for the investigated outcrop, no JRC could be applied to the mechanical aperture. The resultant mean mechanical aperture values of the FC (0.78-2.3 mm) are higher compared to the DZ aperture values (0.63-0.7 mm), which is plausible considering the origin and the dimension of the studied fault zone. Also Panza et al. (2018) reported similar mechanical aperture values for their fault zone DFN model (0.2-1.5 mm).

The **fracture length** is one of the main factors controlling the fracture network connectivity. Typically there are many small and a diminishing number of large fractures in a set (Gillespie et al., 1993; Marrett, 1997; Odling et al., 1999; Gillespie et al., 2001; Hooker et al., 2013). The length of a set can be described (analogous to the aperture) by different distributions, of which the log-normal, power-law, and exponential ones are mostly used (see chapter 3.4.5). Based on the field data the author decided to apply a log-normal distribution. For the DZ Figure 70 shows a comparison of the field data with its corresponding calculated DFN “G”. A comparison for the FC can be seen in Figure 71. Considering the differing frequencies of the graphs (except for the DZ Set 3) the log-normal distribution is a good choice to mirror the field data. The FC data again reflects the difficulties of gathering a satisfying amount of field measurements, as already discussed before for the aperture data. In case of FC Set 3 no length data was available. A plausible length distribution was derived from the aperture values under consideration of length-aperture relationships (see chapter 3.4.5). The resulting mean length values for the DZ are 1.4-2.2 m and 0.5-1.5 m for the FC. The chosen minimum length is 0.2 m, while the maximum length amounts for 20 m for the DZ and 10 m for the FC. These values are comparable with length parameters for a DZ of other studies, e.g. Giuffrida et al. (2019), who reported minimum and maximum length values of 0.02 and 14 m, respectively. The smaller length values for the FC in comparison to the DZ are understandable as the FC shows a higher facies heterogeneity. Incorporated gouges and unconsolidated material leads to an increase of fracture truncation.

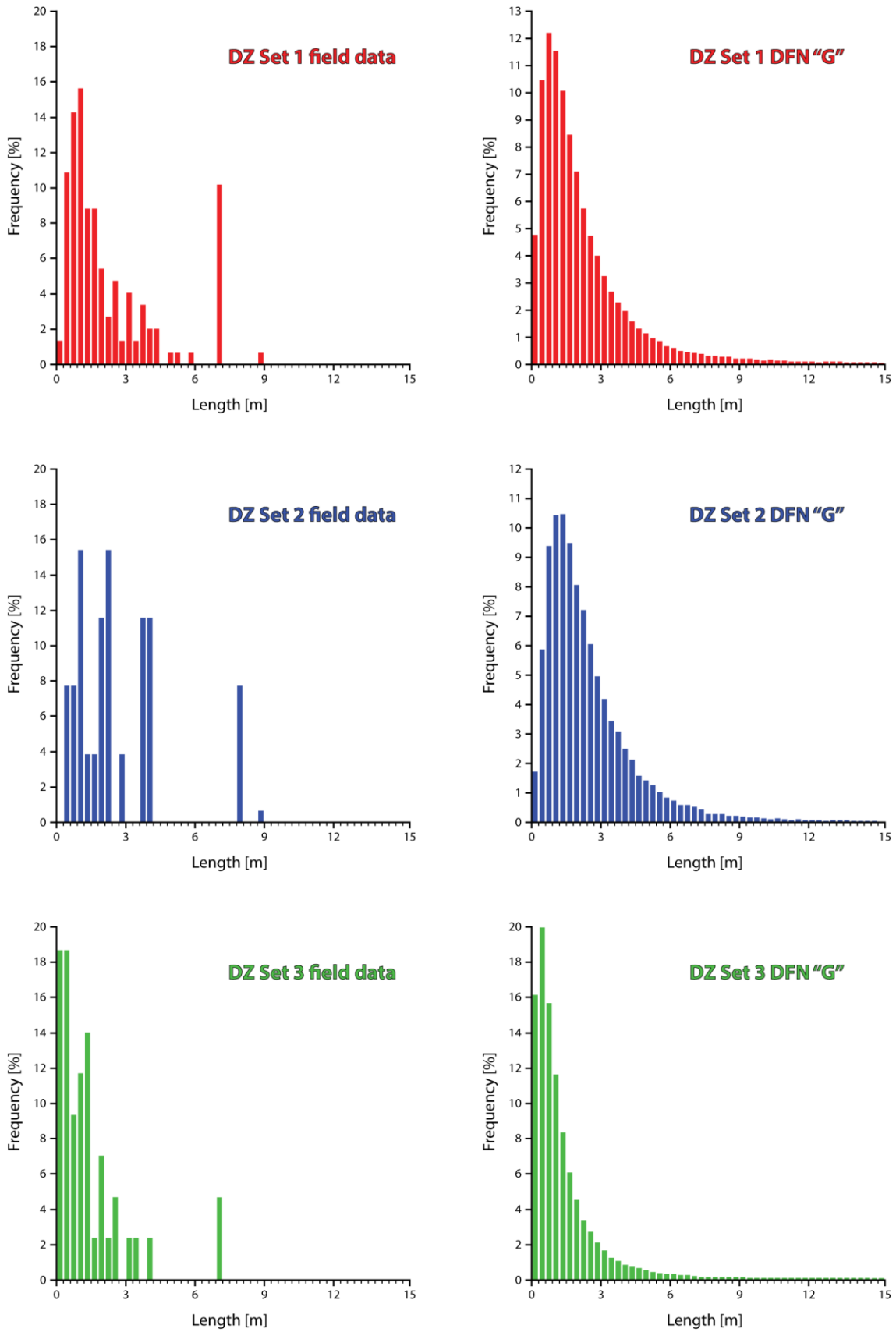


Figure 70: Comparison of the length distribution of the field data and its corresponding calculated length distribution of the DFN "G" for the DZ Sets 1, 2 and 3.

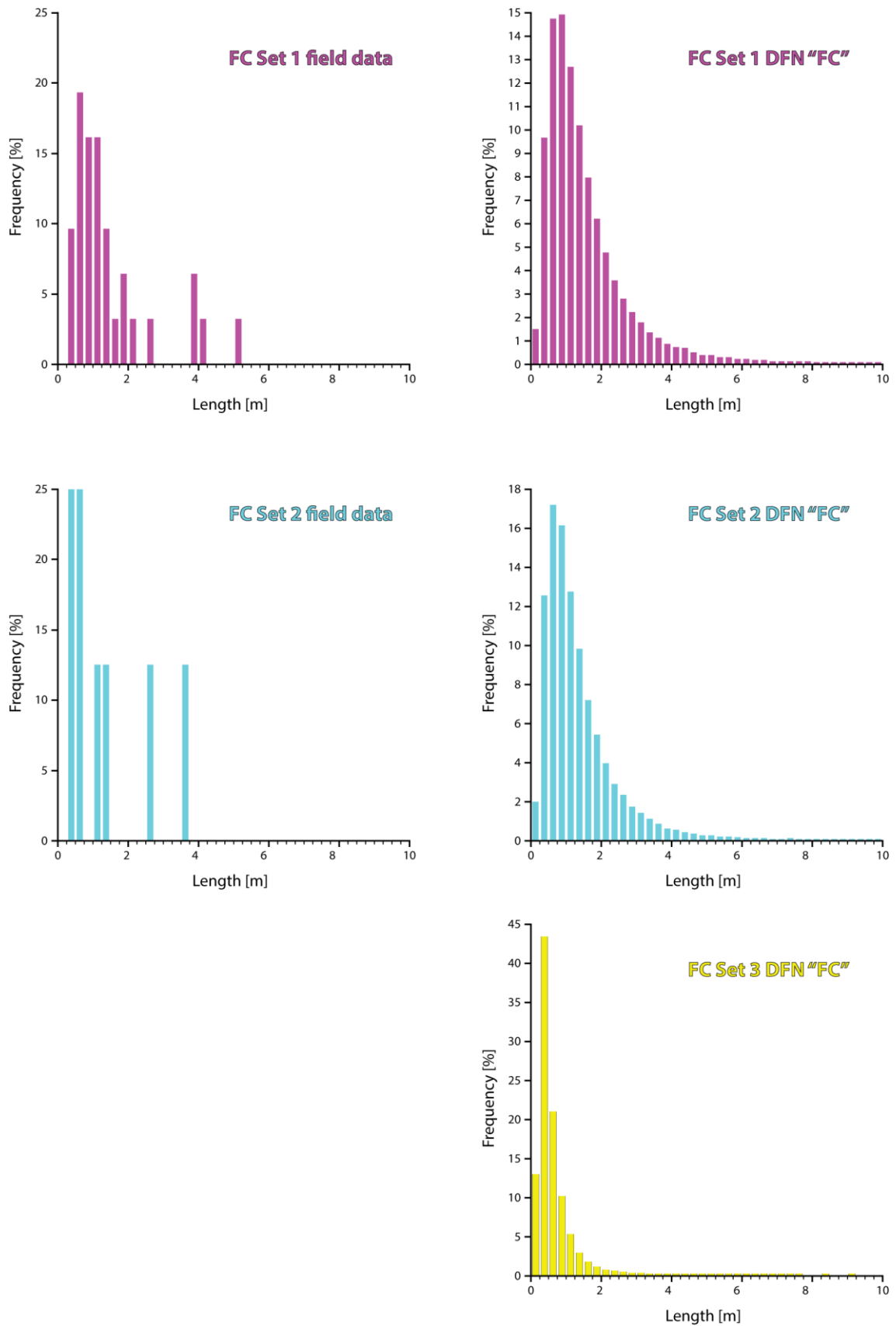


Figure 71: Comparison of the length distribution of the field data and its corresponding calculated length distribution of the DFN "FC" for the FC Sets 1, 2. Because no length data were available for FC Set 3, values were derived from aperture data (see text).

The  $P_{32}$  **fracture intensity** was calculated based on the scanline information provided by the project partners. The reasonability of the resultant mean values of 1.7-2.5  $\text{m}^2/\text{m}^3$  for the DZ and 4.4-10.3  $\text{m}^2/\text{m}^3$  for the FC are corroborated by Volatili et al. (2019) and Parrino et al. (2019), who reported from other areas  $P_{32}$  values of 2.08–11.84  $\text{m}^2/\text{m}^3$  and 0.81-10.90  $\text{m}^2/\text{m}^3$ , respectively. The higher  $P_{32}$  values in the FC result from the nature of its environment. A FC constitutes the zone of most displacement (Caine et al., 1996) and a thick core zone shows parts with higher fracture intensity values. Different from other studies is the method to not distribute the  $P_{32}$  fracture intensity over the whole FC geobody, but to omit it in FCFTs considered as non-fracture bearing. This is the case for “Sandstone unconsolidated (Su)”, “Gouge, silt unconsolidated (Gs)”, and “Gouge, clay unconsolidated (Gc)”.

The aperture and intensity constitute the most important parameters regarding upscaled fracture properties and subsequent fluid flow simulations, followed by the fracture length (Ghosh et al., 2018; Liu et al., 2018). It is of utmost importance to lay special emphasis on these parameters. The encountered challenge during the parametrization of the DZ and FC fracture sets within this thesis demonstrates the importance of thorough preceding field work in order to facilitate DFN models as close to nature as possible. Although more data, especially from the FC, would have been desirable, the extensive parametrization carried out in the present study gives a profound base for modeling.

#### 5.4.2 Fracture Network Properties

In this subchapter the DFN properties are discussed in detail. The IFN part of the fracture network upscaled with the Oda method has nearly no impact on fracture porosity in the DZ ( $3.22 \cdot 10^{-8}$  % difference to the minimum value) and no measurable impact on the FC values. Its impact on the fracture permeability is also negligible with a difference of 0-1 D in the DZ and 2-3 D in the FC, equal to a variation of 0.14-0.19 % and 0.005-0.009 %, respectively. This is interpreted to be due to the small share of the IFN in contrast to the DFN, reasoned by the chosen minimum discrete fracture length (see chapter 3.5.1). Only the sigma factor within the FC shows a higher IFN impact, which will be discussed in the corresponding section. By discussing the different DFNs of the two geobodies DZ and FC, no additional explicit comparison of the complete DFNs “G+FC”, “T+FC”, and “Tc+FC” is necessary, as they simply represent a combination of the other DFNs.



Table 17: Mean values of the fracture network property results for the DZ and FC comprising the fracture permeability, the fracture porosity, the connectivity index (CI), and the sigma factor. FN: fracture network; PUM: permeability upscaling method; DFN: discrete fracture network; IFN: implicate fracture network. \*CI refers only to the OdaC results.

Geo-body	FN	PUM	Network type		Permeability [D]			Porosity [%]	CI	Sigma [1/m <sup>2</sup> ]
			DFN	IFN	ki	kj	kk			
DZ	G	Oda	✓	✓	497	291	658	0.38		150
		Oda	✓		497	291	659	0.38		150
		OdaC	✓		371	190	622	0.38	1.21	150
	T	Oda	✓	✓	521	332	712	0.4		162
		Oda	✓		522	332	713	0.4		162
		OdaC	✓		381	216	671	0.4	1.29	162
	Tc	Oda	✓	✓	532	345	720	0.41		166
		Oda	✓		533	345	720	0.41		166
		OdaC	✓		386	223	675	0.41	1.31	166
FC	FC	Oda	✓	✓	22,944	44,313	55,186	2.38		471
		Oda	✓		22,942	44,310	55,183	2.38		527
		OdaC	✓		14,130	29,572	51,749	2.38	2.94	527

The **fracture permeability** tensors computed through the Oda and OdaC methods are most difficult to compare, because they are affected by a variety of fracture parameters (see 3.5.2.1). Every study treats these parameters at a different scale of detail, and uses all too often constant values for parameters like the fracture aperture (Bisdom et al., 2016; Kluge et al., 2017). The different parametrization of the fracture aperture is by far the main reason for problems in the comparability of fracture permeability tensor results, as it constitutes the most important parameter for its calculation (Laux, 2017; Panza et al., 2018). This complication starts with the decision if a JRC should be applied to the mechanical aperture or not, as discussed in the previous chapter. The differences in permeability between mechanical and hydraulic aperture are of one to four orders of magnitude (e.g. Panza et al., 2018; Giuffrida et al., 2019) depending on the chosen JRC value and correlation type. This decision has therefore severe impacts on the final fracture permeability tensor results. The subsequently calculated intrinsic fracture permeability, which is conducted by the cubic law (see chapter 3.5.1), is governed by a power term on the aperture. This can lead to very large intrinsic fracture permeability values of tens of thousands or even millions of D (Lyons et al., 2016). For more information about fracture permeability the reader is referred to van Golf-Racht (1982),

Ran et al. (2014), Lyons et al. (2016), and Shojaei and Shao (2017). Rong et al. (2013) examined the impact of different fracture parameters on permeability tensors. They observed a fracture aperture change of one magnitude to result in a change of three orders of magnitude on the principal permeability. In addition, Laux (2017) analyzed the impact of fracture aperture by calculating two Oda permeability models with aperture sizes of 0.01 and 1 mm. The resultant permeability values were between 0.042 and 0.162 D and 410 and 1600 D, respectively, confirming the proportional behavior of permeability to the apertures square. To demonstrate the validity of the fracture permeability results of the own study (Table 17) and to support its comparability with other studies considering the applied aperture size, the author decided to conduct a supplementary fracture permeability calculation. Its aim was to examine: (i) the impact of aperture size change on fracture permeability, and (ii) the difference between log-normal and constant aperture size distribution in terms of fracture permeability. Table 18 lists the results of the mentioned supplementary calculation, which corroborate the statements of Rong et al. (2013) and Laux (2017). It also reveals the important finding, that the application of a log-normal fracture aperture distribution, in contrast to constant apertures values, results in fracture permeabilities larger by a factor of 4.47 to 6.44. The DZ fracture permeability results of the own study between 190 and 720 D are therefore corroborated by the aperture related permeability tests of Laux (2017). In addition, Volatili et al. (2019) conducted Oda fracture permeability calculations by applying apertures size values for a different DZ of 0.039 to 0.079 mm, comparable to the own mean aperture size values of the DZ within the presented study, although being one order of magnitude lower. The permeability tensor results of Volatili et al. (2019) are therefore comparable to the DZ results of the presented study if multiplied by 1000.

Table 18: Results of the supplementary fracture permeability and porosity calculation dependent on the aperture distribution type and the mean size. All calculation were conducted on the basis of the DFN "G" of the DZ.

Fracture distribution type	Mean aperture size [mm] of fracture set			Permeability [D]			Porosity [%]
	1	2	3	ki	kj	kk	
Log-normal	0.632	0.661	0.697	497	291	659	0.38
Log-normal	0.0632	0.0661	0.0697	0.477	0.286	0.641	0.04
Constant	0.632	0.661	0.697	77.22	63.54	116.08	0.35
Constant	0.0632	0.0661	0.0697	0.077	0.064	0.116	0.04

Applying this factor, the results of Volatili et al. (2019) show fracture permeabilities between 73 and 1133 D, corroborating the validity of the calculated fracture permeability values of the own study. As seen in Table 17, the mean permeability values of the FC (14,130 to 55,189 D) are of two orders of magnitude higher compared to the DZ values. The difference can be explained by the slightly higher mean aperture size of FC Set 3 and the significantly higher mean apertures of the FC Sets 1 and 2 compared to the mean aperture sizes of the DZ. Furthermore, the intensity values of the FC are about 2.5 to 6 times higher than in the DZ, and as stated by Laux (2017), the calculated Oda permeability is proportional to the intensity values. Taking into account the higher fracture aperture and intensity parameters the resulting FC fracture permeability is entirely comprehensible. Unfortunately, no comparable studies could be found that calculated fracture permeability tensors specifically in FC facies bodies, making the own results unique. Future studies providing this kind of information are desirable.

#### Fracture permeability $k_i$ and $k_j$ of DFN "T+FC" (OdaC)

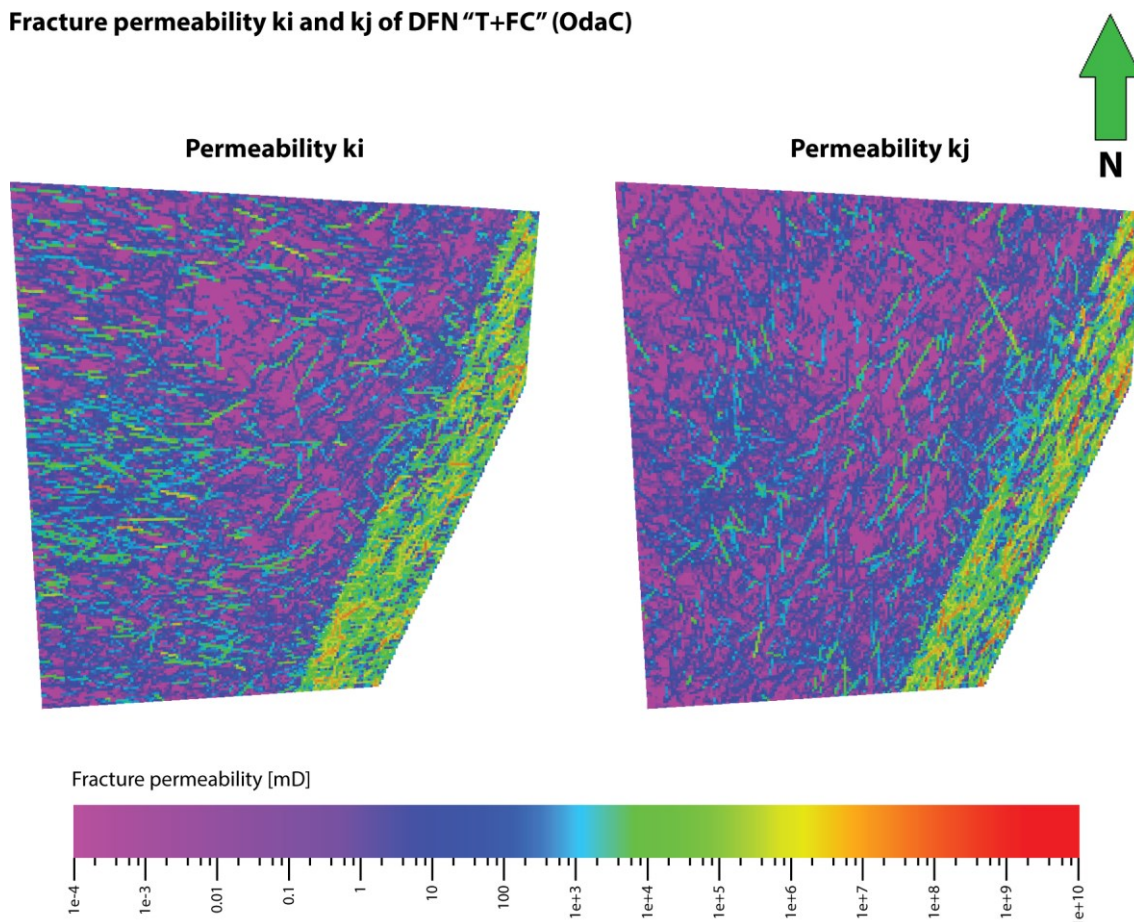


Figure 72: Comparison of the horizontal fracture permeabilities in  $i$ - and  $j$ -direction of DFN "T+FC" computed through the OdaC upscaling method showing a higher fracture connectivity in  $i$ -direction.

Comparing the horizontal fracture permeability results one observes that within the DZ the permeability in i-direction is about 54 to 95 % higher than in j-direction. Considering the nature of fault zones one expects the highest permeability to be parallel to the main slip surface. This is probably also the case within the studied outcrop, but the presented models' main slip surface does not follow exactly the i- or j-direction, meaning that the theoretical highest permeability tensor is split in both directions. The higher values in i-direction are explained by the pattern of the calculated discrete fractures, which favors the connectivity in i-direction (Figure 72). This is probably caused by the distribution of the DZ Set 2, which strikes about  $101^\circ$  and bears the highest mean fracture length. Within the FC the permeability values in j-direction are about double as high as in i-direction. This is simply due to the fact that the FC Set 1, which strikes parallel to the main slip surface, contributes most in j-direction, while showing the highest fracture intensity, aperture and length values of the three FC sets. All permeability results in vertical k-direction show 2 to 3 times higher values compared to its horizontal share. This is considered obvious as it combines the permeability of all fracture sets.

Another important fact is the impact of the fracture networks' connectivity on its permeability. This was investigated by comparing the results of the Oda method, which assumes all fractures to be connected, with the results of the OdaC method, which takes the connectivity of the fracture network into account. Applying the latter method, the permeability within the DZ is decreased by about 26 % in i-direction and 35 % in j-direction. Within the FC, the values in i-direction are reduced by 38 %, and in the j-direction by 33 %. For the DZ and FC the permeability in k-direction is equally reduced by 6 %. In fracture networks of poor interconnectivity it is therefore especially important to incorporate the fractures' connectivity. The higher the connectivity of the fractures network, the lower is the difference between computed Oda and OdaC permeabilities. This is confirmed by Laux (2017) who examined the impact of fracture connectivity on permeability. In the own research, the permeability values in k-direction (with the highest connectivity) is reduced only by 6 %, whereas the values of the DZ for the the worst interconnected j-direction show a difference of 35 %, and in i-direction of 26 %. This additionally confirms the previously made observation of the i-direction of the DZ being better interconnected than the j-direction (Figure 72).

The incorporation of fracture truncation on top and basis of geological units increases the fracture permeability with increased truncation percentages throughout all permeability tensors. Compared to the DFN "G" in both upscaling methods, the

### GU 10 fracture patches of DZ Set 1

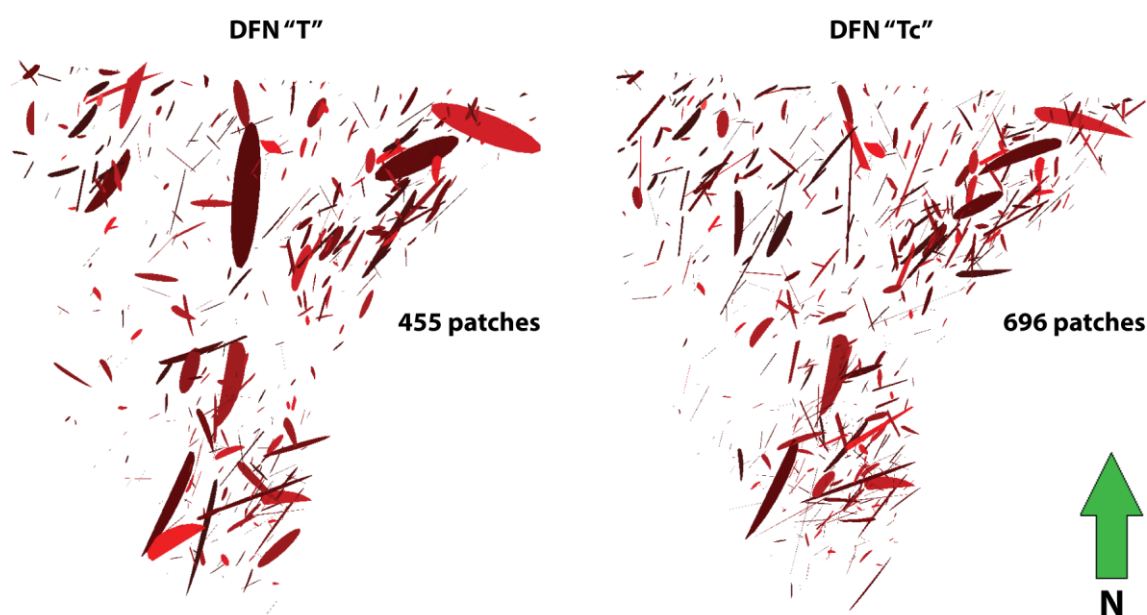


Figure 73: Comparison of the generated fracture patches of geological unit (GU) 10 of DZ Set 1 within the DFNs “T” and “Tc”. View from above.

truncated DFN “T” shows a mean permeability increase of 8 to 9 %. The DFN “Tc” with increased truncation values in turn shows an increase in fracture permeability of 2 % on the “T” values. This is contrary to the presumed decrease of fracture permeability values, because a (higher) truncation of fractures is assumed to reduce the connectivity. The author supposes that this effect is related to the defined  $P_{32}$  intensity. For explanation it is to remember that the modeling software generates fracture patches based on multiple parameters, of which the  $P_{32}$  intensity defines the area of fractures per unit volume ( $\text{m}^2/\text{m}^3$ ). By truncating and cutting fractures, smaller fracture patches are generated. However, the present  $P_{32}$  values have to be reached during modeling, which leads to more patches being generated per unit volume, which in turn leads to a higher connectivity resulting in a higher fracture permeability. This modeling effect is assumed to be the greater the smaller the thickness of geological units is. In addition, this is corroborated by the connectivity index, which increases with higher truncation percentages. Figure 73 shows an extreme example, geological unit 10 of DZ Set 1, which has an extraordinarily low thickness and spatial extent because it is strongly truncated by the over- and underlying beds. In case of the DFN “T” 455 fracture patches were generated. By applying higher truncation values (e.g. DFN “Tc”) the amount of generated patches is increased to 696. This effect shows that the truncation of fractures has to be applied with high caution, as it may lead to a distortion of fracture permeability. In order to make a precise statement whether an additional fracture truncation is reasonable or

not, or more specifically from which thicknesses of beds to apply, an additional thorough series of tests would be necessary.

The **fracture porosity** is governed by the mechanical aperture and therefore facilitates an uncomplicated comparison. The mean fracture porosity of the presented data amounts to 2.38 % in the FC and lies between 0.38 and 0.41 % within the DZ. Other studies report fracture porosity values within DZs and their surrounding rock of 0.45 to 0.47 % (Panza et al., 2018), 0.5 to 0.85 % (Giuffrida et al., 2019), 0.11 to 0.23 % (Volatili et al., 2019), and 0.6 to 1.16 % (Parrino et al., 2019). The noticeably increased porosity values of the FC are due to higher mean aperture values as compared to the DZ, however, no comparable studies with explicit FC fracture porosity values could be found. The slightly increased fracture porosity with increased fracture truncation percentages underpins the previously discussed observations, that more fracture patches are generated with more fractures truncated.

The **connectivity index** quantifies the average number of fracture intersections per fracture within a given cell and shows values between 1.21 to 1.31 in the DZ and 2.94 in the FC. The 2.5 to 6 times higher  $P_{32}$  intensity values of the FC probably caused these higher values in the FC. The increase of the connectivity index with increasing fracture truncation percentages is, as already discussed before, linked to the  $P_{32}$  intensity: more fractures patches are generated the higher the truncation values are (also see Figure 73).

The **sigma factor** is used to describe the fluid exchange between matrix and fracture and is important for subsequent fluid flow simulations (see 3.5.2.2). The calculated values of this thesis are 150 to 166 per  $m^2$  in the DZ and 471 to 527 per  $m^2$  in the FC. It is noticeable that the sigma factor shows no variability within the DZ, no matter which network arrangement is considered (DFN or DFN+IFN). However, within the FC the network type “DFN+IFN” shows a sigma factor value of about 11 % less than in the “DFN” network types. Reason might be that in the model no fractures were distributed within three FCFTs, and therefore those grid cells were not populated with  $P_{32}$  intensities, while the modeling software carries out two independent upscaling processes for each FN type (DFN and IFN) and merges the results. However, the sigma factor is of importance for potential subsequent simulations, which are not part of the presented work. The effect was not further investigated, but should be mentioned as an observation to be considered for future work. Calculations of the sigma factor by Laux (2017) showed values of 144 and 259 per  $m^2$  in his final model, corroborating the results of the presented study.

## 5.5 Implications on Reservoir Quality

The quality of a fractured reservoirs is dependent on the petrophysical matrix and fracture properties, and their interplay. These properties and their relations differ within the two separately modeled geobodies and thus have a different impact on the reservoir quality. The DZ shows matrix porosity values between 10.19 and 20.75 % and permeability values of 9.62 to 959.53 mD. This would represent a medium to high quality reservoir in terms of matrix, although low permeable beds occur within the studied outcrop. The high degree of bed amalgamation and truncation within the succession makes the presence of low permeability beds less important. Soyk (2015), who incorporated the studied outcrop in his thesis, also stated a considerable potential for a high-quality matrix reservoir of the Lower and Middle Buntsandstein present near the western flank of the URG. Haffen et al. (2015) and Böcker et al. (2016) considered the studied succession as a good reservoir for its high porosity. In addition, the accidentally discovered Römerberg oil field within the Buntsandstein near Speyer in 2003 strongly underlines its significance as a hydrocarbon reservoir. This oil field is being successfully exploited since 2008 and produced nearly 1.4 million tons of oil until 2019 (LBEG, 2019), encouraging new research within the Buntsandstein (Böcker et al., 2016). Within the FC the matrix porosity and permeability values (9 to 55 % and 0.01 to 1000 mD) show a wide scatter, it could therefore form a barrier or a pathway for flow. Which setting is present strongly depends on the FC architecture and FCFT distribution. While keeping the matrix potential in mind, one should be aware that the main flow pathways in a fractured reservoir are usually given by fractures, provided that they are open. The effect of mineralization on the fracture network properties cannot be incorporated in the DFN modeling. Mineralization is taken into account in subsequent simulation steps, which are not part of the presented thesis. However, in case of the studied outcrop, Bauer et al. (2015) reported most fractures to remain open, which was additionally confirmed by Soyk (2015) who found most observed fractures non- or hardly mineralized. In case of the DZ the succession bears a high potential for geothermal production, as also assumed by Soyk (2015). Fluid pathways within the FC, on the other hand, depend strongly on the FC architecture and FCFT distribution, as not every FCFT comprises fractures in its matrix. Figure 74 shows the three modeled FCFT distribution cases, underlining the severe impact of this modeling decision. The facies bodies of case A have elongation values of 10-25 m parallel to the main slip surface, while the case B shows elongation values of 25-50 m and case C >50 m. It is obvious that the probability of the FC to act as a fluid barrier perpendicular to the main slip surface rises significantly

with increased elongation values of the facies bodies. A validation of this assumption would require a subsequent simulation of fluid pathways through the FC, which is not part of the presented study. However, Qu et al. (2017) constructed models with different fault facies distributions comparable to the ones in Figure 74 to investigate exactly this problem. According to these authors cases with higher elongation values parallel to the main slip surface (like case C) show much lower oil recovery and lower water cut than cases with smaller elongations (like case A), corroborating the previously made assumptions by this author. Case B has been used within the own work for further modeling steps. It is assumed to constitute a compound of fluid barriers and flow paths. This assumption is in accordance with Bauer et al. (2015) who tried to classify the studied outcrop after schemes of Caine et al. (1996) and Rawling et al. (2001). Their conclusion was, that both of these fault zone models are not applicable and the FC itself represents a combined conduit-barrier system, which corresponds to the most likely setting after the own modeling.

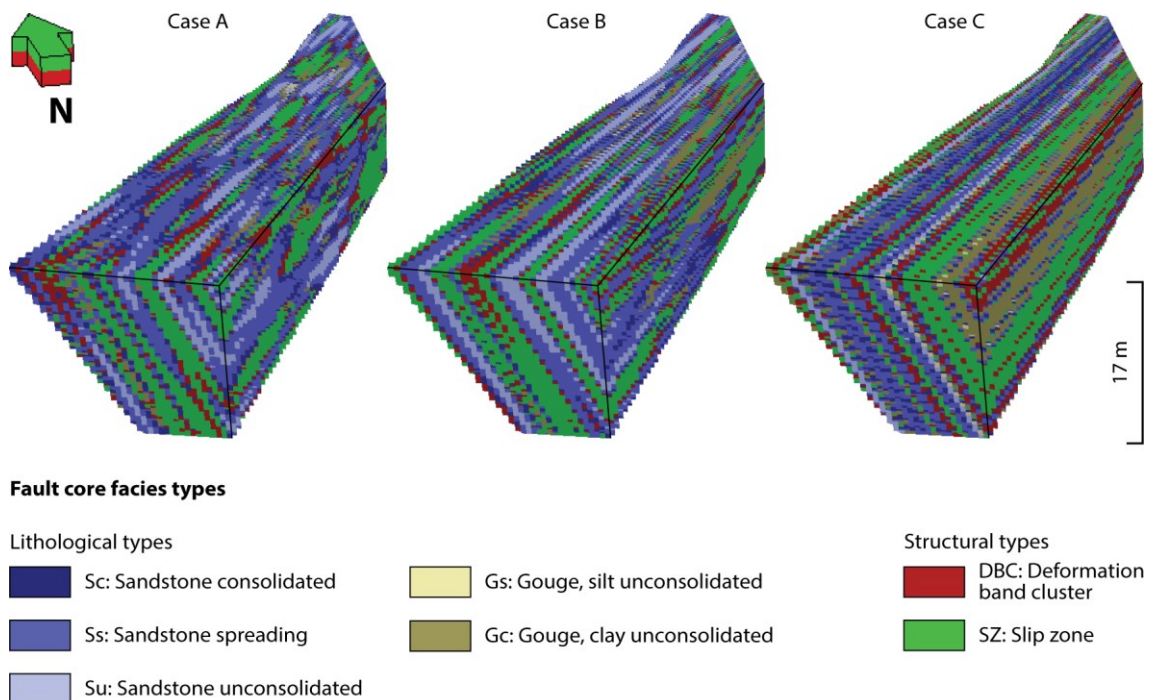


Figure 74: Illustration of the three distribution cases of the FC facies bodies of the presented study. Case B has been used for the final model. No fractures have been distributed within the FCFTs "Su", "Gs", and "Gc" making them impermeable in terms of fracture permeability.



## 6 Conclusion

The presented work constitutes the first multi-approach modeling study of a real fault zone combining: (i) terrestrial laser scanning, (ii) fault facies modeling, (iii) volumetric fault zone modeling, and (iv) discrete fracture network modeling. The results highlight (i) the currently existing challenges and limitations, but (ii) show also exciting possibilities for modeling real fault zones, and (iii) last not least reveal the specific importance of fault zones on strategies for geothermal or hydrocarbon exploration.

The studied outcrop represents a braided river succession consisting predominantly of fine- to medium-grained sandstones deposited in an arid to very arid environment with a distance of about 150 km to the primary source area of the clastic sediment, the Armorican Massif in the WSW. The depositional area was characterized by a high degree of erosion and channel amalgamation. The sandstones formed primarily under flow velocities belonging to the upper part of the lower flow regime and the transition to the upper flow regime with water depths of several to 10 m. Deposition took place during a transitional period from decreasing to increasing realized accommodation (after the sequence stratigraphic concept of genetic units). The sedimentary area belonged to the lower part of a genetic unit from braided rivers within an arid alluvial plain (Bourquin et al., 2009), deposited according to the latter authors during a time interval from tens to hundreds of thousands of years. It is located at the main fault of the western Rhine Graben within the Hochwald Horst of the Saverne fracture field. The fault is planar oblique-slip with a displacement of about 1000 m (Doebel, 1967; Doebel and Olbrecht, 1974; Eisbacher and Fielitz, 2010).

To develop a volumetric fault zone model it is inevitable to apply a fault zone facies concept. The scope of this concept depends strongly on the dimension of the studied fault zone, its morphology, and the geobodies considered (protolith, damage zone, fault core). The elaboration of this fault zone facies model has to take place simultaneously to, and under consideration of the construction of the applied grid. Grids with pillar faults bear the possibility to export locally refined grids, handle them separately, and import them thereafter, but lack the possibility of high complexity. Grids with stair-step faults are practically insensitive to complexity but cannot include separately modeled locally refined grids leading to a reduced cell size flexibility. For small scale surveys stair-stepped fault grids are recommended, but have to be accompanied by a thoroughly considered choice of the cell size, dependent on the smallest geological objects within the fault zone geobodies taken into account, but also on the computational resources. It

is essential for future models to allow the combination of complex stair-stepped fault grids with locally refined grids. Lithological and petrophysical fault core data have to be collected under generally accepted procedures and schemes. This is necessary to ensure the comparability of the generated different fault zone models. In the end this might lead to a common fault zone model database.

The characterization of the fracture aperture and its processing is the most important part of the parametrization. Although the exactly same values for mechanical aperture are used, different subsequent methods can lead to distinct differences in the modeled final fracture permeabilities, spanning multiple orders of magnitude. The decision to define the aperture through an equation instead of a constant mean value increases the fracture permeability tensor by a factor of 5 to 6. In the presented study the influence of the IFN part of the fracture network is negligible. Fracture permeabilities in vertical direction are two to three times higher as in horizontal direction. In the latter, in the damage zone the values vary by 54 to 95 % dependent on the connectivity, which in turn is governed by the fracture length. Fracture permeabilities in the fault core are per se two orders of magnitude higher than in the damage zone, but are much more affected by facies bodies representing conduit barriers. The presence of such hindrances is strongly dependent on the fault core architecture and the elongation of facies bodies parallel to the main slip surface. Fracture porosity in the fault core is six times higher than in the damage zone. A significant difference in the permeability tensor results was observed by comparing the Oda and OdaC upscaling methods. Horizontal permeability values of the OdaC computations were decreased by 26 to 38 % compared to the Oda results, in vertical direction by 6 %. This reflects the impact of the fracture network connectivity considered in OdaC. The smaller the connectivity, the greater is the difference between the results regarding the permeability tensors of the Oda and OdaC methods. Within the damage zone, the implementation of fractures truncated at the geological units' tops and bases increased the fracture network permeabilities if higher truncation percentages were introduced. The increase of the truncated DFNs in comparison to the untruncated ones amounts to about 10 % on average. This effect is the greater the smaller the thickness of geological units is, as reasoned by the  $P_{32}$  intensity parameter. It is advised to utilize the possibility of truncation with caution as it may be counterproductive within models with low bed thicknesses. If fracture porosities are compared with fracture permeabilities, the former are more insensitive to parameter changes, because of the dependence on the width of the mechanical aperture.

## 7 References

- Adler, P.M., Thovert, J.-F., Mourzenko, V.V., 2012. *Fractured Porous Media*, Oxford University Press, Oxford, 184 pp.
- Agada, S., Chen, F., Geiger, S., Toigulova, G., Agar, S., Shekhar, R., Benson, G., Hehmeyer, O., Amour, F., Mutti, M., 2014. Numerical simulation of fluid-flow processes in a 3D high-resolution carbonate reservoir analogue, *Petroleum Geoscience*, 20 (1), p. 125-142.
- Agar, S.M., Geiger, S., 2015. Fundamental controls on fluid flow in carbonates: current workflows to emerging technologies, *In: Agar, S.M., Geiger, S. (Eds.), Fundamental Controls on Fluid Flow in Carbonates - Current Workflows to Emerging Technologies*, Geological Society, London, Special Publications, 406, p. 1-59.
- Agosta, F., Alessandrini, M., Antonellini, M., Tondi, E., Giorgioni, M., 2010. From fractures to flow: a field-based quantitative analysis of an outcropping carbonate reservoir, *Tectonophysics*, 490 (3), p. 197-213.
- Ahmed-Elfeel, M., Couples, G., Geiger, S., Ma, J., 2010. Upscaled multi-phase flow properties of fracture corridors, *SPE Caspian Carbonates Technology Conference*, 8-10 November, 14 pp.
- Ahmed-Elfeel, M., Geiger, S., 2012. Static and dynamic assessment of DFN permeability upscaling, *SPE Europe/EAGE Annual Conference*, 4-7 June, 16 pp.
- Aigner, T., Bachmann, G.H., 1992. Sequence-stratigraphic framework of the German Triassic, *Sedimentary Geology*, 80 (1), p. 115-135.
- Al-Busafi, B., Fisher, Q.J., Harris, S.D., 2005. The importance of incorporating the multi-phase flow properties of fault rocks into production simulation models, *Marine and Petroleum Geology*, 22 (3), p. 365-374.
- Aler, J., Du Mouza, J., Arnould, M., 1996. Measurement of the fragmentation efficiency of rock mass blasting and its mining applications, *International Journal of Rock Mechanics and Mining Sciences & Geomechanics Abstracts*, 33 (2), p. 125-139.
- Alexander, J., 1993. A discussion on the use of analogues for reservoir geology, *In: Ashton, M. (Ed.), Advances in Reservoir Geology*, Geological Society, London, Special Publications, 69, p. 175-194.
- Alexander, J., Bridge, J.S., Cheel, R.J., Leclair, S.F., 2001. Bedforms and associated sedimentary structures formed under supercritical water flows over aggrading sand beds, *Sedimentology*, 48 (1), p. 133-152.

- Allen, J.R.L., 1964. Studies in fluvial sedimentation: six cyclothems from the Lower Old Red Sandstone, Anglowelsh Basin, *Sedimentology*, 3 (3), p. 163-198.
- Allen, J.R.L., 1982. *Developments in Sedimentology: Sedimentary Structures, Their Character and Physical Basis Volume 1*, Elsevier, Amsterdam, 592 pp.
- Allmendinger, R.W., 2018. Stereonet 10.0 - Stereonet Help, R. W. Allmendinger, Ithaca, 32 pp.
- Allmendinger, R.W., Cardozo, N., Fisher, D.M., 2011. *Structural Geology Algorithms: Vectors and Tensors*, Cambridge University Press, Cambridge, 302 pp.
- Anderle, H.J., 1987. The evolution of the South Hunsrück and Taunus borderzone, *Tectonophysics*, 137 (1-4), p. 101-114.
- Andreae, A., Benecke, E.W., Schumacher, E., van Werveke, L., 1892. *Erläuterungen zur geologischen Spezialkarte von Elsass-Lothringen, Blatt Weissenburg (No 42)*, Verlag der Strassburger Druckerei und Verlagsanstalt, Strassburg, 90 pp.
- Antonellini, M., Aydin, A., 1994. Effect of faulting on fluid flow in porous sandstones: petrophysical properties, *American Association of Petroleum Geologists Bulletin*, 78 (3), p. 355-377.
- Antonellini, M., Aydin, A., Orr, L., 1999. Outcrop-aided characterization of a faulted hydrocarbon reservoir: Arroyo Grande oil field, California, USA, *In: Haneberg, W.C., Mozley, P.S., Moore, J.C., Goodwin, L.B. (Eds.), Faults and Subsurface Fluid Flow in the Shallow Crust*, American Geophysical Union, Washington, p. 7-26.
- Asghari, O., Soltani, F., Amnieh, H.B., 2009. The comparison between Sequential Gaussian Simulation (SGS) of Choghart ore deposit and geostatistical estimation through ordinary kriging, *Australian Journal of Basic and Applied Sciences*, 3 (1), p. 330-341.
- Aydin, A., 1978. Small faults formed as deformation bands in sandstone, *In: Byerlee, J.D., Wyss, M. (Eds.), Rock Friction and Earthquake Prediction*, Springer, Basel, p. 913-930.
- Aydin, A., Johnson, A.M., 1978. Development of faults as zones of deformation bands and as slip surfaces in sandstones, *In: Byerlee, J.D., Wyss, M. (Eds.), Rock Friction and Earthquake Prediction*, Springer, Basel, p. 931-942.
- Bachmann, G.H., Beutler, G., Hagdorn, H., Hauschke, N., 1999. Stratigraphie der germanischen Trias, *In: Hauschke, N., Wilde, V. (Eds.), Trias - Eine ganz andere Welt: Mitteleuropa im frühen Erdmittelalter*, Pfeil Verlag, München, p. 81-104.
- Backhaus, E., 1974. Limnische und fluviale Sedimentation im südwestdeutschen Buntsandstein, *Geologische Rundschau*, 63 (3), p. 925-942.

- Backhaus, E., Reul, K., 1971. Der Mittlere und Obere Buntsandstein im Bereich der Rhön-Schwelle, Notizblätter des hessischen Landesamtes für Bodenforschung, 99, p. 142-192.
- Baecher, G.B., 1983. Statistical analysis of rock mass fracturing, Journal of the International Association for Mathematical Geology, 15 (2), p. 329-348.
- Baecher, G.B., Lanney, N.A., Einstein, H.H., 1977. Statistical description of rock properties and sampling, The 18th US Symposium on Rock Mechanics (USRMS), 22-24 June pp.
- Barenblatt, G.I., Zheltov, I.P., Kochina, I.N., 1960. Basic concepts in the theory of seepage of homogeneous liquids in fissured rocks, Journal of Applied Mathematics and Mechanics, 24 (5), p. 1286-1303.
- Bartz, J., 1974. Die Mächtigkeit des Quartärs im Oberrheingraben, *In: Illies, J., Fuchs, K. (Eds.), Approaches to Taphrogenesis: Proceedings of an International Rift Symposium held in Karlsruhe April 13-15, 1972*, Schweizerbart, Stuttgart, p. 78-87.
- Bastesen, E., Braathen, A., 2010. Extensional faults in fine grained carbonates – analysis of fault core lithology and thickness–displacement relationships, Journal of Structural Geology, 32 (11), p. 1609-1628.
- Bastesen, E., Braathen, A., Skar, T., 2013. Comparison of scaling relationships of extensional fault cores in tight carbonate and porous sandstone reservoirs, Petroleum Geoscience, 19 (4), p. 385-398.
- Bauer, J.F., 2018. On the significance and predictability of geological parameters in the exploration for geothermal energy, Doctoral Thesis, Georg-August-Universität Göttingen, Göttingen, 162 pp.
- Bauer, J.F., Krumbholz, M., Meier, S., Tanner, D.C., 2017. Predictability of properties of a fractured geothermal reservoir: the opportunities and limitations of an outcrop analogue study, Geothermal Energy, 5 (1), p. 24.
- Bauer, J.F., Meier, S., Philipp, S.L., 2015. Architecture, fracture system, mechanical properties and permeability structure of a fault zone in Lower Triassic sandstone, Upper Rhine Graben, Tectonophysics, 647-648, p. 132-145.
- Bear, J., 1972. Dynamics of Fluids in Porous Media, American Elsevier Publishing Company, New York, 757 pp.
- Belfield, W.C., Sovich, J.P., 1995. Fracture statistics from horizontal wellbores, Journal of Canadian Petroleum Technology, 34 (6), p. 47-50.

- Bellian, J.A., Kerans, C., Jennette, D.C., 2005. Digital outcrop models: applications of terrestrial scanning lidar technology in stratigraphic modeling, *Journal of Sedimentary Research*, 75 (2), p. 166-176.
- Bense, V.F., Gleeson, T., Loveless, S.E., Bour, O., Scibek, J., 2013. Fault zone hydrogeology, *Earth-Science Reviews*, 127, p. 171-192.
- Benson, G.S., Franseen, E.K., Goldstein, R.H., Li, Z., 2012. Data collection, interpretation, and geologic modeling of outcrop: Cerro La Molata, Cabo de Gata, Spain, AAPG/SPE/SEG Hedberg Research Conference "Fundamental controls on flow in carbonates", 8-13 July 2012, 6 pp.
- Berg, S.S., Øian, E., 2007. Hierarchical approach for simulating fluid flow in normal fault zones, *Petroleum Geoscience*, 13 (1), p. 25-35.
- Berger, J.P., 2002. Eocene-Pliocene time scale, stratigraphy and terrace dating, *In: Ziegler, P., Dèzes, P. (Eds.), Abstract Volume to 2nd EUCOR-URGENT Workshop in Mt. St. Odile, France, EUCOR-URGENT Project, Mt. St. Odile*, p. 5.
- Bergerat, F., 1985. Déformations cassantes et champs de contrainte tertiaires dans la plateforme européenne, *Doctoral Thesis, Université Pierre et Marie Curie, Paris*, 364 pp.
- Bergerat, F., 1987. Stress fields in the European platform at the time of Africa-Eurasia collision, *Tectonics*, 6 (2), p. 99-132.
- Berkowitz, B., 2002. Characterizing flow and transport in fractured geological media: a review, *Advances in Water Resources*, 25 (8-12), p. 861-884.
- Best, D.J., Fisher, N.I., 1981. The BIAS of the maximum likelihood estimators of the von Mises-Fisher concentration parameters, *Communications in Statistics-Simulation and Computation*, 10 (5), p. 493-502.
- Beutler, G., 1991. Zur Frage der Eichsfeld-Schwelle im Keuper, *Zeitschrift für Geologische Wissenschaften*, 19 (1), p. 79-89.
- Beutler, G., Szulc, J., 1999. Die paläogeographische Entwicklung des Germanischen Beckens in der Trias und die Verbindung zur Tethys, *In: Hauschke, N., Wilde, V. (Eds.), Trias - Eine ganz andere Welt: Mitteleuropa im frühen Erdmittelalter*, Pfeil Verlag, München, p. 71-80.
- Bingham, C., 1964. Distributions on the Sphere and on the Projective Plane, *Unpublished Doctoral Thesis, Yale University, New Haven*, 93 pp.
- Bingham, C., 1974. An antipodally symmetric distribution on the sphere, *The Annals of Statistics*, 2 (6), p. 1201-1225.

- Bisdom, K., Bertotti, G., Nick, H.M., 2016. The impact of in-situ stress and outcrop-based fracture geometry on hydraulic aperture and upscaled permeability in fractured reservoirs, *Tectonophysics*, 690, p. 63-75.
- Bisdom, K., Gauthier, B.D.M., Bertotti, G., Hardebol, N.J., 2014. Calibrating discrete fracture-network models with a carbonate three-dimensional outcrop fracture network: implications for naturally fractured reservoir modeling, *American Association of Petroleum Geologists Bulletin*, 98 (7), p. 1351-1376.
- Blodgett, R.H., Stanley, K.O., 1980. Stratification, bedforms, and discharge relations of the Platte braided river system, Nebraska, *Journal of Sedimentary Research*, 50 (1), p. 139-148.
- Böcker, J., Littke, R., Forster, A., 2016. An overview on source rocks and the petroleum system of the central Upper Rhine Graben, *International Journal of Earth Sciences*, 106 (2), p. 707-742.
- Boguchwal, L.A., Southard, J.B., 1990. Bed configurations in steady unidirectional water flows. Part 2. Synthesis of flume data, *Journal of Sedimentary Research*, 60 (5), p. 658-679.
- Bohnenstiehl, D.R., Kleinrock, M.C., 1999. Faulting and fault scaling on the median valley floor of the trans-Atlantic geotraverse (TAG) segment, ~ 26°N on the Mid-Atlantic Ridge, *Journal of Geophysical Research: Solid Earth*, 104 (B12), p. 29351-29364.
- Boigk, H., 1959. Zur Gliederung und Fazies des Buntsandsteins zwischen Harz und Emsland, *Geologisches Jahrbuch*, 76, p. 597-636.
- Bonnet, E., Bour, O., Odling, N.E., Davy, P., Main, I., Cowie, P., Berkowitz, B., 2001. Scaling of fracture systems in geological media, *Reviews of geophysics*, 39 (3), p. 347-383.
- Boro, H., Rosero, E., Bertotti, G., 2014. Fracture-network analysis of the Latemar Platform (northern Italy): integrating outcrop studies to constrain the hydraulic properties of fractures in reservoir models, *Petroleum Geoscience*, 20 (1), p. 79-92.
- Borradaile, G.J., 2013. *Statistics of Earth Science Data: Their Distribution in Time, Space and Orientation*, Springer Verlag, Berlin, Heidelberg, 351 pp.
- Bossennec, C., Géraud, Y., Moretti, I., Mattioni, L., Stemmelen, D., 2018. Pore network properties of sandstones in a fault damage zone, *Journal of Structural Geology*, 110, p. 24-44.
- Botter, C., Cardozo, N., Qu, D., Tveranger, J., Kolyukhin, D., 2017. Seismic characterization of fault facies models, *Interpretation*, 5 (4), p. SP9-SP26.

- Bourquin, S., Durand, M., Diez, J.B., Broutin, J., Fluteau, F., 2007. The Permian-Triassic boundary and Lower Triassic sedimentation in the Western European basins: an overview, *Journal of Iberian Geology*, 33 (2), p. 221-236.
- Bourquin, S., Guillocheau, F., Péron, S., 2009. Braided rivers within an arid alluvial plain (example from the Lower Triassic, western German Basin): recognition criteria and expression of stratigraphic cycles, *Sedimentology*, 56 (7), p. 2235-2264.
- Bourquin, S., Peron, S., Durand, M., 2006. Lower Triassic sequence stratigraphy of the western part of the Germanic Basin (west of Black Forest): fluvial system evolution through time and space, *Sedimentary Geology*, 186 (3-4), p. 187-211.
- Bourquin, S., Rigollet, C., Bourges, P., 1998. High-resolution sequence stratigraphy of an alluvial fan-fan delta environment: stratigraphic and geodynamic implications—an example from the Keuper Chaunoy Sandstones, Paris Basin, *Sedimentary Geology*, 121 (3-4), p. 207-237.
- Braathen, A., Tveranger, J., Fossen, H., Skar, T., Cardozo, N., Semshaug, S.E., Bastesen, E., Sverdrup, E., 2009. Fault facies and its application to sandstone reservoirs, *American Association of Petroleum Geologists Bulletin*, 93 (7), p. 891-917.
- Brookfield, M.E., 1992. Eolian systems, *In: Walker, R.G., James, N.P. (Eds.), Facies Models, Response to Sea Level Change*, Geological Association of Canada, St. John's, p. 143-156.
- Brun, J.P., Gutscher, M.A., 1992. Deep crustal structure of the Rhine Graben from DEKORP-ECORS seismic reflection data: a summary, *Tectonophysics*, 208 (1-3), p. 139-147.
- Bryant, I., Carr, D., Cirilli, P., Drinkwater, N., McCormick, D., Tilke, P., Thurmond, J., 2000. Use of 3D digital analogues as templates in reservoir modelling, *Petroleum Geoscience*, 6 (2), p. 195-201.
- Bryant, I.D., Flint, S.S., 1993. Quantitative clastic reservoir geological modelling: problems and perspectives, *In: Flint, S.S., Bryant, I.D. (Eds.), The Geological Modelling of Hydrocarbon Reservoirs and Outcrop Analogues*, Blackwell Scientific Publications, Oxford, p. 3-20.
- Buck, S.G., 1983. The Saaiplaas Quartzite Member: a braided system of gold- and uranium-bearing channel placers within the Proterozoic Witwatersrand Supergroup of South Africa, *In: Collinson, J.D., Lewin, J. (Eds.), Modern and Ancient Fluvial Systems*, International Association of Sedimentologists, Oxford, Special Publication 6, p. 549-562.



- Buckley, S.J., Howell, J.A., Enge, H.D., Kurz, T.H., 2008. Terrestrial laser scanning in geology: data acquisition, processing and accuracy considerations, *Journal of the Geological Society*, 165 (3), p. 625-638.
- Buness, H., Gabriel, G., Ellwanger, D., 2008. The Heidelberg Basin drilling project: geophysical pre-site surveys, *E&G Quaternary Science Journal*, 57, p. 338-366.
- Byerlee, J.D., 1993. Model for episodic flow of high-pressure water in fault zones before earthquakes, *Geology*, 21 (4), p. 303-306.
- Caine, J.S., Evans, J.P., Forster, C.B., 1996. Fault zone architecture and permeability structure, *Geology*, 24 (11), p. 1025-1028.
- Call, R.D., Savely, J.P., Nicholas, D.E., 1976 of Conference. Estimation of joint set characteristics from surface mapping data, *The 17th US Symposium on Rock Mechanics (USRMS)*, 25-27 August, paper ARMA-76-0153.
- Cant, D.J., Walker, R.G., 1976. Development of a braided-fluvial facies model for the Devonian Battery Point Sandstone, Quebec, *Canadian Journal of Earth Sciences*, 13 (1), p. 102-119.
- Cardozo, N., Allmendinger, R.W., 2013. Spherical projections with OSX Stereonet, *Computers & Geosciences*, 51, p. 193-205.
- Cassinis, G., Durand, M., Ronchi, A., 2007. Remarks on the Permian-Triassic transition in Central and Eastern Lombardy (Southern Alps, Italy), *Journal of Iberian Geology*, 33 (2), p. 143-162.
- Chesnaux, R., Allen, D.M., Jenni, S., 2009. Regional fracture network permeability using outcrop scale measurements, *Engineering Geology*, 108 (3), p. 259-271.
- Chester, F.M., Logan, J.M., 1987. Composite planar fabric of gouge from the Punchbowl Fault, California, *Journal of Structural Geology*, 9 (5-6), p. 621-634.
- Childs, C., Manzocchi, T., Walsh, J.J., Bonson, C.G., Nicol, A., Schöpfer, M.P.J., 2009. A geometric model of fault zone and fault rock thickness variations, *Journal of Structural Geology*, 31 (2), p. 117-127.
- Chilingarian, G.V., 1964. Relationship between porosity, permeability, and grain size distribution of sands and sandstones, *In: van Straaten, L.M.J.U. (Ed.), Developments in Sedimentology Vol. 1, Deltaic and Shallow Marine Deposits*, Elsevier, New York, p. 71-75.

- Choi, J.-H., Edwards, P., Ko, K., Kim, Y.-S., 2016. Definition and classification of fault damage zones: a review and a new methodological approach, *Earth-Science Reviews*, 152, p. 70-87.
- Church, M., Jones, D., 1982. Channel bars in gravel-bed rivers, *In: Hey, R.D., C, B.J., Thorne, C.R. (Eds.), Gravel-Bed Rivers. Fluvial Processes, Engineering, and Management*, Wiley, Chisester, Now York, p. 291-324.
- Clark, M.B., Brantley, S.L., Fisher, D.M., 1995. Power-law vein-thickness distributions and positive feedback in vein growth, *Geology*, 23 (11), p. 975-978.
- Clemmensen, L.B., 1991. Controls on aeolian sand sheet formation exemplified by the Lower Triassic of Helgoland, *In: Barndorff-Nielsen, O.E., Willetts, B.B. (Eds.), Aeolian Grain Transport 2, The Erosional Environment*, Springer, Vienna, p. 161-170.
- Clemmensen, L.B., Abrahamsen, K., 1983. Aeolian stratification and facies association in desert sediments, Arran basin (Permian), Scotland, *Sedimentology*, 30 (3), p. 311-339.
- Clemmensen, L.B., Tirsgaard, H., 1990. Sand-drift surfaces: a neglected type of bounding surface, *Geology*, 18 (11), p. 1142-1145.
- Cloos, H., 1939. Hebung - Spaltung - Vulkanismus, *Geologische Rundschau*, 30 (6), p. 637-640.
- Cottureau, N., Garcia, M.H., Gosselin, O.R., Vigier, L., 2010. Effective fracture network permeability: comparative study of calculation methods, *SPE Europec/EAGE Annual Conference and Exhibition*, 14-17 June, 31 pp.
- Crawford, B.R., 1998. Experimental fault sealing: shear band permeability dependency on cataclastic fault gouge characteristics, *In: Coward, M.P., Johnson, H., Daltaban, T.S. (Eds.), Structural Geology in Reservoir Characterization*, Geological Society, London, Special Publications, 127, p. 83-97.
- Cross, T.A., Baker, M.R., Chapin, M.A., Clark, M.S., Gardner, M.H., Hanson, M.S., Lessenger, M.A., Little, L.D., McDonough, K.J., Sonnenfeld, M.D., 1993. Applications of high-resolution sequence stratigraphy to reservoir analysis, *In: Eschard, R., Doligez, B. (Eds.), Subsurface Reservoir Characterization from Outcrop Observations*, IFP Exploration and Production Research Conferences, Technip Editions, Paris, p. 11-33.
- Cruden, D.M., 1977. Describing the size of fractures, *International Journal of Rock Mechanics and Mining Sciences & Geomechanics Abstracts*, 14, p. 133-137.

- Cunningham, J., Cardozo, N., Townsend, C., Iacopini, D., Wærum, G.O., 2019. Fault deformation, seismic amplitude and unsupervised fault facies analysis: Snøhvit Field, Barents Sea, *Journal of Structural Geology*, 118, p. 165-180.
- Currie, B.S., 1997. Sequence stratigraphy of nonmarine Jurassic–Cretaceous rocks, central Cordilleran foreland-basin system, *Geological Society of America Bulletin*, 109 (9), p. 1206-1222.
- Dachroth, W., 1985. Fluvial sedimentary styles and associated depositional environments in the Buntsandstein west of river Rhine in Saar area and Pfalz (F.R. Germany) and Vosges (France), *In: Mader, D. (Ed.), Aspects of Fluvial sedimentation in the Lower Triassic Buntsandstein of Europe: Lecture Notes in Earth Sciences*, Springer, Berlin, Heidelberg, p. 197-248.
- Davis, G.H., 1999. *Structural Geology of the Colorado Plateau Region of Southern Utah. With Special Emphasis on Deformation Bands*, Geological Society of America, Boulder, Special Paper 342, 157 pp.
- Davis, J.C., 2002. *Statistics and Data Analysis in Geology*, Wiley, New York, 656 pp.
- Davison, C.C., Wang, C.Y., 1988. Hydrogeologic characteristics of major fracture zones in a large granite batholith of the Canadian shield, *In: Hitchon, B., Bachu, S. (Eds.), Proceedings Fourth Canadian/American Conference on Hydrogeology: Fluid Flow, Heat Transfer and Mass Transport in Fractured Rocks*, Banff, Alberta, Canada, June 21-24, National Water Well Association, Dublin, USA, p. 283.
- Dawers, N.H., Anders, M.H., 1995. Displacement-length scaling and fault linkage, *Journal of Structural Geology*, 17 (5), p. 607-614.
- de Dreuzy, J.R., Davy, P., Bour, O., 2001a. Hydraulic properties of two-dimensional random fracture networks following a power law length distribution: 1. Effective connectivity, *Water Resources Research*, 37 (8), p. 2065-2078.
- de Dreuzy, J.R., Davy, P., Bour, O., 2001b. Hydraulic properties of two-dimensional random fracture networks following a power law length distribution: 2. Permeability of networks based on lognormal distribution of apertures, *Water Resources Research*, 37 (8), p. 2079-2095.
- Delbari, M., Afrasiab, P., Loiskandl, W., 2009. Using Sequential Gaussian Simulation to assess the field-scale spatial uncertainty of soil water content, *Catena*, 79 (2), p. 163-169.
- Delouis, B., Haessler, H., Cisternas, A., Rivera, L., 1993. Stress tensor determination in France and neighbouring regions, *Tectonophysics*, 221 (3-4), p. 413-438.

- Demoulin, A., Launoy, T., Zippelt, K., 1998. Recent crustal movements in the southern Black Forest (western Germany), *Geologische Rundschau*, 87 (1), p. 43-52.
- Dershowitz, B., LaPointe, P., Eiben, T., Wei, L., 2000. Integration of discrete feature network methods with conventional simulator approaches, *SPE Reservoir Evaluation & Engineering*, 3 (2), p. 165-170.
- Dershowitz, W., La Pointe, P., Doe, T., 2004. Advances in discrete fracture network modeling, *Proceedings of the US EPA/NGWA Fractured Rock Conference, Portland*, 882-894 pp.
- Dershowitz, W.S., 1998. *FracMan Interactive Discrete Feature Data Analysis, Geometric Modeling and Exploration Simulation*, Golder Associates Inc., Seattle, 197 pp.
- Dershowitz, W.S., Herda, H.H., 1992. Interpretation of fracture spacing and intensity, *The 33th US Symposium on Rock Mechanics (USRMS)*, 3-5 June, 10 pp.
- Deschamps, A., Tivey, M., Embley, R.W., Chadwick, W.W., 2007. Quantitative study of the deformation at Southern Explorer Ridge using high-resolution bathymetric data, *Earth and Planetary Science Letters*, 259 (1-2), p. 1-17.
- Deutsch, C.V., Journel, A.G., 1998. *GSLIB Geostatistical Software Library and User'S Guide*, Oxford University Press, New York, Oxford, 384 pp.
- Dèzes, P., Schmid, S.M., Ziegler, P.A., 2004. Evolution of the European Cenozoic Rift System: interaction of the Alpine and Pyrenean orogens with their foreland lithosphere, *Tectonophysics*, 389 (1-2), p. 1-33.
- Doehl, F., 1967. The Tertiary and Pleistocene sediments of the northern and central part of the Upper Rhine Graben, *In: Rothe, J., Sauer, K. (Eds.), The Rhinegraben Progress Report 1967, Abhandlungen des Geologischen Landesamtes Baden-Württemberg, Freiburg*, p. 48-54.
- Doehl, F., 1970. Die tertiären und quartären Sedimente des südlichen Rheingrabens, *In: Illies, J., Mueller, S. (Eds.), Graben Problems: Proceedings of an International Rift Symposium held in Karlsruhe October 10-12, 1968, Schweizerbart, Stuttgart*, p. 56-66.
- Doehl, F., Olbrecht, W., 1974. An isobath map of the Tertiary base in the Rhinegraben, *In: Illies, J., Fuchs, K. (Eds.), Approaches to Taphrogenesis: Proceedings of an International Rift Symposium held in Karlsruhe April 13-15, 1972, Schweizerbart, Stuttgart*, p. 71-72.
- Doehl, F., Teichmüller, R., 1979. Zur Geologie und heutigen Geothermik im mittleren Oberrhein-Graben, *Fortschritte in der Geologie von Rheinland und Westfalen*, 27, p. 1-27.

- Dreuzy, J.R., Méheust, Y., Pichot, G., 2012. Influence of fracture scale heterogeneity on the flow properties of three-dimensional discrete fracture networks (DFN), *Journal of Geophysical Research: Solid Earth*, 117 (B11), p. 1-21.
- Drews, T., Miernik, G., Anders, K., Höfle, B., Profe, J., Emmerich, A., Bechstädt, T., 2018. Validation of fracture data recognition in rock masses by automated plane detection in 3D point clouds, *International Journal of Rock Mechanics and Mining Sciences*, 109, p. 19-31.
- Durand, M., 1978. Paléocourants et reconstitution paléogéographique: l'exemple du Buntsandstein des Vosges méridionales (Trias inférieur et moyen continental), *Sciences de la Terre*, 22 (4), p. 301-309.
- Durand, M., 2006. The problem of the transition from the Permian to the Triassic Series in southeastern France: comparison with other Peritethyan regions, *Geological Society, London, Special Publications*, 265 (13), p. 281-296.
- Edel, J.B., Fluck, P., 1989. The upper Rhenish Shield basement (Vosges, Upper Rhinegraben and Schwarzwald): main structural features deduced from magnetic, gravimetric and geological data, *Tectonophysics*, 169 (4), p. 303-316.
- Edel, J.B., Weber, K., 1995. Cadomian terranes, wrench faulting and thrusting in the central Europe Variscides: geophysical and geological evidence, *Geologische Rundschau*, 84 (2), p. 412-432.
- Ehrenberg, S.N., Nadeau, P.H., 2005. Sandstone vs. carbonate petroleum reservoirs: a global perspective on porosity-depth and porosity-permeability relationships, *American Association of Petroleum Geologists Bulletin*, 89 (4), p. 435-445.
- Eisbacher, G.H., Fielitz, W., 2010. Karlsruhe und seine Region: Nordschwarzwald, Kraichgau, Neckartal, Oberrhein-Graben, Pfälzerwald und westliche Schwäbische Alb, *Sammlung geologischer Führer Band 103*, Borntraeger, Stuttgart, 342 pp.
- Enge, H.D., Buckley, S.J., Rotevatn, A., Howell, J.A., 2007. From outcrop to reservoir simulation model: workflow and procedures, *Geosphere*, 3 (6), p. 469-490.
- Eschard, R., Lemouzy, P., Bacchiana, C., Desaubliaux, G., Parpant, J., Smart, B., 1998. Combining sequence stratigraphy, geostatistical simulations, and production data for modeling a fluvial reservoir in the Chaunoy field (Triassic, France), *American Association of Petroleum Geologists Bulletin*, 82 (4), p. 545-568.
- Esmaili, K., Hadjigeorgiou, J., Grenon, M., 2015. Capturing the complete stress-strain behaviour of jointed rock using a numerical approach, *International Journal for Numerical and Analytical Methods in Geomechanics*, 39 (10), p. 1027-1044.

- Evans, D.J., Rees, J.G., Holloway, S., 1993. The Permian to Jurassic stratigraphy and structural evolution of the central Cheshire Basin, *Journal of the Geological Society*, 150 (5), p. 857-870.
- Evans, D.L., Roberts, S.D., McCombs, J.W., Harrington, R.L., 2001. Detection of regularly spaced targets in small-footprint LIDAR data: research issues for consideration, *Photogrammetric Engineering and Remote Sensing*, 67 (10), p. 1133-1136.
- Fabuel-Perez, I., Hodgetts, D., Redfern, J., 2009. A new approach for outcrop characterization and geostatistical analysis of a low-sinuosity fluvial-dominated succession using digital outcrop models: Upper Triassic Oukaimeden Sandstone Formation, central High Atlas, Morocco, *American Association of Petroleum Geologists Bulletin*, 93 (6), p. 795-827.
- Fabuel-Perez, I., Hodgetts, D., Redfern, J., 2010. Integration of digital outcrop models (DOMs) and high resolution sedimentology - workflow and implications for geological modelling: Oukaimeden Sandstone Formation, High Atlas (Morocco), *Petroleum Geoscience*, 16 (2), p. 133-154.
- Fachri, M., Tveranger, J., Braathen, A., Røe, P., 2016. Volumetric faults in field-sized reservoir simulation models: a first case study, *American Association of Petroleum Geologists Bulletin*, 100 (5), p. 795-817.
- Fachri, M., Tveranger, J., Braathen, A., Schueller, S., 2013. Sensitivity of fluid flow to deformation-band damage zone heterogeneities: a study using fault facies and truncated Gaussian simulation, *Journal of Structural Geology*, 52, p. 60-79.
- Fachri, M., Tveranger, J., Cardozo, N., Pettersen, O., 2011. The impact of fault envelope structure on fluid flow: a screening study using fault facies, *American Association of Petroleum Geologists Bulletin*, 95 (4), p. 619-648.
- Færseth, R.B., 2006. Shale smear along large faults: continuity of smear and the fault seal capacity, *Journal of the Geological Society*, 163 (5), p. 741-751.
- Faulkner, D.R., Jackson, C.A.L., Lunn, R.J., Schlische, R.W., Shipton, Z.K., Wibberley, C.A.J., Withjack, M.O., 2010. A review of recent developments concerning the structure, mechanics and fluid flow properties of fault zones, *Journal of Structural Geology*, 32 (11), p. 1557-1575.
- Faulkner, D.R., Mitchell, T.M., Jensen, E., Cembrano, J., 2011. Scaling of fault damage zones with displacement and the implications for fault growth processes, *Journal of Geophysical Research*, 116 (B5), p. 1-11.
- Faybishenko, B., Witherspoon, P.A., Benson, S.M., 2000. *Dynamics of Fluids in Fractured Rock*, American Geophysical Union, Washington DC, 400 pp.

- Feist-Burkhardt, S., Götz, A.E., Szulc, J., Borkhataria, R., Geluk, M., Haas, J., Hornung, J., Jordan, P., Kempf, O., Michalik, J., Nawrocki, J., Reinhardt, L., Ricken, W., Röhling, H.-G., Ruffer, T., Török, Á., Zühlke, R., 2008. Triassic, *In*: McCann, T. (Ed.), *The Geology of Central Europe, Volume 2: Mesozoic and Cenozoic*, Geological Society, London, p. 749-821.
- Fielding, C.R., 2006. Upper flow regime sheets, lenses and scour fills: extending the range of architectural elements for fluvial sediment bodies, *Sedimentary Geology*, 190 (1-4), p. 227-240.
- Fielding, C.R., Webb, J.A., 1996. Facies and cyclicity of the Late Permian Bainmedart Coal Measures in the Northern Prince Charles Mountains, MacRobertson Land, Antarctica, *Sedimentology*, 43 (2), p. 295-322.
- Filomena, C.M., Stollhofen, H., 2011. Ultrasonic logging across unconformities - outcrop and core logger sonic patterns of the Early Triassic Middle Buntsandstein Hardegsen unconformity, southern Germany, *Sedimentary Geology*, 236 (3-4), p. 185-196.
- Firoozabadi, A., Thomas, L.K., 1990. Sixth SPE comparative solution project: dual-porosity simulators, *Journal of Petroleum Technology*, 42 (6), p. 710-763.
- Fisher, N.I., Lewis, T.L., Embleton, B.J.J., 1987. *Statistical Analysis of Spherical Data*, Cambridge University Press, Cambridge, 329 pp.
- Fisher, Q.J., Knipe, R.J., 2001. The permeability of faults within siliciclastic petroleum reservoirs of the North Sea and Norwegian Continental Shelf, *Marine and Petroleum Geology*, 18 (10), p. 1063-1081.
- Fisher, R.A., 1953. Dispersion on a sphere, *Proceedings of the Royal Society of London. Series A. Mathematical and Physical Sciences*, 217 (1130), p. 295-305.
- Flodin, E.A., Aydin, A., Durlofsky, L.J., Yeten, B., 2001. Representation of fault zone permeability in reservoir flow models, *SPE Annual Technical Conference and Exhibition*, 10 pp.
- Forster, C.B., Evans, J.P., 1991. Hydrogeology of thrust faults and crystalline thrust sheets: results of combined field and modeling studies, *Geophysical Research Letters*, 18 (5), p. 979-982.
- Fossen, H., Hesthammer, J., 2000. Possible absence of small faults in the Gullfaks Field, northern North Sea: implications for downscaling of faults in some porous sandstones, *Journal of Structural Geology*, 22 (7), p. 851-863.
- Fossen, H., Schultz, R.A., Shipton, Z.K., Mair, K., 2007. Deformation bands in sandstone: a review, *Journal of the Geological Society*, 164 (4), p. 755-769.

- Foxford, K.A., Garden, I.R., Guscott, S.C., Burley, S.D., Lewis, J.J.M., Walsh, J.J., Watterson, J., 1996. The field geology of the Moab fault, *In: Huffman Jr., A.C., Lund, W.R., Godwin, L.H. (Eds.), Geology and Resources of the Paradox Basin, 1996 Special Symposium, Guidebook 25, Utah Geological Association, Salt Lake City, p. 265-283.*
- Frank, T., Tertois, A.-L., Mallet, J.-L., 2007. 3D-reconstruction of complex geological interfaces from irregularly distributed and noisy point data, *Computers & Geosciences, 33 (7), p. 932-943.*
- Fredman, N., Tveranger, J., Cardozo, N., Braathen, A., Soleng, H., Roe, P., Skorstad, A., Syversveen, A.R., 2008. Fault facies modeling: technique and approach for 3-D conditioning and modeling of faulted grids, *American Association of Petroleum Geologists Bulletin, 92 (11), p. 1457-1478.*
- Fröhlich, C., Mettenleiter, M., 2004. Terrestrial laser scanning - new perspectives in 3D surveying, *In: Thies, M., Koch, B., Spiecker, H., Weinacker, H. (Eds.), ISPRS WG VIII/2 Workshop, Laser-Scanners for Forest and Landscape Assessment, International Archives of Photogrammetry, Remote Sensing and Spatial Information Sciences, Freiburg, p. 7-13.*
- Füchtbauer, H., 1967. Der Einfluss des Ablagerungsmilieus auf die Sandsteindiagenese im Mittleren Buntsandstein, *Sedimentary Geology, 1, p. 159-179.*
- Gabrielsen, R.H., Braathen, A., Kjemperud, M., Valdresbråten, M.L.R., 2017. The geometry and dimensions of fault-core lenses, *In: Childs, C., Holdsworth, R.E., Jackson, C.A.L., Manzocchi, T., Walsh, J.J., Yielding, G. (Eds.), The Geometry and Growth of Normal Faults, Geological Society, London, Special Publications, 439, p. 249-269.*
- Gale, J.E., 1987. Comparison of coupled fracture deformation and fluid flow models with direct measurements of fracture pore structure and stress-flow properties, *The 28th US Symposium on Rock Mechanics (USRMS), 29 June-1 July, 1213-1222 pp.*
- Galloway, W.E., Williams, T.A., 1991. Sediment accumulation rates in time and space: paleogene genetic stratigraphic sequences of the northwestern Gulf of Mexico basin, *Geology, 19 (10), p. 986-989.*
- Garven, G., Appold, M.S., Toptygina, V.I., Hazlett, T.J., 1999. Hydrogeologic modeling of the genesis of carbonate-hosted lead-zinc ores, *Hydrogeology Journal, 7 (1), p. 108-126.*
- Geluk, M.C., 2005. Stratigraphy and tectonics of Permo-Triassic basins in the Netherlands and surrounding areas, *Doctoral Thesis, Utrecht University, Utrecht, 171 pp.*



- Geluk, M.C., Röhling, H.G., 1997. High-resolution sequence stratigraphy of the Lower Triassic "Buntsandstein" in the Netherlands and northwestern Germany, *Geologie en Mijnbouw*, 76 (3), p. 227-246.
- GeORG-Projektteam, 2013. Geopotenziale des tieferen Untergrundes im Oberrheingraben - Teil 2: Geologische Ergebnisse und Nutzungsmöglichkeiten, Landesamt für Geologie, Rohstoffe und Bergbau, Freiburg i. Br., 346 pp.
- German Stratigraphic Commission, 2016. Stratigraphic Table of Germany 2016, Editing, coordination and layout: Menning, M. and Hendrich, A., German Research Centre for Geosciences, Potsdam, (1) Table plain 100x141 cm, (2) Table folded A4.
- Gexcel, 2010a. 3 Pre-processing and editing, *In: Gexcel (Ed.), JRC 3D Reconstructor Tutorial*, Gexcel, Brescia, p. 17.
- Gexcel, 2010b. 4 Registration, *In: Gexcel (Ed.), JRC 3D Reconstructor Tutorial*, Gexcel, Brescia, p. 17.
- Gexcel, 2010c. 5 Meshing and mesh editing, *In: Gexcel (Ed.), JRC 3D Reconstructor Tutorial*, Gexcel, Brescia, p. 15.
- Gexcel, 2010d. B36 Camera calibration and orientation, *In: Gexcel (Ed.), JRC 3D Reconstructor Tutorial*, Gexcel, Brescia, p. 4.
- Gexcel, 2012. JRC Reconstructor 2, Version 2.8.1.272, Gexcel, Brescia, Italy, <https://gexcel.it>.
- Ghahfarokhi, P.K., 2017. The structured gridding implications for upscaling model discrete fracture networks (DFN) using corrected Oda's method, *Journal of Petroleum Science and Engineering*, 153, p. 70-80.
- Ghosh, S., Hooker, J.N., Bontempi, C.P., Slatt, R.M., 2018. High-resolution stratigraphic characterization of natural fracture attributes in the Woodford Shale, Arbuckle Wilderness and US-77D Outcrops, Murray County, Oklahoma, *Interpretation*, 6 (1), p. SC29-SC41.
- Gibson, R.G., 1994. Fault-zone seals in siliciclastic strata of the Columbus Basin, offshore Trinidad, *American Association of Petroleum Geologists Bulletin*, 78 (9), p. 1372-1385.
- Gibson, R.G., 1998. Physical character and fluid-flow properties of sandstone-derived fault zones, *In: Coward, M.P., Daltaban, T.S., Johnson, H. (Eds.), Structural Geology in Reservoir Characterization*, Geological Society, London, Special Publications, 127, p. 83-97.

- Gillespie, P.A., Howard, C.B., Walsh, J.J., Watterson, J., 1993. Measurement and characterisation of spatial distributions of fractures, *Tectonophysics*, 226 (1-4), p. 113-141.
- Gillespie, P.A., Walsh, J.J., Watterson, J., Bonson, C.G., Manzocchi, T., 2001. Scaling relationships of joint and vein arrays from The Burren, Co. Clare, Ireland, *Journal of Structural Geology*, 23 (2-3), p. 183-201.
- Giuffrida, A., La Bruna, V., Castelluccio, P., Panza, E., Rustichelli, A., Tondi, E., Giorgioni, M., Agosta, F., 2019. Fracture simulation parameters of fractured reservoirs: analogy with outcropping carbonates of the Inner Apulian Platform, southern Italy, *Journal of Structural Geology*, 123, p. 18-41.
- Golonka, J., Ford, D., 2000. Pangean (Late Carboniferous - Middle Jurassic) paleoenvironment and lithofacies, *Palaeogeography, Palaeoclimatology, Palaeoecology*, 161 (1-2), p. 1-34.
- Google LLC, 2018. Google Earth Pro, Version 7.3.2.5491, Google LLC, Mountain View, California, USA, [www.google.com/earth/index.html](http://www.google.com/earth/index.html).
- Gudmundsson, A., 1987a. Geometry, formation and development of tectonic fractures on the Reykjanes Peninsula, southwest Iceland, *Tectonophysics*, 139 (3-4), p. 295-308.
- Gudmundsson, A., 1987b. Tectonics of the Thingvellir fissure swarm, SW Iceland, *Journal of Structural Geology*, 9 (1), p. 61-69.
- Guerriero, V., Iannace, A., Mazzoli, S., Parente, M., Vitale, S., Giorgioni, M., 2010. Quantifying uncertainties in multi-scale studies of fractured reservoir analogues: implemented statistical analysis of scan line data from carbonate rocks, *Journal of Structural Geology*, 32 (9), p. 1271-1278.
- Guerriero, V., Mazzoli, S., Iannace, A., Vitale, S., Carravetta, A., Strauss, C., 2013. A permeability model for naturally fractured carbonate reservoirs, *Marine and Petroleum Geology*, 40, p. 115-134.
- Gunnarsson, N., 2011. 3D modeling in Petrel of geological CO<sub>2</sub> storage site, Master Thesis, Uppsala University, Uppsala, 64 pp.
- Gupta, A., Penuela, G., Avila, R., 2001. An integrated approach to the determination of permeability tensors for naturally fractured reservoirs, *Journal of Canadian Petroleum Technology*, 40 (12), p. 43-48.

- Haffen, S., Géraud, Y., Diraison, M., 2015. Geothermal, structural and petrophysical characteristics of Buntsandstein sandstone reservoir (Upper Rhine Graben, France), Proceedings World Geothermal Congress, Melbourne, Australia, 1-11 pp.
- Hagdorn, H., Nitsch, E., Aigner, T., Simon, T., 2009. 6th International Triassic Field Workshop (Pan-European Correlation of the Triassic) Triassic of Southwest Germany 175th Anniversary of the Foundation of the Triassic System by Friedrich von Alberti, September 7 - 11, 2009, Subkommission für Perm-Trias-Stratigraphie, Tübingen and Ingelfingen, 73 pp.
- Hakami, E., 1995. Aperture Distribution of Rock Fractures, Doctoral Thesis, Royal Institute of Technology, Stockholm, 22 pp.
- Harms, J.C., Fahnestock, R.K., 1965. Stratification, bed forms, and flow phenomena (with example from the Rio Grande), *In*: Middleton, G.V. (Ed.), Primary Sedimentary Structures and Their Hydrodynamic Interpretation, Society of Economic Paleontologists and Mineralogists, Tulsa, Special Publication 12, p. 84-115.
- Harper, T.R., Moftah, I., 1985. Skin effect and completion options in the Ras Budran reservoir, Society of Petroleum Engineers, Middle East Oil Technical Conference and Exhibition, 11-14 March, 211-226 pp.
- Harris, S.D., McAllister, E., Knipe, R.J., Odling, N.E., 2003. Predicting the three-dimensional population characteristics of fault zones: a study using stochastic models, *Journal of Structural Geology*, 25 (8), p. 1281-1299.
- Hatton, C.G., Main, I.G., Meredith, P.G., 1994. Non-universal scaling of fracture length and opening displacement, *Nature*, 367, p. 160-162.
- Heffer, K.J., Bevan, T.G., 1990. Scaling relationships in natural fractures: data, theory, and application, European Petroleum Conference, 21-24 October, 367-376 pp.
- Heidbach, O., Rajabi, M., Cui, X., Fuchs, K., Müller, B., Reinecker, J., Reiter, K., Tingay, M., Wenzel, F., Xie, F., Ziegler, M.O., Zoback, M.-L., Zoback, M., 2018. The world stress map database release 2016: Crustal stress pattern across scales, *Tectonophysics*, 744, p. 484-498.
- Heidbach, O., Tingay, M., Barth, A., Reinecker, J., Kurfeß, D., Müller, B., 2010. Global crustal stress pattern based on the World Stress Map database release 2008, *Tectonophysics*, 482 (1-4), p. 3-15.
- Hodgetts, D., 2013. Laser scanning and digital outcrop geology in the petroleum industry: a review, *Marine and Petroleum Geology*, 46, p. 335-354.

- Hoffman, B.T., Narr, W., 2012. Using production logs (PLT) to estimate the size of fracture networks, *Journal of Petroleum Science and Engineering*, 98 (3), p. 11-18.
- Hollinger, J., 1969. Beitrag zur Gliederung des Deckgebirges der Nordvogesen, *Zeitschrift der Deutschen Geologischen Gesellschaft*, 121, p. 79-91.
- Homewood, R.D., Guillocheau, F., Eschard, R., Cross, T.A., 1992. Corrélations haute résolution et stratigraphie génétique: une démarche intégrée, *Bulletin des Centres de Recherches Exploration - Production Elf-Aquitaine*, 16, p. 357-381.
- Hooker, J.N., Gomez, L.A., Laubach, S.E., Gale, J.F.W., Marrett, R., 2012. Effects of diagenesis (cement precipitation) during fracture opening on fracture aperture-size scaling in carbonate rocks, *In: Garland, J., Neilson, J.E., Laubach, S.E., Whidden, K.J. (Eds.), Advances in Carbonate Exploration and Reservoir Analysis*, Geological Society, London, Special Publications, 370, p. 187-206.
- Hooker, J.N., Laubach, S.E., Gomez, L., Marrett, R., Eichhubl, P., Diaz-Tushman, K., Pinzon, E., 2011. Fracture size, frequency, and strain in the Cambrian Eriboll Formation sandstones, NW Scotland, *Scottish Journal of Geology*, 47 (1), p. 45-56.
- Hooker, J.N., Laubach, S.E., Marrett, R., 2013. Fracture-aperture size-frequency, spatial distribution, and growth processes in strata-bounded and non-strata-bounded fractures, *Journal of Structural Geology*, 54, p. 54-71.
- Hooker, J.N., Laubach, S.E., Marrett, R., 2014. A universal power-law scaling exponent for fracture apertures in sandstones, *GSA Bulletin*, 126 (9-10), p. 1340-1362.
- Huang, N., Jiang, Y., Li, B., Liu, R., 2016. A numerical method for simulating fluid flow through 3-D fracture networks, *Journal of Natural Gas Science and Engineering*, 33, p. 1271-1281.
- Huitt, J.L., 1956. Fluid flow in simulated fractures, *American Institute of Chemical Engineers Journal*, 2 (2), p. 259-264.
- Hull, J., 1988. Thickness-displacement relationships for deformation zones, *Journal of Structural Geology*, 10 (4), p. 431-435.
- Hunter, R.E., 1977. Basic types of stratification in small eolian dunes, *Sedimentology*, 24 (3), p. 361-387.
- Hüttner, R., 1991. Bau und Entwicklung des Oberrheingrabens - Ein Überblick mit historischer Rückschau, *Geologisches Jahrbuch*, 48, p. 17-42.
- Illies, H., 1962. Oberrheinisches Grundgebirge und Rheingraben, *Geologische Rundschau*, 52 (1), p. 317-332.

- Illies, H., 1965. Bauplan und Baugeschichte des Oberrheingrabens; ein Beitrag zum 'Upper Mantle Project', *Oberrheinische Geologische Abhandlungen*, 20, p. 1-54.
- Illies, J.H., 1974. Taphrogenesis and plate tectonics, *In: Illies, J., Fuchs, K. (Eds.), Approaches to Taphrogenesis: Proceedings of an International Rift Symposium held in Karlsruhe April 13-15, 1972*, Schweizerbart, Stuttgart, p. 433-460.
- Illies, J.H., 1975. Recent and paleo-intraplate tectonics in stable Europe and the Rhinegraben rift system, *Developments in Geotectonics*, 9, p. 251-264.
- Illies, J.H., Greiner, G., 1979. Holocene movements and state of stress in the Rhinegraben rift system, *Developments in Geotectonics*, 13, p. 349-359.
- Jambayev, A.S., 2007. Discrete fracture network modeling for a carbonate reservoir, Master Thesis, Colorado School of Mines, Golden, 102 pp.
- Jamison, W.R., Stearns, D.W., 1982. Tectonic deformation of Wingate Sandstone, Colorado National Monument, *American Association of Petroleum Geologists Bulletin*, 66 (12), p. 2584-2608.
- Johns, R.A., Steude, J.S., Castanier, L.M., Roberts, P.V., 1993. Nondestructive measurements of fracture aperture in crystalline rock cores using X ray computed tomography, *Journal of Geophysical Research: Solid Earth*, 98 (B2), p. 1889-1900.
- Jourde, H., Flodin, E.A., Aydin, A., Durlofsky, L.J., Wen, X.-H., 2002. Computing permeability of fault zones in eolian sandstone from outcrop measurements, *American Association of Petroleum Geologists Bulletin*, 86 (7), p. 1187-1200.
- Karimi-Fard, M., Durlofsky, L.J., Aziz, K., 2004. An efficient discrete-fracture model applicable for general-purpose reservoir simulators, *SPE Journal*, 9 (2), p. 227-236.
- Karra, S., O'Malley, D., Hyman, J.D., Viswanathan, H.S., Srinivasan, G., 2018. Modeling flow and transport in fracture networks using graphs, *Physical Review E*, 97 (3), p. 1-9.
- Kazemi, H., Merrill Jr, L., Porterfield, K., Zeman, P., 1976. Numerical simulation of water-oil flow in naturally fractured reservoirs, *Society of Petroleum Engineers Journal*, 16 (06), p. 317-326.
- Keller, A.A., 1996. Single and Multiphase Flow and Transport in Fractured Porous Media, Doctoral Thesis, Stanford University, Stanford, 237 pp.
- Keller, A.A., Roberts, P.V., Blunt, M.J., 1999. Effect of fracture aperture variations on the dispersion of contaminants, *Water Resources Research*, 35 (1), p. 55-63.

- Klimczak, C., Schultz, R.A., Parashar, R., Reeves, D.M., 2010. Cubic law with aperture-length correlation: implications for network scale fluid flow, *Hydrogeology Journal*, 18 (4), p. 851-862.
- Kluge, C., Milsch, H., Blöcher, G., 2017. Permeability of displaced fractures, *Energy Procedia*, 125, p. 88-97.
- Knipe, R.J., Fisher, Q.J., Jones, G., Clennell, M.R., Farmer, A.B., Harrison, A., Kidd, B., McAllister, E., Porter, J.R., White, E.A., 1997. Fault seal analysis: successful methodologies, application and future directions, *In: Møller-Pedersen, P., Koestler, A.G. (Eds.), Hydrocarbon Seals: Importance for Exploration and Production, Norwegian Petroleum Society Special Publication, Elsevier, Singapore*, p. 15-38.
- Knott, S.D., 1993. Fault seal analysis in the North Sea, *American Association of Petroleum Geologists Bulletin*, 77 (5), p. 778-792.
- Knott, S.D., 1994. Fault zone thickness versus displacement in the Permo-Triassic sandstones of NW England, *Journal of the Geological Society*, 151 (1), p. 17-25.
- Kocurek, G., Fielder, G., 1982. Adhesion structures, *Journal of Sedimentary Research*, 52 (4), p. 1230-1241.
- Konrad, H.J., 1971. Über die Verbreitung von Unterem Buntsandstein in den Nordvogesen, *Abhandlungen des Hessischen Landesamtes für Bodenforschung*, 60, p. 258-262.
- Krämer, F., Kunz, H., 1969. Leithorizonte und Schichtausfälle im Buntsandstein Hessens und Thüringens, *Oberrheinische Geologische Abhandlungen*, 18, p. 67-76.
- Kraus, K., Pfeifer, N., 1998. Determination of terrain models in wooded areas with airborne laser scanner data, *ISPRS Journal of Photogrammetry and Remote Sensing*, 53 (4), p. 193-203.
- Krohe, A., Eisbacher, G.H., 1988. Oblique crustal detachment in the Variscan Schwarzwald, southwestern Germany, *Geologische Rundschau*, 77 (1), p. 25-43.
- Kulatilake, P.H.S.W., Wathugala, D.N., Stephansson, O., 1993. Joint network modelling with a validation exercise in Stripa Mine, Sweden, *International Journal of Rock Mechanics and Mining Sciences & Geomechanics Abstracts*, 30 (5), p. 503-526.
- Lang, J., Sievers, J., Loewer, M., Igel, J., Winsemann, J., 2017. 3D architecture of cyclic-step and antidune deposits in glacial subaqueous fan and delta settings: integrating outcrop and ground-penetrating radar data, *Sedimentary Geology*, 362, p. 83-100.

- Lang, P.S., Paluszny, A., Zimmerman, R.W., 2014. Permeability tensor of three-dimensional fractured porous rock and a comparison to trace map predictions, *Journal of Geophysical Research: Solid Earth*, 119 (8), p. 6288-6307.
- Langford, R.P., Chan, M.A., 1989. Fluvial-aeolian interactions: Part II, ancient systems, *Sedimentology*, 36 (6), p. 1037-1051.
- Larroque, J.M., Laurent, P., 1988. Evolution of the stress field pattern in the south of the Rhine Graben from the Eocene to the present, *Tectonophysics*, 148 (1-2), p. 41-58.
- Larsen, B., Grunnaleite, I., Gudmundsson, A., 2010. How fracture systems affect permeability development in shallow-water carbonate rocks: an example from the Gargano Peninsula, Italy, *Journal of Structural Geology*, 32 (9), p. 1212-1230.
- Laubscher, H., 1992. Jura kinematics and the Molasse Basin, *Eclogae Geologicae Helvetiae*, 85 (3), p. 653-675.
- Laux, D., 2017. Terrestrisches Laserscanning zur Quantifizierung von Trennflächenparametern für statistisch signifikante Discrete-Fracture-Network-Modelle, Doctoral Thesis, Technische Universität Darmstadt, Darmstadt pp.
- LBEG, 2019. Erdöl und Erdgas in der Bundesrepublik Deutschland 2018, Landesamt für Bergbau, Energie und Geologie, Hannover, 68 pp.
- Le Garzic, E., de L'Hamaide, T., Diraison, M., Géraud, Y., Sausse, J., De Urreiztieta, M., Hauville, B., Champanhet, J.-M., 2011. Scaling and geometric properties of extensional fracture systems in the Proterozoic basement of Yemen: tectonic interpretation and fluid flow implications, *Journal of Structural Geology*, 33 (4), p. 519-536.
- Lee, C.-H., Farmer, I.W., 1993. *Fluid Flow in Discontinuous Rocks*, Chapman & Hall, London, 170 pp.
- Leeder, M.R., 1999. *Sedimentology and Sedimentary Basins: From Turbulence to Tectonics*, Blackwell Science, Oxford, 592 pp.
- Lei, Q., Latham, J.-P., Xiang, J., Tsang, C.-F., Lang, P., Guo, L., 2014. Effects of geomechanical changes on the validity of a discrete fracture network representation of a realistic two-dimensional fractured rock, *International Journal of Rock Mechanics and Mining Sciences*, 70, p. 507-523.
- Lepage, F., Souche, L.A., 2016. Faulted geological structures having unconformities, US Patent No. 9,378,312, 29 pp.
- Lepper, J., Rambow, D., Röhling, H.G., 2006. Der Buntsandstein in der Stratigraphischen Tabelle von Deutschland, *Newsletters on Stratigraphy*, 41 (1-3), p. 129-142.

- Leung, C.T.O., Zimmerman, R.W., 2012. Estimating the hydraulic conductivity of two-dimensional fracture networks using network geometric properties, *Transport in porous media*, 93 (3), p. 777-797.
- Levey, R.A., 1978. Bed-form distribution and internal stratification of coarse-grained point bars, Upper Congaree River, S.C., *In: Miall, A.D. (Ed.), Fluvial Sedimentology*, Canadian Society of Petroleum Geologists, Calgary, Memoir 5, p. 105-127.
- Li, L., Lee, S.H., 2008. Efficient field-scale simulation of black oil in a naturally fractured reservoir through discrete fracture networks and homogenized media, *SPE Reservoir Evaluation & Engineering*, 11 (4), p. 750-758.
- Li, T., Shiozawa, S., McClure, M.W., 2016. Thermal breakthrough calculations to optimize design of a multiple-stage Enhanced Geothermal System, *Geothermics*, 64, p. 455-465.
- Lim, K.T., Aziz, K., 1995. Matrix-fracture transfer shape factors for dual-porosity simulators, *Journal of Petroleum Science and Engineering*, 13 (3-4), p. 169-178.
- Liu, R., Li, B., Jiang, Y., 2016. Critical hydraulic gradient for nonlinear flow through rock fracture networks: the roles of aperture, surface roughness, and number of intersections, *Advances in Water Resources*, 88, p. 53-65.
- Liu, R., Zhu, T., Jiang, Y., Li, B., Yu, L., Du, Y., Wang, Y., 2018. A predictive model correlating permeability to two-dimensional fracture network parameters, *Bulletin of Engineering Geology and the Environment*, 78 (3), p. 1589-1605.
- Long, J., Witherspoon, P.A., 1985. The relationship of the degree of interconnection to permeability in fracture networks, *Journal of Geophysical Research: Solid Earth*, 90 (B4), p. 3087-3098.
- Louis, C., 1969. A study of groundwater flow in jointed rock and its influence on the stability of rock masses, *Rock Mechanics Research Report No. 10*, Imperial College, London, 90 pp.
- Lunn, R.J., Shipton, Z.K., Bright, A.M., 2008. How can we improve estimates of bulk fault zone hydraulic properties?, *In: Wibberley, C., Kurz, W., Imber, J., Holdsworth, R., Collettini, C. (Eds.), The Internal Structure of Fault Zones: Implications for Mechanical and Fluid-Flow Properties*, Geological Society, London, Special Publications, 299, p. 231-237.
- Lyons, W.C., Plisga, G.J., Lorenz, M.D., 2016. *Standard Handbook of Petroleum and Natural Gas Engineering*, Elsevier, Waltham, Oxford, 1822 pp.



- Malinouskaya, I., Thovert, J.-F., Mourzenko, V.V., Adler, P.M., Shekhar, R., Agar, S., Rosero, E., Tsenn, M., 2014. Fracture analysis in the Amellago outcrop and permeability predictions, *Petroleum Geoscience*, 20 (1), p. 93-107.
- Manger, G.E., 1963. Porosity and bulk density of sedimentary rocks, *Geological Survey Bulletin*, 1144-E, p. 1-59.
- Manzocchi, T., Childs, C., Walsh, J.J., 2010. Faults and fault properties in hydrocarbon flow models, *Geofluids*, 10 (1-2), p. 94-113.
- Mardia, K.V., 1972. *Probability and Mathematical Statistics: Statistics of Directional Data*, Academy Press, London, 358 pp.
- Mardia, K.V., Jupp, P.E., 2009. Distributions on Spheres, *In: Mardia, K.V., Jupp, P.E. (Eds.), Directional Statistics - Wiley Series in Probability and Statistics*, Wiley & Sons, Chichester, p. 159-192.
- Marrett, R., 1997. Permeability, porosity, and shear-wave anisotropy from scaling of open fracture populations, *In: Hoak, T.E., Klawitter, A.L., Blomquist, P.K. (Eds.), Fractured Reservoirs: Characterization and Modeling Guidebook*, Rocky Mountain Association of Geologists, Denver, p. 217-226.
- Marrett, R., Allmendinger, R.W., 1992. Amount of extension on "small" faults: an example from the Viking graben, *Geology*, 20 (1), p. 47-50.
- Marrett, R., Ortega, O.J., Kelsey, C.M., 1999. Extent of power-law scaling for natural fractures in rock, *Geology*, 27 (9), p. 799-802.
- Mauldon, M., Dershowitz, W., 2000. A multi dimensional system of fracture abundance measures, *Geological Society of America Annual Meeting*, 13-16 November pp.
- Mauthe, G., Brink, H.J., Burri, P., 1993. Kohlenwasserstoffvorkommen und-potential im deutschen Teil des Oberrheingrabens, *Bulletin der Vereinigung Schweizerischer Petroleum-Geologen und -Ingenieure*, 60 (137), p. 15-29.
- McCaffrey, K.J.W., Johnston, J.D., 1996. Fractal analysis of a mineralised vein deposit: Curraghinalt gold deposit, County Tyrone, *Mineralium Deposita*, 31 (1-2), p. 52-58.
- McCaffrey, K.J.W., Jones, R.R., Holdsworth, R.E., Wilson, R.W., Clegg, P., Imber, J., Holliman, N., Trinks, I., 2005. Unlocking the spatial dimension: digital technologies and the future of geoscience fieldwork, *Journal of the Geological Society*, 162 (6), p. 927-938.
- McGowen, J.H., Garner, L.E., 1970. Physiographic features and stratification types of coarse-grained pointbars: modern and ancient examples, *Sedimentology*, 14 (1-2), p. 77-111.

- Medina-Cascales, I., Koch, L., Cardozo, N., Martin-Rojas, I., Alfaro, P., García-Tortosa, F.J., 2019. 3D geometry and architecture of a normal fault zone in poorly lithified sediments: a trench study on a strand of the Baza Fault, central Betic Cordillera, south Spain, *Journal of Structural Geology*, 121, p. 25-45.
- Meier, L., Eisbacher, G.H., 1991. Crustal kinematics and deep structure of the northern Rhine Graben, Germany, *Tectonics*, 10 (3), p. 621-630.
- Meier, S., Bauer, J.F., Philipp, S.L., 2015. Fault zone characteristics, fracture systems and permeability implications of Middle Triassic Muschelkalk in Southwest Germany, *Journal of Structural Geology*, 70, p. 170-189.
- Meixner, J., Schill, E., Grimmer, J.C., Gaucher, E., Kohl, T., Klingler, P., 2016. Structural control of geothermal reservoirs in extensional tectonic settings: an example from the Upper Rhine Graben, *Journal of Structural Geology*, 82, p. 1-15.
- Ménillet, F., Benecke, W., Schumacher, E., Van Werveke, L., Leppia, A., Thürach, H., Konrad, H.J., Illies, H., Rinck, G., Schwoerer, P., 1989. Carte géologique de la France à 1/50 000, feuille Lembach (168), Bureau de recherches géologiques et minières, Orléans.
- Miall, A.D., 1977. A review of the braided-river depositional environment, *Earth-Science Reviews*, 13 (1), p. 1-62.
- Miall, A.D., 1978. Lithofacies types and vertical profile models in braided river deposits: a summary, *In: Miall, A.D. (Ed.), Fluvial Sedimentology*, Canadian Society of Petroleum Geologists, Alberta, Memoir 5, p. 597-604.
- Miall, A.D., 1985. Architectural-element analysis: a new method of facies analysis applied to fluvial deposits, *Earth-Science Reviews*, p. 261-308.
- Miall, A.D., 1996. *The Geology of Fluvial Deposits. Sedimentary Facies, Basin Analysis, and Petroleum Geology*, Springer, Berlin, 582 pp.
- Middleton, G.V., 1978. Facies, *In: Fairbridge, R.W., Bourgeois, J. (Eds.), Encyclopedia of Sedimentology*, Dowden, Hutchinson & Ross, Stroudsburg, p. 323-325.
- Mitchum, R.M., Jr, Van Wagoner, J.C., 1991. High-frequency sequences and their stacking patterns: sequence-stratigraphic evidence of high-frequency eustatic cycles, *Sedimentary Geology*, 70 (2-4), p. 131-160.
- Moinfar, A., 2013. Development of an Efficient Embedded Discrete Fracture Model for 3D Compositional Reservoir Simulation in Fractured Reservoirs, Doctoral Thesis, The University of Texas, Austin, 232 pp.

- Muto, T., Steel, R.J., 2000. The accommodation concept in sequence stratigraphy: some dimensional problems and possible redefinition, *Sedimentary Geology*, 130 (1-2), p. 1-10.
- Muto, T., Steel, R.J., 2002. Role of autoretreat and A/S changes in the understanding of deltaic shoreline trajectory: a semi-quantitative approach, *Basin research*, 14 (3), p. 303-318.
- Naji, H.S., Hakimi, M.H., Khalil, M., Sharief, F.A., 2010. Stratigraphy, deposition, and structural framework of the Cretaceous (review) and 3D geological model of the Lower Cretaceous reservoirs, Masila oil field, Yemen, *Arabian Journal of Geosciences*, 3 (3), p. 221-248.
- National Research Council, 1996. *Rock Fractures and Fluid Flow: Contemporary Understanding and Applications*, The National Academies Press, Washington, DC, 568 pp.
- Nawrocki, J., 1997. Permian to Early Triassic magnetostratigraphy from the Central European Basin in Poland: implications on regional and worldwide correlations, *Earth and Planetary Science Letters*, 152 (1), p. 37-58.
- Neuman, S.P., 2005. Trends, prospects and challenges in quantifying flow and transport through fractured rocks, *Hydrogeology Journal*, 13 (1), p. 124-147.
- Nichols, G., 2009. *Sedimentology and Stratigraphy - Second Edition*, Wiley-Blackwell, Oxford, 419 pp.
- Nur, A., 1982. The origin of tensile fracture lineaments, *Journal of Structural Geology*, 4 (1), p. 31-40.
- Oda, M., 1985. Permeability tensor for discontinuous rock masses, *Géotechnique*, 35 (4), p. 483-495.
- Oda, M., 1986. An equivalent continuum model for coupled stress and fluid flow analysis in jointed rock masses, *Water Resources Research*, 22 (13), p. 1845-1856.
- Oda, M., Hatsuyama, Y., Ohnishi, Y., 1987. Numerical experiments on permeability tensor and its application to jointed granite at Stripa mine, Sweden, *Journal of Geophysical Research: Solid Earth*, 92 (B8), p. 8037-8048.
- Odling, N.E., 1997. Scaling and connectivity of joint systems in sandstones from western Norway, *Journal of Structural Geology*, 19 (10), p. 1257-1271.
- Odling, N.E., Gillespie, P., Bourguine, B., Castaing, C., Chilés, J.-P., Christensen, N.P., Fillion, E., Genter, A., Olsen, C., Thrane, L., Trice, R., Aarseth, E., Walsh, J.J., Watterson, J., 1999.

- Variations in fracture system geometry and their implications for fluid flow in fractured hydrocarbon reservoirs, *Petroleum Geoscience*, 5 (4), p. 373-384.
- Olson, J.E., Yuan, Q., Holder, J., Rijken, P., 2001. Constraining the spatial distribution of fracture networks in naturally fractured reservoirs using fracture mechanics and core measurements, *SPE Annual Technical Conference and Exhibition*, 30 September-3 October, 12 pp.
- Olsson, R., Barton, N., 2001. An improved model for hydromechanical coupling during shearing of rock joints, *International Journal of Rock Mechanics and Mining Sciences*, 38 (3), p. 317-329.
- Onstott, T.C., 1980. Application of the Bingham distribution function in paleomagnetic studies, *Journal of Geophysical Research: Solid Earth*, 85 (B3), p. 1500-1510.
- Optech Incorporated, 2011. Parser, Version 5.0.3.1, Optech Incorporated, Toronto, Canada, [www.teledyneoptech.com](http://www.teledyneoptech.com).
- Optech Incorporated, 2014. ILRIS Laser Scanner, Optech Incorporated, Vaughan, 2 pp.
- Oron, A.P., Berkowitz, B., 1998. Flow in rock fractures: the local cubic law assumption reexamined, *Water Resources Research*, 34 (11), p. 2811-2825.
- Ortega, O.J., Marrett, R.A., Laubach, S.E., 2006. A scale-independent approach to fracture intensity and average spacing measurement, *American Association of Petroleum Geologists Bulletin*, 90 (2), p. 193-208.
- Ortlam, D., 1974. Inhalt und Bedeutung fossiler Bodenkomplexe in Perm und Trias von Mitteleuropa, *Geologische Rundschau*, 63 (3), p. 850-884.
- Özkaya, S.I., 2003. Fracture length estimation from borehole image logs, *Mathematical Geology*, 35 (6), p. 737-753.
- Panza, E., Sessa, E., Agosta, F., Giorgioni, M., 2018. Discrete Fracture Network modelling of a hydrocarbon-bearing, oblique-slip fault zone: Inferences on fault-controlled fluid storage and migration properties of carbonate fault damage zones, *Marine and Petroleum Geology*, 89, p. 263-279.
- Parrino, N., Agosta, F., Di Stefano, P., Napoli, G., Pepe, F., Renda, P., 2019. Fluid storage and migration properties of sheared Neptunian dykes, *Marine and Petroleum Geology*, 102, p. 521-534.
- Paul, J., 1982. The Lower Buntsandstein of the Germanic Basin, *Geologische Rundschau*, 71 (3), p. 795-811.

- Paul, J., Klarr, K., 1988. Feinstratigraphie und Fazies des Unteren und Mittleren Buntsandsteins in der Bohrung Remlingen 5, GSF Bericht 8/87, München, 148 pp.
- Péron, S., Bourquin, S., Fluteau, F., Guillocheau, F., 2005. Paleoenvironment reconstructions and climate simulations of the Early Triassic: impact of the water and sediment supply on the preservation of fluvial systems, *Geodinamica Acta*, 18 (6), p. 431-446.
- Perriaux, J., 1961. Contribution à l'étude des Vosges gréseuses, Mémoires du Service de la Carte géologique d'Alsace et de Lorraine, 18, p. 1-236.
- Persson, A., Holmgren, J., Soderman, U., 2002. Detecting and measuring individual trees using an airborne laser scanner, *Photogrammetric Engineering and Remote Sensing*, 68 (9), p. 925-932.
- Petit, J.P., Massonnat, G., Pueo, F., Rawnsley, K., 1994. Rapport de forme des fractures de mode 1 dans les roches stratifiées: Une étude de cas dans le Bassin Permian de Lodeve (France), *Bulletin Elf Aquitaine Production*, 18, p. 211-229.
- Pflug, R., 1982. Erträge der Forschung - Bau und Entwicklung des Oberrheingrabens, Wissenschaftliche Buchgesellschaft, Darmstadt, 145 pp.
- Philipp, S.L., 2008. Geometry and formation of gypsum veins in mudstones at Watchet, Somerset, SW England, *Geological Magazine*, 145 (6), p. 831-844.
- Pittman, E.D., 1981. Effect of fault-related granulation on porosity and permeability of quartz sandstones, Simpson Group (Ordovician), Oklahoma, *American Association of Petroleum Geologists Bulletin*, 65 (11), p. 2381-2387.
- Plenefisch, T., Bonjer, K.-P., 1997. The stress field in the Rhine Graben area inferred from earthquake focal mechanisms and estimation of frictional parameters, *Tectonophysics*, 275 (1), p. 71-97.
- Plint, A.G., 1983. Sandy fluvial point-bar sediments from the Middle Eocene of Dorset, England, *In: Collinson, J.D., Lewin, J. (Eds.), Modern and Ancient Fluvial Systems*, International Association of Sedimentologists, Oxford, Special Publication 6, p. 355-368.
- Pollard, D.D., Segall, P., 1987. Theoretical displacements and stresses near fractures in rock: with applications to faults, joints, veins, dikes and solution surfaces, *In: Atkinson, B.K. (Ed.), Fracture Mechanics of Rock*, Academic Press, London, p. 534.
- Polubarinova-Kochina, P.Y., 1962. *Theory of Ground Water Movement*, Princeton University Press, Princeton, New Jersey, 613 pp.

- Priest, S.D., 1993. *Discontinuity Analysis for Rock Engineering*, Chapman & Hall, New York, 473 pp.
- Priest, S.D., Hudson, J.A., 1981. Estimation of discontinuity spacing and trace length using scanline surveys, *International Journal of Rock Mechanics and Mining Sciences & Geomechanics Abstracts*, 18 (3), p. 183-197.
- Pringle, J.K., Howell, J.A., Hodgetts, D., Westerman, A.R., Hodgson, D.M., 2006. Virtual outcrop models of petroleum reservoir analogues: a review of the current state-of-the-art, *First break*, 24 (3), p. 33-42.
- Pringle, J.K., Westerman, A.R., Clark, J.D., Drinkwater, N.J., Gardiner, A.R., 2004. 3D high-resolution digital models of outcrop analogue study sites to constrain reservoir model uncertainty: an example from Alport Castles, Derbyshire, UK, *Petroleum Geoscience*, 10 (4), p. 343-352.
- Prinz, H., Strauß, R., 2018. Geotechnische Aspekte der Geothermie, *In: Prinz, H., Strauß, R. (Eds.), Ingenieurgeologie*, Springer Spektrum, Berlin, p. 785-810.
- Prodehl, C., Mueller, S., Haak, V., 2006. The european cenozoic rift system, *In: Olsen, K. (Ed.), Continental Rifts: Evolution, Structure, Tectonics, Developments in Geotectonics*, Volume 25, Elsevier, Amsterdam, p. 133-212.
- Pyrack-Nolte, L.J., Myer, L.R., Cook, N.G.W., Witherspoon, P.A., 1987. Hydraulic and mechanical properties of natural fractures in low-permeability rock, 6th International Conference on Rock Mechanics, 30 August-3 September, 6 pp.
- Qu, D., Røe, P., Tveranger, J., 2015. A method for generating volumetric fault zone grids for pillar gridded reservoir models, *Computers & Geosciences*, 81, p. 28-37.
- Qu, D., Tveranger, J., Fachri, M., 2017. Influence of deformation-band fault damage zone on reservoir performance, *Interpretation*, 5 (4), p. SP41-SP56.
- Radies, D., Stollhofen, H., Hollmann, G., Kukla, P., 2005. Synsedimentary faults and amalgamated unconformities: insights from 3D-seismic and core analysis of the Lower Triassic Middle Buntsandstein, Ems Trough, north-western Germany, *International Journal of Earth Sciences*, 94 (5-6), p. 863-875.
- Ran, Q., Wang, Y., Sun, Y., Yan, L., Tong, M., 2014. *Volcanic Gas Reservoir Characterization*, Gulf Professional Publishing, Waltham, Kidlington, 604 pp.
- Rarity, F., Van Lanen, X.M.T., Hodgetts, D., Gawthorpe, R.L., Wilson, P., Fabuel-Perez, I., Redfern, J., 2014. LiDAR-based digital outcrops for sedimentological analysis: workflows and techniques, *In: Martinius, A.W., Howell, J.A., Good, T. (Eds.), Sediment-*

- Body Geometry and Heterogeneity: Analogue Studies for Modelling the Subsurface, Geological Society, London, p. 153-183.
- Rawling, G.C., Goodwin, L.B., Wilson, J.L., 2001. Internal architecture, permeability structure, and hydrologic significance of contrasting fault-zone types, *Geology*, 29 (1), p. 43-46.
- Reading, H.G., 1986. *Sedimentary Environments and Facies*, Blackwell Scientific Publications, Oxford, 615 pp.
- Reicherter, K., Froitzheim, N., Jarosinski, M., Badura, J., Franzke, H.-J., Hansen, M., Hübscher, C., Müller, R., Poprawa, P., Reinecker, J., Stackebrandt, W., Voigt, T., von Eynatten, H., Zuchiewicz, W., 2008. Alpine tectonics north of the Alps, *In: McCann, T. (Ed.), The Geology of Central Europe, Volume 2: Mesozoic and Cenozoic*, Geological Society, London, p. 1233-1285.
- Reinhardt, L., Ricken, W., 2000. The stratigraphic and geochemical record of playa cycles: monitoring a Pangaeian monsoon-like system (Triassic, Middle Keuper, S. Germany), *Palaeogeography, Palaeoclimatology, Palaeoecology*, 161 (1-2), p. 205-227.
- Reinhold, C., Schwarz, M., Bruss, D., Heesbeen, B., Perner, M., Suana, M., 2016. The Northern Upper Rhine Graben - re-dawn of a mature petroleum province?, *Swiss Bulletin für angewandte Geologie*, 21 (2), p. 35-56.
- Renshaw, C.E., 1995. On the relationship between mechanical and hydraulic apertures in rough-walled fractures, *Journal of Geophysical Research: Solid Earth*, 100 (B12), p. 24629-24636.
- Renshaw, C.E., 1999. Connectivity of joint networks with power law length distributions, *Water Resources Research*, 35 (9), p. 2661-2670.
- Rettig, B., 1995. Die Solling-Folge (Mittlerer Buntsandstein) im Grenzgebiet Niedersachsen-Thüringen-Hessen, *Mitteilungen aus dem Geologischen Institut der Universität Hannover*, 35, p. 1-107.
- Reutebuch, S.E., Andersen, H.-E., McGaughey, R.J., 2005. Light detection and ranging (LIDAR): an emerging tool for multiple resource inventory, *Journal of Forestry*, 103 (6), p. 286-292.
- Richter-Bernburg, G., 1974. Stratigraphische Synopsis des deutschen Buntsandsteins, *Geologisches Jahrbuch, A* 25, p. 127-132.
- Rogers, S., Elmo, D., Webb, G., Catalan, A., 2015. Volumetric fracture intensity measurement for improved rock mass characterisation and fragmentation assessment in block caving operations, *Rock Mechanics and Rock Engineering*, 48 (2), p. 633-649.

- Röhling, H.G., 1991. A lithostratigraphic subdivision of the Lower Triassic in the northwest German lowlands and the German sector of the North Sea, based on gamma-ray and sonic logs, *Geologisches Jahrbuch*, A 119, p. 3-24.
- Roman, A., 2004. Sequenzstratigraphie und Fazies des Unteren und Mittleren Buntsandsteins im östlichen Teil des Germanischen Beckens (Deutschland, Polen), Doctoral Thesis, Martin-Luther-Universität Halle-Wittenberg, Halle (Saale), 247 pp.
- Rong, G., Peng, J., Wang, X., Liu, G., Hou, D., 2013. Permeability tensor and representative elementary volume of fractured rock masses, *Hydrogeology Journal*, 21 (7), p. 1655-1671.
- Rotstein, Y., Behrmann, J.H., Lutz, M., Wirsing, G., Luz, A., 2005. Tectonic implications of transpression and transtension: Upper Rhine Graben, *Tectonics*, 24 (6), p. 1-12.
- Rotstein, Y., Schaming, M., 2011. The Upper Rhine Graben (URG) revisited: Miocene transtension and transpression account for the observed first-order structures, *Tectonics*, 30 (3), p. 1-14.
- Rouleau, A., Gale, J.E., 1985. Statistical characterization of the fracture system in the Stripa granite, Sweden, *International Journal of Rock Mechanics and Mining Sciences & Geomechanics Abstracts*, 22 (6), p. 353-367.
- Sanderson, D.J., Roberts, S., Gumiel, P., 1994. A fractal relationship between vein thickness and gold grade in drill core from La Codosera, Spain, *Economic Geology*, 89 (1), p. 168-173.
- Sarkar, S., Toksoz, M.N., Burns, D.R., 2004. Fluid flow modeling in fractures, Massachusetts Institute of Technology, Earth Resources Laboratory, Cambridge, 41 pp.
- Sauer, K., Naegele, R., Tietze, R., Kreuzkamp, H., 1982. Geothermal Inventory of the Upper Rhinegraben between Karlsruhe and Mannheim (situated in Baden-Wuerttemberg), Report, Commission of the European Communities, Luxembourg, 168 pp.
- Sbrana, A., Marianelli, P., Pasquini, G., Costantini, P., Palmieri, F., Ciani, V., Sbrana, M., 2018. The integration of 3D modeling and simulation to determine the energy potential of low-temperature geothermal systems in the Pisa (Italy) sedimentary plain, *Energies*, 11 (6), p. 1-20.
- Scheck-Wenderoth, M., Krzywiec, P., Zühlke, R., Maystrenko, Y., Froitzheim, N., 2008. Permian to Cretaceous tectonics, *In: McCann, T. (Ed.), The Geology of Central Europe, Volume 2: Mesozoic and Cenozoic*, Geological Society, London, p. 999-1030.



- Scheidegger, A.E., 1965. On the statistics of the orientation of bedding planes, grain axes, and similar sedimentological data, US Geological Survey Professional Paper, 525, p. 164-167.
- Schlumberger, 2016. Petrel E&P Software Platform, 2016.3 (64-bit), Schlumberger, Houston, Texas, USA, <https://www.software.slb.com/products/petrel>.
- Schmincke, H.-U., Fisher, R.V., Waters, A.C., 1973. Antidune and chute and pool structures in the base surge deposits of the Laacher See area, Germany, *Sedimentology*, 20 (4), p. 553-574.
- Scholz, C.H., 1987. Wear and gouge formation in brittle faulting, *Geology*, 15 (6), p. 493-495.
- Scholz, C.H., Anders, M.H., 1994. The permeability of faults, *In: Hickman, S., Sibson, R., Bruhn, R. (Eds.), Introduction to Special Section: Mechanical Involvement of Fluids in Faulting*, US Geological Survey, Menlo Park, p. 247-253.
- Schumacher, M.E., 2002. Upper Rhine Graben: role of preexisting structures during rift evolution, *Tectonics*, 21 (1), p. 1-17.
- Schumann, A., Arndt, D., Wiatr, T., Götz, A.E., Hoppe, A., 2011. High-resolution terrestrial laser scanning and 3D modelling of a mineral deposit for extraction management optimisation, *Zeitschrift der Deutschen Gesellschaft für Geowissenschaften*, 162 (4), p. 435-442.
- Schwarz, J., 1997. Charophyten aus dem Tertiär des Oberrheingrabens (Mittelleozän - Untermiozän), *Palaeontographica*, B 243 (1-3), p. 1-84.
- Schwarz, M., 2005. Evolution und Struktur des Oberrheingrabens: quantitative Einblicke mit Hilfe dreidimensionaler thermomechanischer Modellrechnungen, Doctoral Thesis, Albert-Ludwigs-Universität Freiburg, Freiburg, 314 pp.
- Schwarz, M., Henk, A., 2005. Evolution and structure of the Upper Rhine Graben: insights from three-dimensional thermomechanical modelling, *International Journal of Earth Sciences*, 94 (4), p. 732-750.
- Segall, P., Pollard, D.D., 1983. Joint formation in granitic rock of the Sierra Nevada, *Geological Society of America Bulletin*, 94 (5), p. 563-575.
- Shipton, Z.K., Cowie, P.A., 2001. Damage zone and slip-surface evolution over  $\mu\text{m}$  to km scales in high-porosity Navajo sandstone, Utah, *Journal of Structural Geology*, 23 (12), p. 1825-1844.
- Shipton, Z.K., Evans, J.P., Robeson, K.R., Forster, C.B., Snelgrove, S., 2002. Structural heterogeneity and permeability in faulted eolian sandstone: implications for

- subsurface modeling of faults, *American Association of Petroleum Geologists Bulletin*, 86 (5), p. 863-883.
- Shipton, Z.K., Evans, J.P., Thompson, L.B., 2005. The geometry and thickness of deformation-band fault core and its influence on sealing characteristics of deformation-band fault zones, *In: Sorkhabi, R., Tsuji, Y. (Eds.), Faults, Fluid Flow, & Petroleum Traps: American Association of Petroleum Geologists Memoir 85, AAPG, Tulsa, p. 181-195.*
- Shipton, Z.K., Soden, A.M., Kirkpatrick, J.D., Bright, A.M., Lunn, R.J., 2006. How thick is a fault? Fault displacement-thickness scaling revisited, *In: Abercrombie, R. (Ed.), Earthquakes: Radiated Energy and the Physics of Faulting, American Geophysical Union, Washington, DC, p. 193-198.*
- Shojaei, A.K., Shao, J., 2017. *Porous Rock Fracture Mechanics with Application to Hydraulic Fracturing, Drilling and Structural Engineering, Woodhead Publishing, Duxford, Cambridge, Kidlington, 336 pp.*
- Sibson, R.H., 1977. Fault rocks and fault mechanisms, *Journal of the Geological Society*, 133 (3), p. 191-213.
- Skar, T., Berg, S.S., Gabrielsen, R.H., Braathen, A., 2017. Fracture networks of normal faults in fine-grained sedimentary rocks: examples from Kilve Beach, SW England, *In: Childs, C., Holdsworth, R.E., Jackson, C.A.L., Manzocchi, T., Walsh, J.J., Yielding, G. (Eds.), The Geometry and Growth of Normal Faults, Geological Society, London, Special Publications, 439, p. 289-306.*
- Slob, S., Hack, R., 2004. 3D terrestrial laser scanning as a new field measurement and monitoring technique, *In: Hack, R., Azzam, R., Charlier, R. (Eds.), Engineering Geology for Infrastructure Planning in Europe. A European Perspective, Springer, Berlin, p. 179-189.*
- Smith, D.G., 1983. Anastomosed fluvial deposits: modern examples from Western Canada, *In: Collinson, J.D., Lewin, J. (Eds.), Modern and Ancient Fluvial Systems, International Association of Sedimentologists, Oxford, Special Publication 6, p. 155-168.*
- Smith, N.D., 1978. Some comments on terminology for bars in shallow rivers, *In: Miall, A.D. (Ed.), Fluvial Sedimentology, Canadian Society of Petroleum Geologists, Calgary, Memoir 5, p. 85-92.*
- Snow, D.T., 1965. *A Parallel Plate Model of Fractured Permeable Media, Unpublished Doctoral Thesis, University of California, Berkeley, 331 pp.*

- Souche, L., Lepage, F., Iskenova, G., 2013. Volume based modeling - automated construction of complex structural models, 75th EAGE Conference & Exhibition incorporating SPE EUROPEC 2013, 10-13 Jule, 5 pp.
- Soyk, D., 2015. Diagenesis and reservoir quality of the Lower and Middle Buntsandstein (Lower Triassic), SW Germany, Doctoral Thesis, Ruprecht-Karls-Universität Heidelberg, Heidelberg, 201 pp.
- Stapf, K.R.G., 1988. Zur Tektonik des westlichen Rheingrabenrandes zwischen Nierstein am Rhein und Wissembourg (Elsass), Jahresberichte und Mitteilungen des Oberrheinischen Geologischen Vereins, 70, p. 399-410.
- Stapf, K.R.G., 1996. Neue Erkenntnisse zur Tektonik des pfälzischen Rheingrabenrandes, *In*: Geiger, M. (Ed.), Haardt und Weinstraße: Beiträge zur Landeskunde, Pfälzische Gesellschaft zur Förderung der Wissenschaften, Speyer, p. 60-96.
- Strobl, R.S., Wightman, D.M., Muwais, W.K., Cotterill, D.K., Yuan, L., 1997. Application of outcrop analogues and detailed reservoir characterization to the AOSTRA underground test facility, McMurray Formation, North Eastern Alberta, *In*: Pemberton, S.G., James, D.P. (Eds.), Petroleum Geology of the Cretaceous Mannville Group, Western Canada - Memoir 18, Canadian Society of Petroleum Geologists, Calgary, p. 375-391.
- Szurlies, M., 2001. Zyklische Stratigraphie und Magnetostratigraphie des Unteren Buntsandsteins in Mitteldeutschland, Doctoral Thesis, Martin-Luther-Universität Halle-Wittenberg, Halle (Saale), 153 pp.
- Szurlies, M., 2007. Latest Permian to Middle Triassic cyclo-magnetostratigraphy from the Central European Basin, Germany: implications for the geomagnetic polarity timescale, *Earth and Planetary Science Letters*, 261 (3-4), p. 602-619.
- Szurlies, M., Bachmann, G.H., Menning, M., Nowaczyk, N.R., Käding, K.-C., 2003. Magnetostratigraphy and high-resolution lithostratigraphy of the Permian-Triassic boundary interval in Central Germany, *Earth and Planetary Science Letters*, 212 (3), p. 263-278.
- Szurlies, M., Kozur, H.W., 2004. Preliminary paleomagnetic results from the Permian-Triassic boundary interval, Central and NW Iran, *Albertiana*, 31, p. 41-46.
- Teichert, C., 1958. Concepts of facies, *American Association of Petroleum Geologists Bulletin*, 42 (11), p. 2718-2744.
- Temam, R., 2001. Navier-Stokes Equations: Theory and Numerical Analysis, American Mathematical Society, Providence, Rhode island, 408 pp.

- Thurmond, J.B., Løseth, T.M., Rivenæs, J.C., Martinsen, O.J., Aiken, C., Xu, X., 2007. Chapter 118. Collection, evaluation, and use of outcrop data in the 21st century - new methods and applications, with an example from the Ainsa turbidite system, Spain, *In*: Nilsen, T.H., Shew, R.D., Steffens, G.S., Studlick, J.R.J. (Eds.), *Atlas of Deep-Water Outcrops*, AAPG Studies in Geology 56, Tulsa, p. 1-20.
- Tikoff, B., Fossen, H., 1999. Three-dimensional reference deformations and strain facies, *Journal of Structural Geology*, 21 (11), p. 1497-1512.
- Tinker, S.W., 1996. Building the 3-D jigsaw puzzle: applications of sequence stratigraphy to 3-D reservoir characterization, Permian Basin, *American Association of Petroleum Geologists Bulletin*, 80 (4), p. 460-484.
- Tobien, H., 1987. The position of the "Grande Coupure" in the Paleogene of the Upper Rhine Graben and the Mainz Basin, *Münchner Geowissenschaftliche Abhandlungen*, A 10, p. 197-202.
- Tomás, S., Zitzmann, M., Homann, M., Rumpf, M., Amour, F., Benisek, M., Marcano, G., Mutti, M., Betzler, C., 2010. From ramp to platform: building a 3D model of depositional geometries and facies architectures in transitional carbonates in the Miocene, northern Sardinia, *Facies*, 56 (2), p. 195-210.
- Tonon, F., Chen, S., 2007. Closed-form and numerical solutions for the probability distribution function of fracture diameters, *International Journal of Rock Mechanics and Mining Sciences*, 44 (3), p. 332-350.
- Torabi, A., Fossen, H., Braathen, A., 2013. Insight into petrophysical properties of deformed sandstone reservoirs, *American Association of Petroleum Geologists Bulletin*, 97 (4), p. 619-637.
- Toy, V.G., Boulton, C.J., Sutherland, R., Townend, J., Norris, R.J., Little, T.A., Prior, D.J., Mariani, E., Faulkner, D., Menzies, C.D., 2015. Fault rock lithologies and architecture of the central Alpine fault, New Zealand, revealed by DFDP-1 drilling, *Lithosphere*, 7 (2), p. 155-173.
- Trusheim, F., 1963. Zur Gliederung des Buntsandsteins, *Erdöl-Zeitschrift*, 79, p. 277-292.
- Tsang, Y.W., Witherspoon, P., 1981. Hydromechanical behavior of a deformable rock fracture subject to normal stress, *Journal of Geophysical Research: Solid Earth*, 86 (B10), p. 9287-9298.
- Tyler, N., Ethridge, F.G., 1983. Fluvial architecture of Jurassic uranium-bearing sandstones, Colorado Plateau, western United States, *In*: Collinson, J.D., Lewin, J. (Eds.), *Modern and*

- Ancient Fluvial Systems, International Association of Sedimentologists, Oxford, Special Publication 6, p. 533-548.
- Van der Zwan, C.J., Spaak, P., 1992. Lower to Middle Triassic sequence stratigraphy and climatology of the Netherlands, a model, *Palaeogeography, Palaeoclimatology, Palaeoecology*, 91 (3-4), p. 277-290.
- van Golf-Racht, T.D., 1982. *Fundamentals of fractured reservoir engineering*, Elsevier.
- van Lanen, X.M.T., Hodgetts, D., Redfern, J., Fabuel-Perez, I., 2009. Applications of digital outcrop models: two fluvial case studies from the Triassic Wolfville Fm., Canada and Oukaimeden Sandstone Fm., Morocco, *Geological Journal*, 44 (6), p. 742-760.
- Vennin, E., Van Buchem, F.S.P., Joseph, P., Gaumet, F., Sonnenfeld, M., Rebelle, M., Jemia, H.F.-B., Zijlstra, H., 2003. A 3D outcrop analogue model for Ypresian nummulitic carbonate reservoirs: Jebel Ousselat, northern Tunisia, *Petroleum Geoscience*, 9 (2), p. 145-161.
- Vermilye, J.M., Scholz, C.H., 1995. Relation between vein length and aperture, *Journal of Structural Geology*, 17 (3), p. 423-434.
- Verwer, K., Adams, D., Kenter, J.A.M., 2007. Digital outcrop models: technology and applications, *First break*, 25 (8), p. 57-63.
- Villaescusa, E., Brown, E.T., 1992. Maximum likelihood estimation of joint size from trace length measurements, *Rock Mechanics and Rock Engineering*, 25 (2), p. 67-87.
- Volatili, T., Zambrano, M., Cilona, A., Huisman, B.A.H., Rustichelli, A., Giorgioni, M., Vittori, S., Tondi, E., 2019. From fracture analysis to flow simulations in fractured carbonates: the case study of the Roman Valley Quarry (Majella Mountain, Italy), *Marine and Petroleum Geology*, 100, p. 95-110.
- von Alberti, F., 1834. *Beitrag zu einer Monographie des bunten Sandsteins, Muschelkalks und Keupers, und die Verbindung dieser Gebilde zu einer Formation*, Verlag der J.G. Cotta'schen Buchhandlung, Stuttgart und Tübingen, 366 pp.
- Vosselman, G., Maas, H.-G., 2010. *Airborne and Terrestrial Laser Scanning*, CRC, Boca Raton, 318 pp.
- Wang, L., Cardenas, M.B., Slotke, D.T., Ketcham, R.A., Sharp, J.M., 2015. Modification of the Local Cubic Law of fracture flow for weak inertia, tortuosity, and roughness, *Water Resources Research*, 51 (4), p. 2064-2080.
- Warren, J.E., Root, P.J., 1963. The behavior of naturally fractured reservoirs, *Society of Petroleum Engineers Journal*, 3 (3), p. 245-255.

- Wenli, Y., Sharifzadeh, M., Yang, Z., Xu, G., Fang, Z., 2019. Assessment of fracture characteristics controlling fluid flow in discrete fracture networks (DFN), *Journal of Petroleum Science and Engineering*, 178, p. 1104-1111.
- Wenzel, F., Brun, J.-P., 1991. A deep reflection seismic line across the Northern Rhine Graben, *Earth and Planetary Science Letters*, 104 (2-4), p. 140-150.
- Wetzel, A., Allia, V., 2000. The significance of hiatus beds in shallow-water mudstones: an example from the Middle Jurassic of Switzerland, *Journal of Sedimentary Research*, 70 (1), p. 170-180.
- Wheeler, H.E., 1964. Base level, lithosphere surface and time stratigraphy, *Geological Society of America Bulletin*, 75, p. 599-610.
- Wickert, F., Eisbacher, G.H., 1988. Two-sided Variscan thrust tectonics in the Vosges Mountains, northeastern France, *Geodinamica Acta*, 2 (3), p. 101-120.
- Will, R., Archer, R.A., Dershowitz, W.S., 2005. Integration of seismic anisotropy and reservoir performance data for characterization of naturally fractured reservoirs using discrete feature network models, *SPE Reservoir Evaluation & Engineering*, 8 (2), p. 132-142.
- Wilson, C.E., Aydin, A., Karimi-Fard, M., Durlofsky, L.J., Sagy, A., Brodsky, E.E., Kreylos, O., Kellogg, L.H., 2011. From outcrop to flow simulation: constructing discrete fracture models from a LIDAR survey, *American Association of Petroleum Geologists Bulletin*, 95 (11), p. 1883-1905.
- Witherspoon, P.A., Wang, J.S.Y., Iwai, K., Gale, J.E., 1979. Validity of cubic law for fluid flow in a deformable rock fracture, *Water Resources Research*, 16 (6), p. 1016-1024.
- Wolburg, J., 1961. Sedimentationszyklen und Stratigraphie des Buntsandstein in NW Deutschland, *Geotektonische Forschung*, 14, p. 7-74.
- Wolburg, J., 1968. Vom zyklischen Aufbau des Buntsandsteins, *Neues Jahrbuch für Geologie und Paläontologie, Monatshefte*, 9, p. 535-559.
- Wong, T.F., Fredrich, J.T., Gwanmesia, G.D., 1989. Crack aperture statistics and pore space fractal geometry of Westerly Granite and Rutland Quartzite: implications for an elastic contact model of rock compressibility, *Journal of Geophysical Research: Solid Earth*, 94 (B8), p. 10267-10278.
- Woodcock, N.H., 1977. Specification of fabric shapes using an eigenvalue method, *Geological Society of America Bulletin*, 88 (9), p. 1231-1236.
- Zeeb, C., 2013. Characterization and flow simulations of discrete fracture networks, *Doctoral Thesis, Eberhard Karls Universität Tübingen, Tübingen*, 161 pp.

- 
- Zhang, L., Einstein, H.H., Dershowitz, W.S., 2002. Stereological relationship between trace length and size distribution of elliptical discontinuities, *Géotechnique*, 52 (6), p. 419-433.
- Zhao, Z., 2017. Application of discrete element approach in fractured rock masses, *In: Shojaei, A.K., Shao, J. (Eds.), Porous Rock Fracture Mechanics with Application to Hydraulic Fracturing, Drilling and Structural Engineering*, Woodhead Publishing, Duxford, Cambridge, Kidlington, p. 145-176.
- Ziegler, P.A., 1990. Geological Atlas of Western and Central Europe, Shell International Petroleum Maatschappij, The Hague, 239 pp.
- Ziegler, P.A., 1992. European Cenozoic rift system, *Tectonophysics*, 208 (1-3), p. 91-111.
- Ziegler, P.A., 1994. Cenozoic rift system of Western and Central Europe: an overview, *Geologie en Mijnbouw*, 73 (2-4), p. 99-127.
- Ziegler, P.A., Dèzes, P., 2006. Crustal evolution of Western and Central Europe, *In: Gee, D.G., Stephenson, R.A. (Eds.), European Lithosphere Dynamics*, Geological Society, London, Memoir 32, p. 43-56.





## **Appendix 1      Lithofacies Types after Miall (1977)**

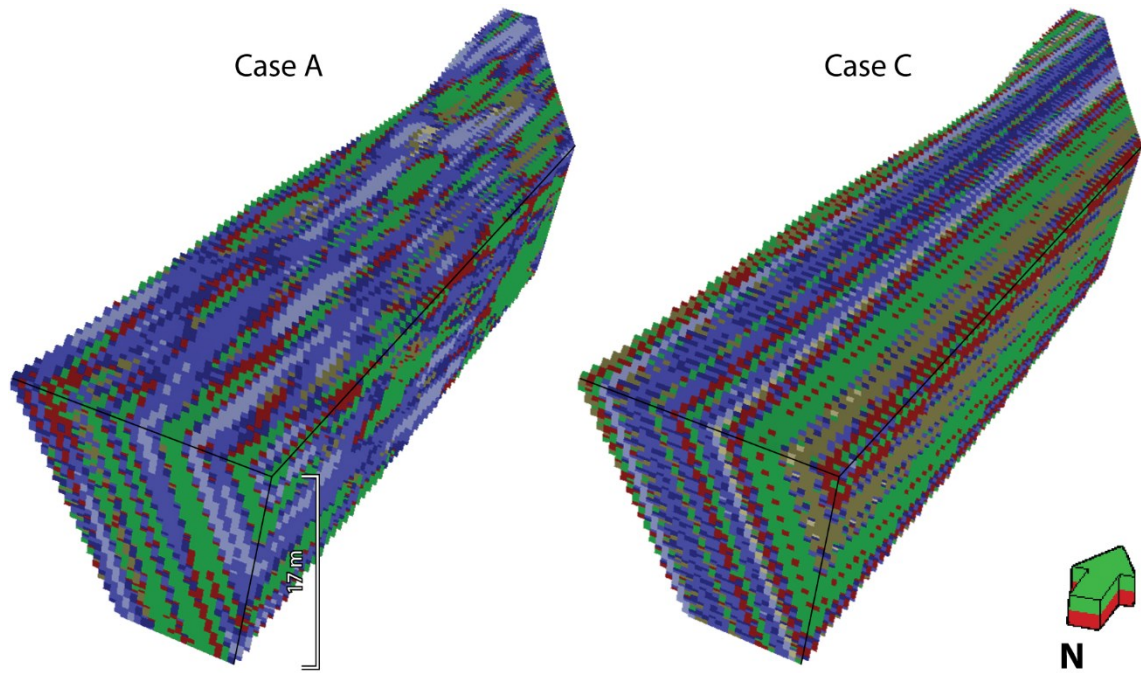


Facies Code	Lithofacies	Sedimentary structures	Interpretation
Gms	Massive, matrix supported gravel	None	Debris flow deposits
Gm	Massive or crudely bedded gravel	Horizontal bedding, imbrication	Longitudinal bars, lag deposits, sieve deposits
Gt	Gravel, stratified	Trough crossbeds	Minor channel fills
Gp	Gravel, stratified	Planar crossbeds	Linguoid bars or deltaic growths from older bar remnants
St	Sand, medium to very coarse, may be pebbly	Solitary (theta) or grouped (pi) trough crossbeds	Dunes (lower flow regime)
Sp	Sand, medium to coarse, may be pebbly	Solitary (alpha) or grouped (omicron) planar crossbeds	Linguoid, transverse bars, sand waves (lower flow regime)
Sr	Sand, very fine to coarse	Ripple marks of all types	Ripples (lower flow regime)
Sh	Sand, very fine to very coarse, may be pebbly	Horizontal lamination, parting or streaming lineation	Planar bed flow (l. and u. flow regime)
Sl	Sand, fine	Low angle (<10°) crossbeds	Scour fills, crevasse splays, antidunes
Se	Erosional scours with intraclasts	Crude crossbedding	Scour fills
Ss	Sand, fine to coarse, may be pebbly	Broad, shallow scours including eta cross-stratification	Scour fills
Sse, She, Spe	Sand	Analogous to Ss, Sh, Sp	Eolian deposits
Fl	Sand, silt, mud	Fine lamination, very small ripples	Overbank or waning flood deposits
Fsc	Silt, mud	Laminated to massive	Backswamp deposits
Fcf	Mud	Massive, with freshwater molluscs	Backswamp pond deposits
Fm	Mud, silt	Massive, desiccation cracks	Overbank or drape deposits
Fr	Silt, mud	Rootlets	Seatearth
C	Coal, carbonaceous mud	Plants, mud films	Swamp deposits
P	Carbonate	Pedogenic features	Soil



## **Appendix 2      Fault Core Facies Type Distribution Cases A and C**







**Fault core facies types**

Lithological types

- |  |  |
|--|--|
|  Sc: Sandstone consolidated     |  Gs: Gouge, silt unconsolidated   |
|  Ss: Sandstone spreading      |  Gc: Gouge, clay unconsolidated |
|  Su: Sandstone unconsolidated |  |

Structural types

- |   |
|---|
|  DBC: Deformation band cluster |
|  SZ: Slip zone               |





## **Appendix 3      Calculation of Truncation Values**



<b>Original truncation values</b>				
DZ Set	Top truncation [%]		Base truncation [%]	
	Original	Rounded	Original	Rounded
1	68.39	70	32.90	30
2	58.50	60	56.60	60
3	70.59	70	44.12	40

<b>Mean correction values (MCV)</b>				
DZ Set	No. of reached top zones		No. of reached base zones	
	Mean	Rounded	Mean	Rounded
1	3.56	4	2.89	3
2	4.22	4	4.11	4
3	3.33	3	3.67	4

<b>Corrected truncation values of each geological unit (GU)</b>					
GU	DZ Set	No. of reached zones		Corrected truncation value	
		Top	Base	Top	Base
1	1	3	MCV	90	60
	2	3	MCV	90	90
	3	3	MCV	90	80
2	1	2	MCV	90	60
	2	4	MCV	90	90
	3	2	MCV	90	80
3	1	5	MCV	90	60
	2	6	MCV	90	90
	3	5	MCV	90	80
4	1	2	3	90	60
	2	2	3	80	90
	3	1	3	80	70
5	1	4	4	90	70
	2	6	4	90	90
	3	5	4	90	80

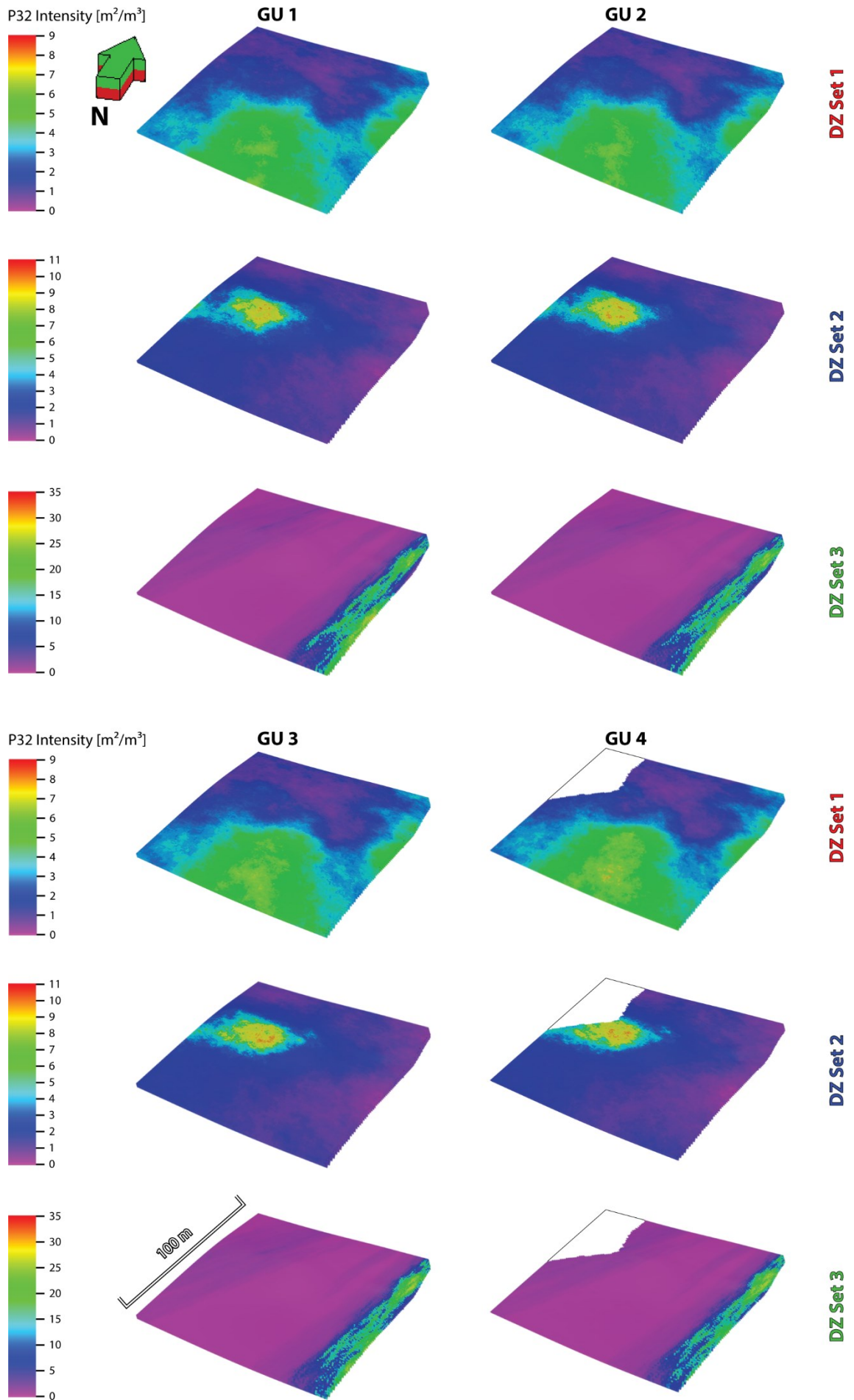
## Calculation of Truncation Values

### Corrected truncation values of each geological unit (GU)

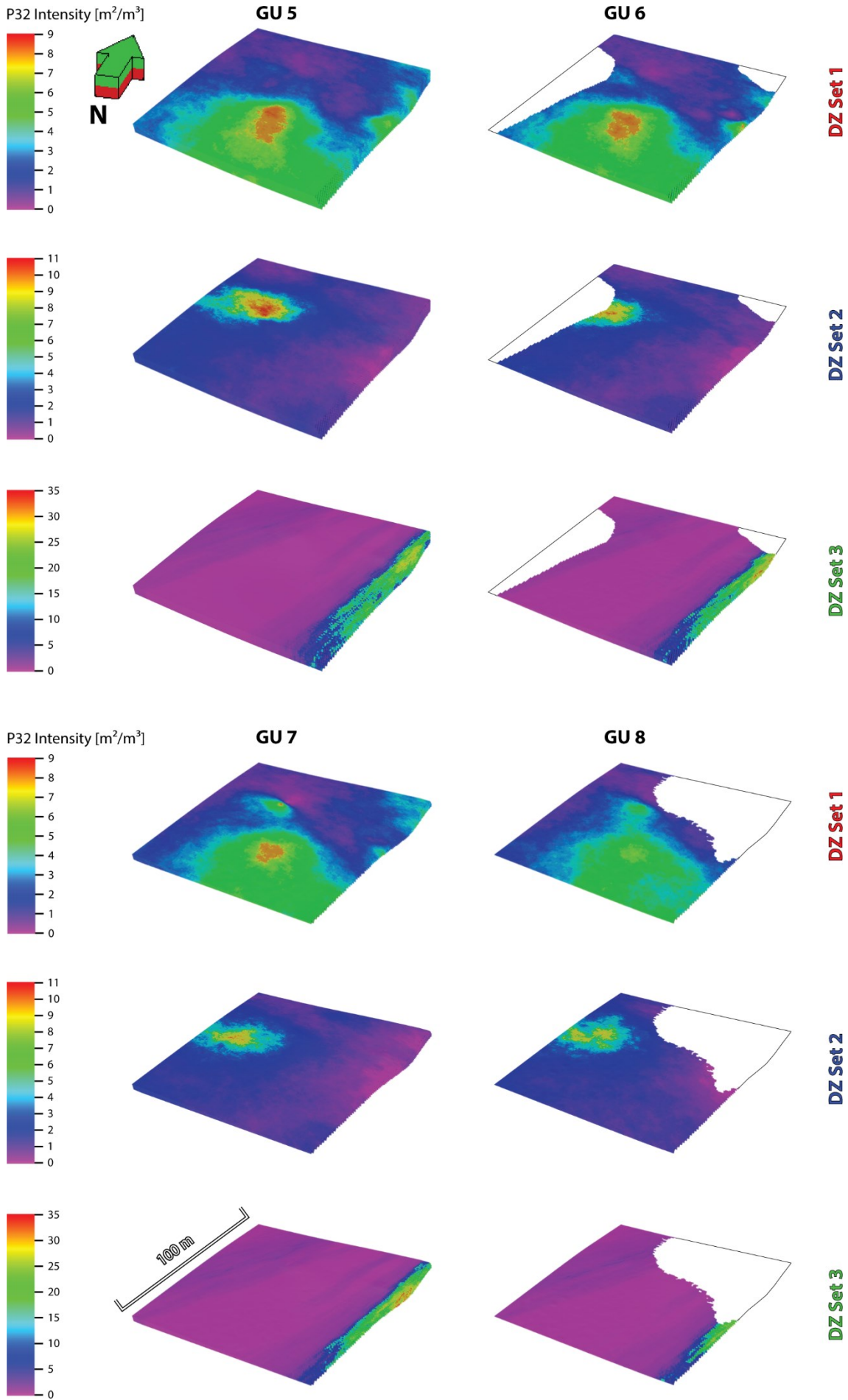
GU	DZ Set	No. of reached zones		Corrected truncation value	
		Top	Base	Top	Base
6	1	5	2	90	50
	2	5	4	90	90
	3	4	3	90	70
7	1	5	3	90	60
	2	5	5	90	90
	3	4	3	90	70
8	1	3	2	90	50
	2	4	2	90	80
	3	3	2	90	60
9	1	3	3	90	60
	2	3	4	90	90
	3	3	4	90	80
10	1	MCV	4	90	70
	2	MCV	4	90	90
	3	MCV	4	90	80
11	1	MCV	5	90	80
	2	MCV	6	90	90
	3	MCV	4	90	80
12	1	MCV	5	80	80
	2	MCV	5	90	90
	3	MCV	6	90	90

## **Appendix 4      Intensity Results of all Geological Units of the DZ**

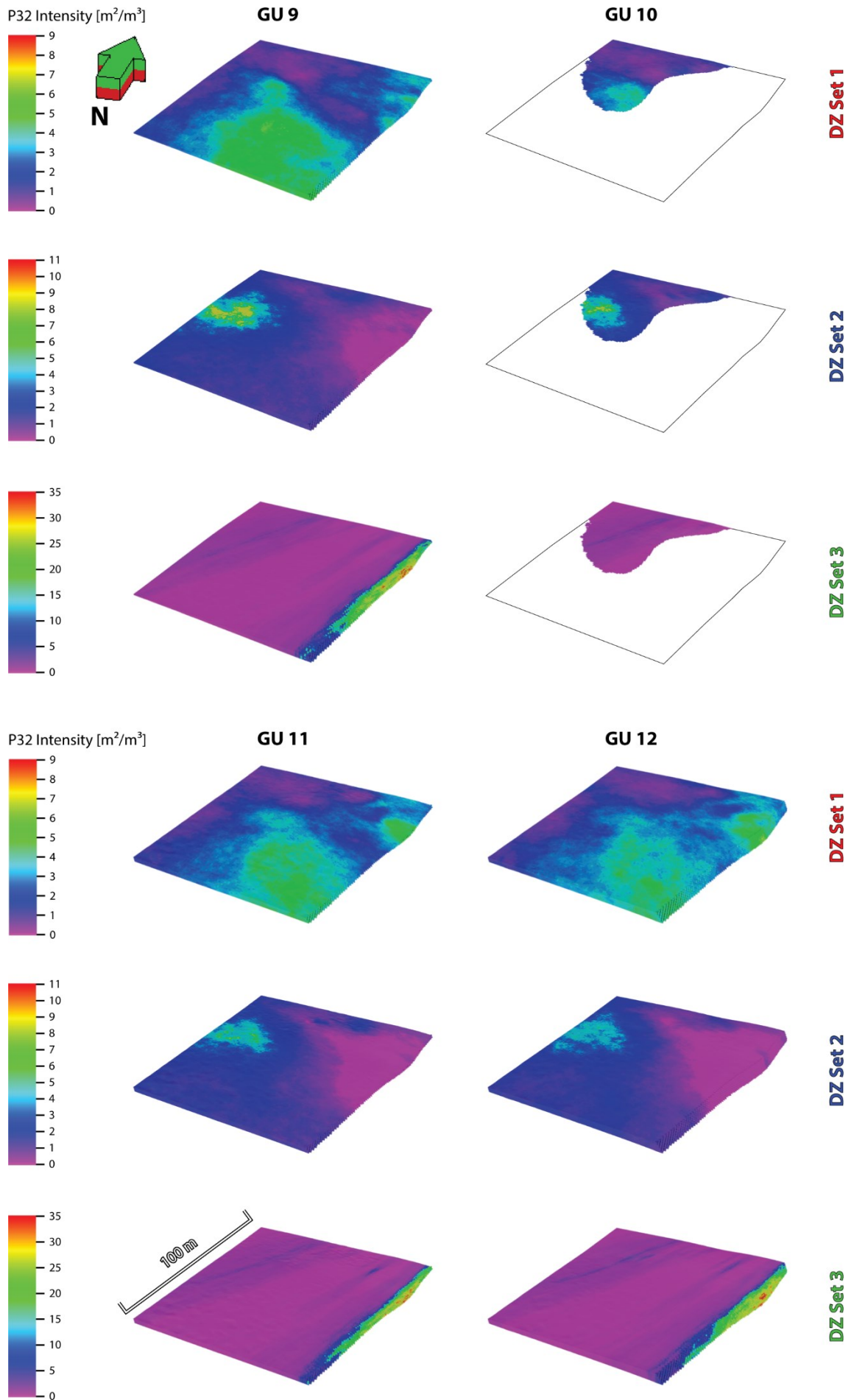




Intensity Results of all Geological Units of the DZ



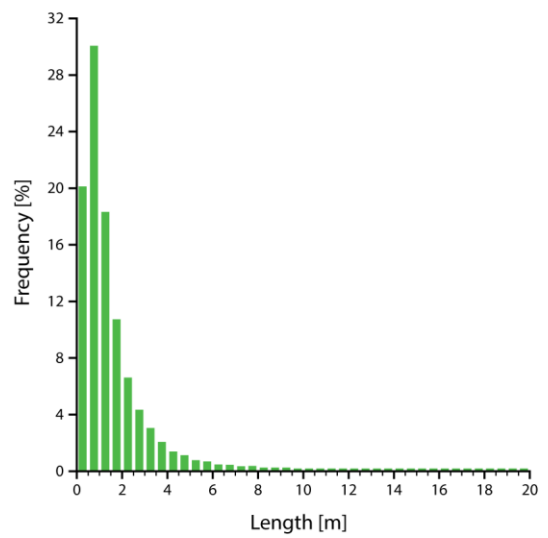
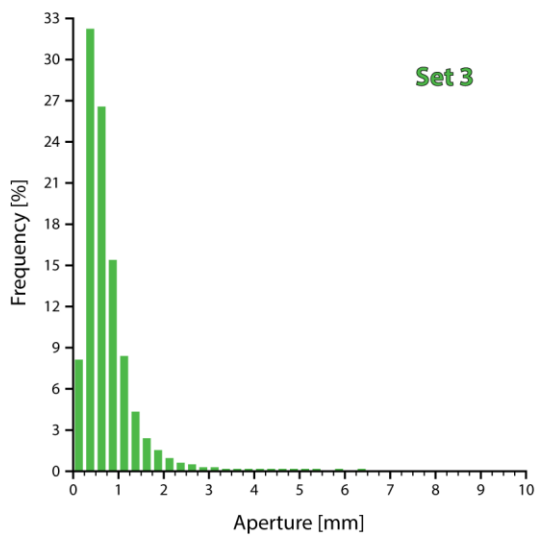
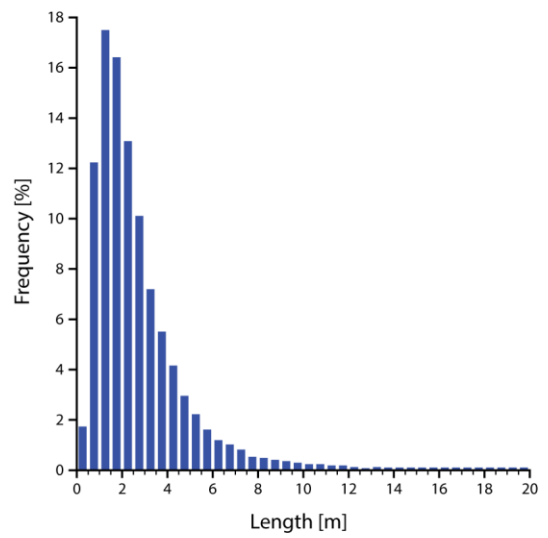
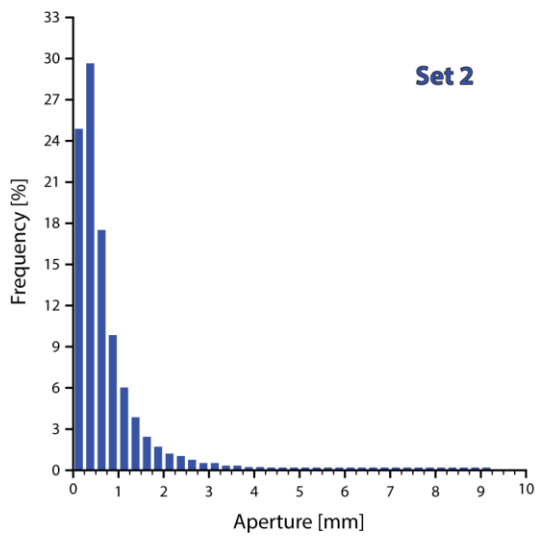
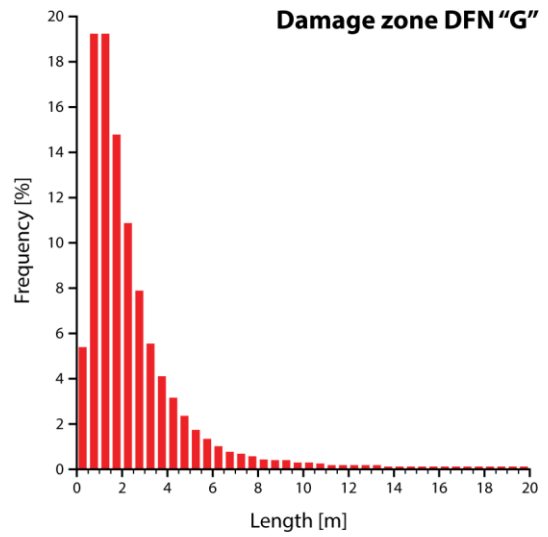
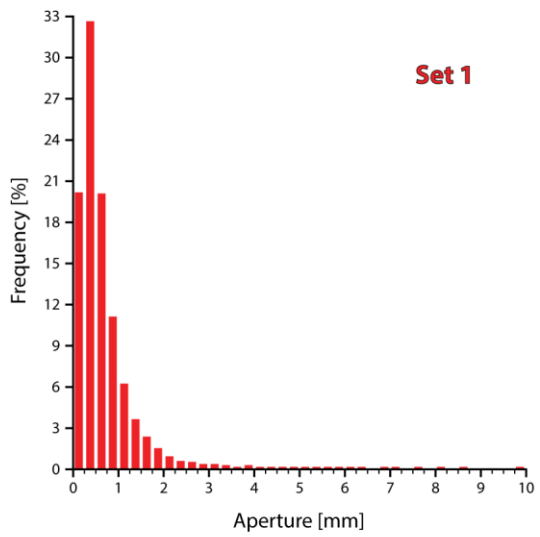




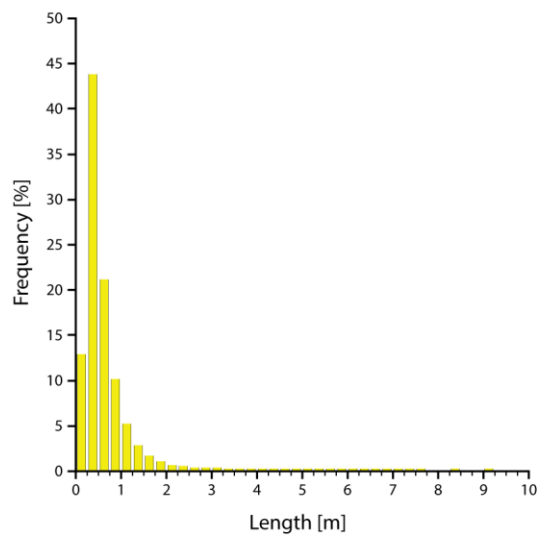
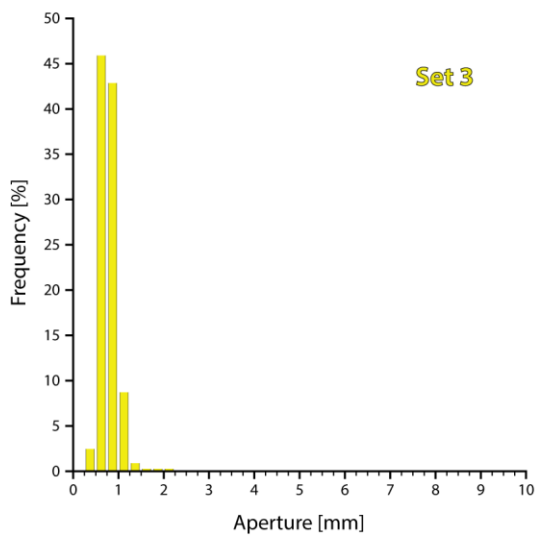
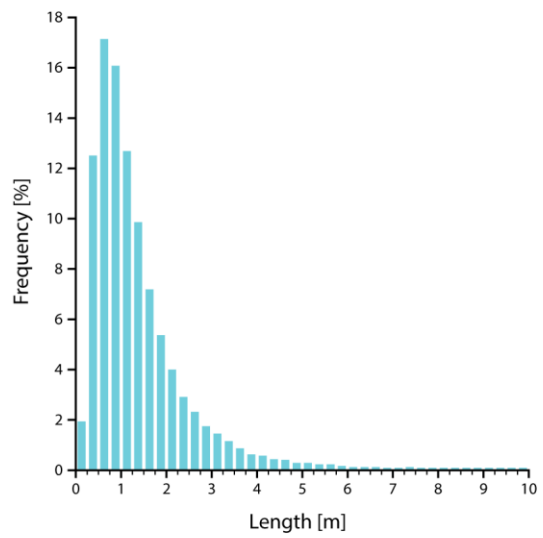
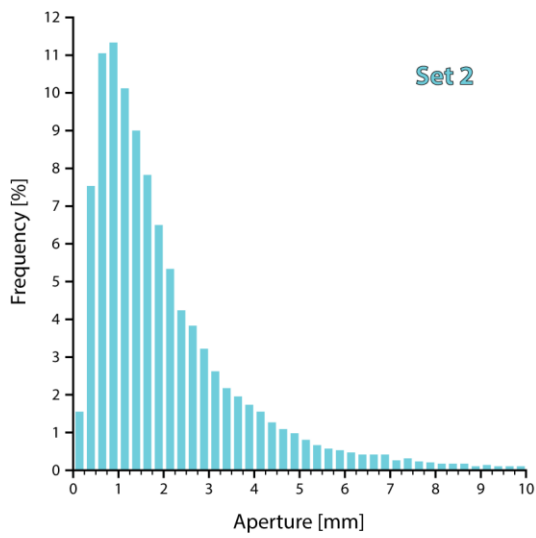
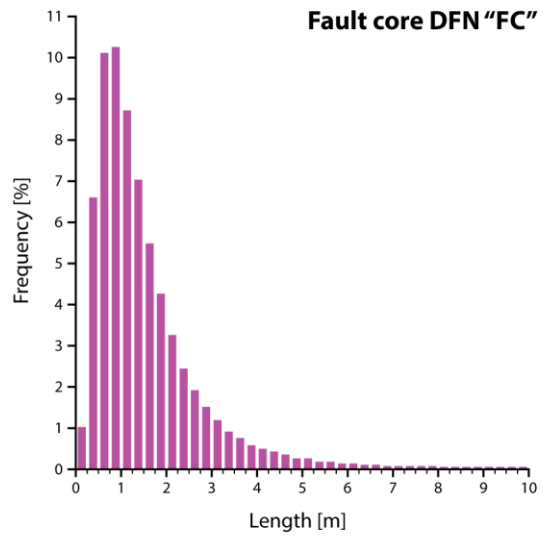
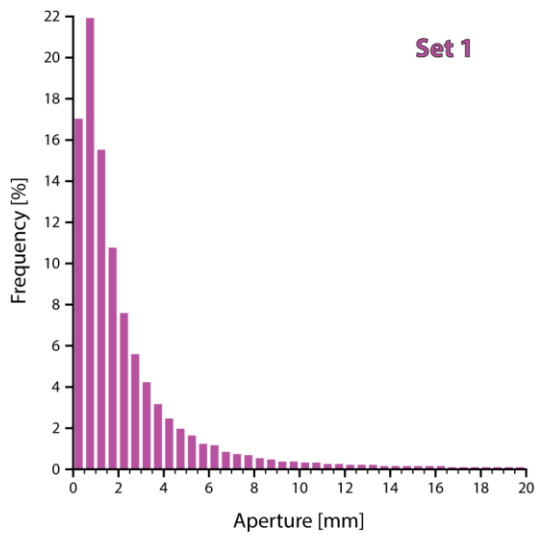


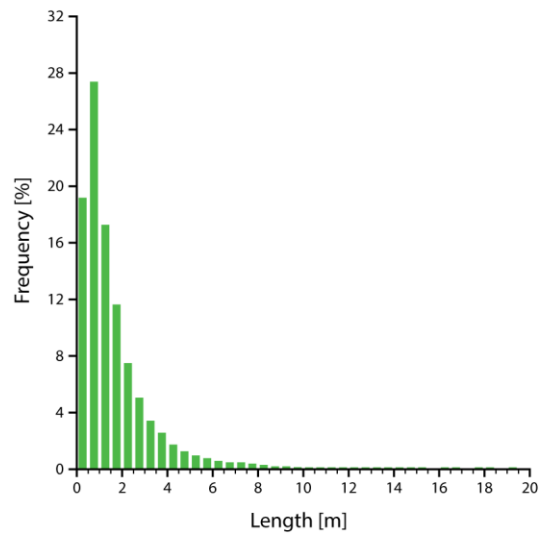
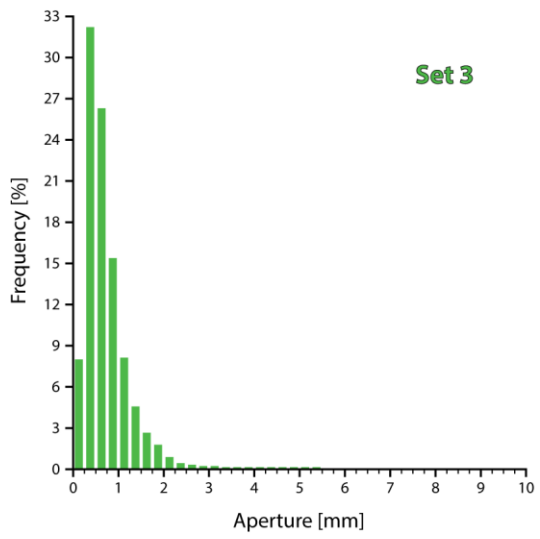
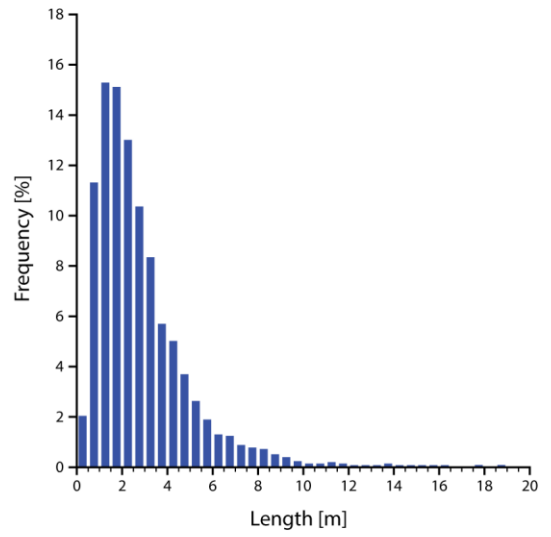
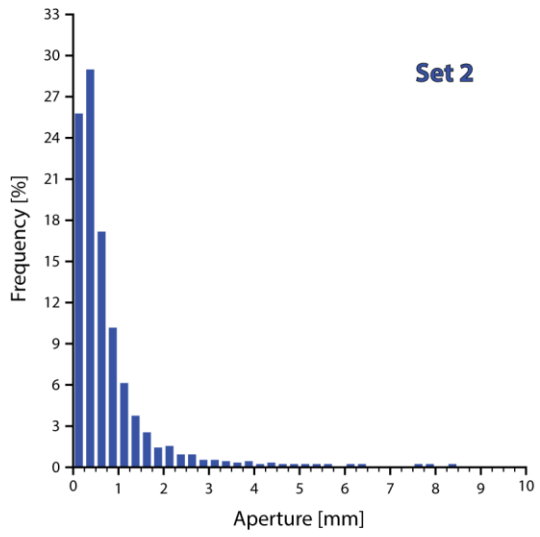
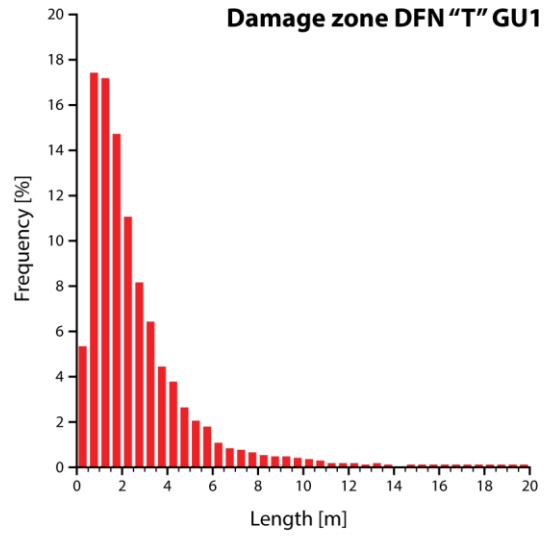
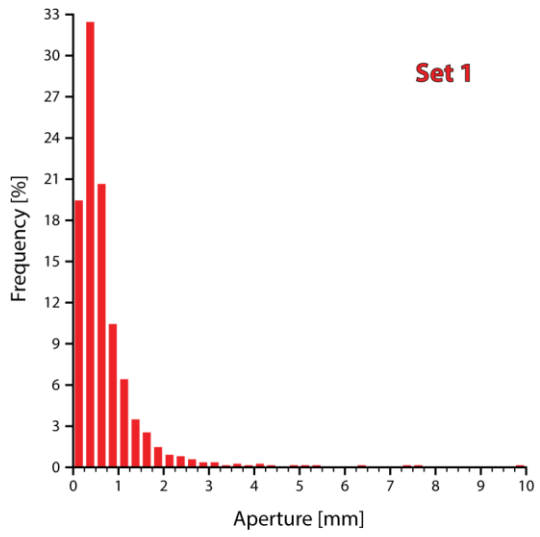
## **Appendix 5      Full Aperture and Length Distribution Results**



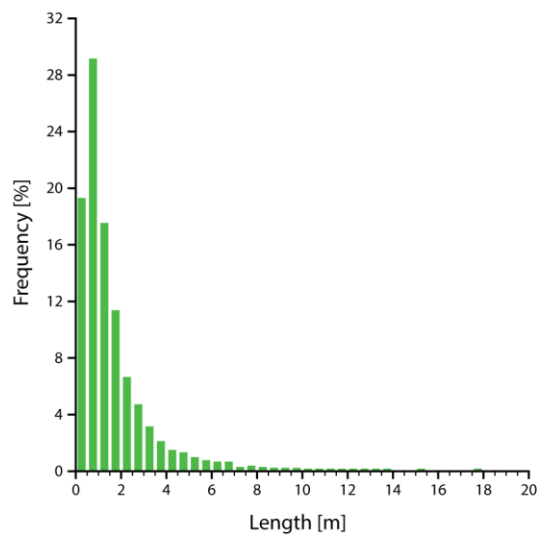
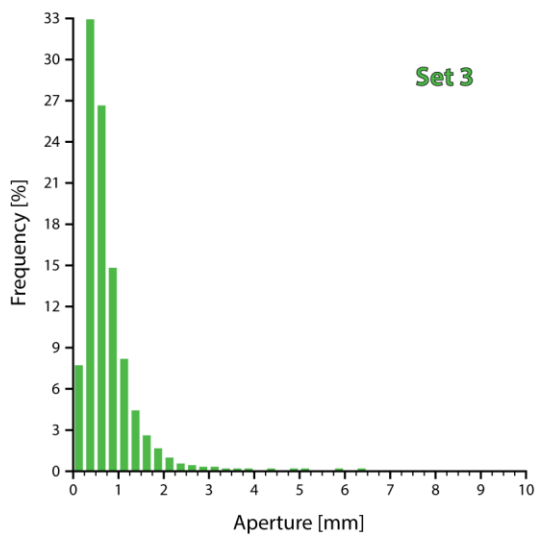
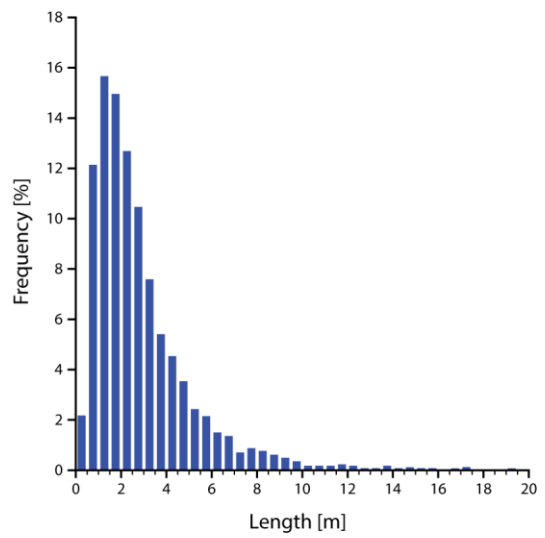
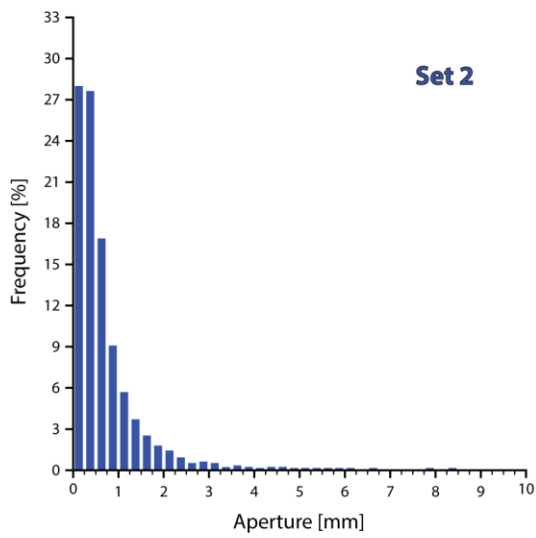
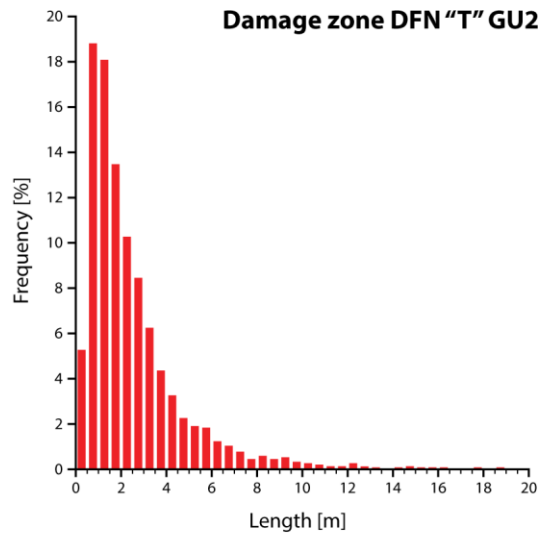
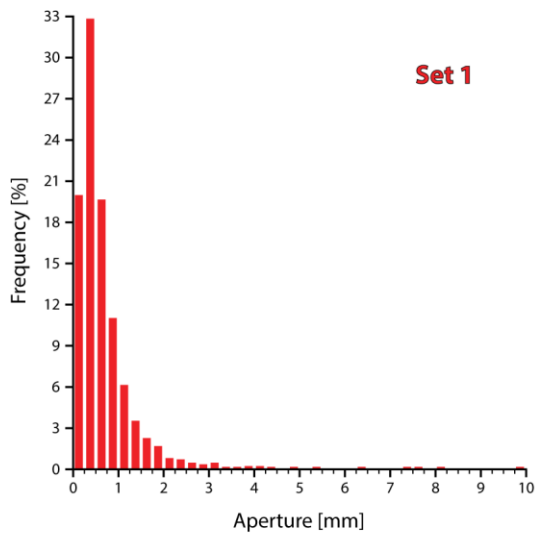


# Full Aperture and Length Distribution Results



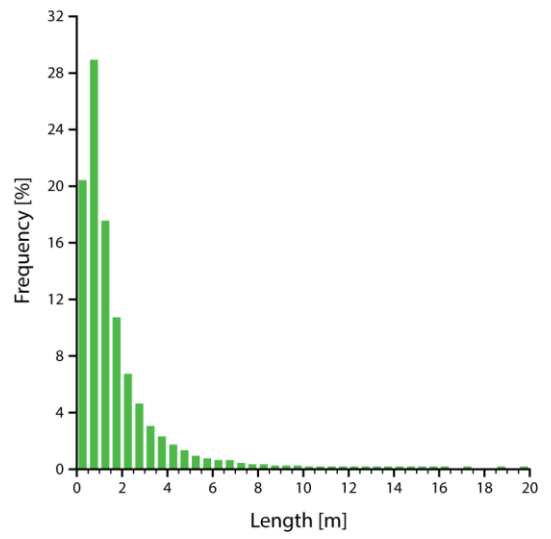
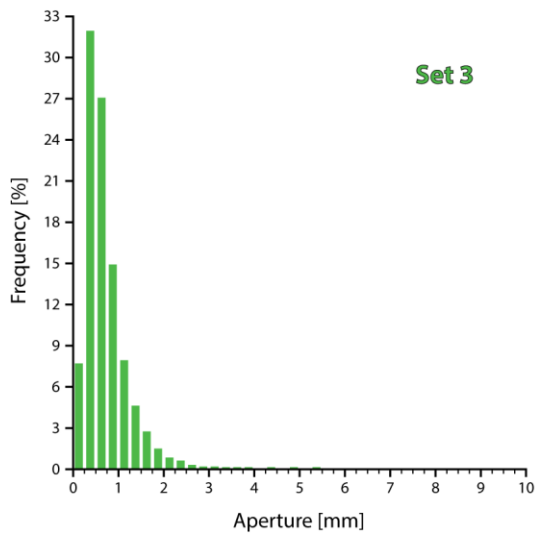
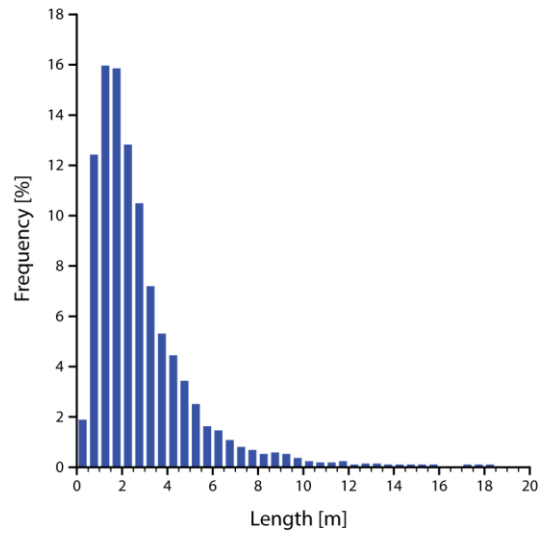
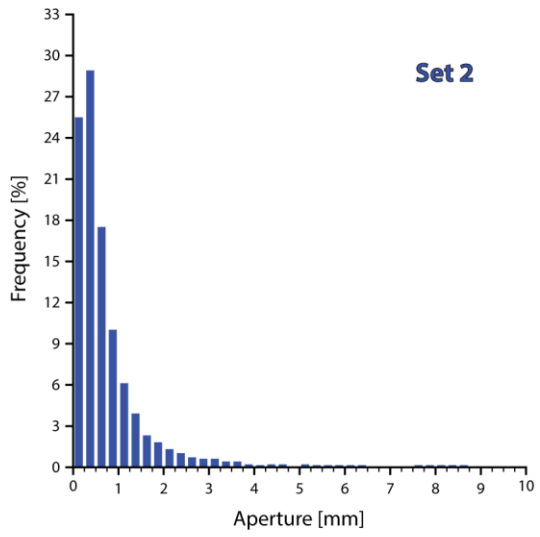
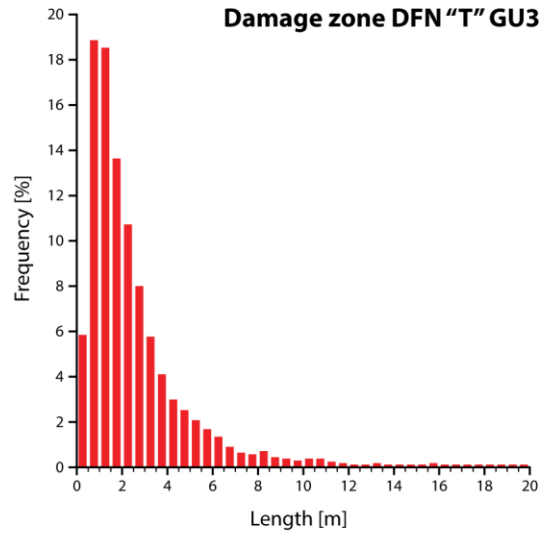
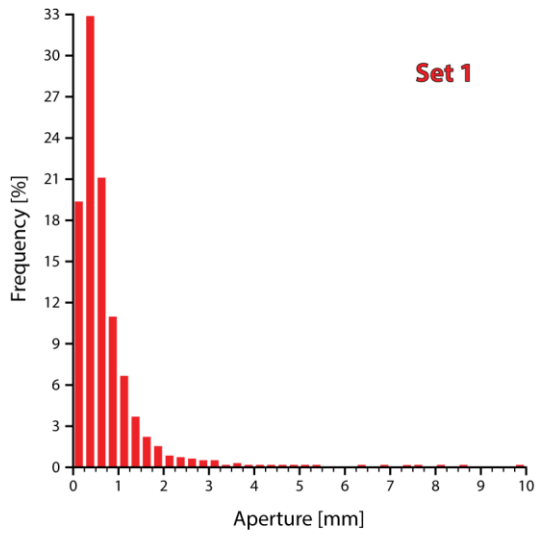


# Full Aperture and Length Distribution Results

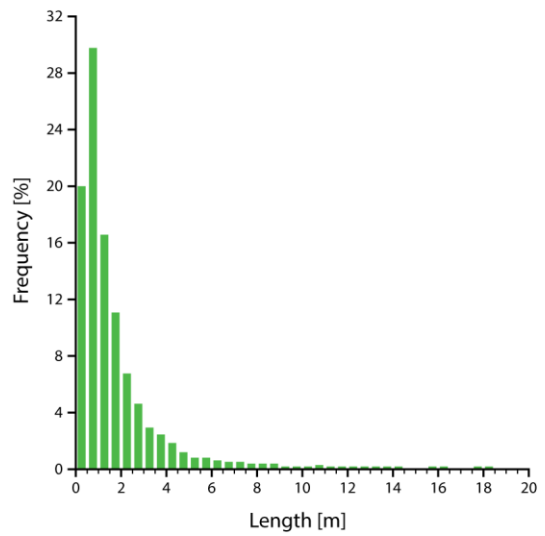
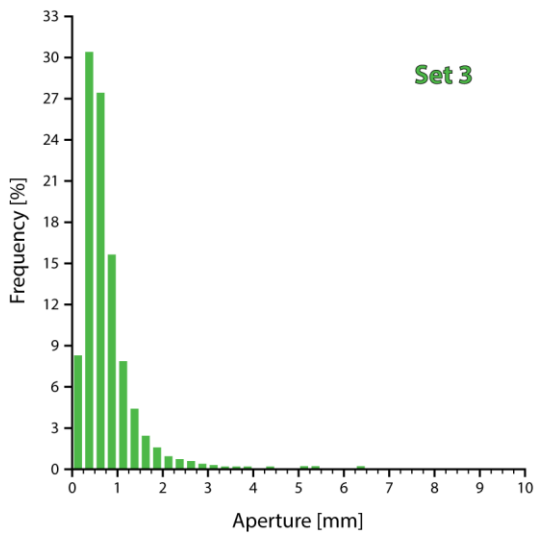
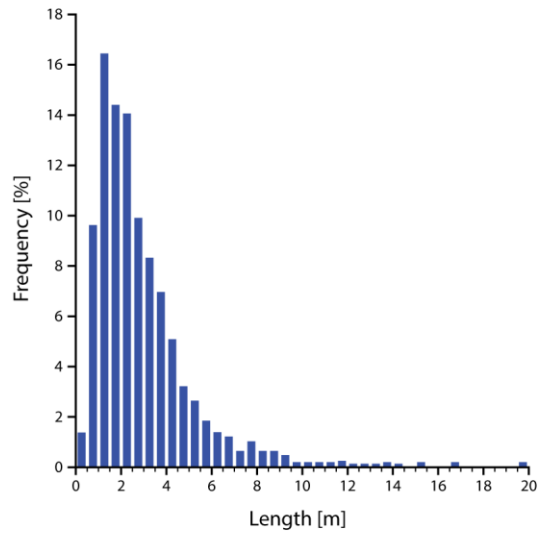
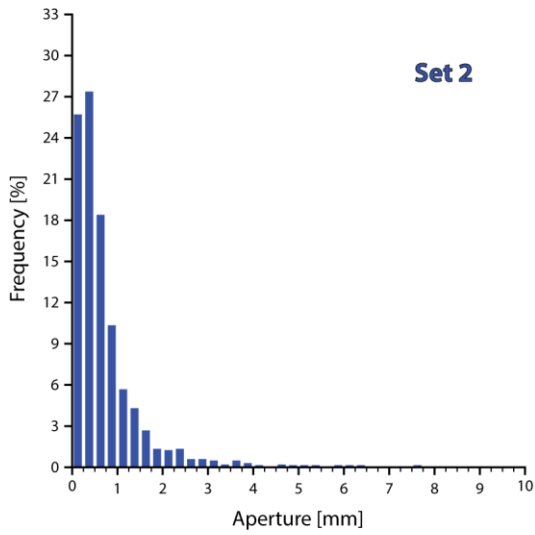
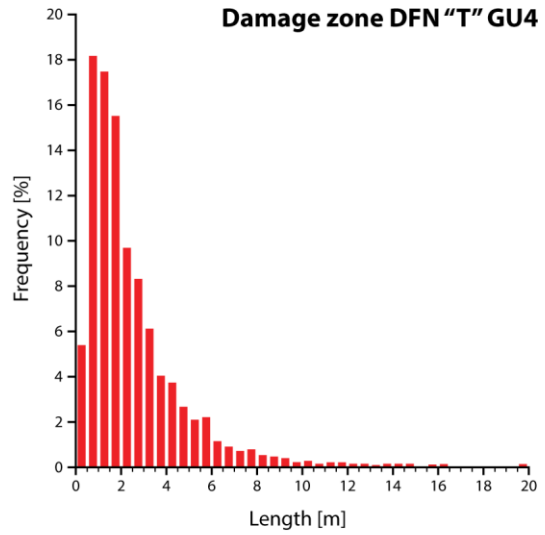
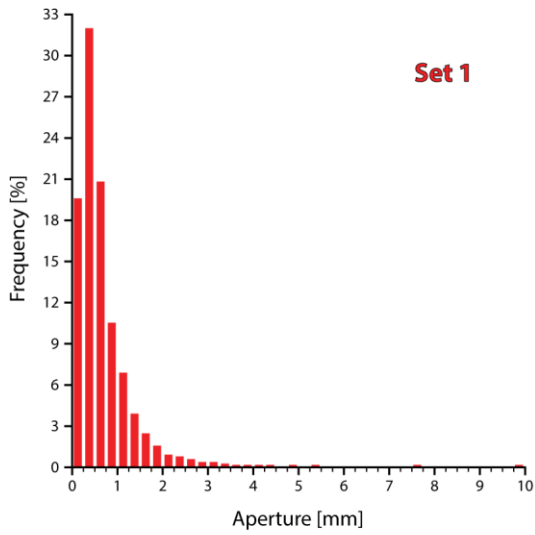


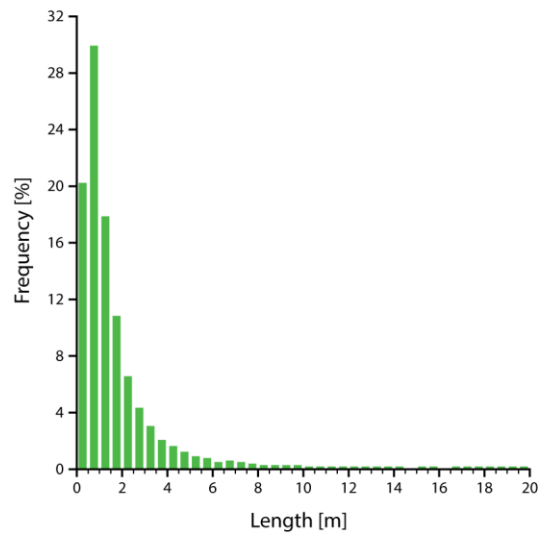
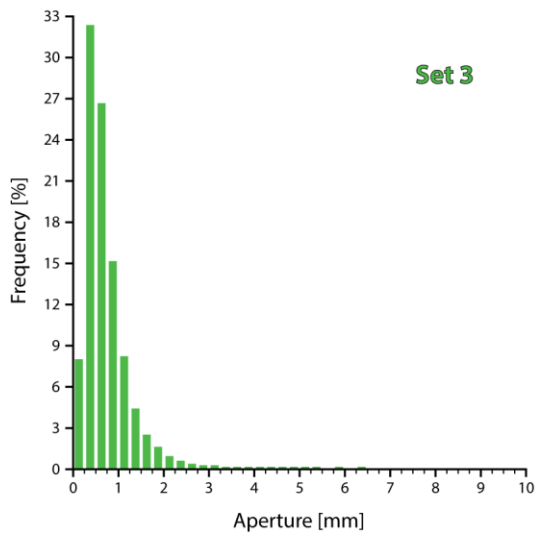
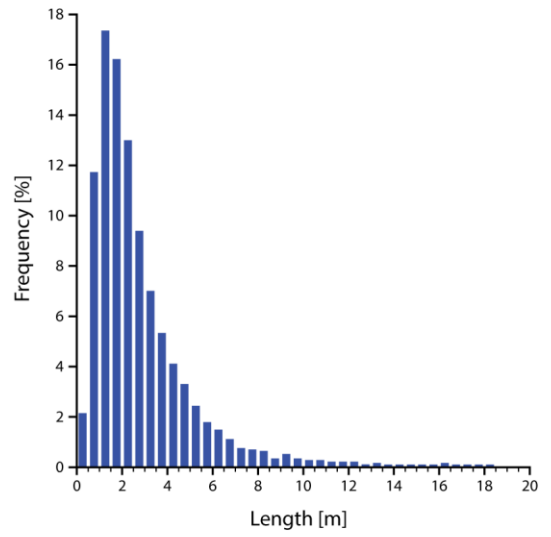
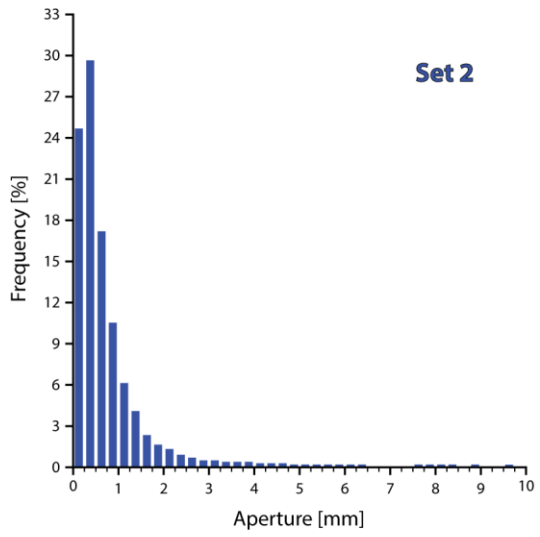
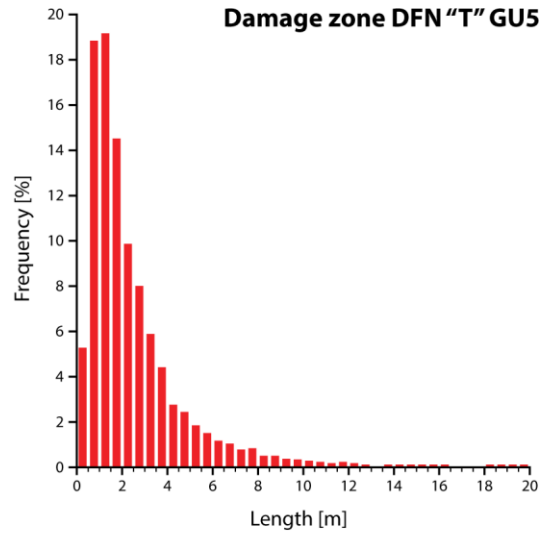
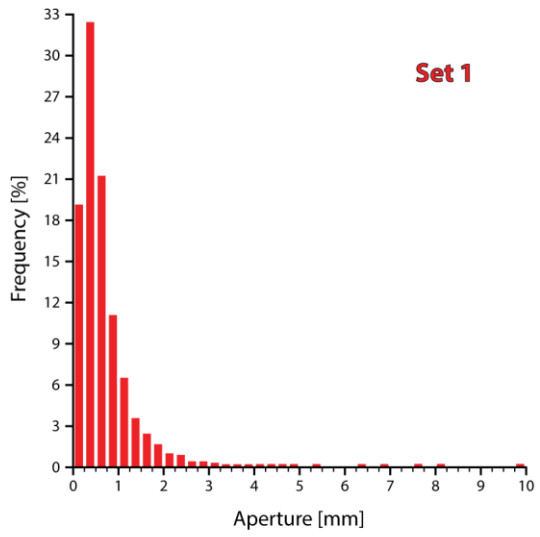


# Full Aperture and Length Distribution Results

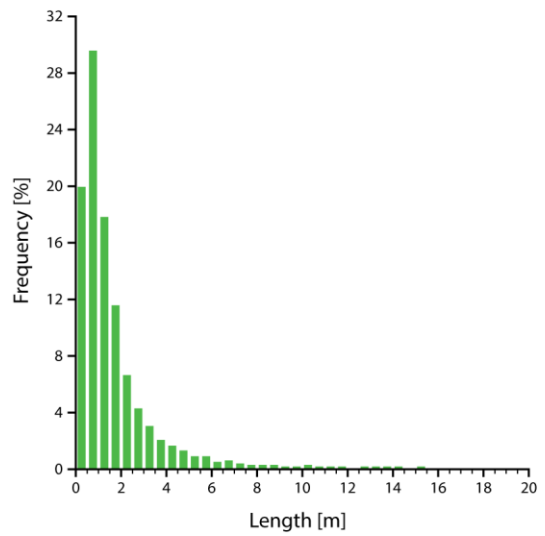
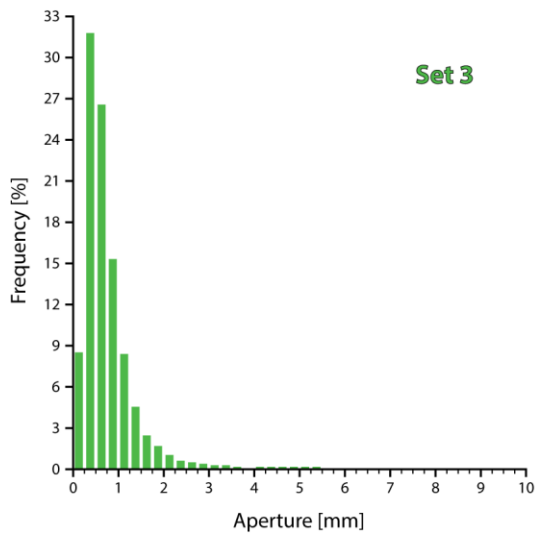
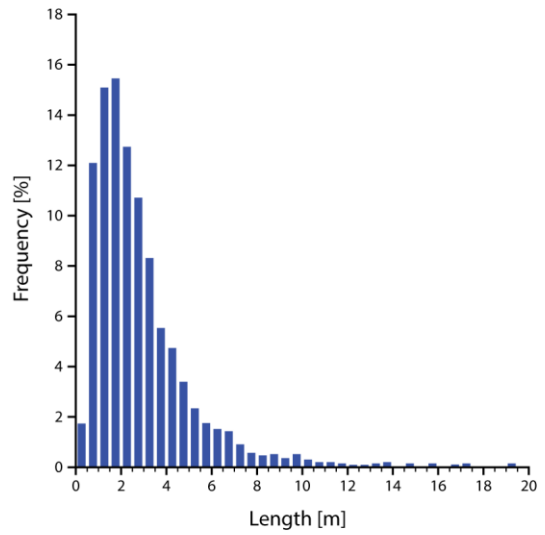
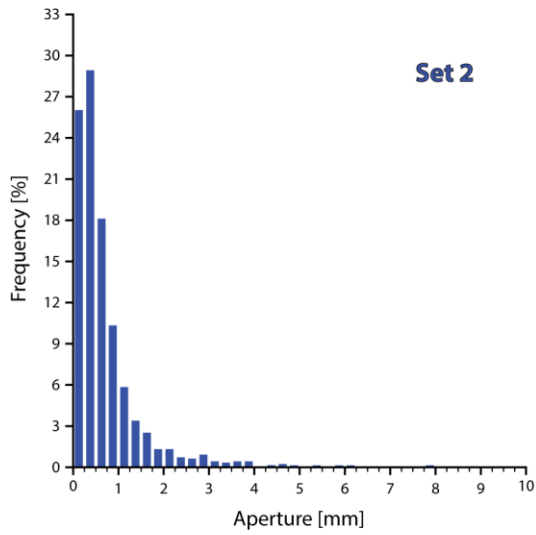
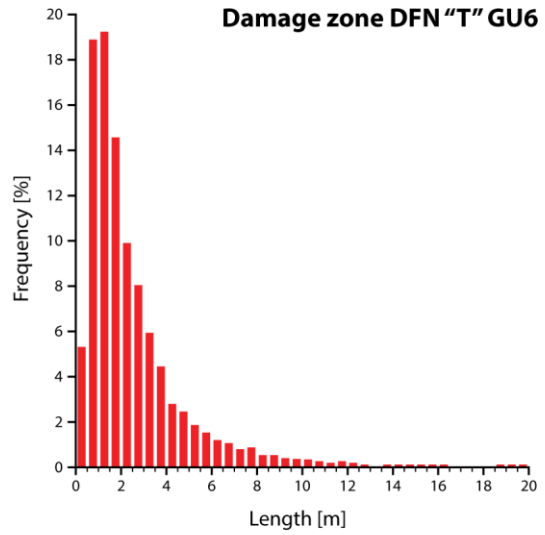
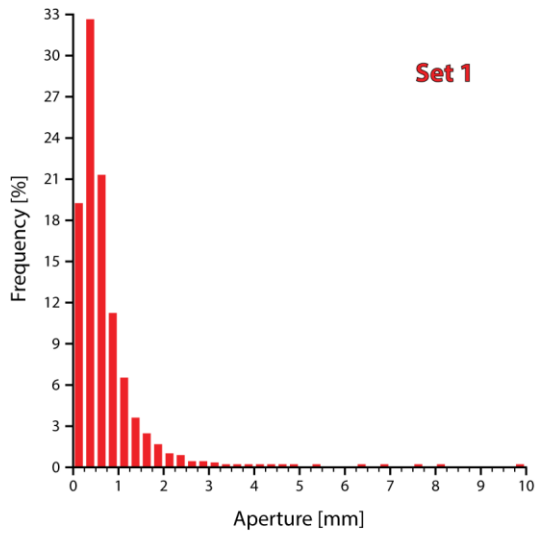


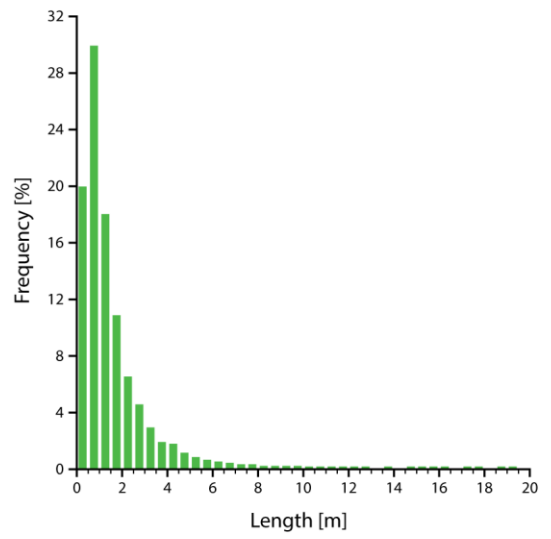
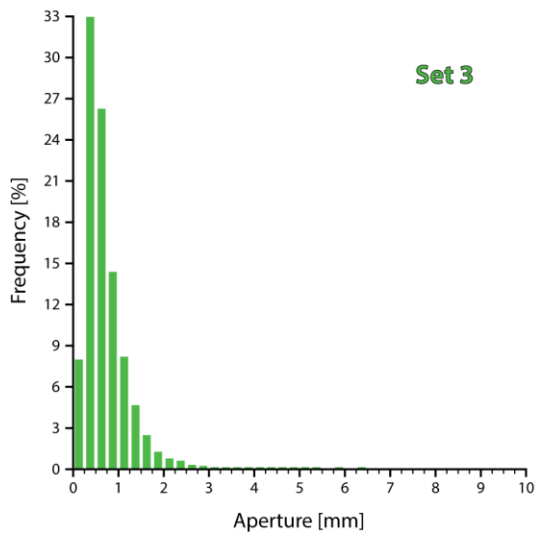
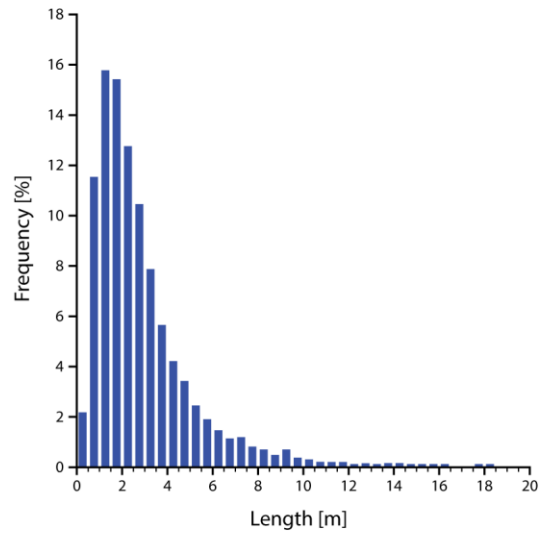
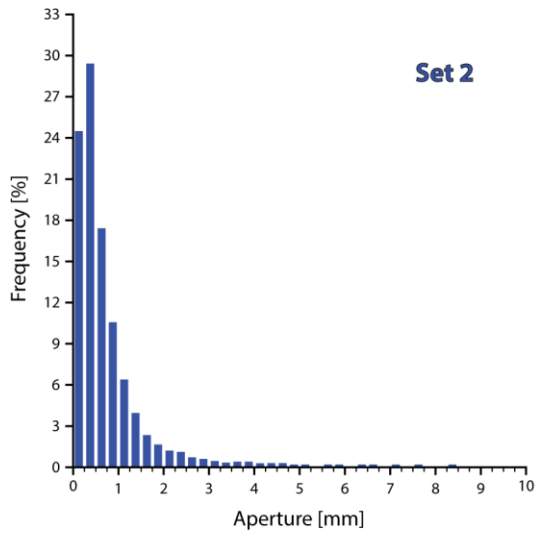
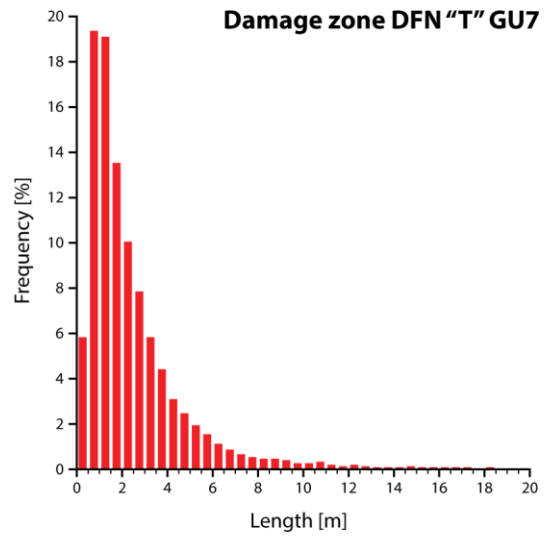
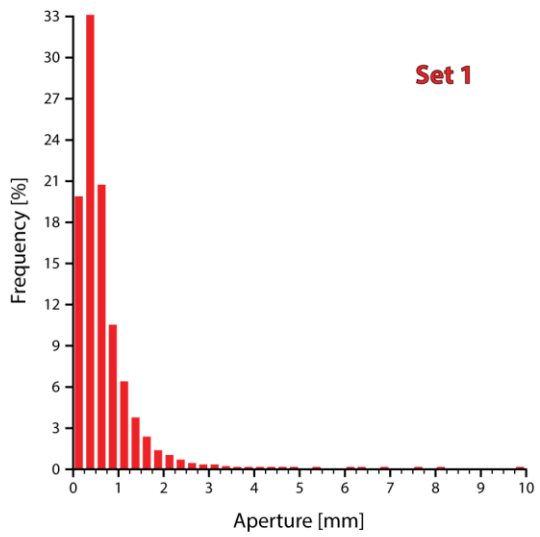
# Full Aperture and Length Distribution Results



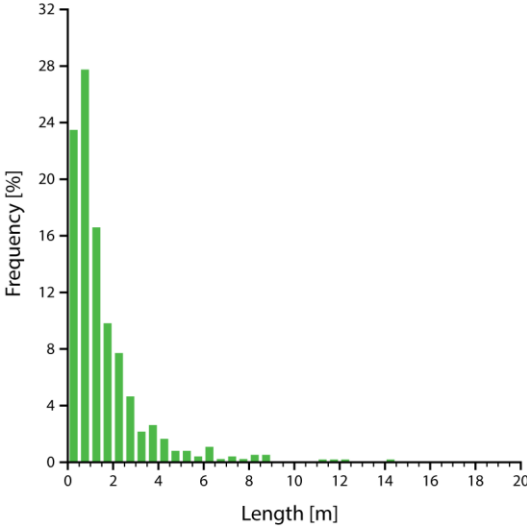
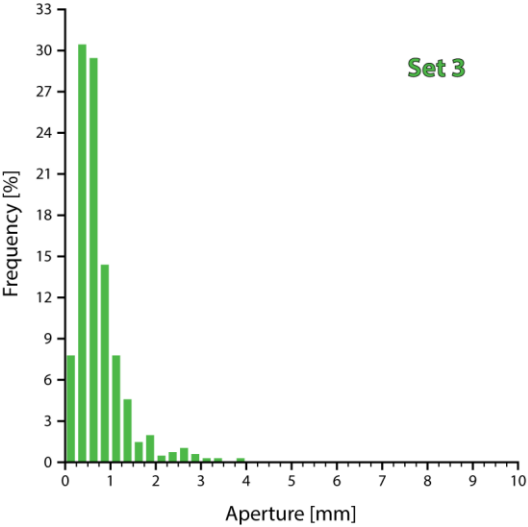
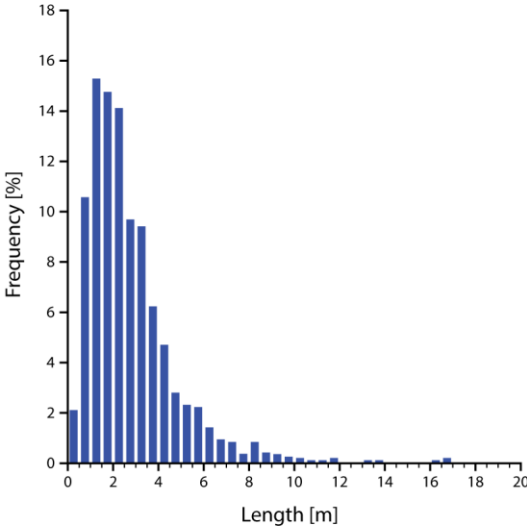
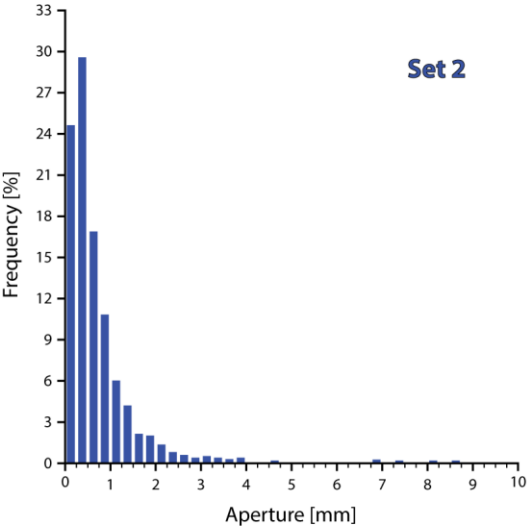
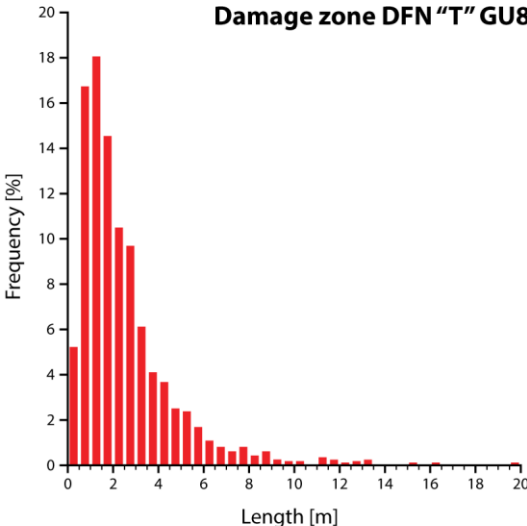
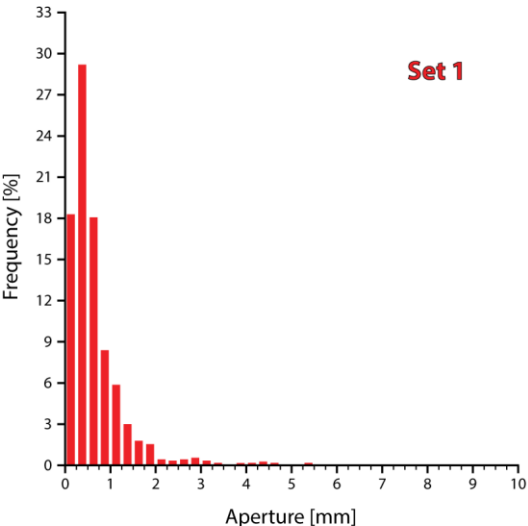


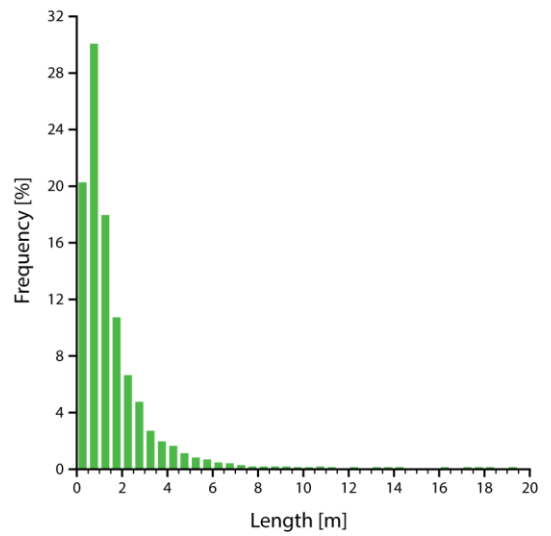
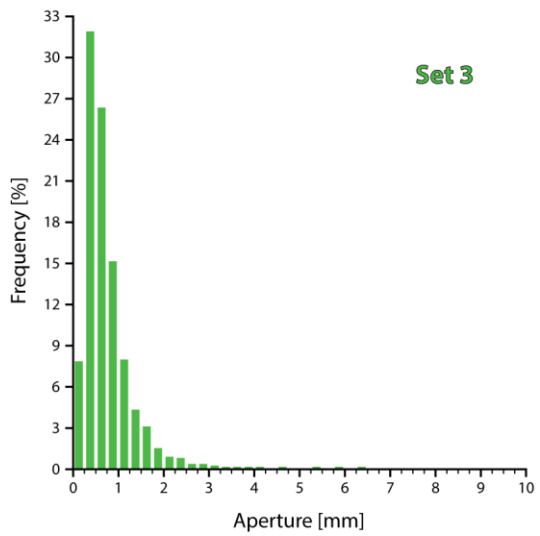
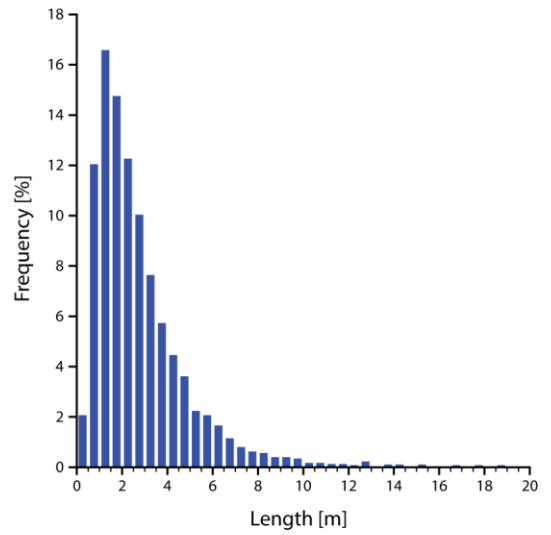
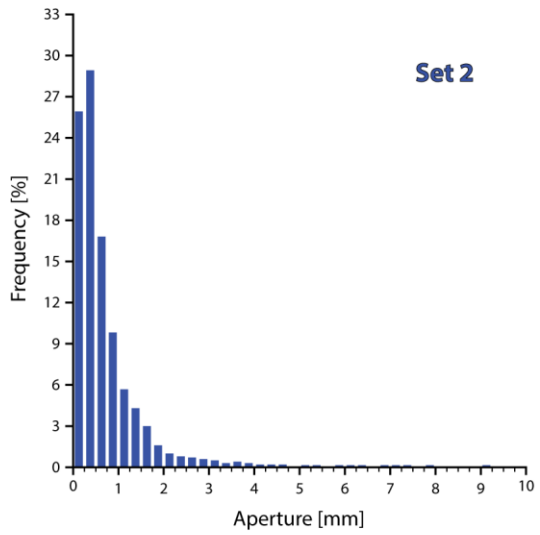
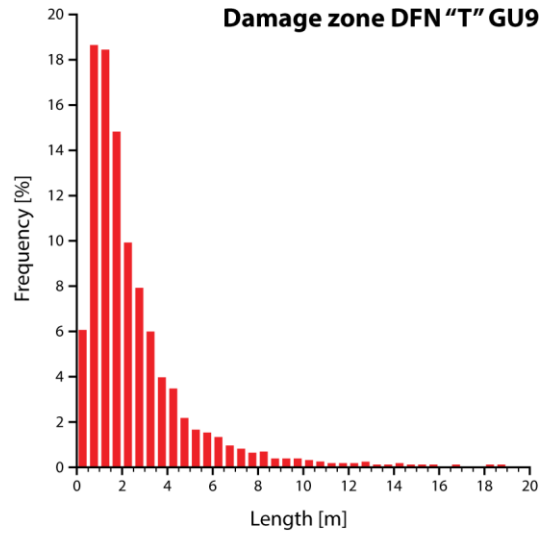
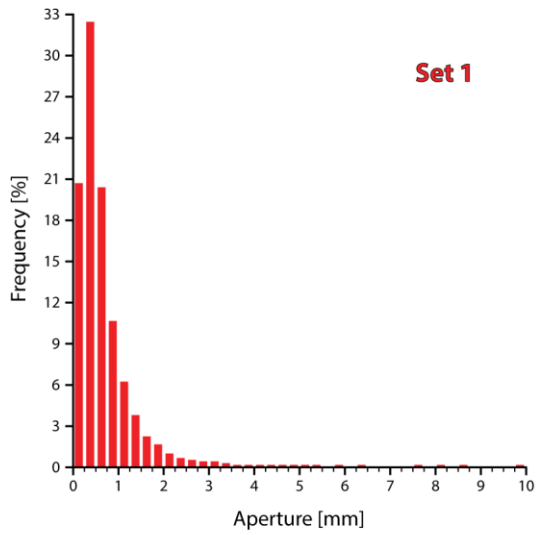
# Full Aperture and Length Distribution Results



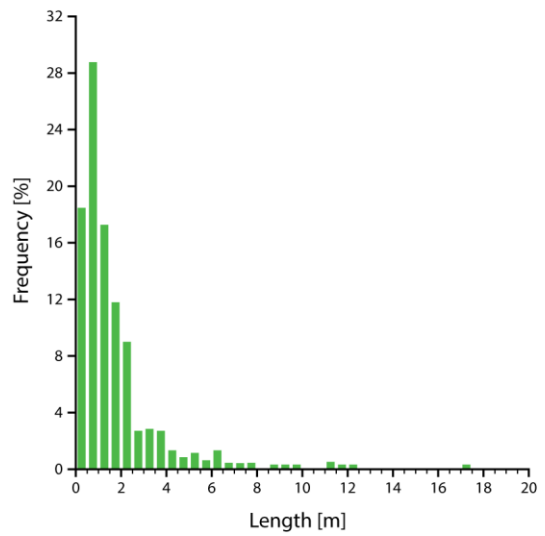
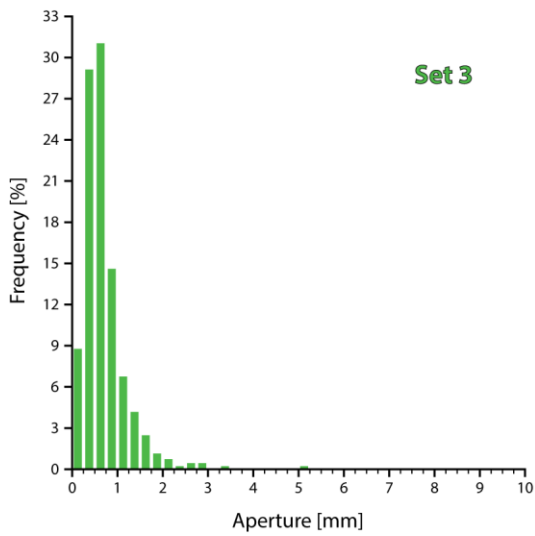
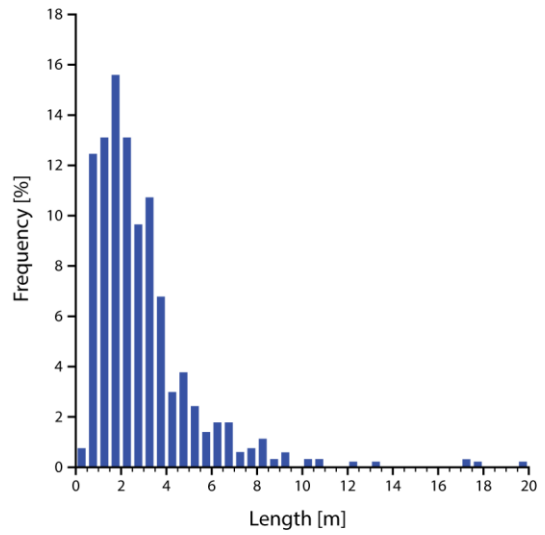
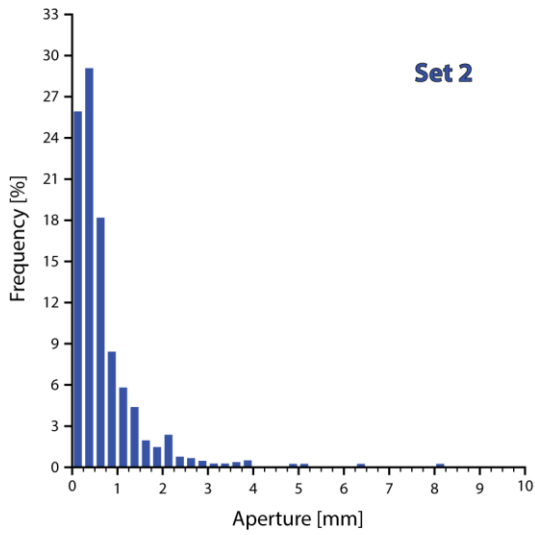
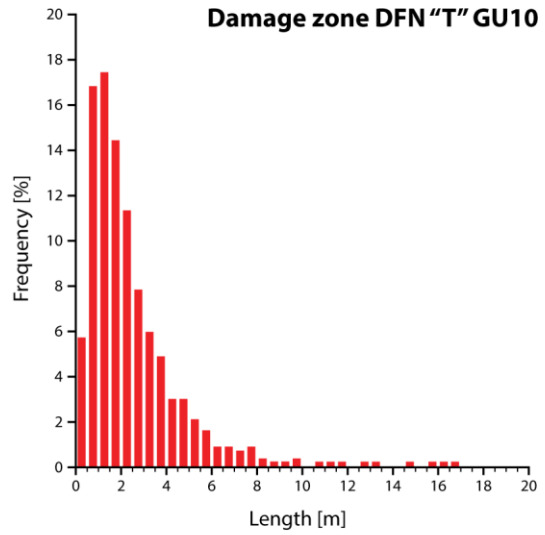
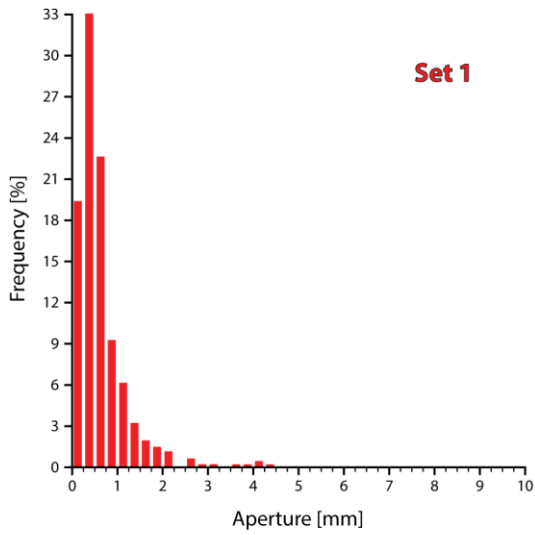


Full Aperture and Length Distribution Results

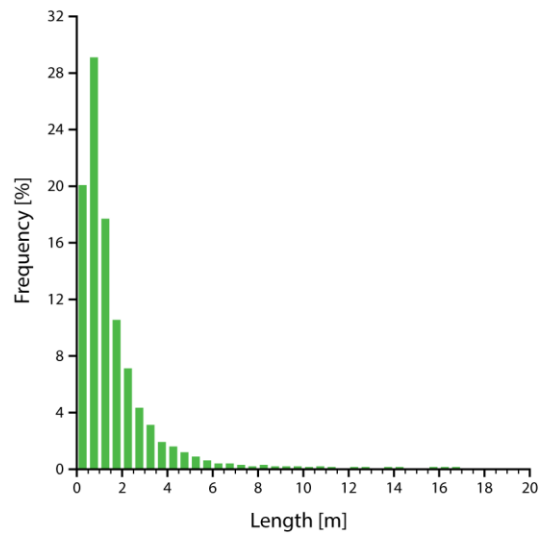
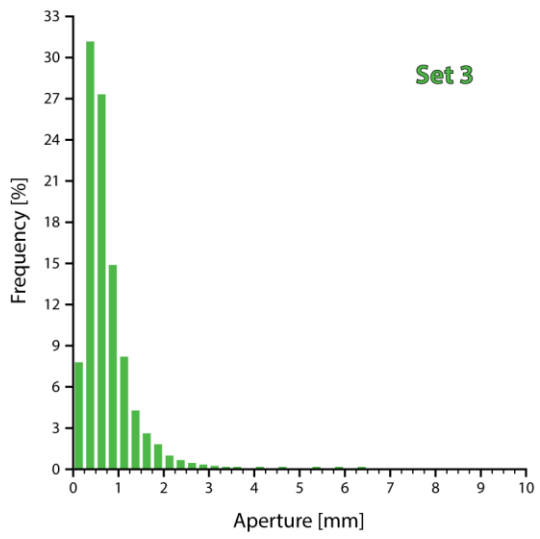
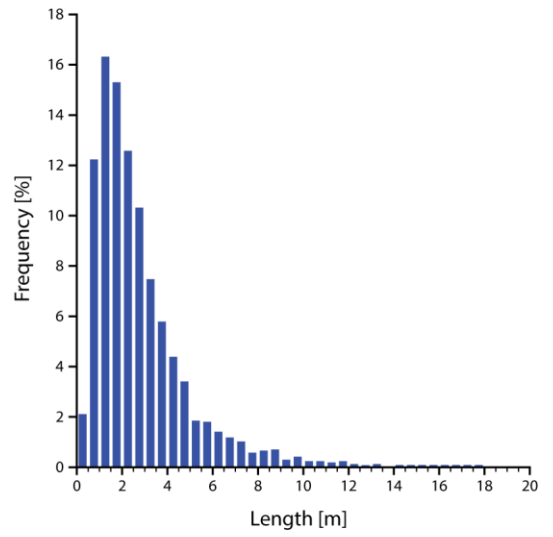
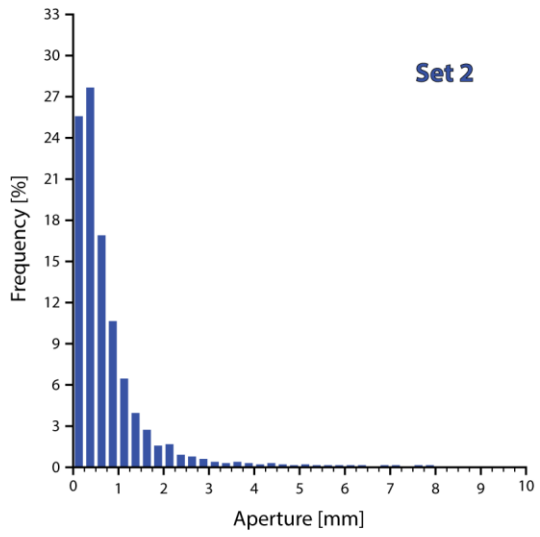
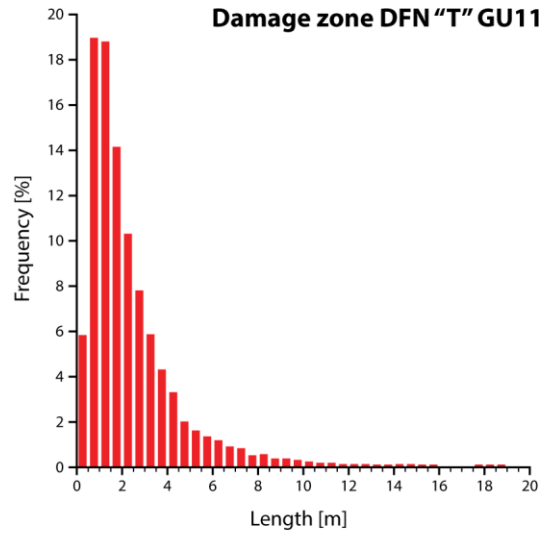
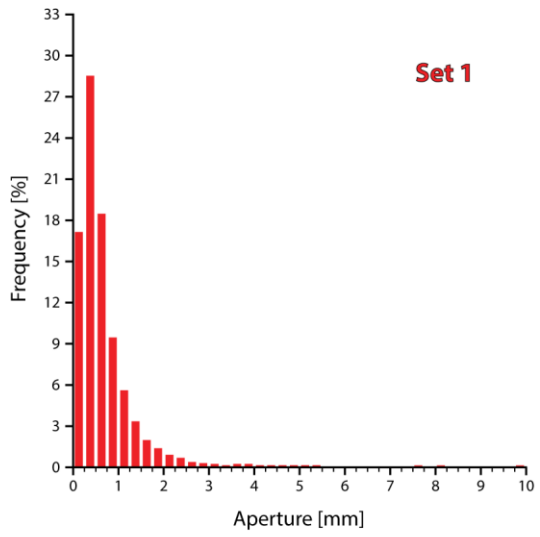




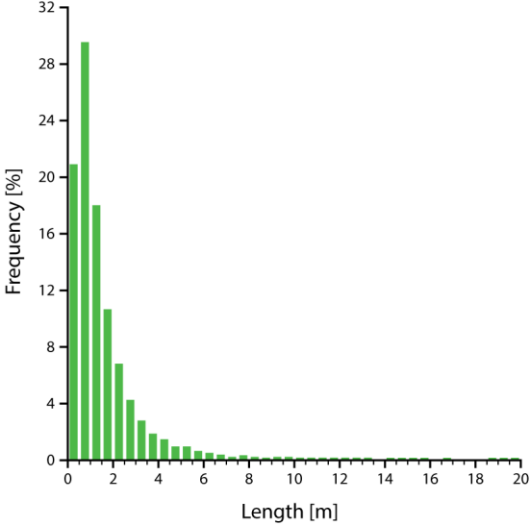
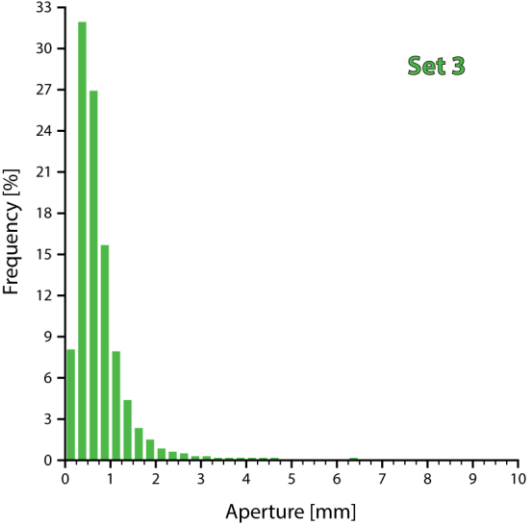
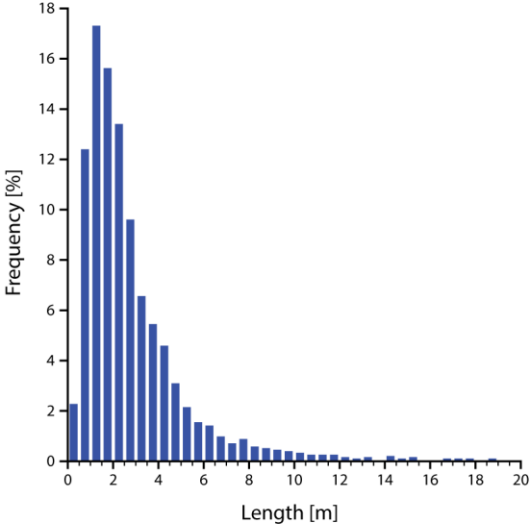
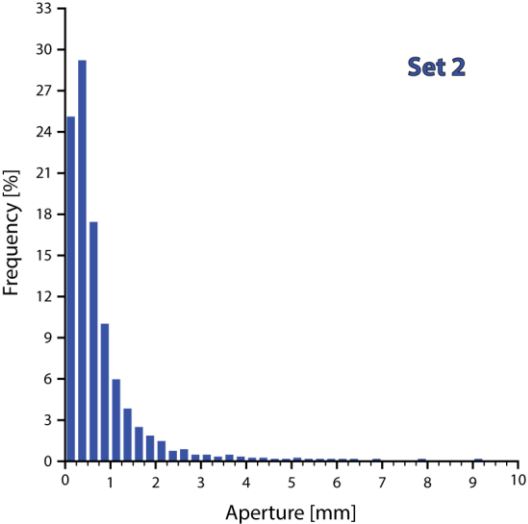
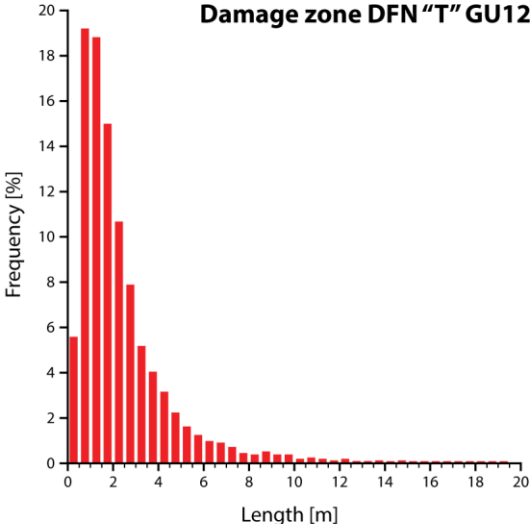
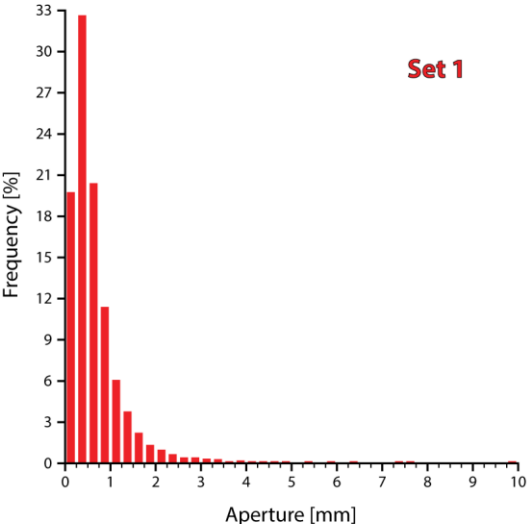
# Full Aperture and Length Distribution Results

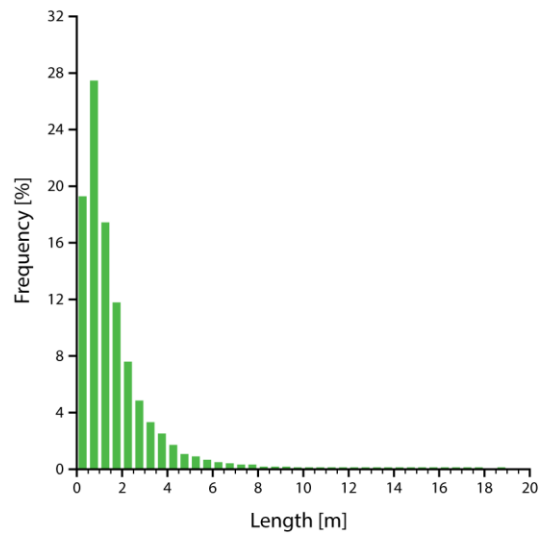
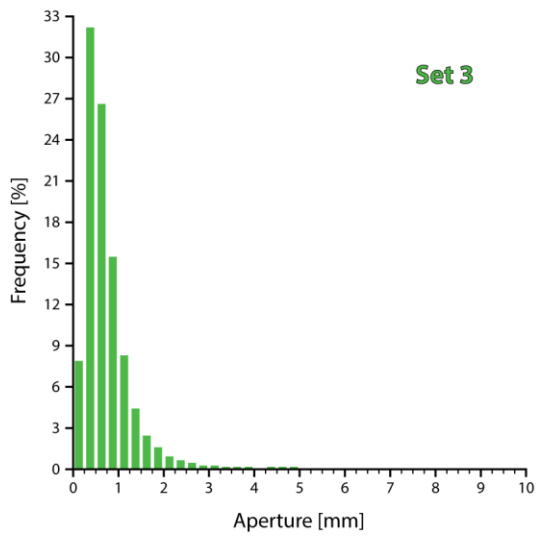
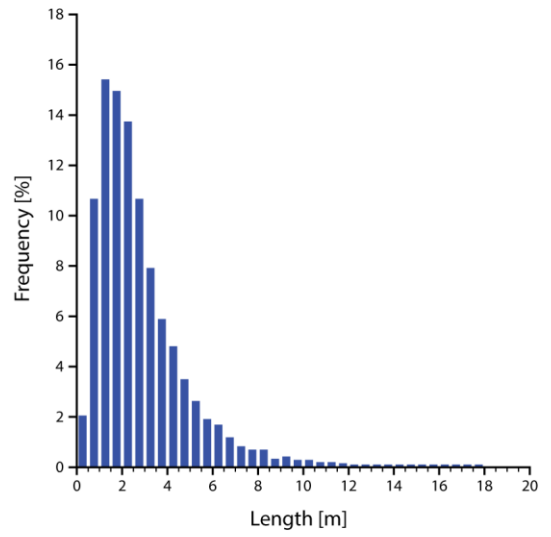
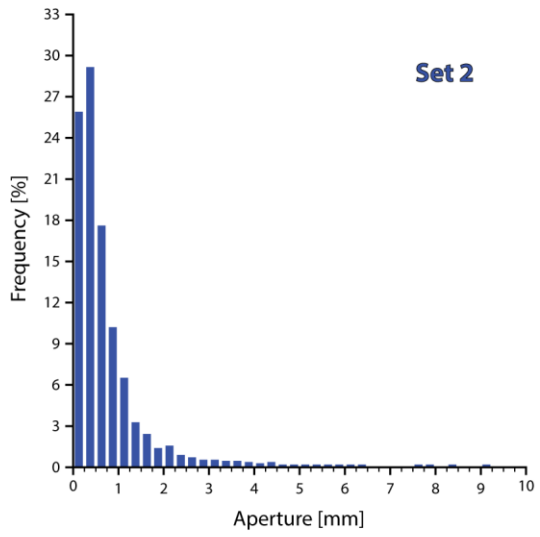
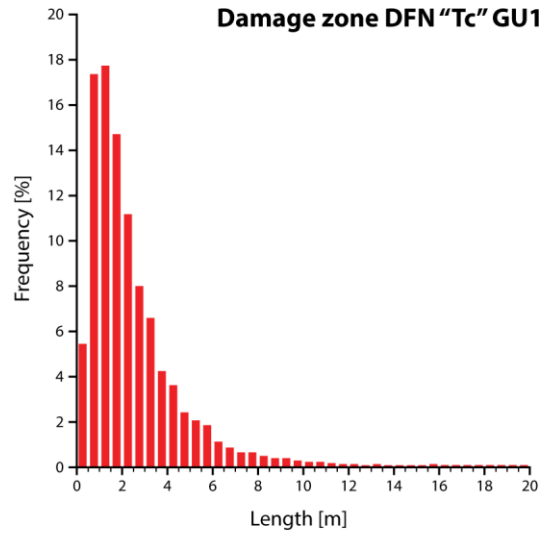
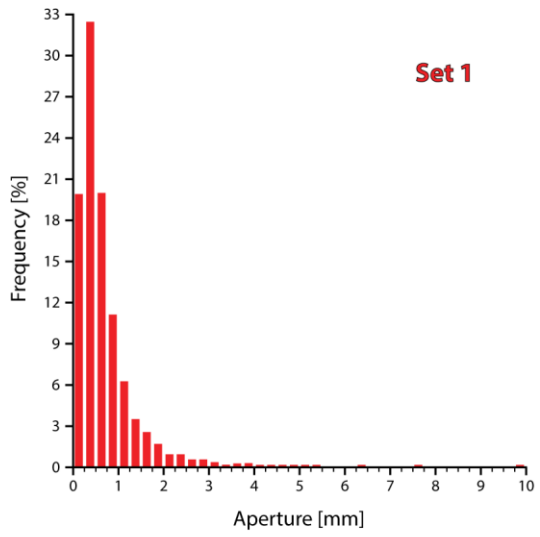




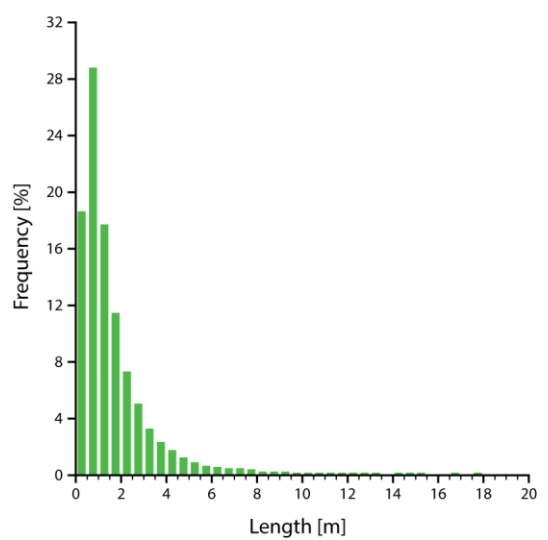
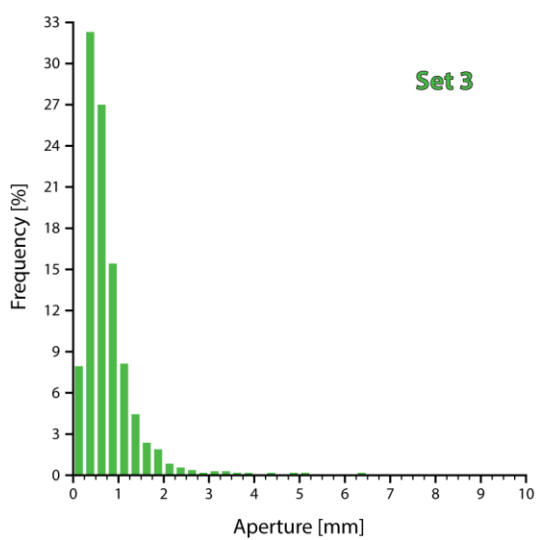
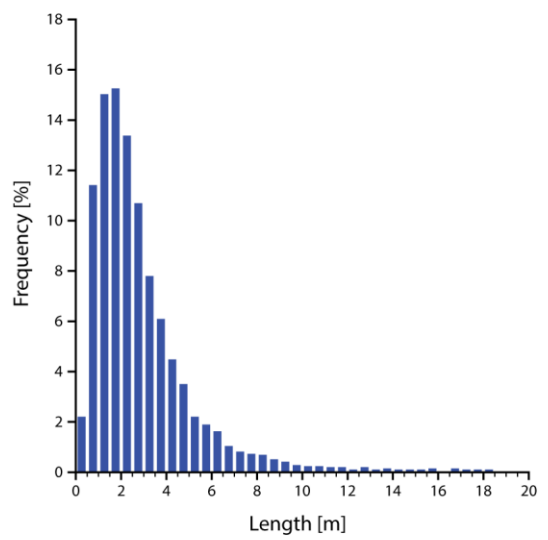
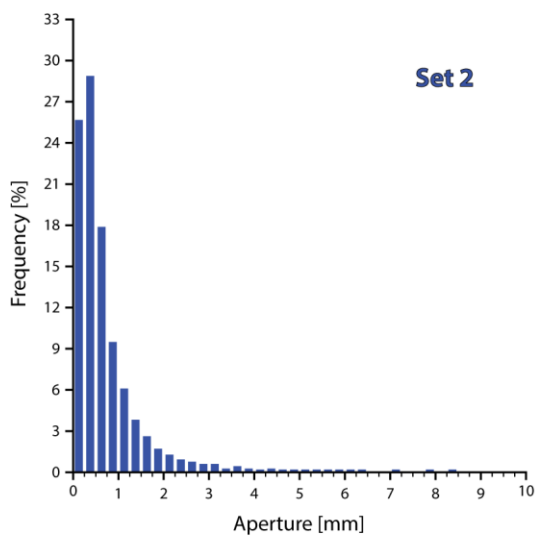
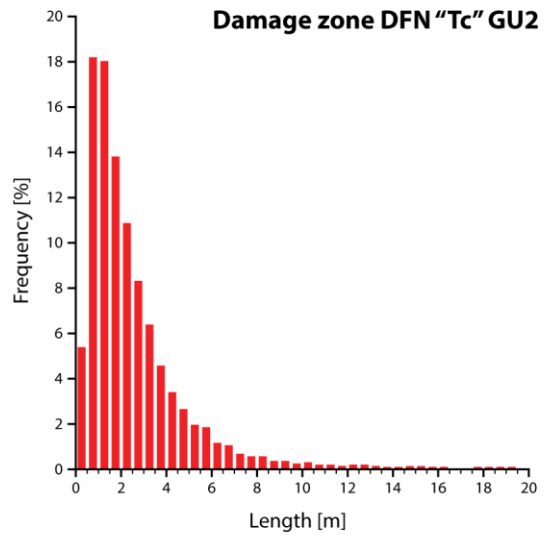
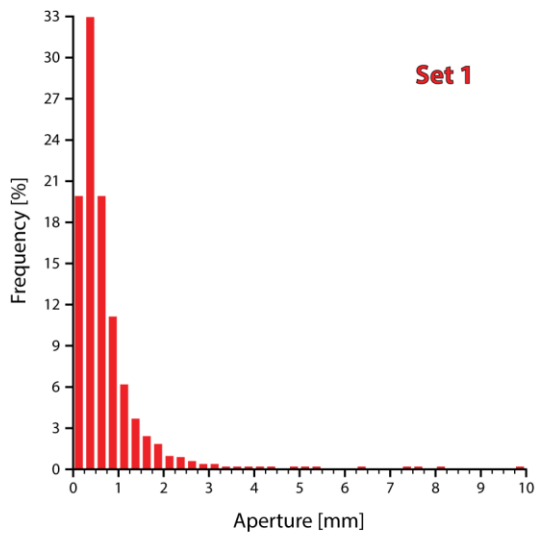


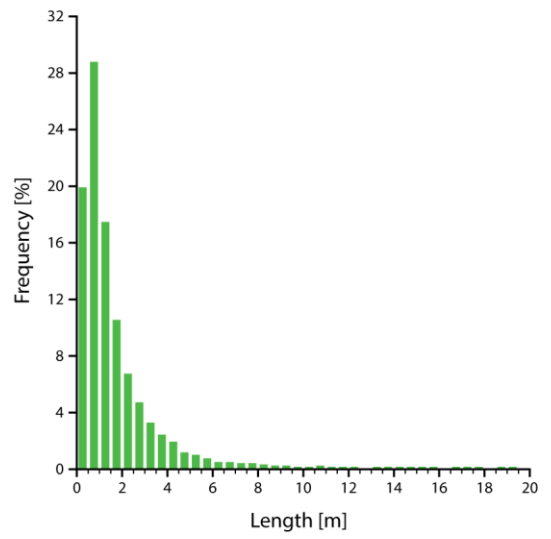
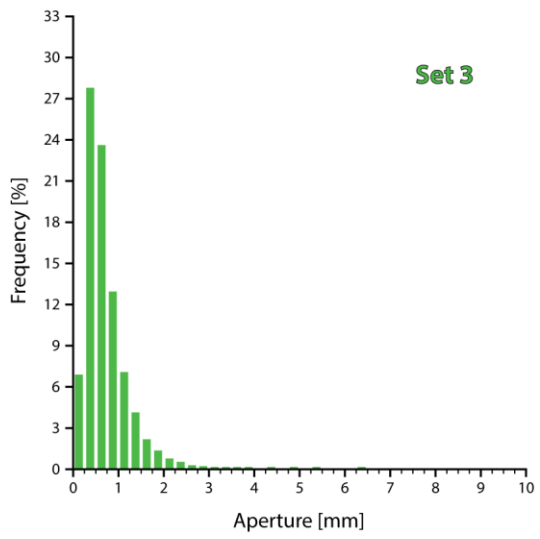
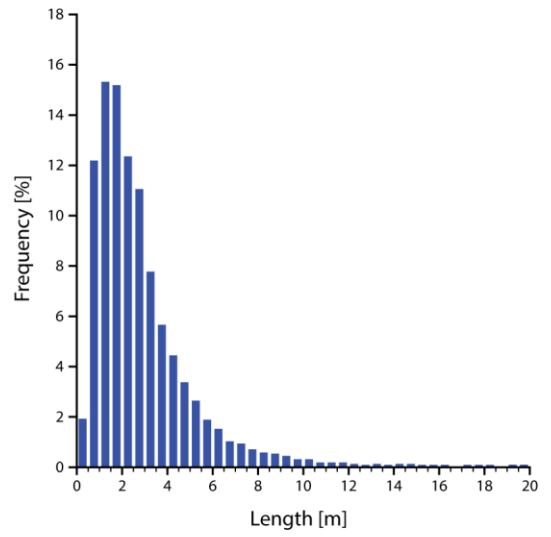
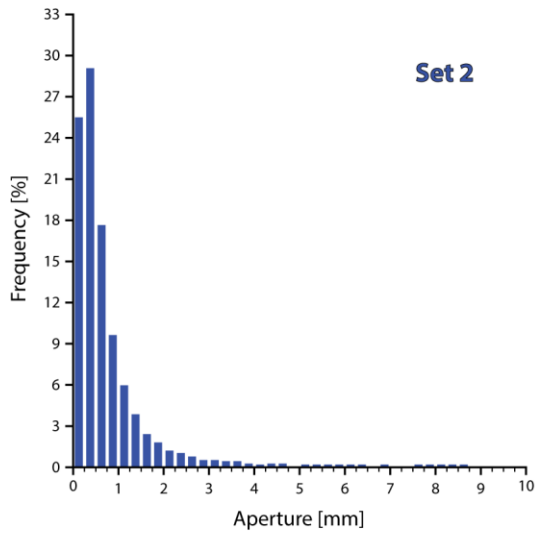
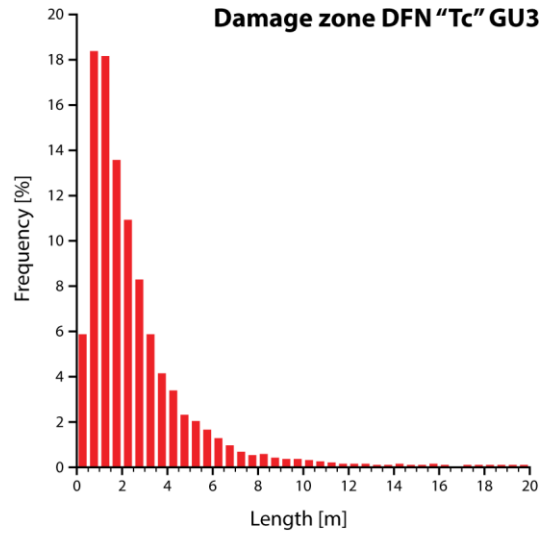
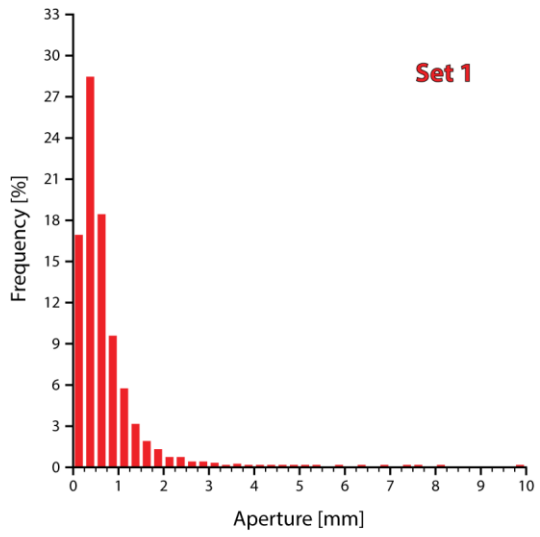
Full Aperture and Length Distribution Results



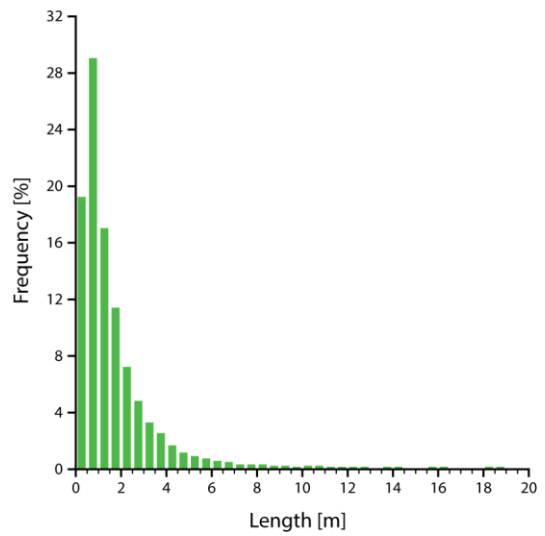
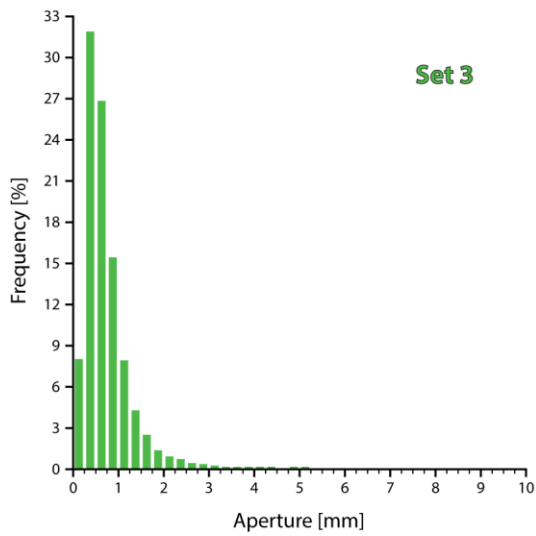
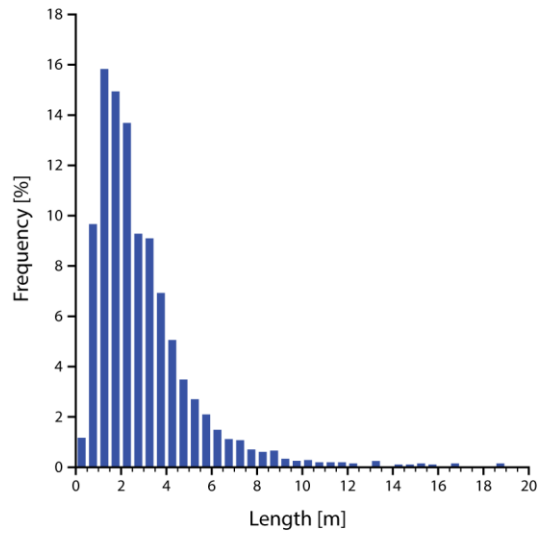
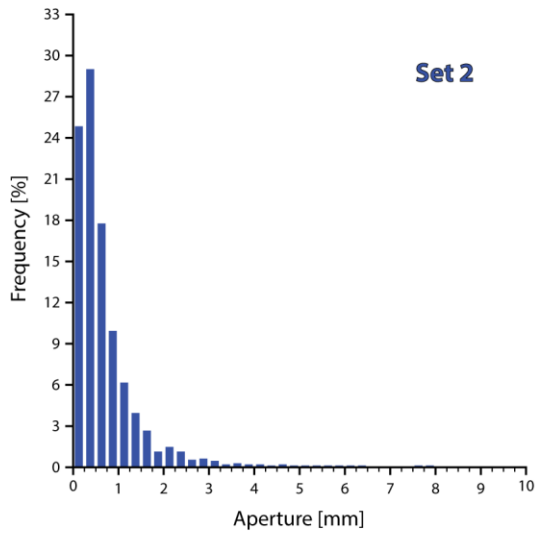
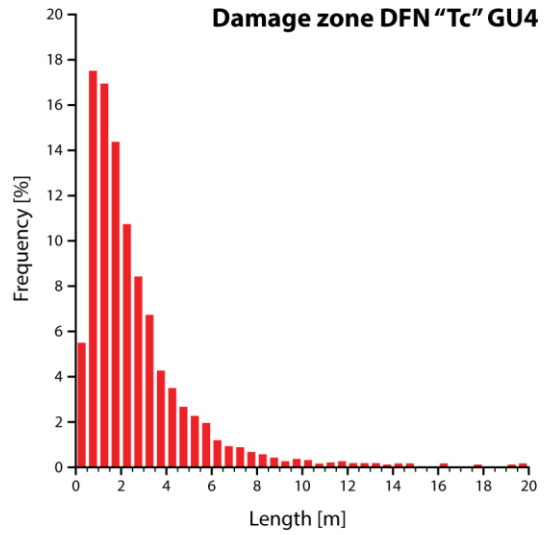
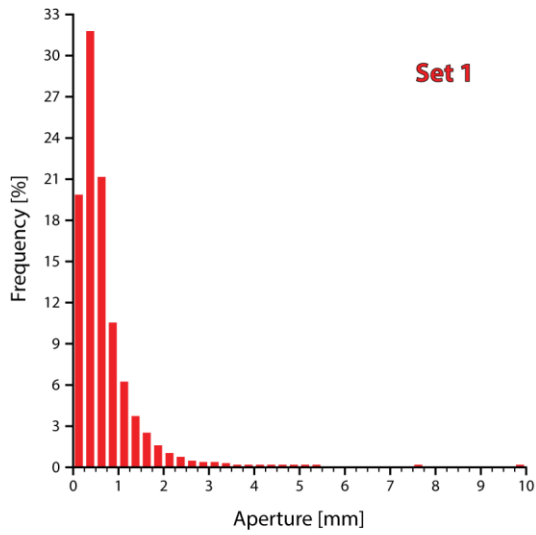


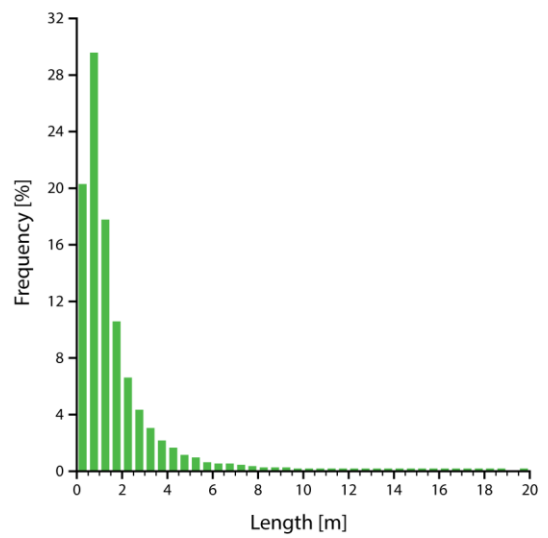
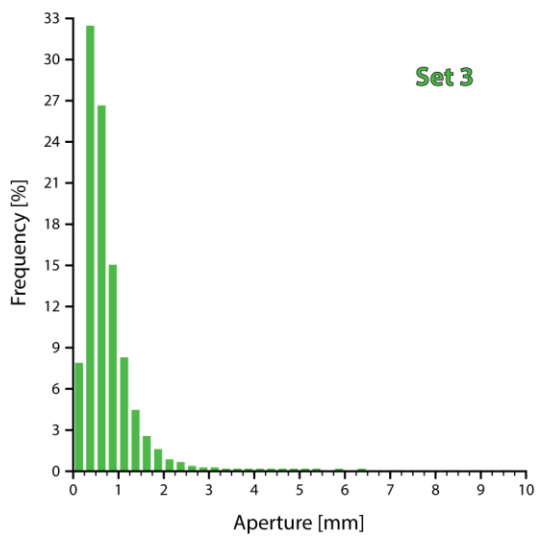
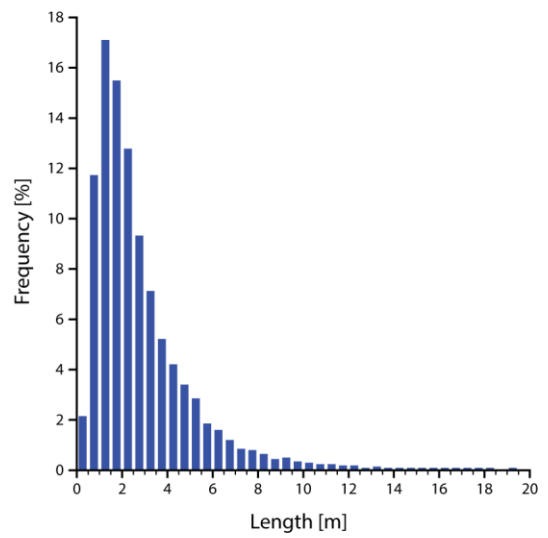
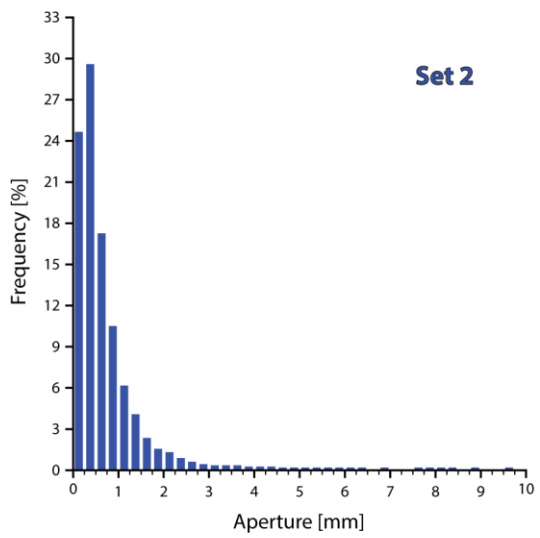
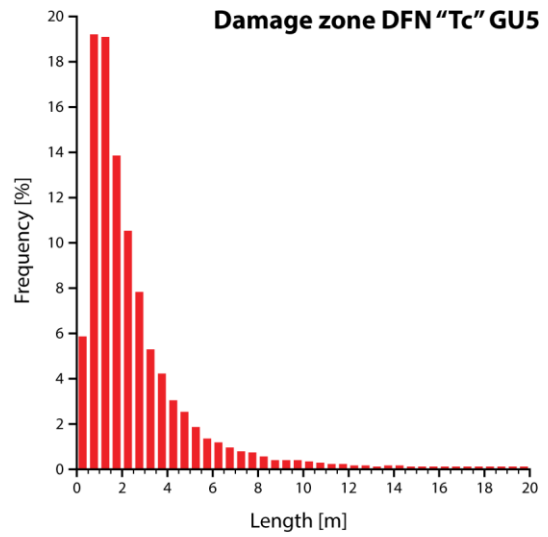
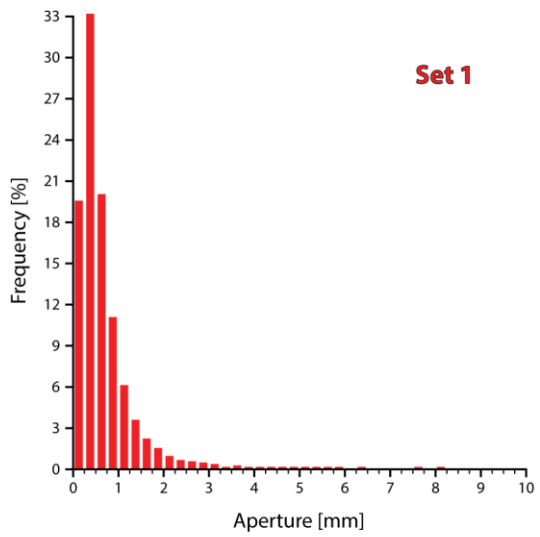
# Full Aperture and Length Distribution Results



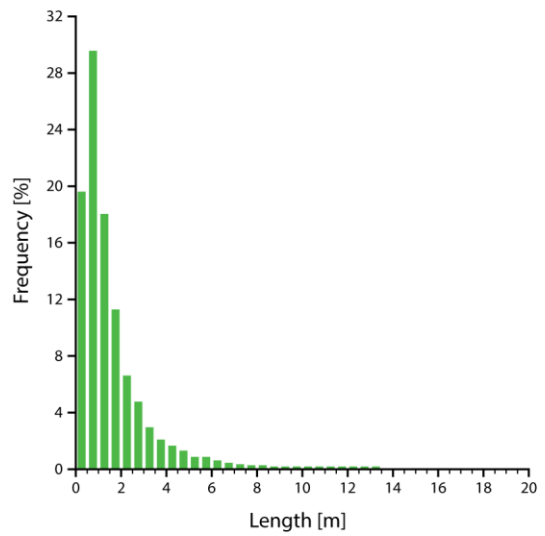
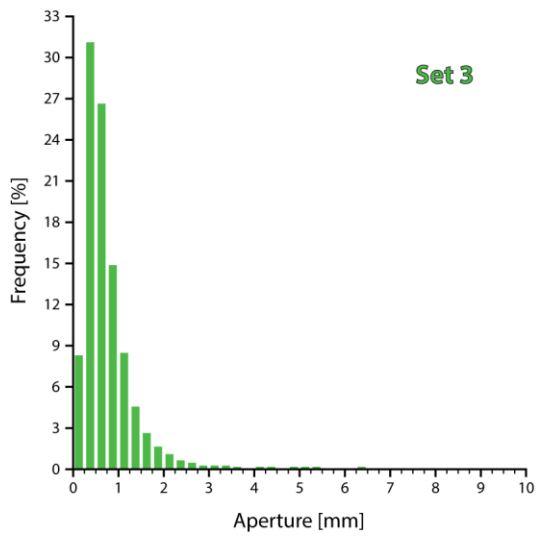
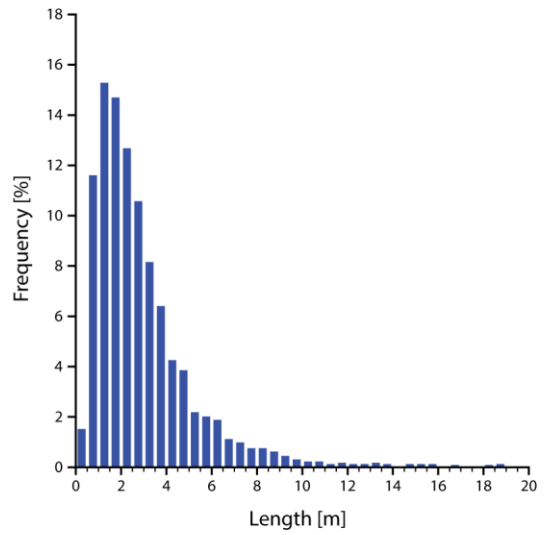
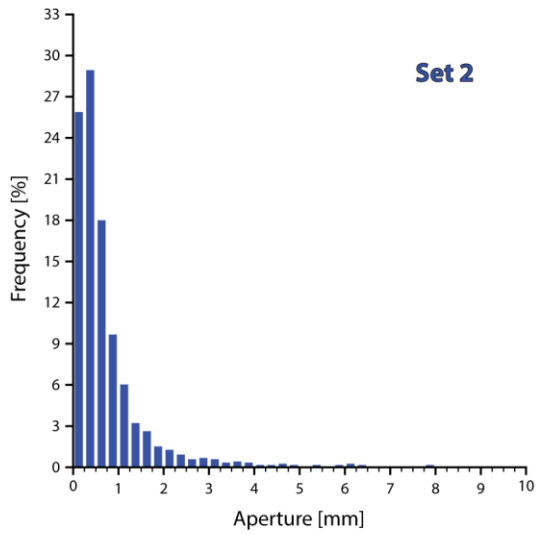
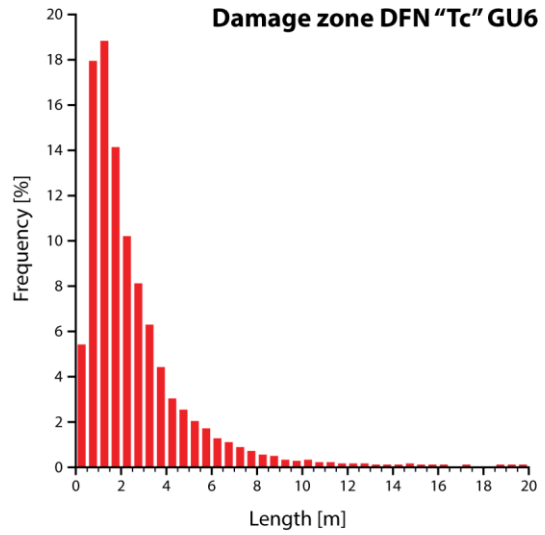
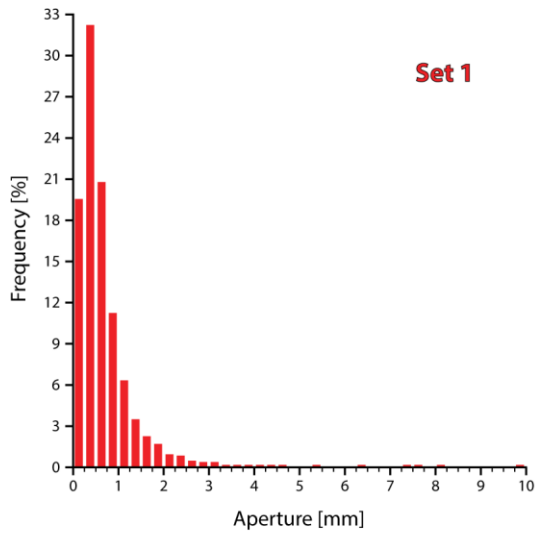


# Full Aperture and Length Distribution Results

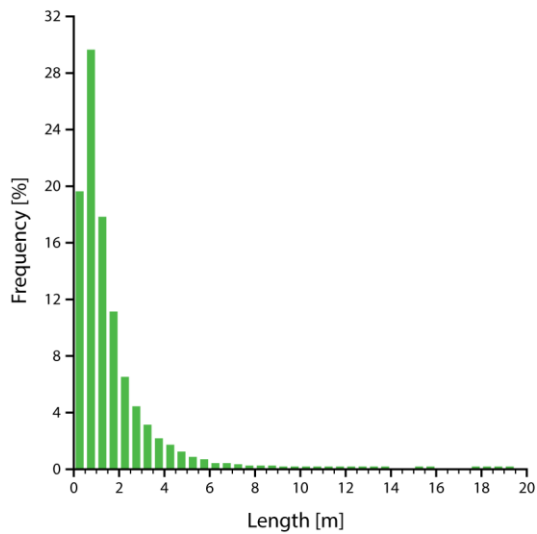
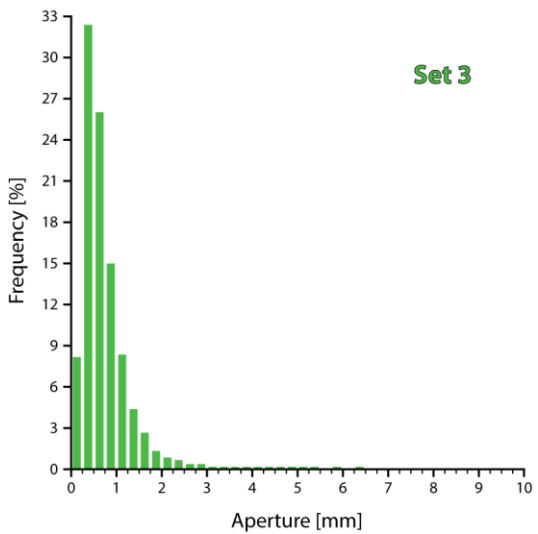
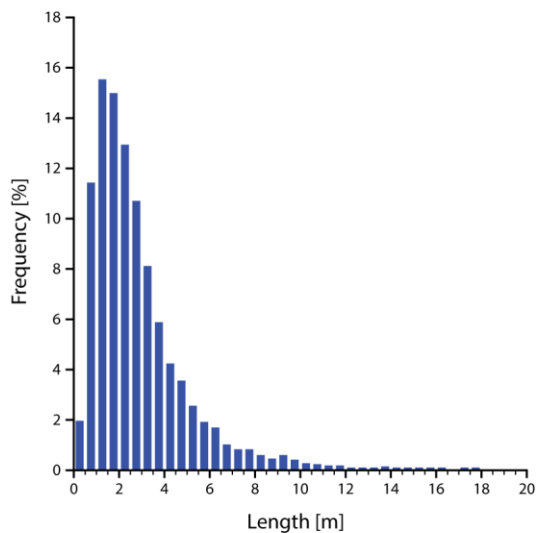
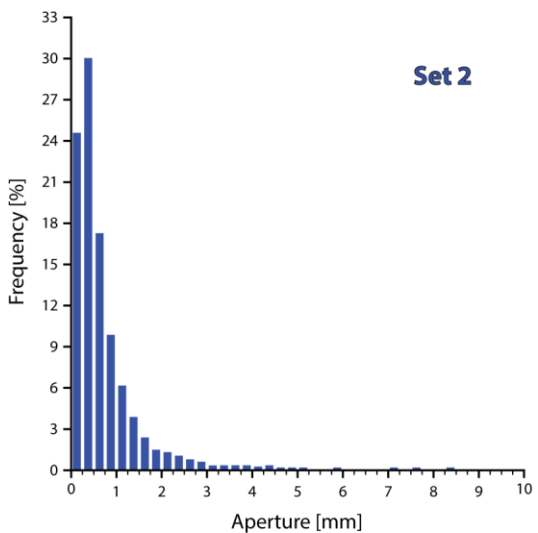
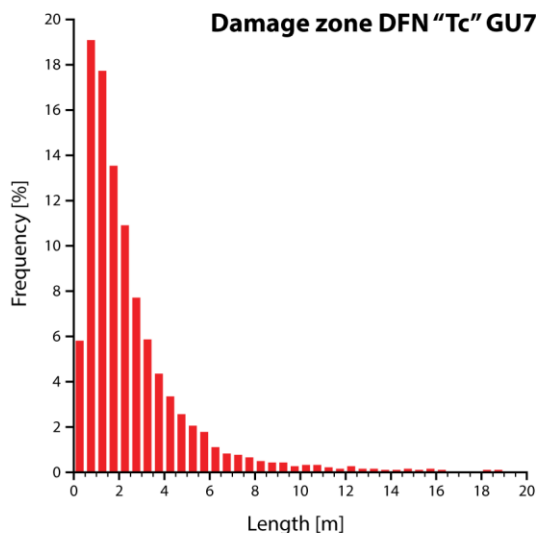
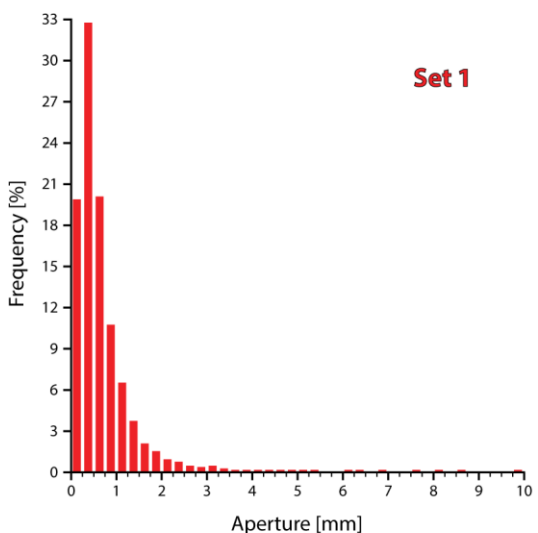




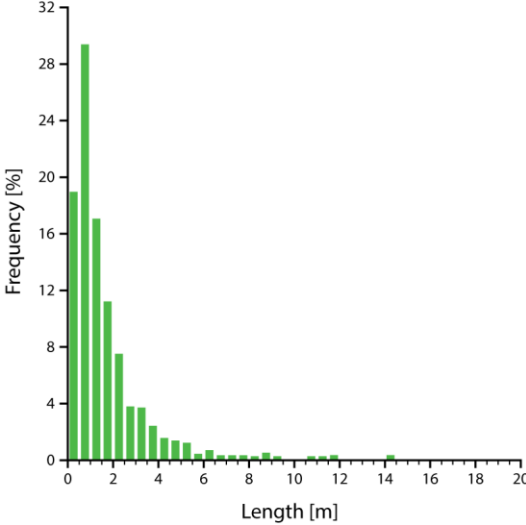
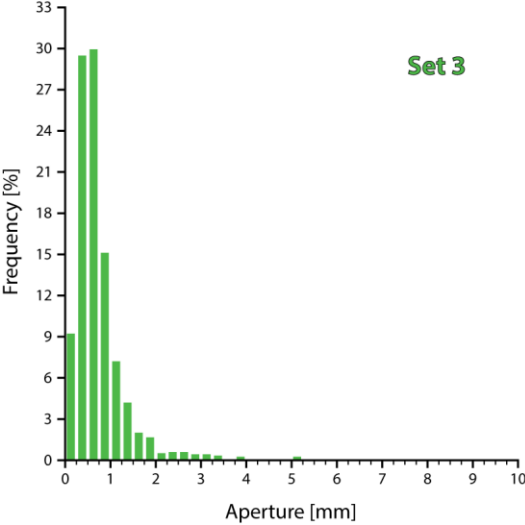
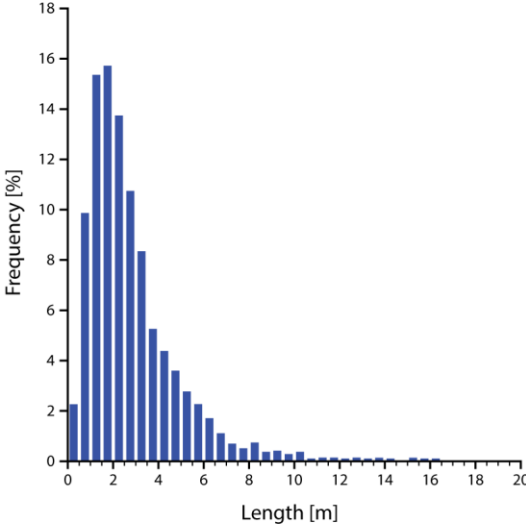
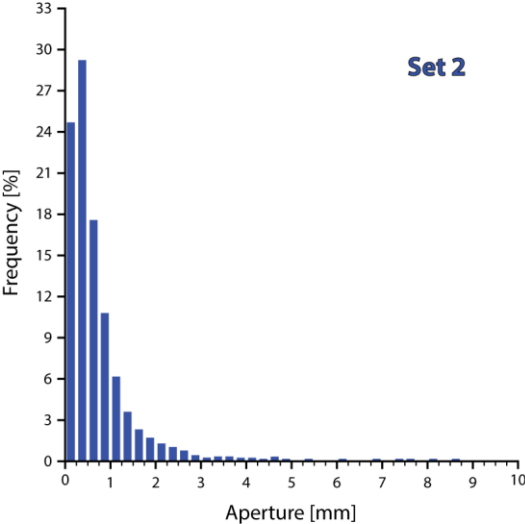
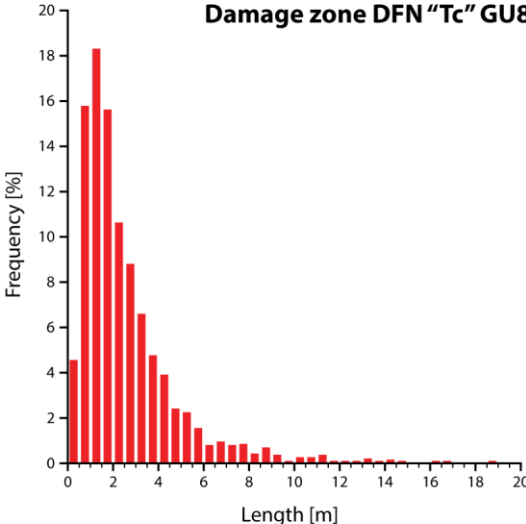
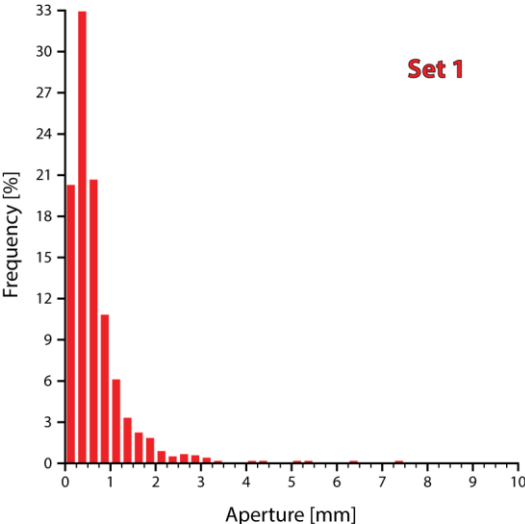
# Full Aperture and Length Distribution Results

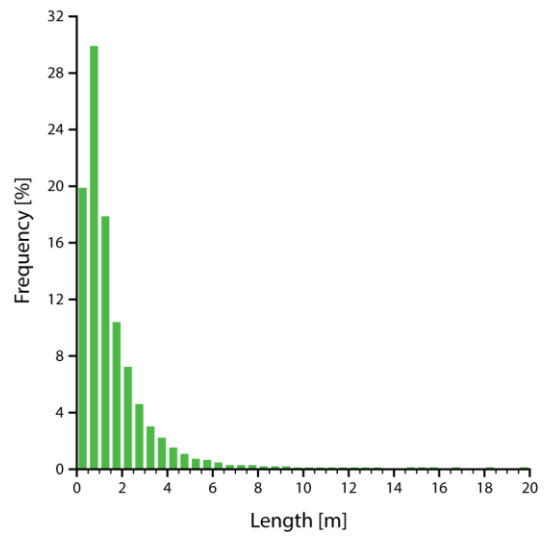
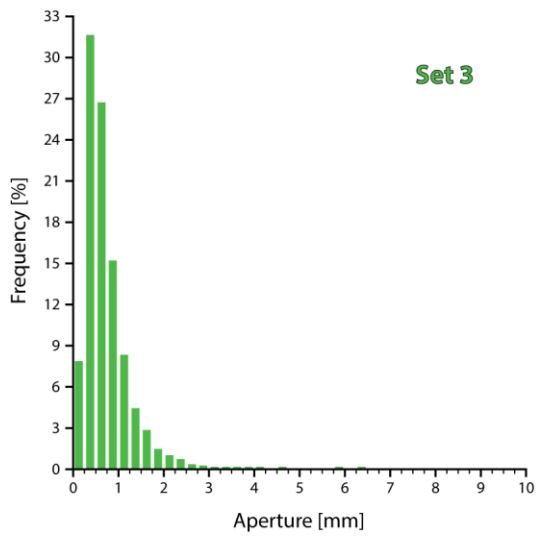
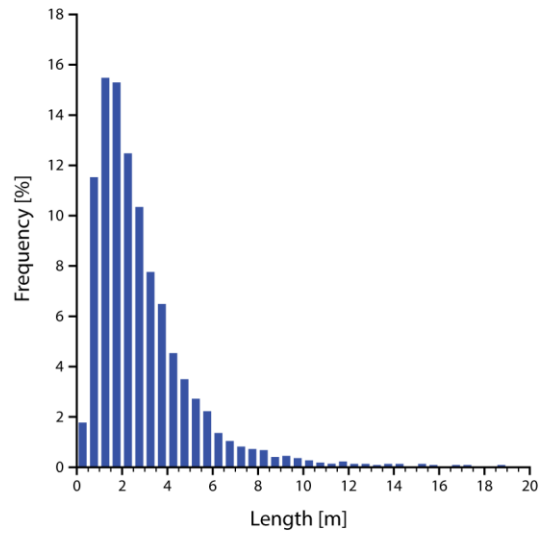
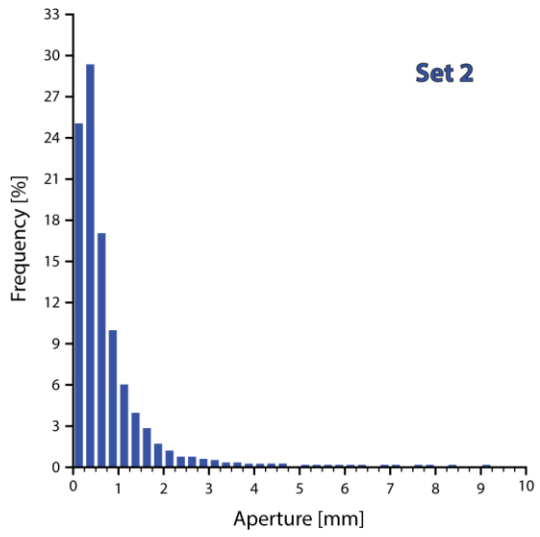
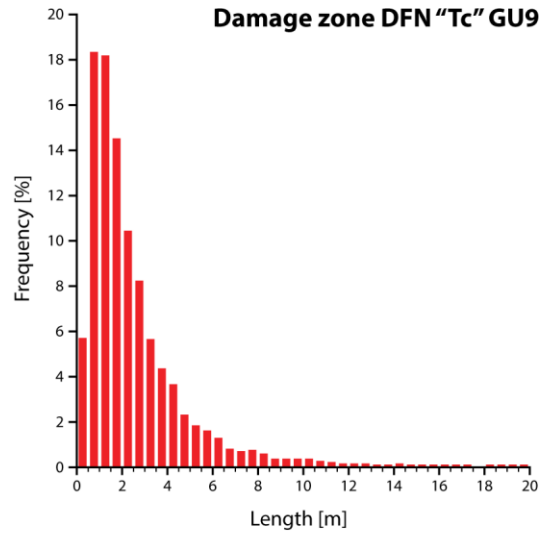
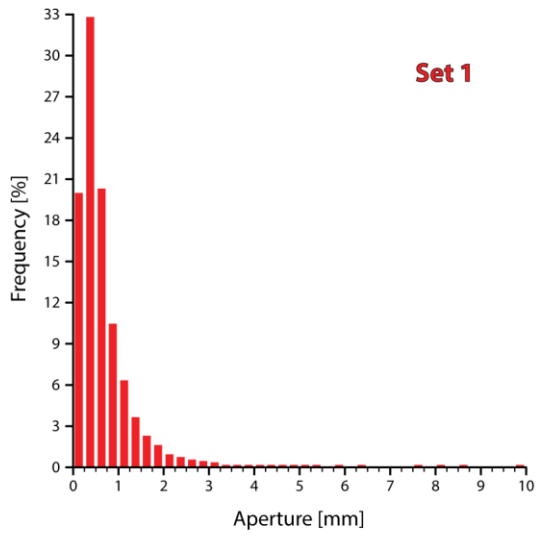




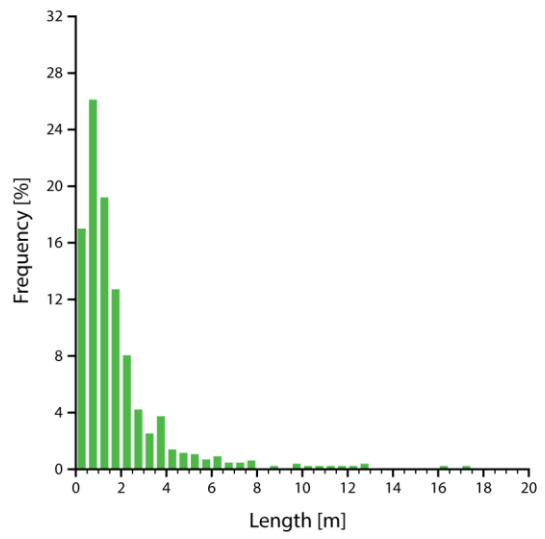
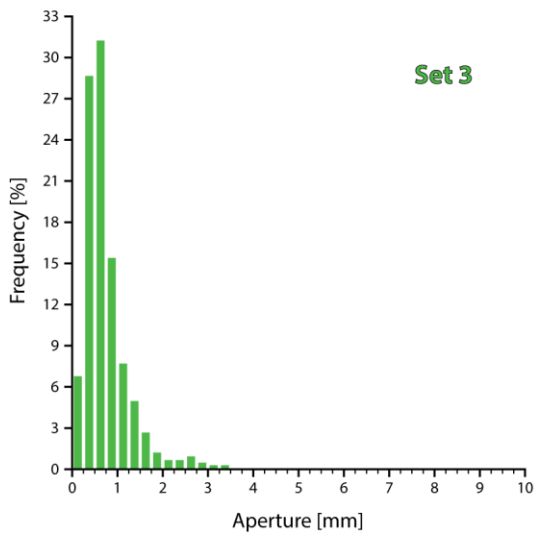
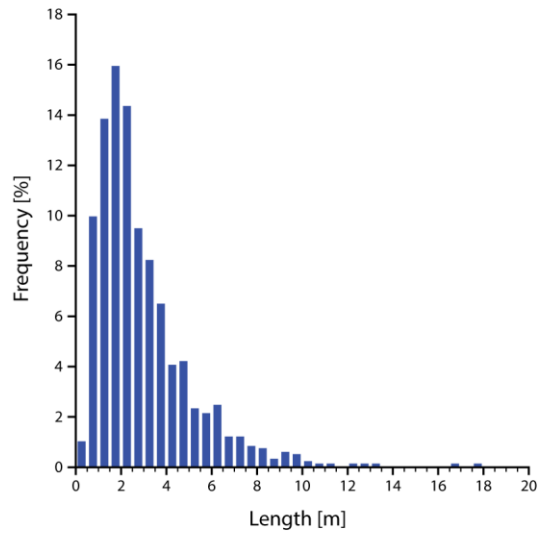
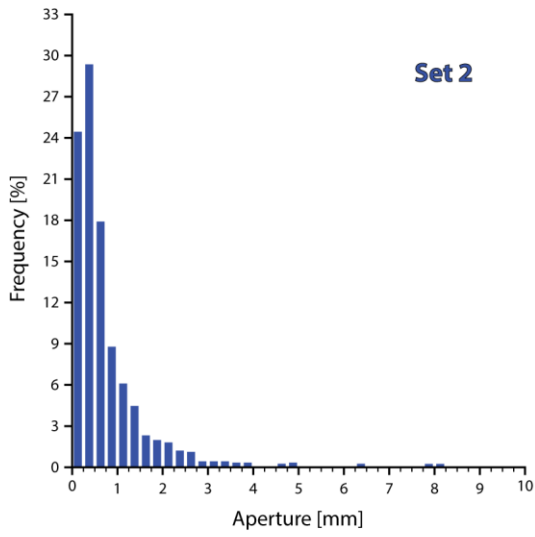
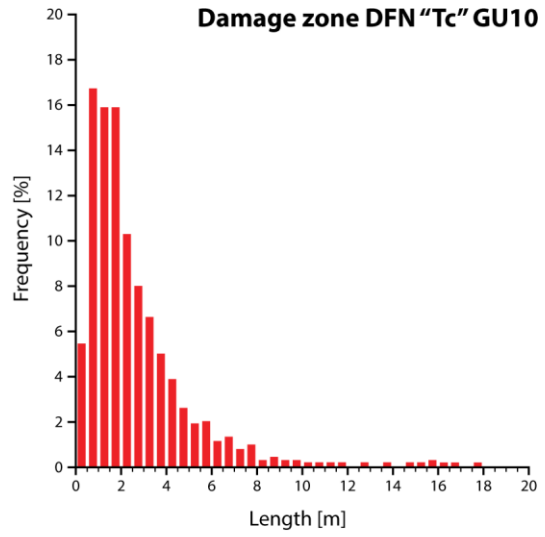
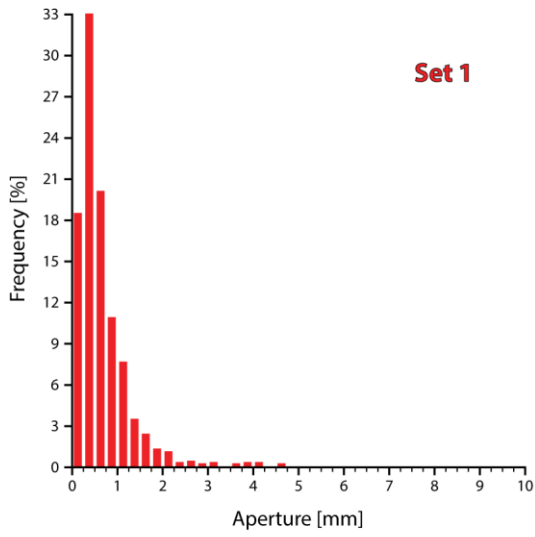


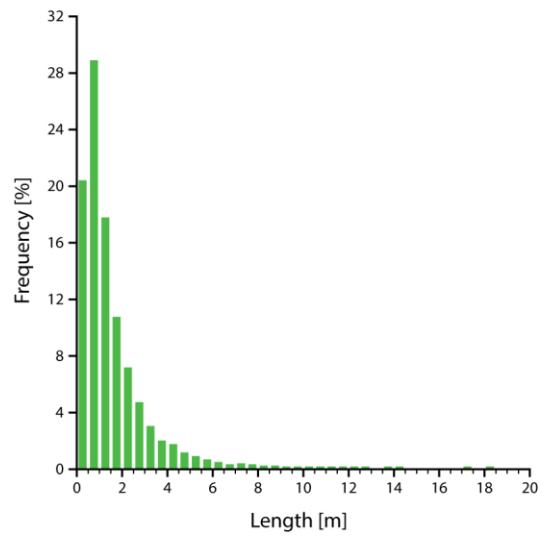
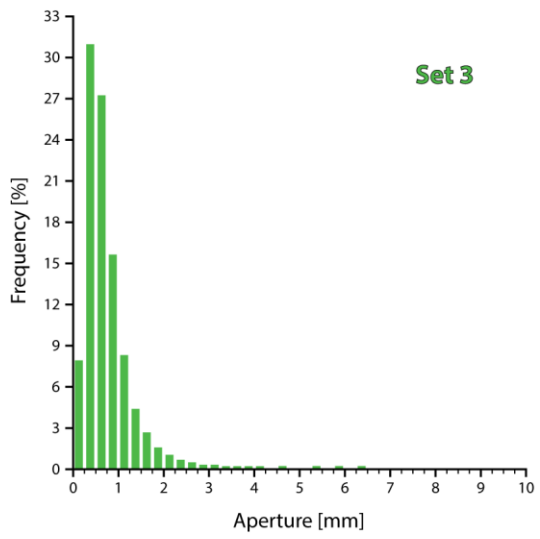
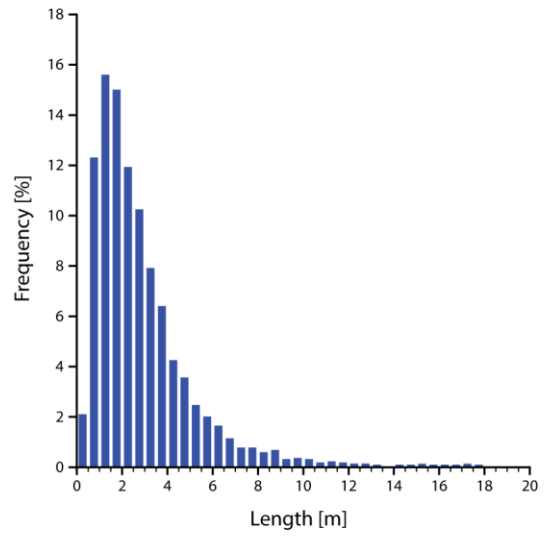
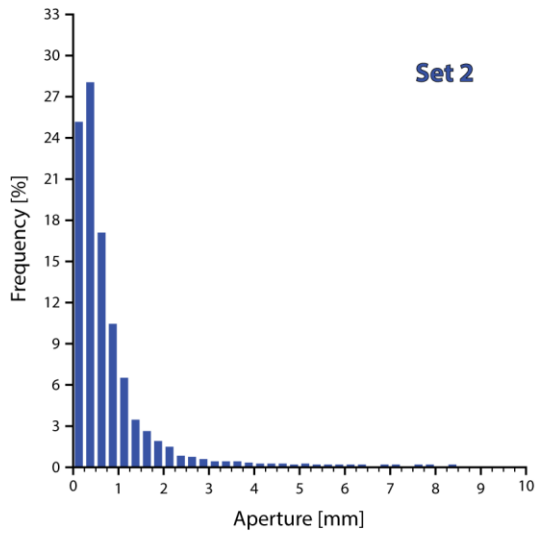
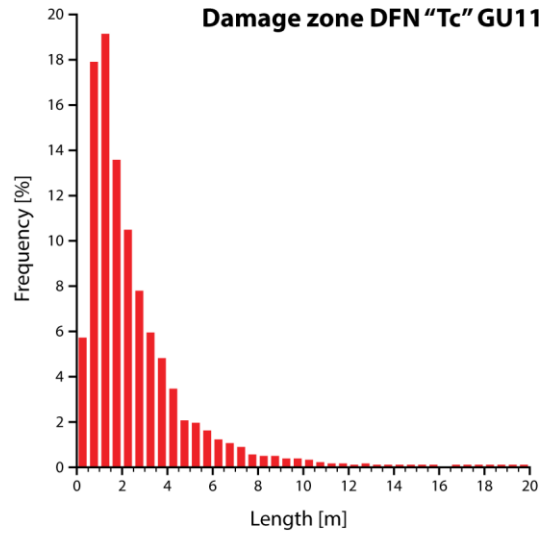
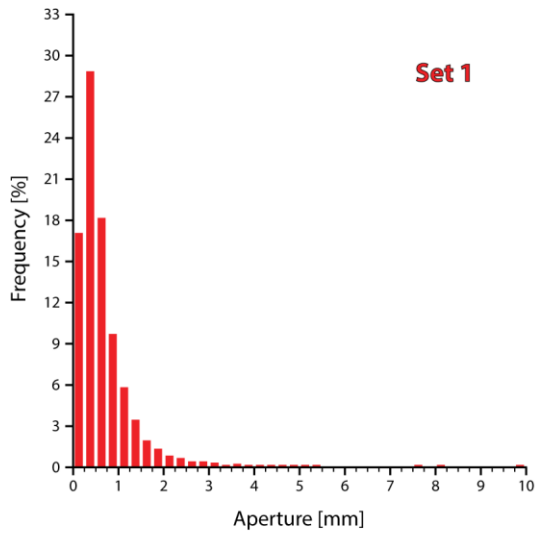
Full Aperture and Length Distribution Results



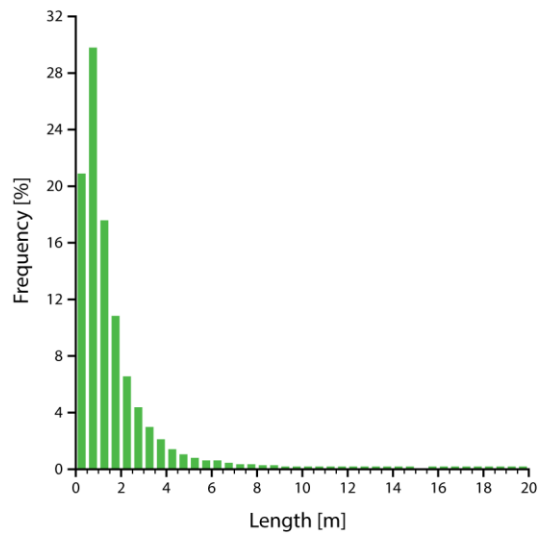
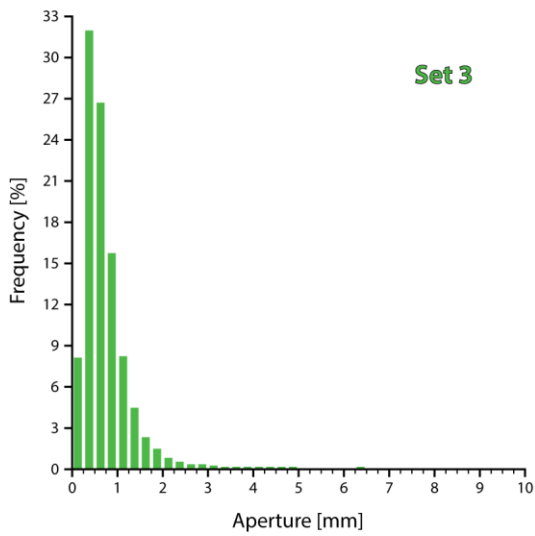
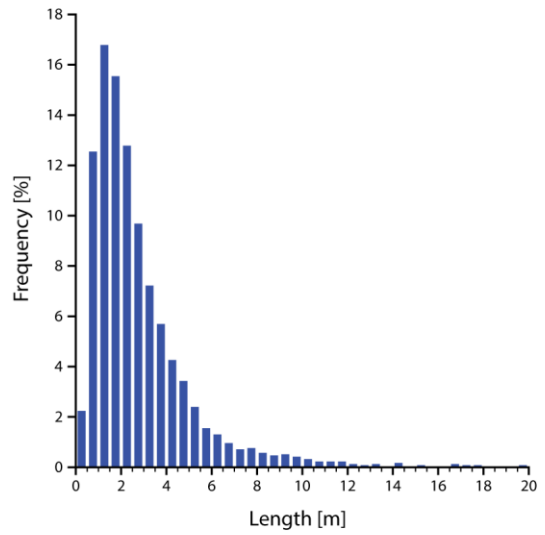
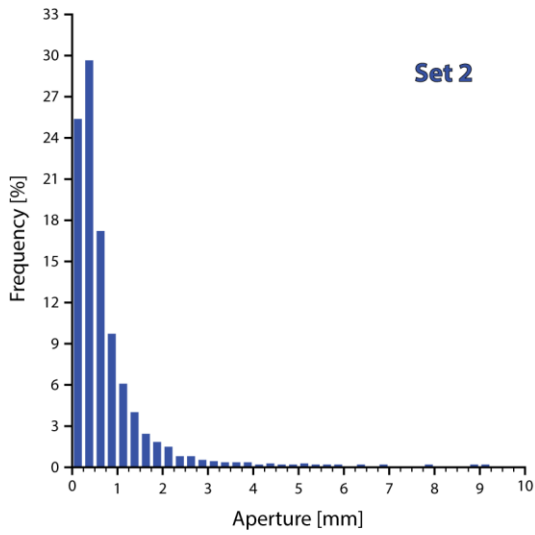
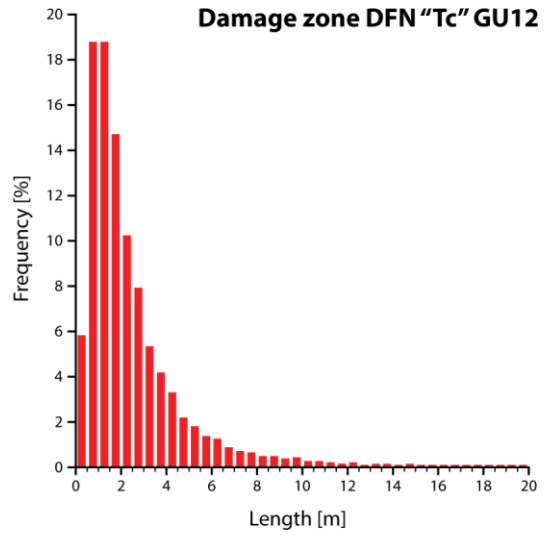
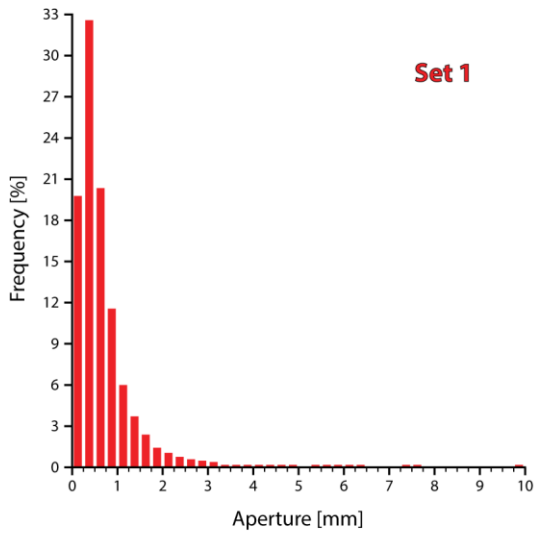


# Full Aperture and Length Distribution Results





Full Aperture and Length Distribution Results

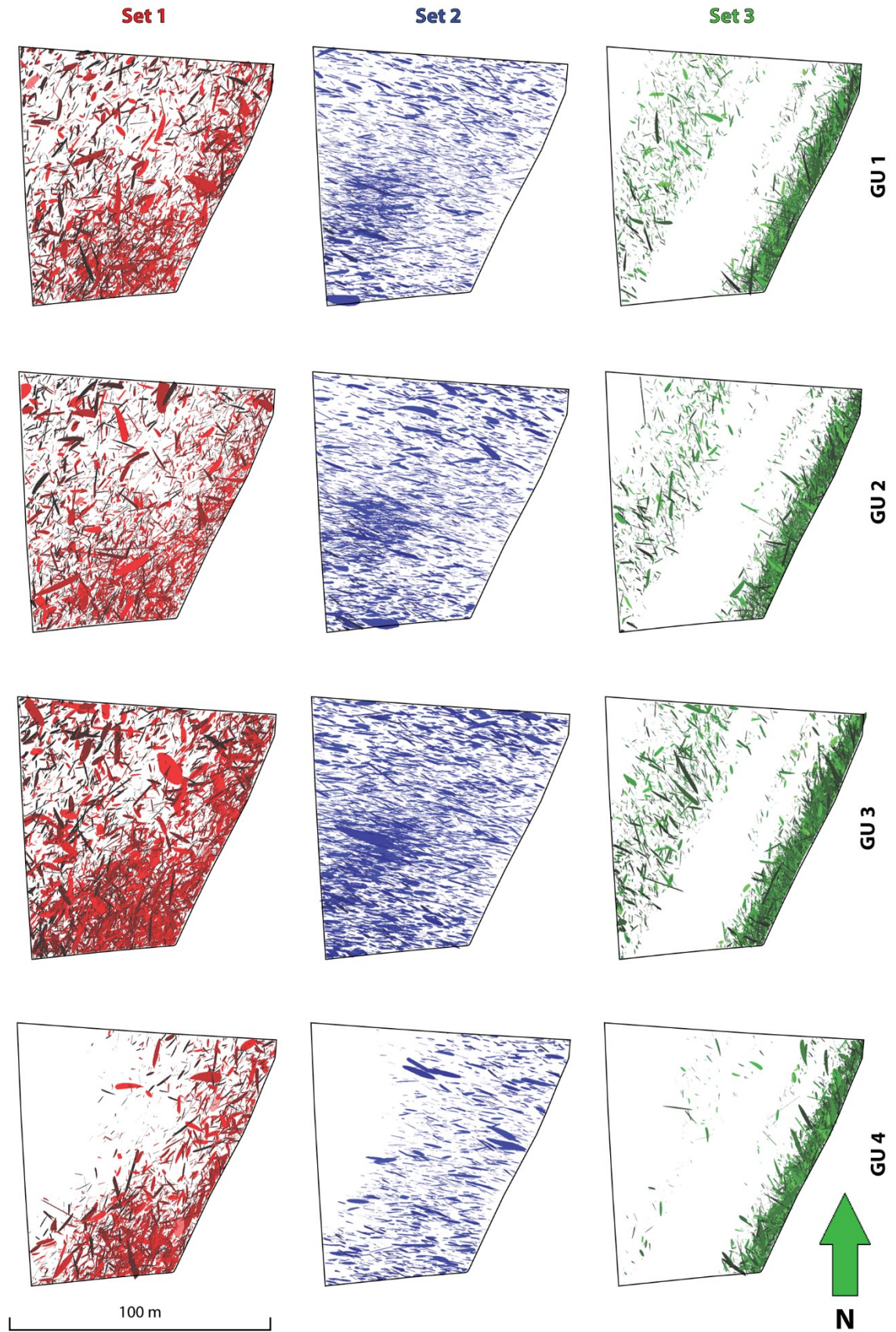


## **Appendix 6      Remaining Calculated DFN Results**

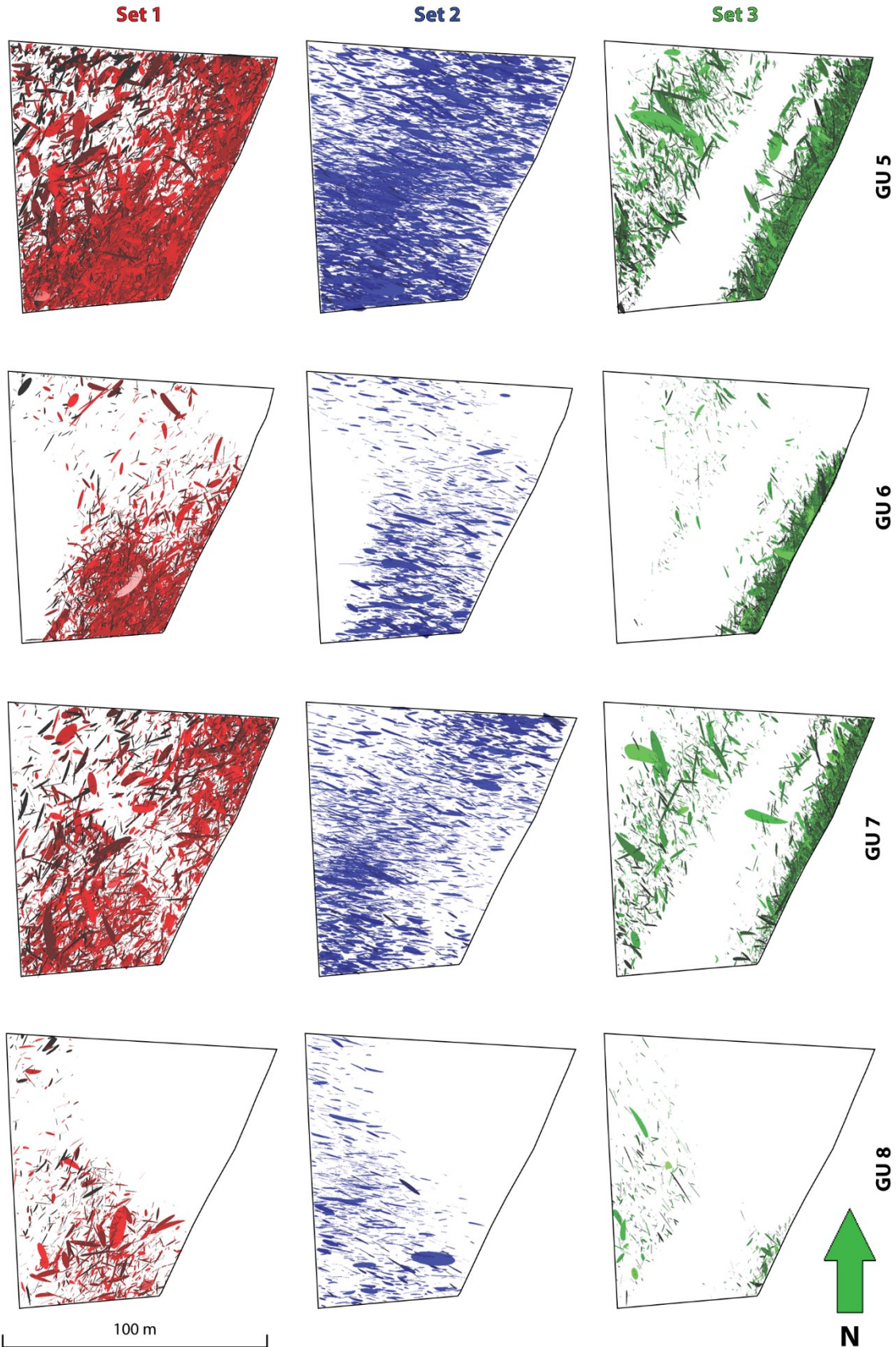




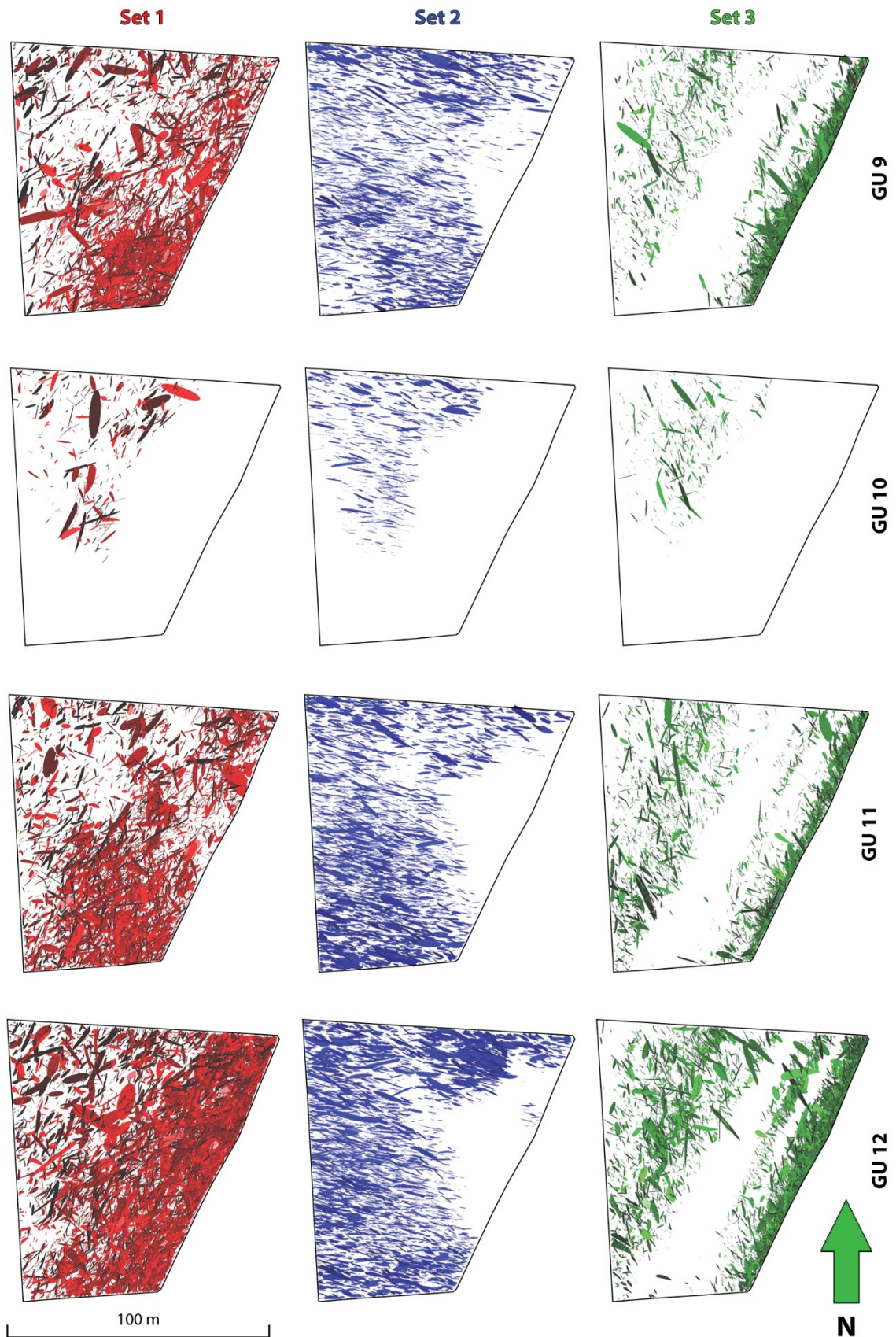
Damage zone fracture network "T"



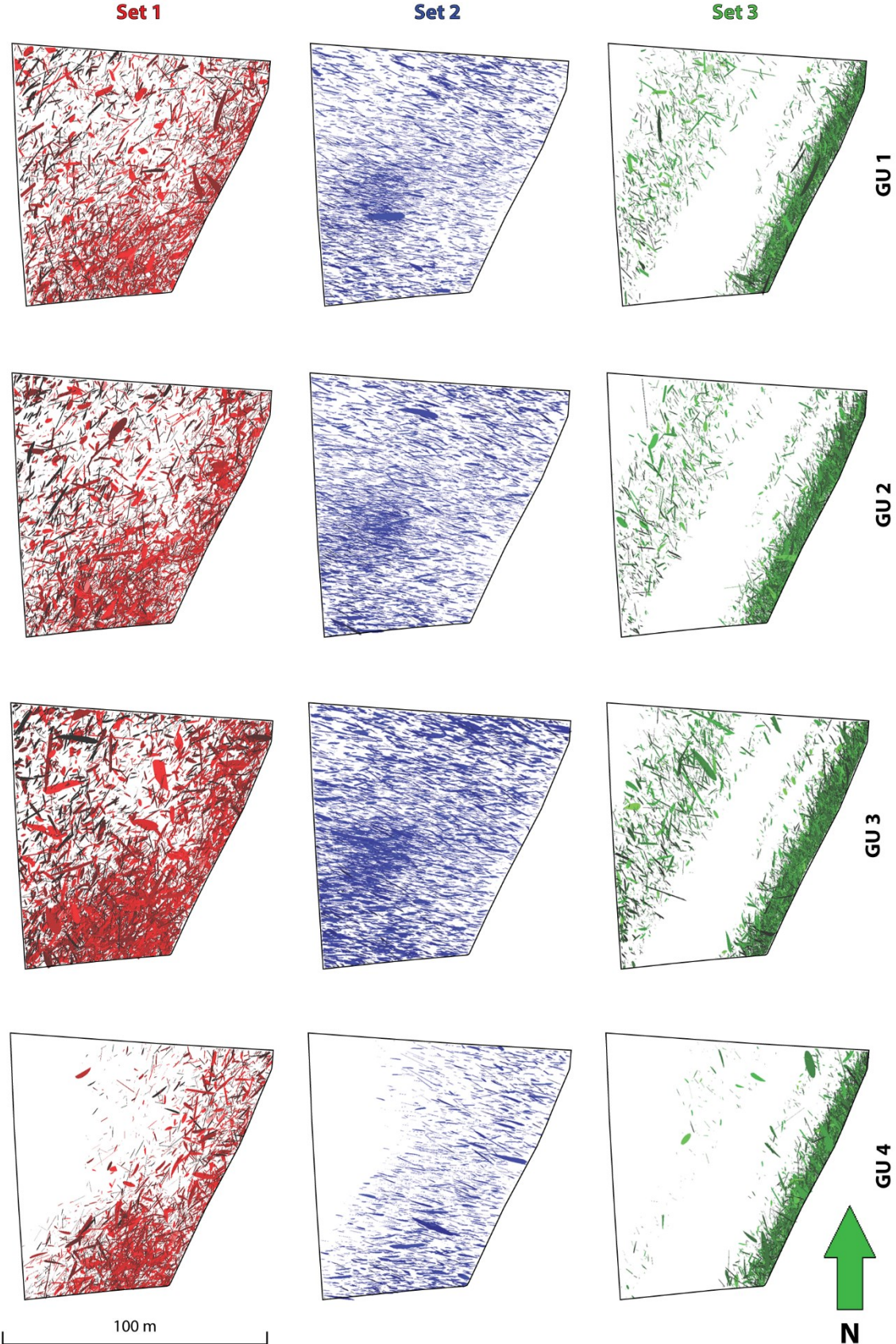
Damage zone fracture network "T"



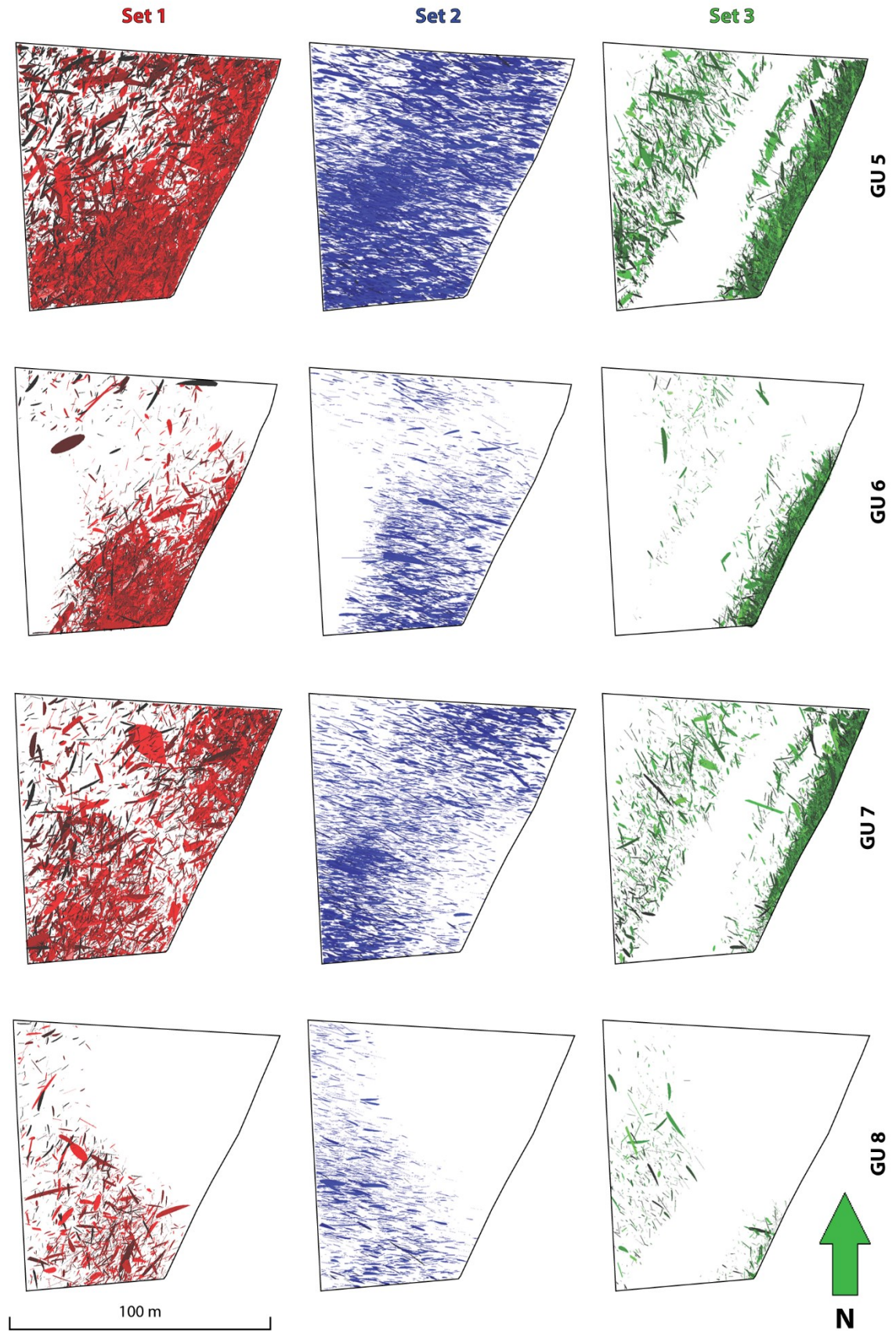
Damage zone fracture network "T"



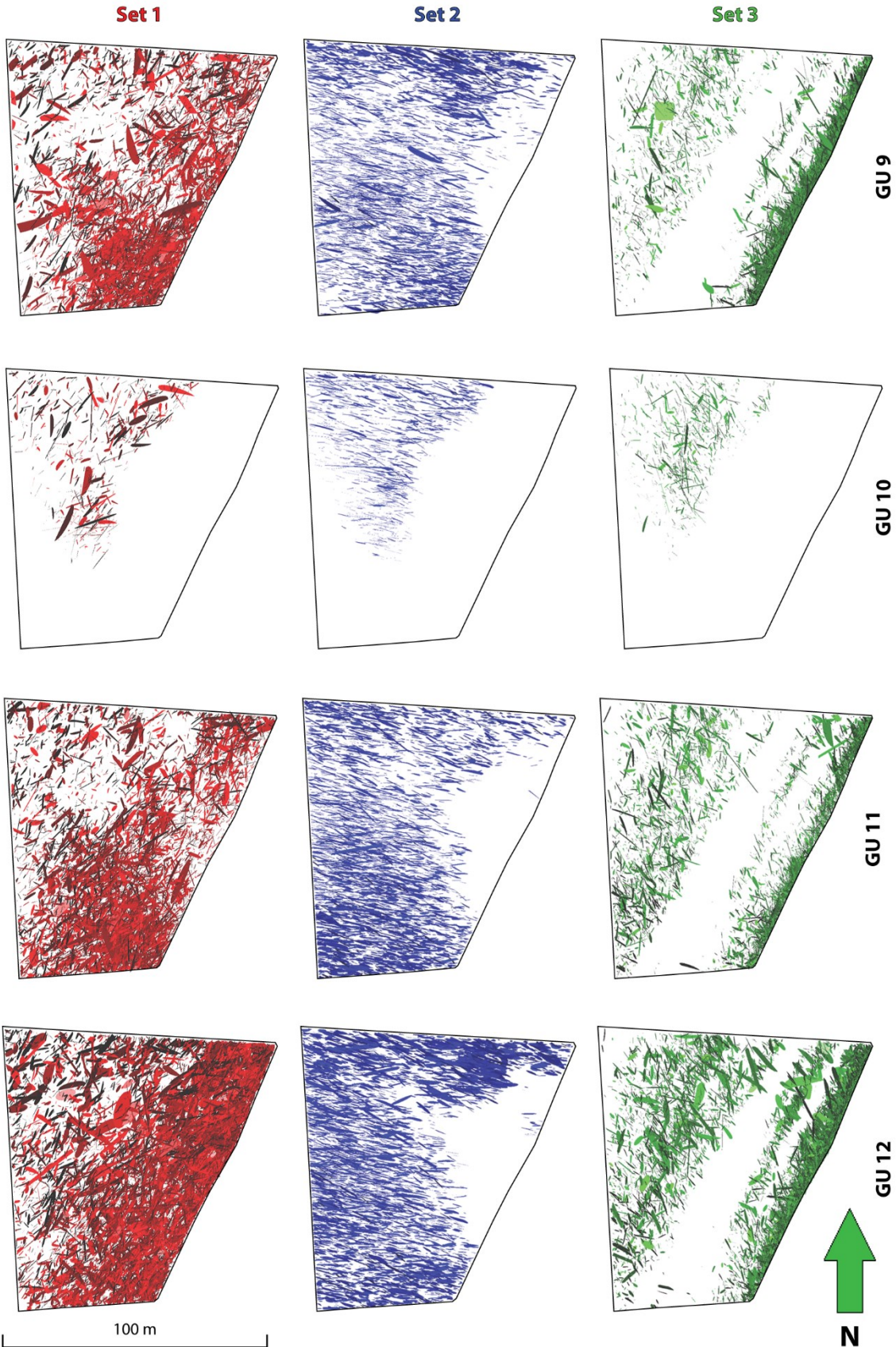
Damage zone fracture network "Tc"



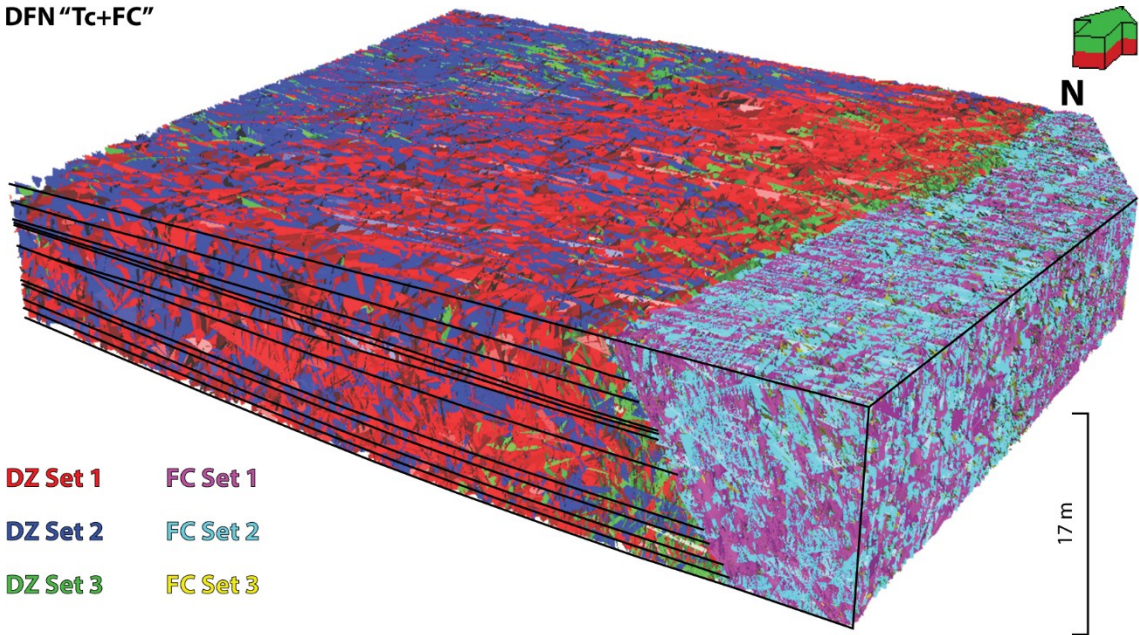
Damage zone fracture network "Tc"



Damage zone fracture network "Tc"

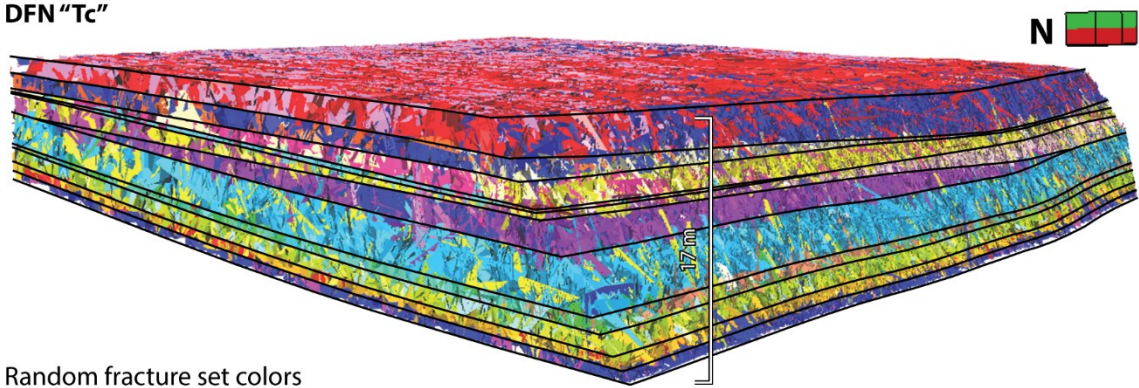


DFN "Tc+FC"



- |          |          |
|----------|----------|
| DZ Set 1 | FC Set 1 |
| DZ Set 2 | FC Set 2 |
| DZ Set 3 | FC Set 3 |

DFN "Tc"



Random fracture set colors





## **Appendix 7      Full List of Fracture Network Property Results**



Full List of Fracture Network Property Results

DFN "G"	Geobody		Damage zone		
	Network type	DFN + IFN	DFN	DFN	
	PUM	Oda	Oda	OdaC	
Permeability [D]	ki	Mean	497.20	497.70	370.70
		Std. dev.	2,939.49	2,940.61	2,276.85
		Min	0.00	0.00	0.00
		Max	403,628.00	403,628.00	383,312.99
	kj	Mean	290.63	291.22	189.97
		Std. dev.	1,877.61	1,879.17	1,331.70
		Min	0.00	0.00	0.00
		Max	400,485.98	400,485.98	380,181.98
	kk	Mean	658.36	659.28	622.13
		Std. dev.	2,806.64	2,809.14	2,658.74
		Min	0.00	0.00	0.00
		Max	179,014.02	179,014.00	170,062.99
Porosity [%]	Mean	0.38	0.38	0.38	
	Std. dev.	0.40	0.40	0.40	
	Min	1.02*10 <sup>-7</sup>	0.00	0.00	
	Max	5.75	5.75	5.75	
CI	Mean	1.21	1.21	1.21	
	Std. dev.	1.48	1.48	1.48	
	Min	0.00	0.00	0.00	
	Max	17.64	17.64	17.64	
Sigma factor [1/m <sup>2</sup> ]	Mean	150.19	150.49	150.49	
	Std. dev.	319.46	301.07	301.07	
	Min	3.80*10 <sup>-11</sup>	1.20*10 <sup>-11</sup>	1.20*10 <sup>-11</sup>	
	Max	99,270.10	10818.41	10818.41	

## Full List of Fracture Network Property Results

DFN "T"	Geobody		Damage zone		
	Network type	DFN + IFN	DFN	DFN	
	PUM	Oda	Oda	OdaC	
Permeability [D]	ki	Mean	521.30	521.73	380.88
		Std. dev.	2,355.04	2,355.94	1,817.64
		Min	0.00	0.00	0.00
		Max	219,706.00	219,706.00	208,720.99
	kj	Mean	332.08	332.45	215.58
		Std. dev.	1,768.51	1,769.16	1,222.75
		Min	0.00	0.00	0.00
		Max	210,918.00	210,918.00	126,949.00
	kk	Mean	712.31	712.95	670.82
		Std. dev.	2,871.72	2,872.76	2,714.82
		Min	0.00	0.00	0.00
		Max	211,411.01	211,410.99	200,840.00
Porosity [%]	Mean	0.40	0.40	0.40	
	Std. dev.	0.42	0.42	0.42	
	Min	3.22*10 <sup>-8</sup>	0.00	0.00	
	Max	5.26	5.26	5.26	
CI	Mean	1.29	1.29	1.29	
	Std. dev.	1.55	1.55	1.55	
	Min	0.00	0.00	0.00	
	Max	17.62	17.62	17.62	
Sigma factor [1/m <sup>2</sup> ]	Mean	161.85	161.88	161.88	
	Std. dev.	324.71	321.99	321.99	
	Min	1.9210* <sup>-11</sup>	1.20*10 <sup>-11</sup>	1.20*10 <sup>-11</sup>	
	Max	49,382.85	9779.08	9779.08	

Full List of Fracture Network Property Results

DFN "Tc"	Geobody	Damage zone			
	Network type	DFN + IFN	DFN	DFN	
	PUM	Oda	Oda	OdaC	
Permeability [D]	ki	Mean	532.33	532.61	386.44
		Std. dev.	2,369.97	2,370.64	1,818.42
		Min	0.00	0.00	0.00
		Max	219,422.00	219,422.00	157,558.99
	kj	Mean	344.64	344.89	222.59
		Std. dev.	1,815.15	1,815.52	1,245.00
		Min	0.00	0.00	0.00
		Max	210,890.99	210,890.99	115,364.00
	kk	Mean	719.73	720.19	674.67
		Std. dev.	2,866.06	2,866.76	2,697.99
		Min	0.00	0.00	0.00
		Max	169,120.00	169,382.99	160,914.00
Porosity [%]	Mean	0.41	0.41	0.41	
	Std. dev.	0.43	0.43	0.43	
	Min	1.86*10 <sup>-7</sup>	0.00	0.00	
	Max	5.92	5.92	5.92	
CI	Mean	1.31	1.31	1.31	
	Std. dev.	1.57	1.57	1.57	
	Min	0.00	0.00	0.00	
	Max	18.28	18.28	18.28	
Sigma factor [1/m <sup>2</sup> ]	Mean	166.12	166.28	166.28	
	Std. dev.	345.83	342.68	342.68	
	Min	1.92*10 <sup>-11</sup>	1.20*10 <sup>-11</sup>	1.20*10 <sup>-11</sup>	
	Max	49,382.85	12271.26	12271.26	

## Full List of Fracture Network Property Results

DFN "FC"	Geobody		Fault core		
	Network type	DFN + IFN	DFN	DFN	
	PUM	Oda	Oda	OdaC	
Permeability [D]	ki	Mean	22,944.40	22,942.15	14,129.53
		Std. dev.	52,184.47	52,174.18	32,922.99
		Min	0.00	0.00	0.00
		Max	1,702,993.54	1,702,989.95	1,155,280.00
	kj	Mean	44,313.22	44,310.23	29,571.79
		Std. dev.	113,291.47	113,291.06	77,474.79
		Min	0.00	0.00	0.00
		Max	2,088,353.92	2,088,349.95	1,466,669.95
	kk	Mean	55,186.06	55,183.17	51,749.32
		Std. dev.	124,300.80	124,300.37	117,169.82
		Min	0.00	0.00	0.00
		Max	1,950,044.67	1,950,039.94	1,852,540.03
Porosity [%]	Mean	0.70	0.70	0.70	
	Std. dev.	1.11	1.11	1.11	
	Min	0.00	0.00	0.00	
	Max	18.99	18.99	18.99	
CI	Mean	2.94	2.94	2.94	
	Std. dev.	2.03	2.03	2.03	
	Min	0.00	0.00	0	
	Max	17.06	17.06	17.06	
Sigma factor [1/m <sup>2</sup> ]	Mean	471.48	526.76	526.76	
	Std. dev.	629.58	605.85	605.8498	
	Min	0.00	1.20*10 <sup>-11</sup>	1.20*10 <sup>-11</sup>	
	Max	9,248.94	9,225.38	9225.377	

Full List of Fracture Network Property Results

DFN "G+FC"	Geobody	Damage zone and fault core			
	Network type	DFN + IFN	DFN	DFN	
	PUM	Oda	Oda	OdaC	
Permeability [D]	ki	Mean	4,100.13	4,099.77	2,604.36
		Std. dev.	23,434.39	23,434.01	14,995.41
		Min	0.00	0.00	0.00
		Max	1,703,773.57	1,703,869.98	1,338,380.03
	kj	Mean	7,146.92	7,146.44	4,803.68
		Std. dev.	46,834.50	46,833.98	32,174.71
		Min	0.00	0.00	0.00
		Max	2,231,117.57	2,231,109.89	1,762,400.00
	kk	Mean	9,273.76	9,273.31	8,711.50
		Std. dev.	53,581.69	53,581.15	50,479.67
		Min	0.00	0.00	0.00
		Max	1,930,227.20	1,930,220.03	1,833,709.95
Porosity [%]	Mean	0.70	0.70	0.70	
	Std. dev.	1.11	1.11	1.11	
	Min	0.00	0.00	0.00	
	Max	18.99	18.99	18.99	
CI	Mean	1.51	1.51	1.51	
	Std. dev.	1.78	1.78	1.78	
	Min	0.00	0.00	0.00	
	Max	17.64	17.64	17.64	
Sigma factor [1/m <sup>2</sup> ]	Mean	206.81	216.95	216.95	
	Std. dev.	424.28	412.39	412.39	
	Min	0.00	1.20*10 <sup>-11</sup>	1.20*10 <sup>-11</sup>	
	Max	99,260.62	10,818.41	10,818.41	

## Full List of Fracture Network Property Results

DFN "T+FC"	Geobody	Damage zone and fault core			
	Network type	DFN + IFN	DFN	DFN	
	PUM	Oda	Oda	OdaC	
Permeability [D]	ki	Mean	3,992.24	3,991.78	2,517.82
		Std. dev.	22,139.95	22,139.56	13,990.94
		Min	0.00	0.00	0.00
		Max	1,702,993.54	1,702,989.95	1,155,280.00
	kj	Mean	7,086.26	7,085.78	4,739.42
		Std. dev.	47,035.76	47,035.25	32,160.35
		Min	0.00	0.00	0.00
		Max	2,088,353.92	2,088,349.95	1,466,669.95
	kk	Mean	9,102.39	9,101.94	8,543.21
		Std. dev.	52,483.98	52,483.44	49,462.26
		Min	0.00	0.00	0.00
		Max	1,950,054.78	1,950,050.05	1,852,550.02
Porosity [%]	Mean	0.71	0.71	0.71	
	Std. dev.	1.09	1.09	1.09	
	Min	0.00	0.00	0.00	
	Max	20.46	20.46	20.46	
CI	Mean	1.55	1.55	1.55	
	Std. dev.	1.76	1.76	1.76	
	Min	0.00	0.00	0.00	
	Max	17.62	17.62	17.62	
Sigma factor [1/m <sup>2</sup> ]	Mean	211.17	220.23	220.23	
	Std. dev.	409.33	408.58	408.5759	
	Min	0.00	1.20*10 <sup>-11</sup>	1.20*10 <sup>-11</sup>	
	Max	49,382.85	8,978.58	8978.5801	



Full List of Fracture Network Property Results

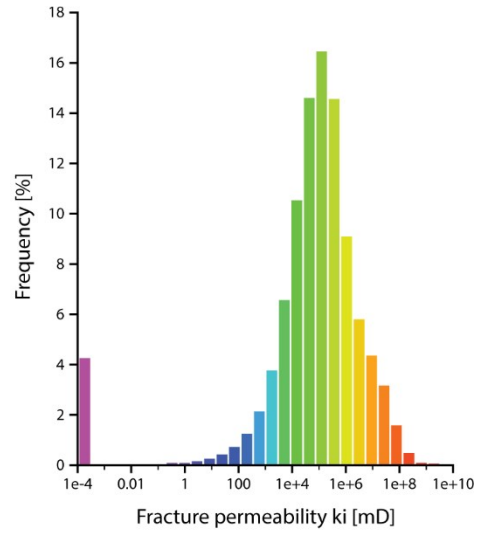
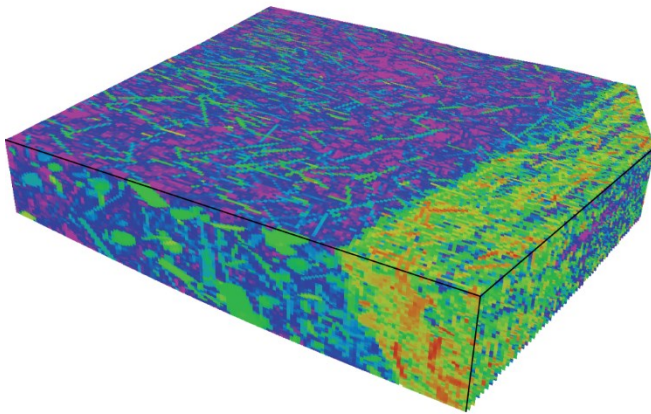
DFN "Tc+FC"	Geobody	Damage zone and fault core			
	Network type	DFN + IFN	DFN	DFN	
	PUM	Oda	Oda	OdaC	
Permeability [D]	ki	Mean	3,999.96	3,999.59	2,515.02
		Std. dev.	22,134.31	22,133.91	13,952.83
		Min	0.00	0.00	0.00
		Max	1,702,993.54	1,702,989.95	1,155,280.00
	kj	Mean	7,094.84	7,094.36	4,732.70
		Std. dev.	47,034.40	47,033.89	32,095.61
		Min	0.00	0.00	0.00
		Max	2,088,353.92	2,088,349.95	1,466,669.95
	kk	Mean	9,106.33	9,105.88	8,536.97
		Std. dev.	52,478.47	52,477.93	49,424.75
		Min	0.00	0.00	0.00
		Max	1,950,044.67	1,950,039.94	1,852,540.03
Porosity [%]	Mean	0.71	0.71	0.71	
	Std. dev.	1.09	1.09	1.09	
	Min	0.00	0.00	0.00	
	Max	20.46	20.46	20.46	
CI	Mean	1.56	1.56	1.56	
	Std. dev.	1.77	1.77	1.77	
	Min	0.00	0.00	0.00	
	Max	18.28	18.28	18.28	
Sigma factor [1/m <sup>2</sup> ]	Mean	213.96	222.55	222.55	
	Std. dev.	422.78	419.29	418.29	
	Min	0.00	1.20*10 <sup>-11</sup>	1.20*10 <sup>-11</sup>	
	Max	49,385.93	12,271.18	12,271.18	



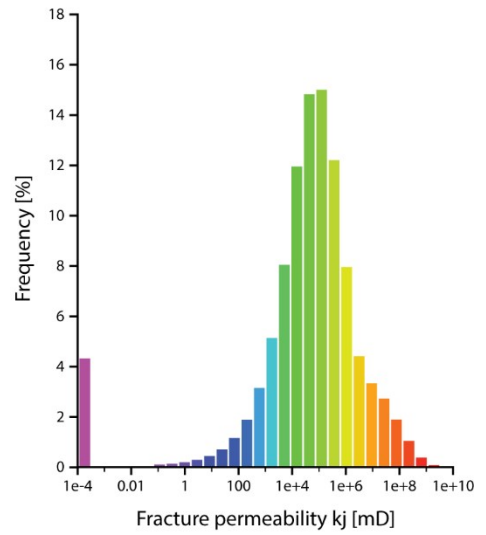
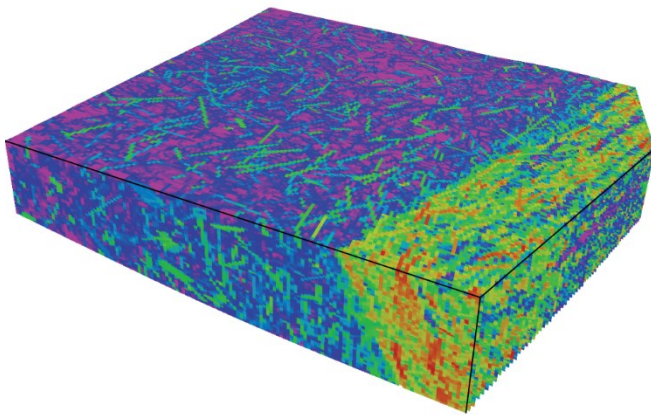
## **Appendix 8      All Illustrations of DFN Property Results**



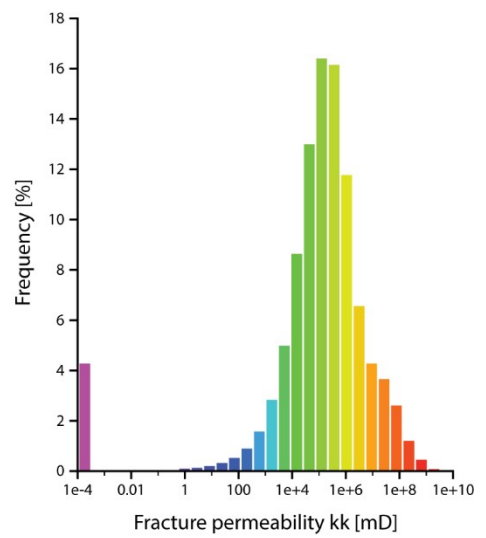
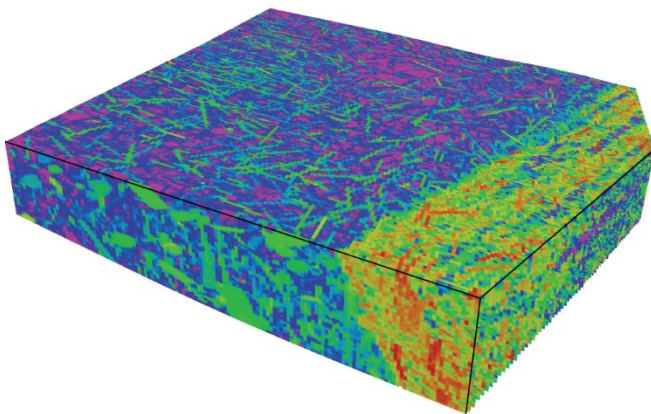
**Fracture permeability  $k_i$  of DFN "G+FC" (Oda)**



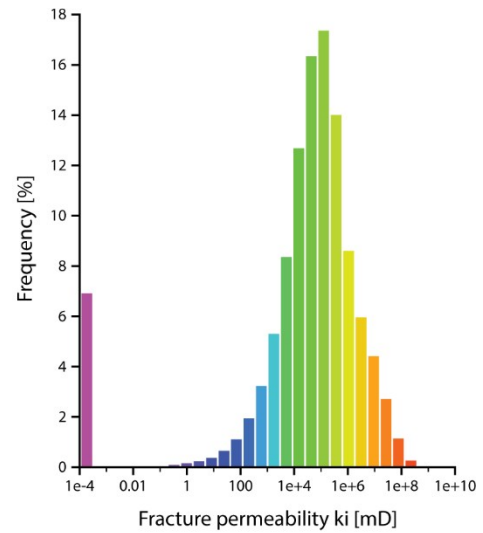
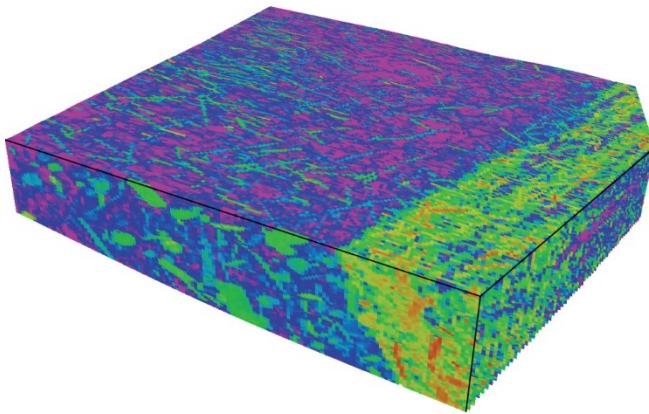
**Fracture permeability  $k_j$  of DFN "G+FC" (Oda)**



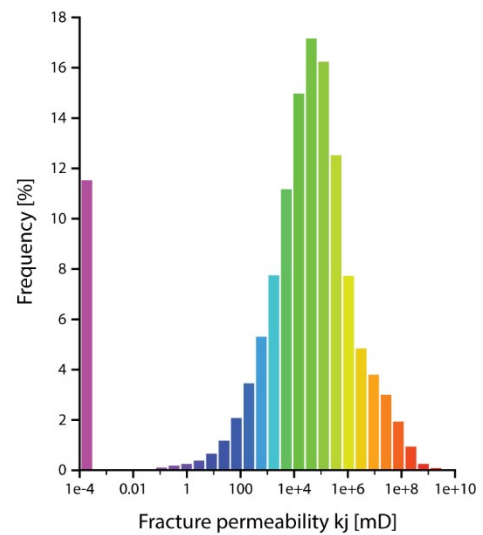
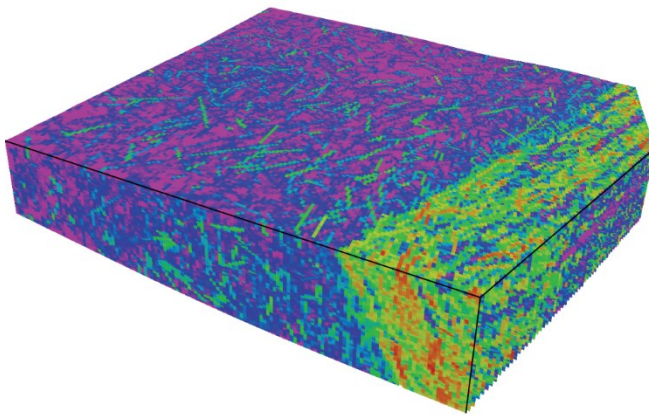
**Fracture permeability  $k_k$  of DFN "G+FC" (Oda)**



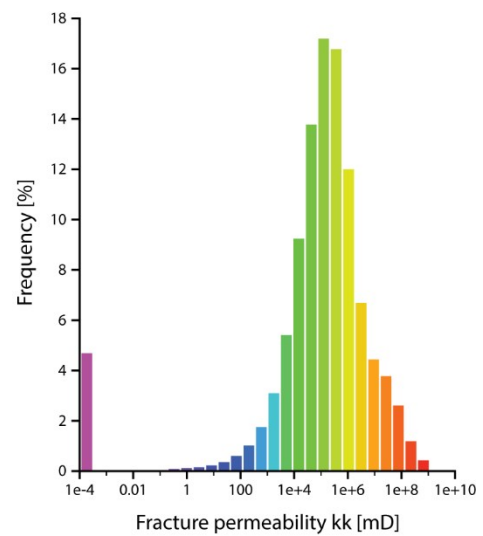
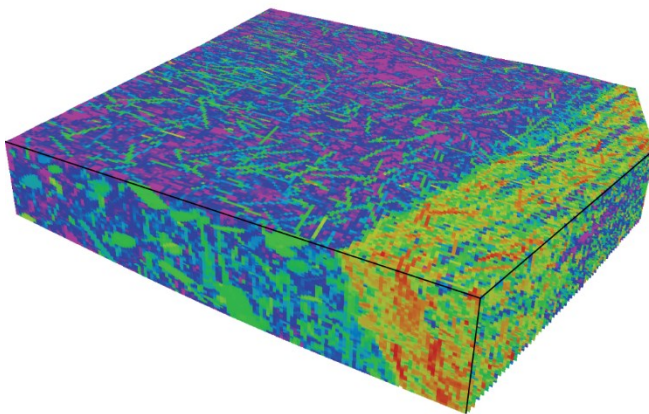
**Fracture permeability  $k_i$  of DFN "G+FC" (OdaC)**



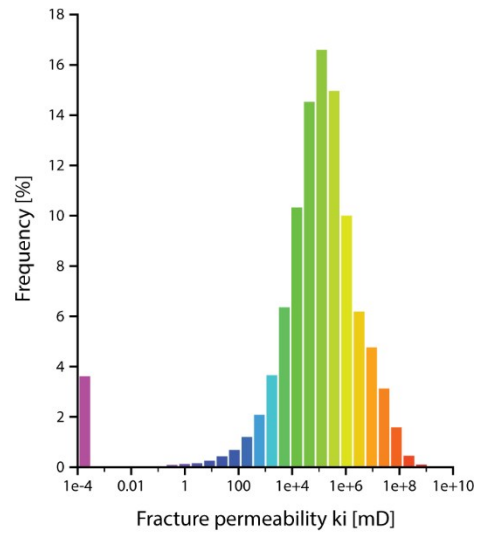
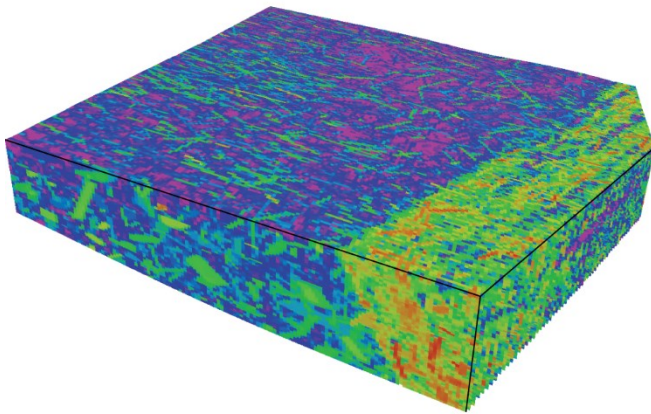
**Fracture permeability  $k_j$  of DFN "G+FC" (OdaC)**



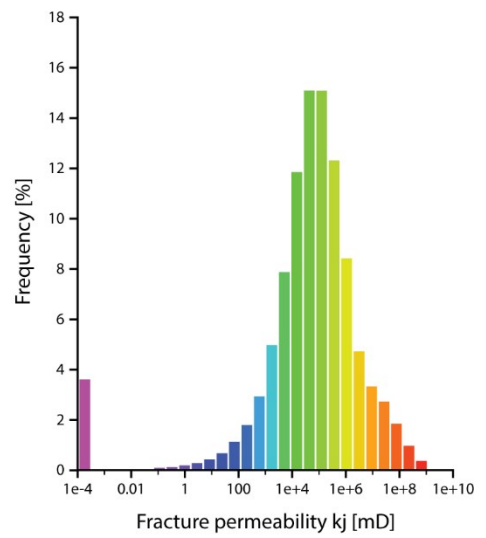
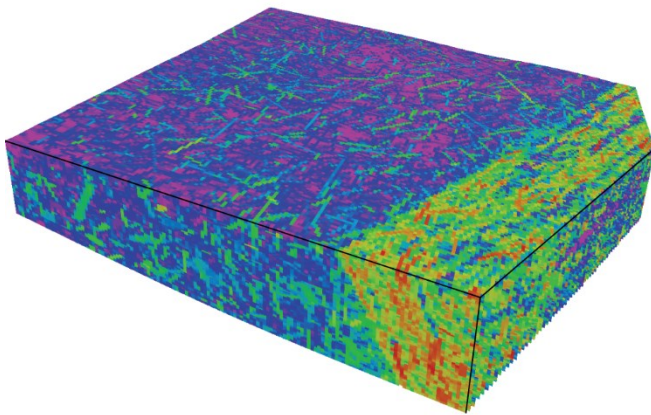
**Fracture permeability  $k_k$  of DFN "G+FC" (OdaC)**



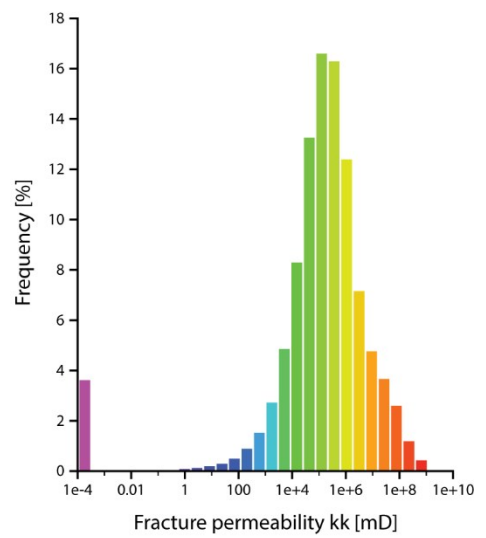
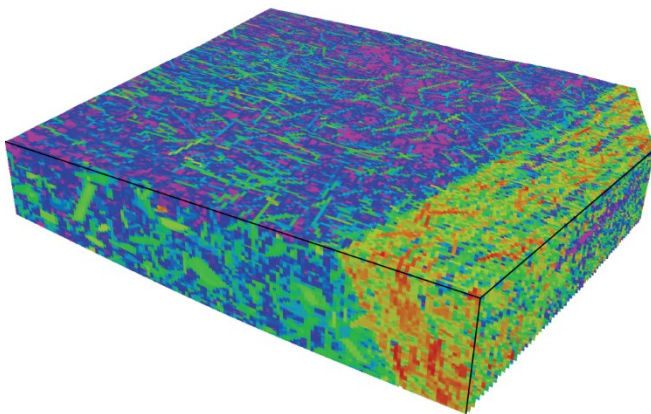
Fracture permeability  $k_i$  of DFN "T+FC" (Oda)



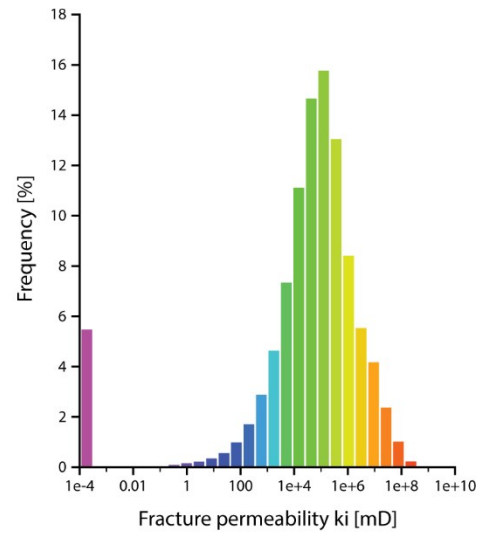
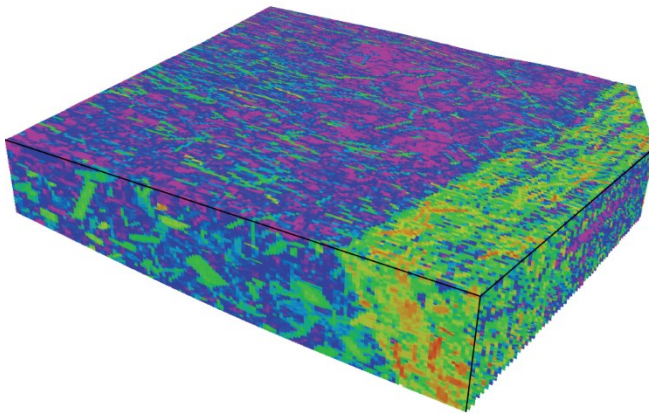
Fracture permeability  $k_j$  of DFN "T+FC" (Oda)



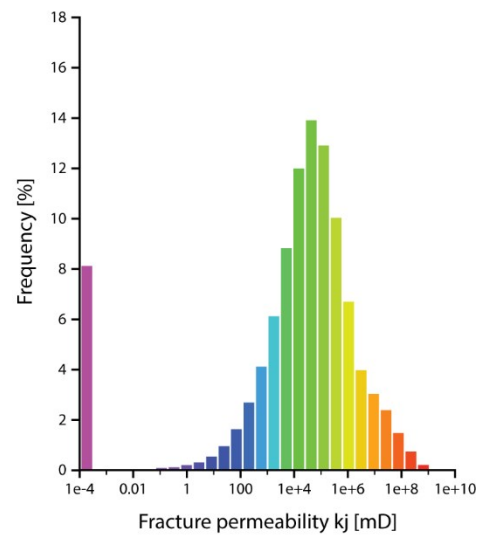
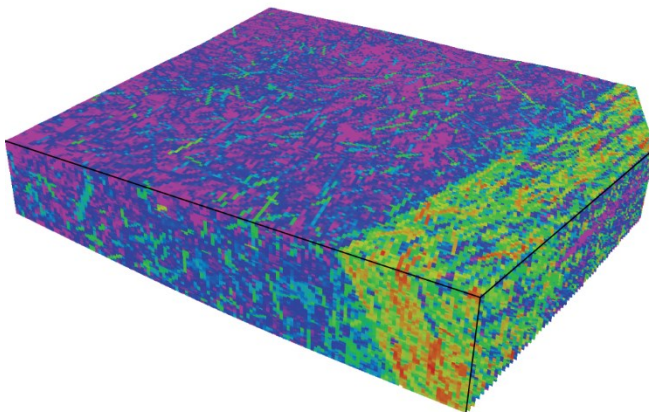
Fracture permeability  $k_k$  of DFN "T+FC" (Oda)



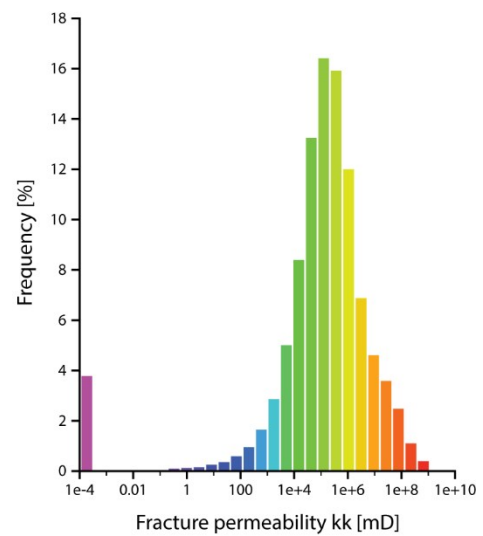
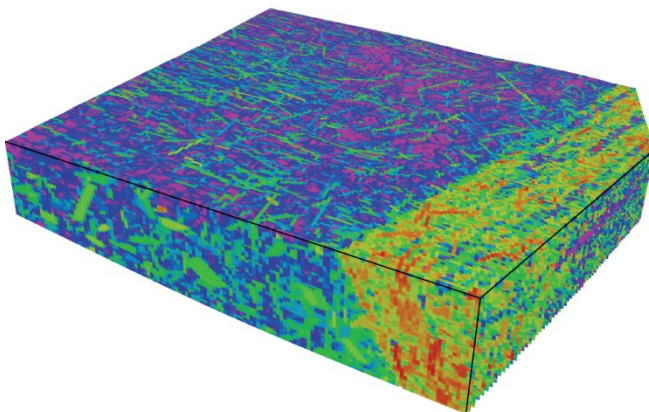
**Fracture permeability  $k_i$  of DFN "T+FC" (OdaC)**



**Fracture permeability  $k_j$  of DFN "T+FC" (OdaC)**

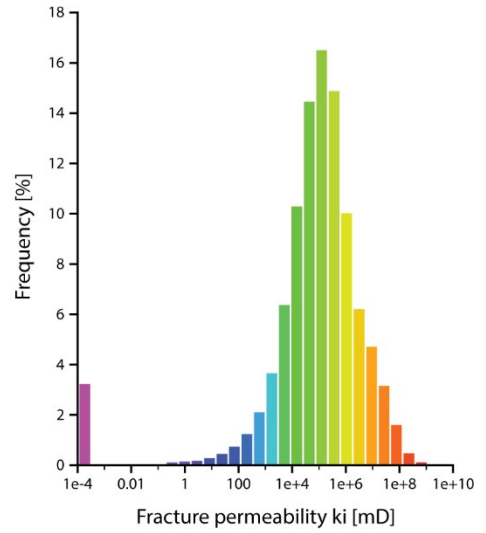
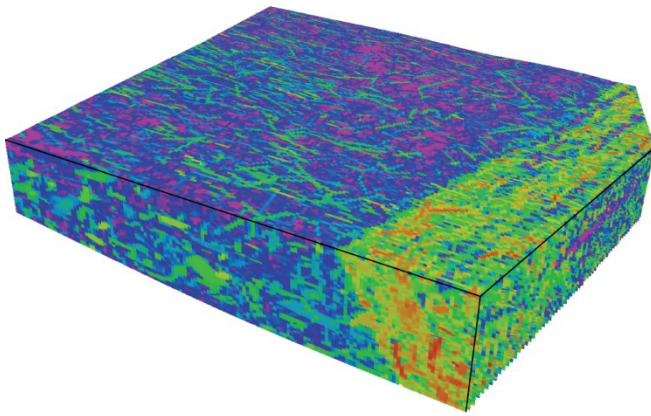


**Fracture permeability  $k_k$  of DFN "T+FC" (OdaC)**

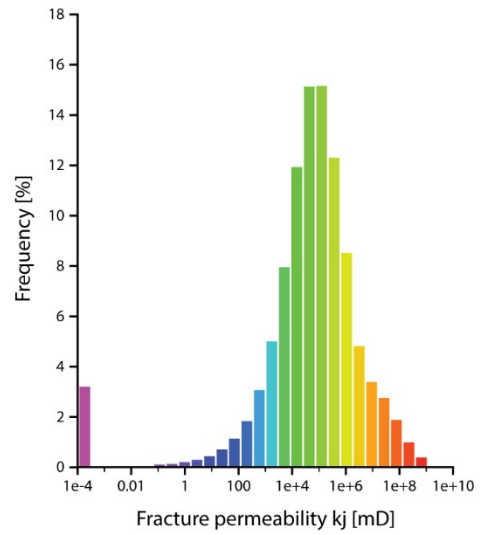
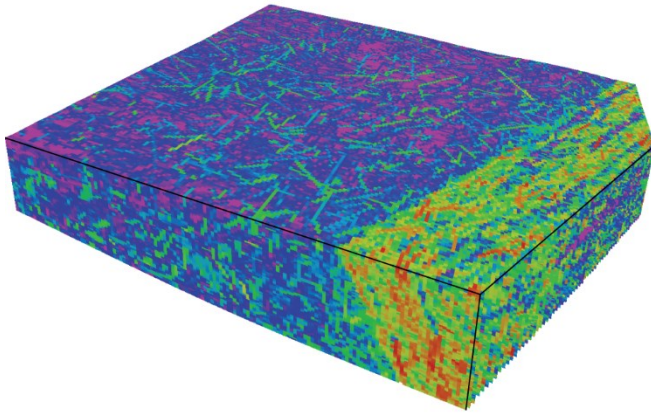




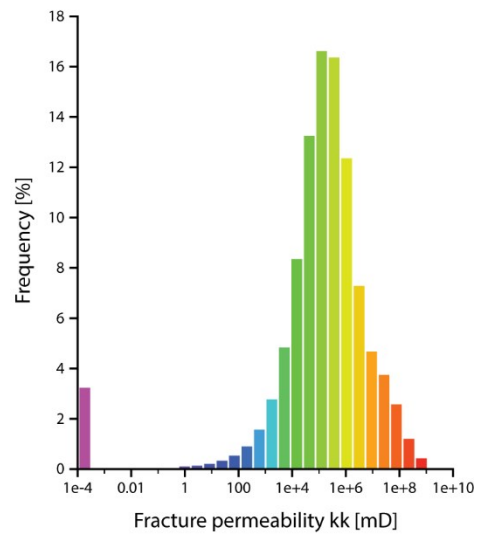
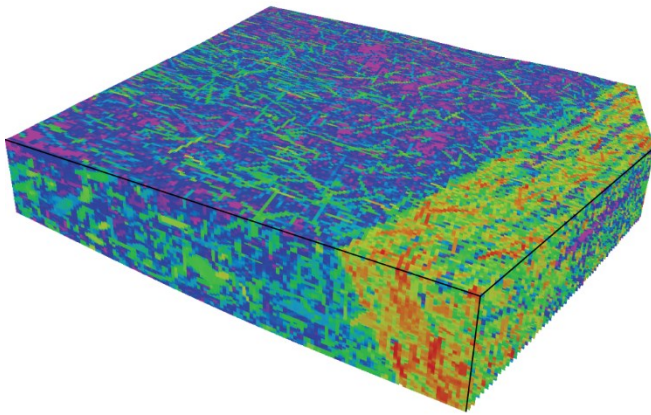
Fracture permeability  $k_i$  of DFN "Tc+FC" (Oda)



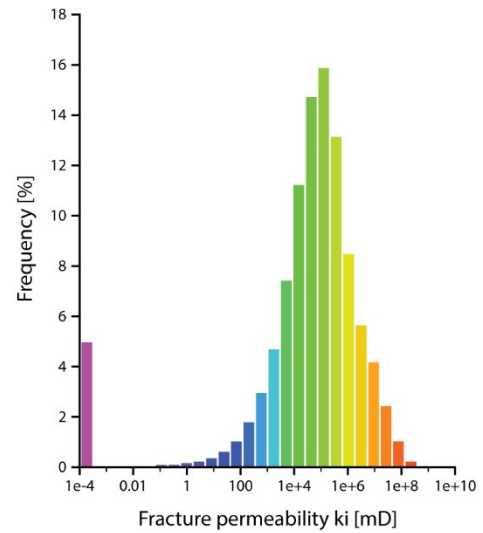
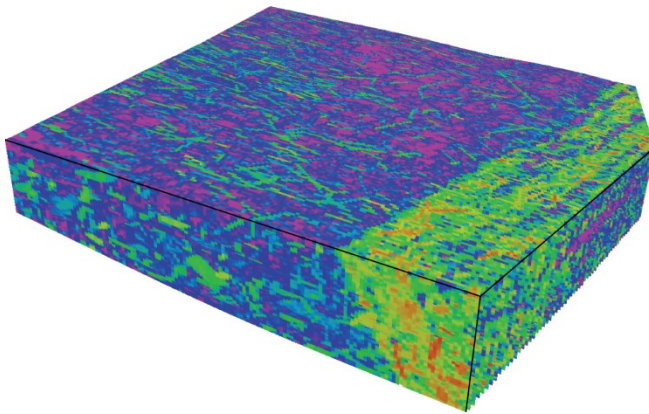
Fracture permeability  $k_j$  of DFN "Tc+FC" (Oda)



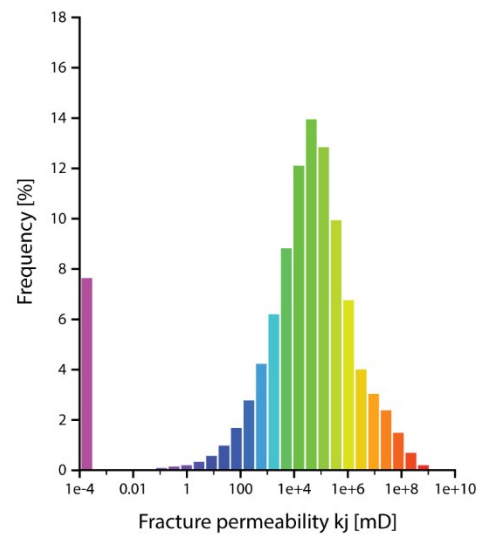
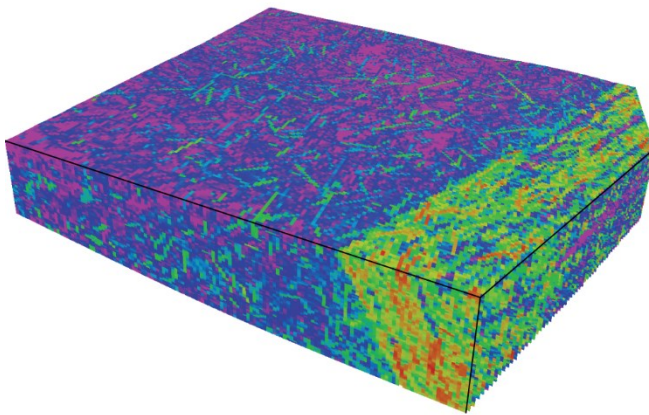
Fracture permeability  $k_k$  of DFN "Tc+FC" (Oda)



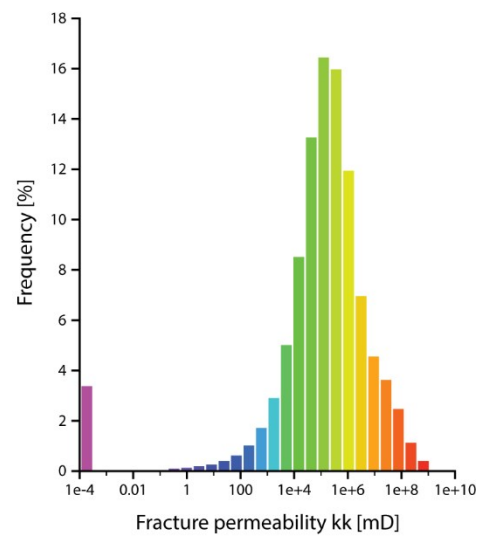
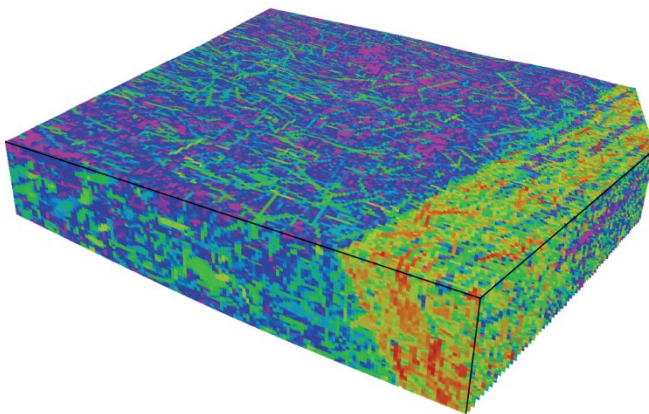
**Fracture permeability  $k_i$  of DFN "Tc+FC" (OdaC)**



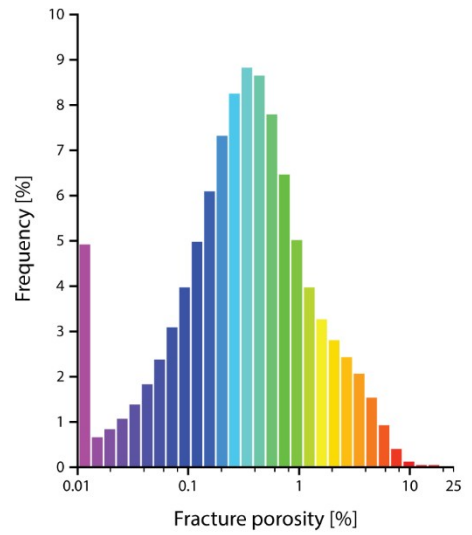
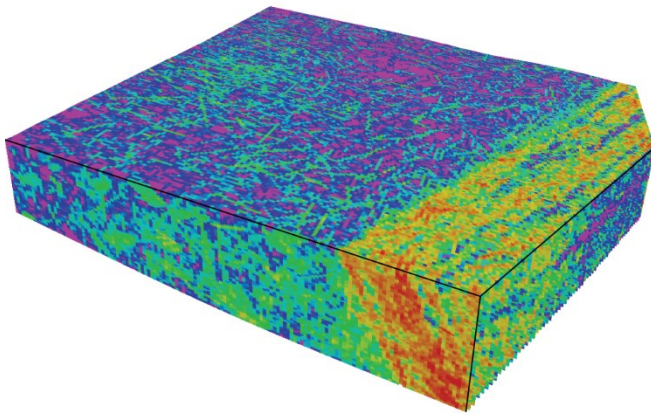
**Fracture permeability  $k_j$  of DFN "Tc+FC" (OdaC)**



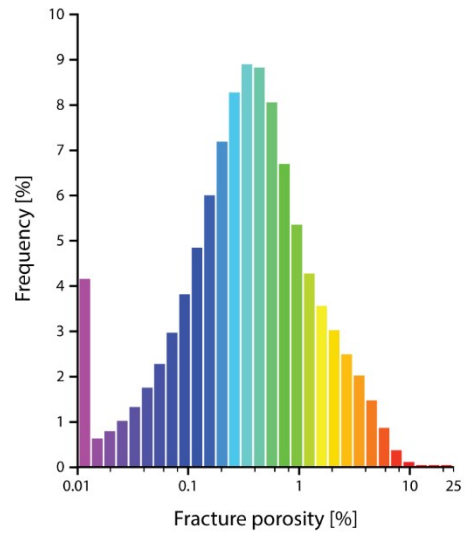
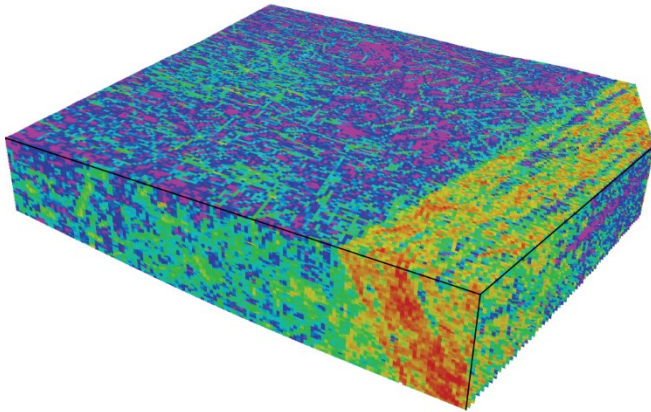
**Fracture permeability  $k_k$  of DFN "Tc+FC" (OdaC)**



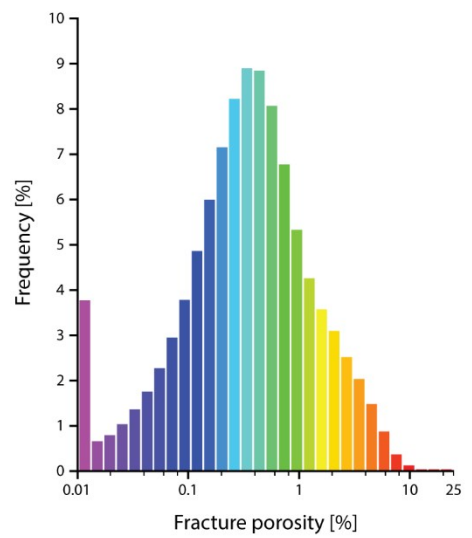
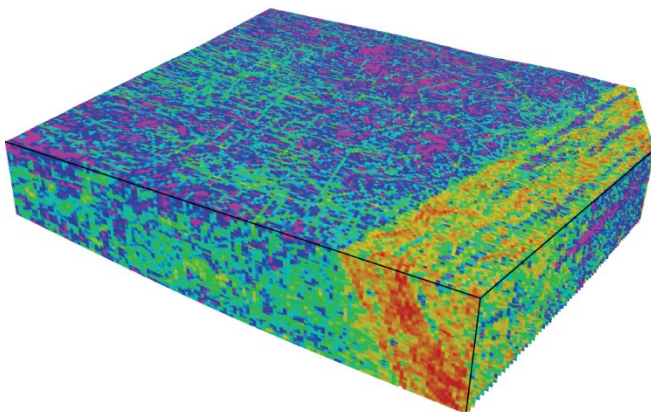
**Fracture porosity of DFN "G+FC"**



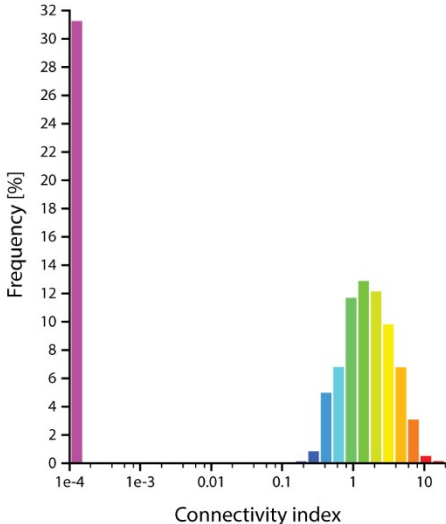
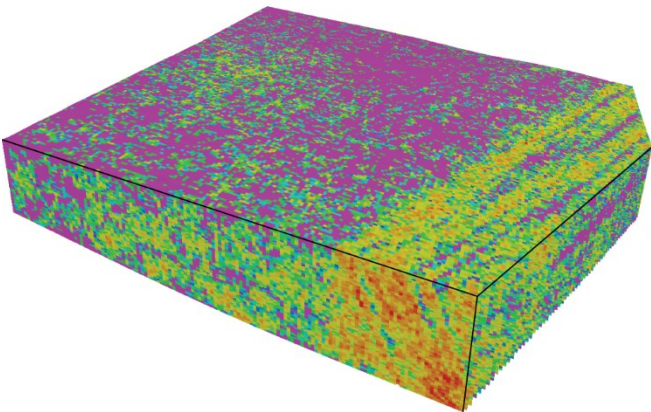
**Fracture porosity of DFN "T+FC"**



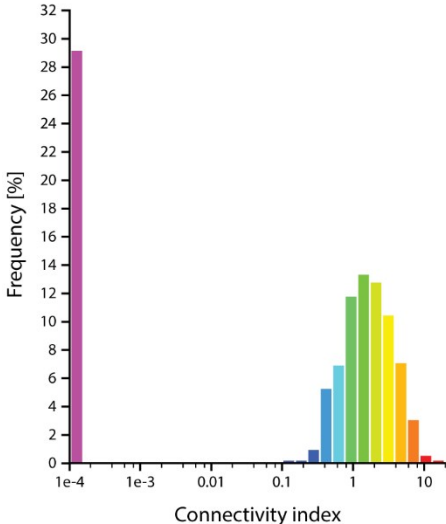
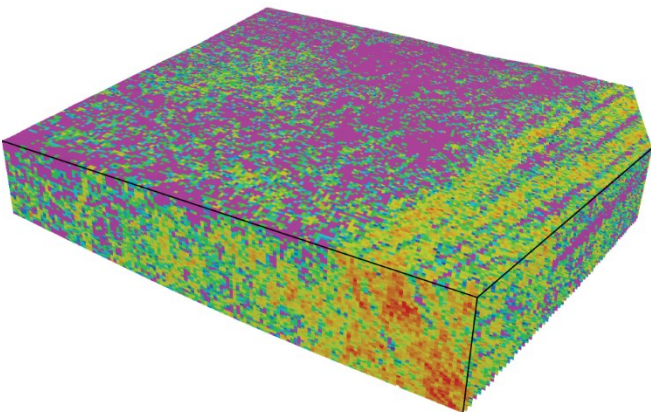
**Fracture porosity of DFN "Tc+FC"**



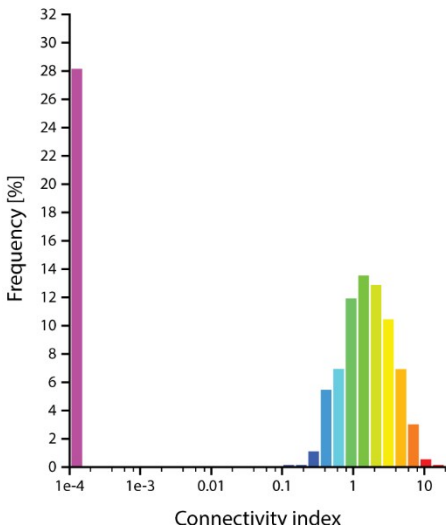
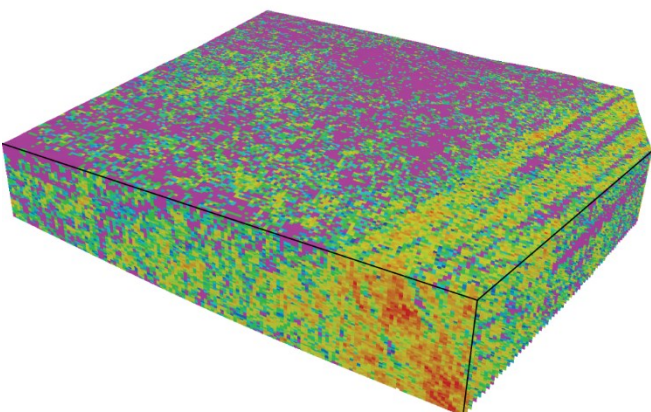
**Fracture connectivity index of DFN "G+FC"**



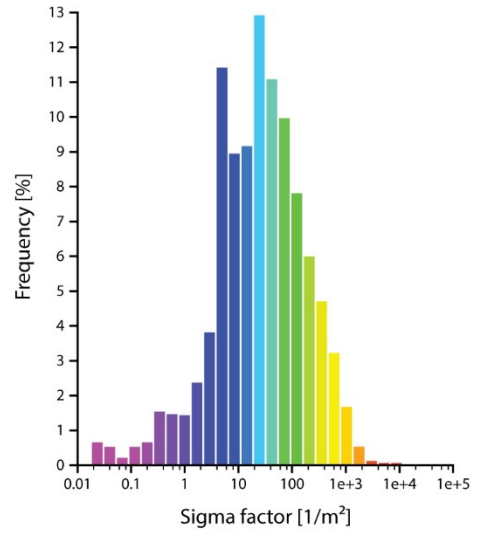
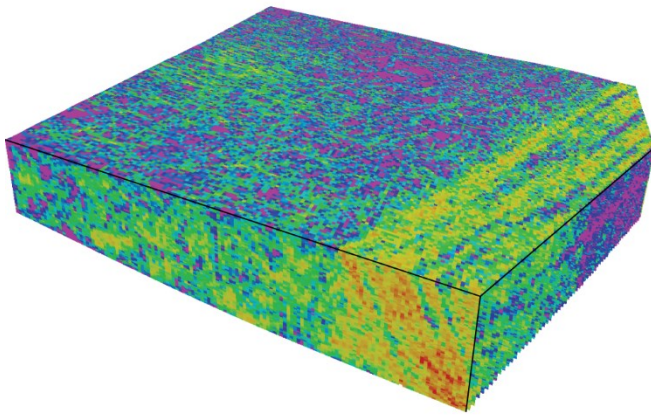
**Fracture connectivity index of DFN "T+FC"**



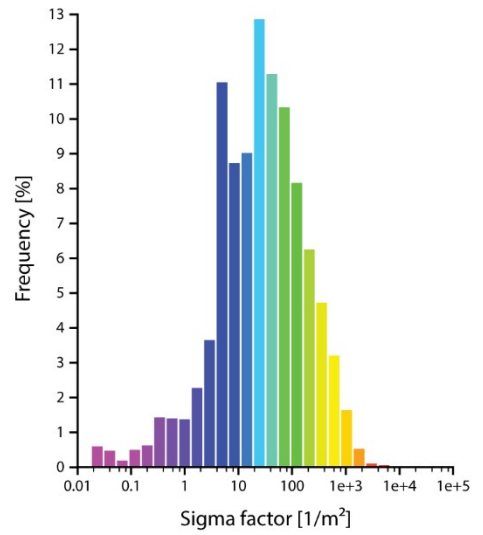
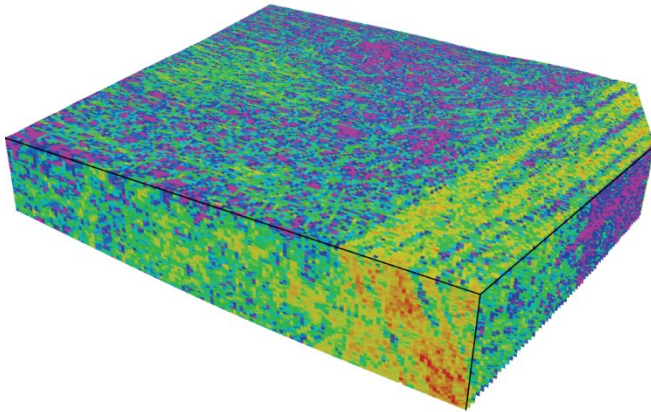
**Fracture connectivity index of DFN "Tc+FC"**



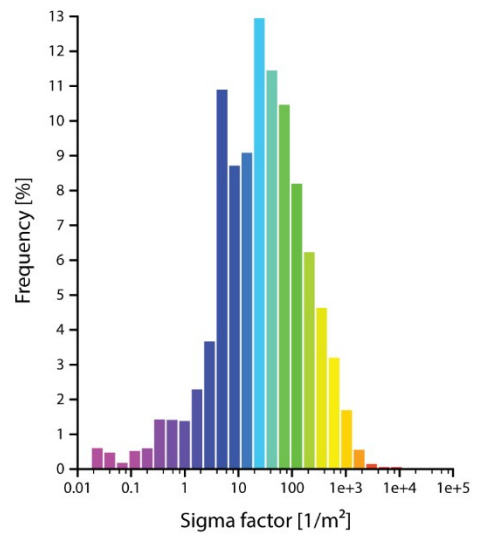
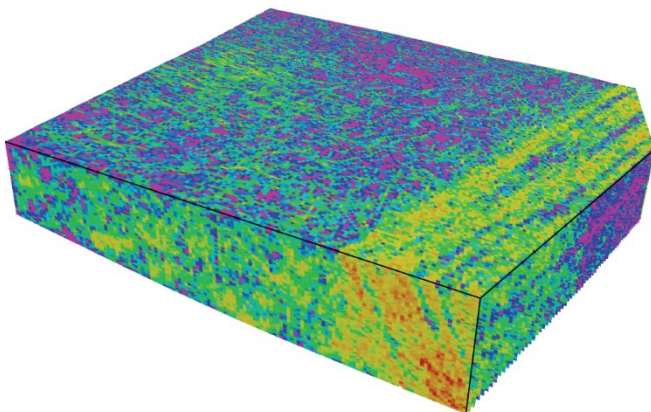
**Sigma factor of DFN "G+FC"**



**Sigma factor of DFN "T+FC"**



**Sigma factor of DFN "Tc+FC"**





## **Danksagung**

Ich danke meinem Betreuer Wolfgang Stinnesbeck. Deine stete Unterstützung und das mir entgegengebrachte Vertrauen ermöglichten es mir, meine Ideen zu verfolgen und zu verwirklichen.

Ein herzlicher Dank geht an Thilo Bechstädt, der mir über all die Jahre hinweg immer mit Rat und Tat zur Seite stand. Deine konstruktive Kritik und überaus hilfreichen Verbesserungsvorschläge haben maßgeblich zum erfolgreichen Abschluss dieser Arbeit beigetragen.

Ein besonderer Dank geht an Axel Emmerich für die Opferung seiner Freizeit, um auch noch zu später Stunde über die Entwicklung und die Möglichkeiten meiner Arbeit zu diskutieren. Unsere Gespräche brachten immer wieder neue Ideen hervor und haben meine Arbeit essentiell beeinflusst.

Axel Wenke, Hartmut Jäger und Rainer Zühlke danke ich herzlichst für das stets offene Ohr und unsere Gespräche, insbesondere zu meiner Anfangszeit am Institut.

Meinen Kollegen Till, Dominik, Christian, Lennart, Hermann, Sven, Melissa, Tom, Torben, Patrick, Fabio und Seija. Ich danke Euch für die angenehme Atmosphäre und die Möglichkeit stets fachliche, aber auch „fachfremde“ Diskussionen zu führen.

Ein Dank geht auch an die Kooperationspartner aus dem Projekt AuGE: Axel, René, John, Johanna, Maria, Silke, Harald Stollhofen und Sonja Philipp.

Ich möchte dem Bundesministerium für Umwelt und dem Bundesministerium für Wirtschaft danken, diese Arbeit ermöglicht zu haben. Darüber hinaus danke ich Schlumberger für die Bereitstellung akademischer Lizenzen.

An meine geliebten Eltern und meinen (auch geliebten) Bruder: Ich danke Euch für die absolut uneingeschränkte Unterstützung während all der Jahre. Ohne Euch wäre diese Arbeit nicht realisierbar gewesen!

Und vielen Dank auch an Bone, Chris, Deus, Flo, Flomo, Geri, Snaky, Spike, Volker und Zonk für die permanente Frage, wie denn meine Steine schmecken. Das war ungemein hilfreich.





**Eidesstattliche Versicherung gemäß §8 der Promotionsordnung  
der Naturwissenschaftlich-Mathematischen Gesamtfakultät  
der Universität Heidelberg**

1. Bei der eingereichten Dissertation zu dem Thema

**TLS supported volumetric and DFN modeling of a fault zone in the Lower  
Buntsandstein, SW Germany**

handelt es sich um eine eigenständig erbrachte Leistung.

2. Ich habe nur die angegebenen Quellen und Hilfsmittel benutzt und mich keiner unzulässigen Hilfe Dritter bedient. Insbesondere habe ich wörtlich oder sinngemäß aus anderen Werken übernommene Inhalte als solche kenntlich gemacht.
3. Die Arbeit oder Teile davon habe ich bislang nicht an einer Hochschule des In- oder Auslands als Bestandteil einer Prüfungs- oder Qualifikationsleistung vorgelegt.
4. Die Richtigkeit der vorstehenden Erklärungen bestätige ich.
5. Die Bedeutung der eidesstattlichen Versicherung und die strafrechtlichen Folgen einer unrichtigen oder unvollständigen eidesstattlichen Versicherung sind mir bekannt.

Ich versichere an Eides statt, dass ich nach bestem Wissen die reine Wahrheit erklärt und nichts verschwiegen habe.

\_\_\_\_\_  
Ort und Datum

\_\_\_\_\_  
Unterschrift